Project No. 09-777

Liquid Salt Heat Exchanger Technology for VHTR Based Applications

Reactor Concepts RD&D

Dr. Mark Anderson
University of Wisconsin - Madison

In collaboration with:
University of California, Berkeley

Piyush Sabharwall, Technical POC
Carl Sink, Federal POC

NEUP Nuclear Energy University Programs
U.S. Department of Energy


NEUP
Nuclear Energy
University Programs
U.S. Department of Energy

FINAL REPORT

Project Title: Liquid Salt Heat Exchanger Technology for VHTR-based Applications
Covering Period: May 1, 2009 through September 30, 2012
Date of Report: October 30, 2012
Recipient: University of Wisconsin – Madison
Department of Engineering Physics
1500 Engineering Drive
Madison, WI, 53706

Award Number: 09-777
Project Number: 144-PRJ29LY
Principal Investigators:

Anderson, Mark
(608) 263-2802
manderson@engr.wisc.edu

Sridharan, Kumar
(608) 263-4789
kumar@engr.wisc.edu

Todd Allen
(608) 265-4083
allen@engr.wisc.edu

Collaborators:

Peterson, Per
(510) 643-7749
peterson@nuc.berkeley.edu

Project Objective: The primary objective of this project is to study efficient and economical high-temperature system to transfer process heat generated by the very high temperature reactor (VHTR) to chemical processing plants and to determine the feasibility of using liquid salts for nuclear reactor operations. This project has been divided into three tasks.

The first task deals with the material compatibility issues associated with liquid salts and the development of on-line instrumentation capable of measuring corrosion product concentrations to determine material loss in heat exchangers. This task will examine static corrosion of selected candidate materials and will develop an electrochemical probe to measure metallic species' concentrations dissolved in a liquid salt.

The second task deals with the design of heat exchanger systems for the intermediate side (between the reactor helium coolant and the salt) and for the process side (between the salt and the chemical process). The materials used on the reactor side must have good creep-rupture strength at high temperatures while maintaining low pressure losses. These heat exchangers will most likely be metallic structures in the near term with the possibility of using ceramics in the future. On the

process side, it is possible that highly corrosive liquids, such as those associated with the sulfur-iodine hydrogen generation process, will contact the heat exchanger. The pressures on this side are typically low in both fluids, however, depending on the process application, they may be very corrosive and the heat exchanger may need to be constructed with advanced ceramics.

The third task focuses integral testing of flowing liquid salts in a heat transfer/materials loop to determine potential issues of using the salts and to capture realistic behavior of the salts in a small scale prototype system. This includes investigations of plugging issues, heat transfer, pressure drop, and the corrosion and erosion of materials in the flowing system.

Task 1: Corrosion and development of electro-chemical probe

In addition to producing electricity, it is envisioned that the next generation nuclear reactor, the Very High Temperature Reactor (VHTR), will also be designed to provide high temperature process heat for the production of hydrogen. To utilize the high temperature process heat from the reactor, an intermediate heat transport fluid must be used to transfer heat from the reactor to the hydrogen production facility. A number of molten salts have been suggested as heat transfer media including FLiNaK (46.5 mol% LiF-11.5 mol% NaF-42 mol% KF) and $MgCl_2$-KCl (32 mol% $MgCl_2$-68 mol% KCl). Molten salts have excellent heat storage and heat transfer capabilities, but these salts can be corrosive to materials at high temperatures. To use molten salts for this application, an understanding of the underlying corrosion mechanisms of various candidate materials in molten salts is essential. To achieve this objective, an *in situ* probe has been developed using anodic stripping voltammetry (ASV) to detect dissolved metallic impurities, particularly Cr, in the salts. Using this technique, the reduction potential of Cr was determined against a Pt quasi-reference electrode as well as against a Ni(II)/Ni reference electrode in molten FLiNaK at 650 ^{o}C. 10 mol% and 1 mol% Ni(II)/Ni reference electrodes were tested. Neutron activation analysis (NAA) has been used to independently determine concentrations of metal cation impurities that are dissolved into the salt during the corrosion process. Using the high temperature ASV in conjunction with NAA, working curves of integrated current versus concentration were developed for Cr. From the standpoint of advancing basic science, the research provides an insight into corrosion mechanisms *in situ* at high temperatures, and from an applications standpoint, it provides the basis for the development of an on-line high temperature corrosion diagnostics for high temperature molten salt environments.

Neutron activation analysis provided repeatable results when molten samples of FLiNaK were taken and allowed to freeze before irradiation. Neutron activation analysis was also used to determine elemental impurities in FLiNaK and $MgCl_2$-KCl salts used for static corrosion tests and to help choose the best method of purifying $MgCl_2$-KCl salt.

2. Introduction

2.1 Motivation

The next generation nuclear plant (NGNP) proposed by DOE, National Laboratories, and industry will most likely be a very high temperature, helium cooled reactor. It has been proposed that the high temperature process heat from this reactor be used for hydrogen production. The hydrogen plant will be situated in the vicinity of the nuclear reactor, but a minimum distance will be kept between the two for safety. To transport the process heat from the reactor to the hydrogen production plant through this long heat transfer path, an intermediate fluid must be used. FLiNaK (46.5 mol% LiF-11.5 mol% NaF-42 mol% KF) and $MgCl_2$-KCl (32 mol% $MgCl_2$-68 mol% KCl) have been suggested as possible heat transfer fluids due to their excellent heat transfer properties. However, due to their corrosive nature, the corrosion of components in the intermediate heat transfer loop must be monitored during the experiment, from the standpoints of both safety and economics.

2.2 Corrosion Analysis

Corrosion in molten salts is driven by a dissolution process that leads to dealloying of materials rather than oxidation. Understanding and measuring dissolution rates are critical to understanding material performance in molten salts. An *in situ*, on-line probe can lead to a fundamental understanding of dissolution of various elemental species and the role of reducing agents in the mitigation of these corrosion and dissolution processes. The corrosion probe must effectively determine which element is being dissolved into the molten salts, detect concentration levels of these elements in the salt in the 1-1000 parts per million (PPM) range, and take quick measurements with respect to the time frame of the overall test. Additionally, the corrosion probe must be stable in regards to providing reproducible results over multiple tests.

An electrochemical technique, anodic stripping voltammetry (ASV), can potentially fulfill the requirements for this corrosion probe. Initial calibration of the probe can be performed by the determination of the elemental impurities in the salt by neutron activation analysis (NAA). Concentrations are then correlated to integrated peak currents from the voltammetry experiments. Elements of particular interest in ASV and NAA are Cr, Fe, and Ni that form the basis for most high temperature, code-certified metallic alloys.

3. Literature Review

If the reader is unfamiliar with the experimental methods discussed in the following section, a detailed description is given in section 5.

3.1 Prior Research on Molten Fluoride Salts

During the cold war, the concept of a nuclear powered aircraft was attractive due to the ability to fly for long periods of time without refueling. The Aircraft Research Experiment (ARE) analyzed fuels and materials needed to power an aircraft while being light enough to fly, i.e. requiring a very high power density. A fuel that consisted of UF_4 dissolved in molten fluoride salts was found to have a high enough power density. The fuel salt used in the ARE was NaF-ZrF_4-UF_4 (53.09 mol% NaF-40.73 mol% ZrF_4-6.18 mol% UF_4) **[1]**. Other fuel mixtures tested were NaF-KF-LiF-UF_4 (11.2 mol% NaF-41 mol% KF-45.3 mol% LiF-2.5 mol% mol% UF_4) and NaF-ZrF_4-UF_4 (50 mol% NaF-46 mol% ZrF_4-4 mol% UF_4). The main mechanism of corrosion observed was dissolution of metals in a hot leg and redoposition in a cold leg. It was found that when the UF_4 was not added to the salt, corrosion occurred much less rapidly **[2]**. Materials studied by the ARE project included Inconel 600 (15% Cr, 7% Fe, balance Ni), Hastelloy B (28% Mo, 5% Fe, 2.5% CO, balance Ni), Hastelloy N (16% Mo, 7% Cr, 5% Fe, balance Ni), pure Ni, pure Fe, and several types of stainless steel including 316 **[2, 3]**. Hastelloy N was developed specifically to withstand corrosion in molten fluoride systems. **[4]**

Following the ARE, the molten salt reactor experiment (MSRE) began in 1956 **[5]**. Salts investigated during this period include LiF-BeF_2, also called FLiBe, (66 mol% LiF-33 mol% BeF_2), LiF-NaF-KF (46.5 mol% LiF-11.5 mol% NaF-42 mol% KF) **[6]**, and LiF-BeF_2-ZrF_4-UF_4 (64 mol% LiF-30 mol% BeF_2-5 mol% ZrF_4-1 mol% UF_4) **[1]**. A successful method of minimizing corrosion in UF_4 containing salts was by reducing 1% of the UF_4 to UF_3. The method of minimizing corrosion by keeping a reducing environment has also been shown in molten salts not containing UF_4 **[7]**.

3.2 Materials in Molten Salts

FLiNaK salt is hygroscopic (absorbs water out of the air) so all work with the salt must be done in an inert atmosphere **[8, 9]**. Highly pure Ar has been used in many cases **[10, 11]**.

Materials added to obtain standard electrode potentials and working curves of integrated current from anodic stripping voltammetry (ASV) as a function of elemental concentration have been anhydrous metal fluorides **[12, 13, 14, 15]**, pure metals with a current imposed upon them to force dissolution into the salt **[12, 16]**, and alkali-metal-fluoride compounds **[12, 15, 16, 17, 18, 19]**.

The limits of an electrochemical cell are determined by the potential at which the electrodes begin to dissolve and the potential at which the salt begins to electrolyze. Table 3.1 lists the reduction potentials of Pt in FLiNaK and FLiBe as well as the most unstable constituents of FLiNaK and FLiBe, K and Li, respectively. Reference electrodes (RE) and temperatures of each are listed as well. A Pt quasi-reference electrode is abbreviated by Pt-QRE.

Table 3.1 Cathodic and anodic limits of electrochemistry in molten fluoride salts.

Reaction	Potential (V)	RE	Melt Solution	Temperature (°C)	Source
Pt(II)/Pt	1.5	Pt-QRE	FLiNaK	495	**27**
Pt(II)/Pt	1.75	Pt-QRE	FLiBe	500	**32**
K(I)/K	-3	Ni(II)/Ni	FLiNaK	600	**37**
Li(I)/Li	-2.5	HF/(F^- + ½ H_2)	FLiBe	727	**46**

3.3 High Temperature Electrochemistry Probes in FLiNaK

The working electrodes (WE) and counter electrodes (CE) in an electrochemical probe must be inert to the surrounding environment in the temperature range of interest. Materials that have been used previously for the WE and CE are Cu **[20]**, Au **[21]**, W **[22]**, Ta **[15, 19, 22]**, Ir **[23]**, Pt **[14],** glassy carbon **[24, 25]**, and pryolytic carbon **[15, 18, 24, 25, 26]**. Glassy carbon, also called vitreous carbon, is a carbon based material that is extremely resistant to chemical attack in molten fluoride salts. It has been used in the majority of static electrochemical cell research as a container material **[8, 30]**. Other than glassy carbon, pure Ni **[16]** and graphite **[26]** have also been used as a container material. Pt tubing has been used to bubble helium through the molten salt melt **[27]**.

3.4 Reference Electrodes in FLiNaK

Quasi-reference electrodes (QRE) have generally been made out of Pt **[19, 24, 25, 28, 29],** with a few instances of glassy carbon **[30]** or Ir **[21, 23, 31]**.

The most commonly described reference electrode (RE) in FLiNaK is a Ni(II)/Ni RE **[14]** that is made using a Ni wire in a FLiNaK solution with a one of two different concentrations of NiF_2: 1 mol% **[14, 29, 34, 18]** and 0.1 mol% **[14, 28]**. Both types were contained in graphite. A AgF RE has also been described **[33, 34].** All of these studies described placing the RE in the same melt as the WE and CE. Wetting of the graphite container for the RE depends on the graphite's pore size and the permeability, but wetting generally takes place within three to six hours **[34]**. Figure 3.1 shows the potential between the two RE as a function of time which indicates wetting of the RE.

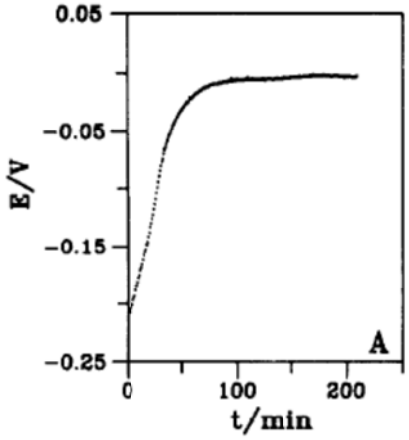

Figure 3.1 Wetting of RE; potential between the two RE initially approaches zero linearly, but asymptotically approaches zero as the potential gets closer to zero. [32]

Electrical insulation of the RE is necessary when the WE or CE may contact the RE, causing an electrical short and possibly polarizing the RE. Electrical insulation of the RE using hot pressed boron nitride is stable below 500 °C; however, boron nitride is wetted by the FLiNaK above 500 °C causing it to no longer be electrically insulating **[29, 34]**. Hot pressed boron nitride coating of the RE was attempted again and was found to fail at 700 °C. Single crystal LaF, which is an electrical insulator and stable up to 700 °C, has also been investigated. However, it is expensive and was found to crack after a few uses **[25]**. Another method of electrically insulating the RE is by coating the container with pyrolytic boron nitride which is stable in FLiNaK up to at least 800 °C **[34]**.

Usually the RE is submerged in the same melt as the WE and CE. A few studies have attempted to use a salt bridge to connect the two melts. Of the materials tested for use as a salt bridge, it was found that alumina readily dissolved in FLiNaK and thus introduced unwanted ions into the melt **[15, 19, 20]**, and a single crystal LaF_3 bridge was noted to result in an excess unexplained potential in the melt. Neither of these two materials has proven to supply a constant, reusable bridge to the RE. A boron nitride bridge was found to be reproducible and steady at 500 °C. **[28]**

3.5 Cyclic Voltammetry of Cr in FLiNaK

Cyclic voltammetry (CV) has been performed on CrF_3 in FLiNaK over the temperature range of 612-983 °C using a Pt QRE **[63]**. The peak current from CV was found to be linearly proportional to the square root of the scan rate. The Cr(III)/Cr(II) and Cr(II)/Cr(0) reduction steps were both found to be quasi-reversible. However, the Cr(III)/Cr(II) reduction was not completely understood due to possible chemical reactions. CV has also been performed on CrF_3 in FLiNaK at 750 °C **[15]**. The reduction of Cr(II)/Cr(0) and Cr(III)/Cr(II) were found to occur at -1.13 and -0.69 V vs. a 1 mol% Ni(II)/Ni RE. Preliminary results noted that the Cr(II)/Cr(0) step was not reversible.

3.6 Effects of Experimental Conditions on Current Peaks

If no plating step is performed, the current peak height for a reversible reaction (i.e. Ni(II)/Ni(0) in FLiNaK) has been shown to obey the Randles-Sevick equation **[26, 35]**. For a WE with cylindrical geometry, the Randles-Sevick equation can be written as equation 3.1 **[36]**.

$$i_p = \left(0.446 + 0.344\left(r\sqrt{\frac{nFv}{RTD}}\right)^{-0.852}\right) n \cdot F \cdot A \cdot C \cdot \left(\sqrt{\frac{n \cdot F \cdot v \cdot D}{RT}}\right) \qquad \text{Equation 3.1}$$

where

r = radius of the cylinder
n = number of electrons transferred
F = Farrady constant
A = area of the electrode
C = concentration of analyte
D = diffusion constant
v = scan rate
R = universal gas constant
T = temperature

Scan rate refers to how quickly the potential is varied linearly with time from a reducing to an oxidizing potential during the stripping step. From equation 3.1, the current peak height will increase linearly with the square root of scan rate and diffusion coefficient, while the current peak height will increase linearly with area of the electrode and concentration of the analyte. To obtain well defined peaks, scan rates above 16 mV/s have been suggested **[25]**. Other scan rates that have been used are 50 mV/s **[26]**, 100 mV/s **[37]**, and 500 mV/s **[38]**. While faster scan rates give larger peaks and better resolution at low concentrations, data acquisition rates of instrumentation must be considered so that sufficient information of the peak (i.e. enough data points) can be gathered. Also, if a peak is too large, it may overshadow another smaller peak.

Integrated current has been shown to be linearly proportional to plating time when performing ASV **[13]**.

3.7 Interference and Other Complications

In tests of molten fuels for the molten salt breeder reactor (MSBR), Zr was found to have a reduction potential that would cause its stripping peak to interfere with Cr **[33]**. One way to alleviate the overlap of peaks is by selectively plating the metal ions of interest. Selective plating is performed by choosing the plating potential such that it is not more negative than the emf of any unwanted ions. This method is applicable if the interfering peak is more negative than the element of interest. If this is not the case, a peak subtraction approach must be used.

Flow loops bring further complications, stemming from vibrations of the pump motor causing unexpected convective mass transfer and thermal gradients around the electrodes. Vibrations also caused the electrodes to contact either other electrodes or the salt container, causing an electric short. More accurate data was obtained if flow in the loop was temporarily suspended prior to take voltammetric measurements **[33]**.

3.8 Electrochemistry in Other Molten Salts including $MgCl_2$-KCl

Molten chloride salts have been widely researched for use in a nuclear fuel reprocessing cycle known as pyroprocessing. In pyroprocessing, spent nuclear fuel is dissolved in molten salt and the desired elements are removed from the rest of the spent fuel by polarizing two electrodes in

a solution that contains spent nuclear fuel. A detailed series of reduction potentials for all elements present in spent nuclear fuel must first be obtained to ensure that only desired elements are removed. Reduction potentials of many elements have been characterized by institutions researching advanced methods of reprocessing spent nuclear fuel. **[39]**

Materials used in molten chloride salts are similar to those used in molten fluoride salts. Metals used for the WE and CE include Au **[40]**, Cu **[40]**, W **[22, 39, 41]**, Ta **[22]**, and Pt **[39, 40, 41]** as they all have reduction potentials much less negative (closer to zero or even greater than zero) than the reaction of interest. Materials used for insulating the WE include soda lead (Corning 0120) glass **[39, 41]** and Pyrex glass **[39, 41]**. Pyrex glass vessels have also been used to contain the salt **[42]**.

A common RE in non-aqueous systems, including molten chloride systems, is the Ag(I)/Ag RE **[22, 40]**. A detailed emf series in $MgCl_2$-KCl has been developed using the Ag(I)/Ag RE **[40]**. Pt(II)/Pt RE have also been used **[41, 42, 43]** since it is reversible and reusable. The construction of the Pt(II)/Pt RE consisted of inserting a Pt wire in a 0.01 molal solution. A Pt-QRE has been found to be unstable in $MgCl_2$-KCl and useful only for measuring relative potentials of peaks **[44].** Materials used for containing the RE are similar to the materials noted above for insulating the WE.

Extensive work has been performed by several investigators on LiF-BeF_2 (67 mol% LiF-33mol% BeF_2) **[45, 46, 47]**. Other fluoride salts that have been studied are NaF-$NaBF_4$ (92 mol% NaF-8 mol% $NaBF_4$) **[38]** and NaF-KF (40 mol% NaF-60 mol% KF) **[14].** Many chloride salts have been studied including LiCl-KCl (50 mol% LiCl-50 mole % KCl) at 475 °C **[22, 48]**, $MgCl_2$-NaCl-KCl (50 mol% $MgCl_2$-30 mol% NaCl-20 mol% KCl) at 475 °C **[39, 42, 49, 40]**, and $PbCl_3$ at 530 °C **[51]**.

3.9 Neutron Activation Analysis in Molten Salts

Minimal work has been found concerning the use of neutron activation analysis (NAA) for evaluating the chemistry of molten salts. Studies have been performed using fast neutron activation analysis (FNAA), but irradiation sources and nuclear reactions are different for FNAA and NAA. FNAA is used for detecting light elements via ballistic collisions while NAA is used for detecting heavy elements via thermal neutron absorption.

Fast neutron activation analysis (FNAA) has been used to determine oxygen, fluorine, and nitrogen concentrations during the process of electowinning and electrorefining metals in molten salt systems **[52].** FNAA has also been used to determine oxygen concentrations in KCl and $MgCl_2$ prior to $MgCl_2$-KCl formation **[53]**.

4. Concurrent Work being Performed at UW

4.1 Materials

Several high temperature alloys that have been code certified by ASME for various high temperature applications such as power boilers, pressure vessels, and construction for nuclear power plants **[54]** have been analyzed for corrosion in molten salt systems. Relatively pure Ni and a refractory based alloy of Nb-1Zr have also been selected. Table 4.1 shows elemental composition of alloys that are being investigated at the University of Wisconsin.

Table 4.1 Nominal composition of alloys (in wt.%) under investigation in the UW molten salt research program for use in F based salts.

Alloy	**Cr**	**Mo**	**W**	**Al**	**Ti**	**Fe**	**C**	**Co**	**Ni**	**Mn**	**Nb**	**Zr**
Inconel-617	22.1	9.58		1.05	0.4	1.09	.08	12.4	52.9	.06		
Haynes-230	22.5	1.2	14.1	0.3		1.8	0.1	0.3	59	0.5		
Hastelloy-N	6.31	16.1	0.06	<.01	<.01	4.03	.03	.15	72.2	0.53		<.01
Hastelloy-X	21.3	8.8	0.4			19.3	.06	1.4	47.5	.54		
Nb-1Zr											99.05	0.95
Incoloy-800H	20.4			0.5	0.6	42.3	.07		31.6	0.8		
Ni-201					.02	.05	.02	.02	99.4	.19		

Cr is added to the Fe- and Ni-based alloys for high temperature oxidation resistance because Cr forms a protective oxide layer on the surface of the material in air and other oxidizing environments. However, in molten fluoride salt systems, Cr oxide is chemically unstable, and corrosion is driven by thermodynamics of dissolution of various elemental constituents. Fluoride compounds with a more negative Gibb's free energies are more likely to form. Figure 4.1 shows the Gibb's free energies of some fluoride compounds that could form with elements typically found in high temperature alloys. The fluoride compounds that make up salt are the most stable and have the most negative Gibb's free energies.

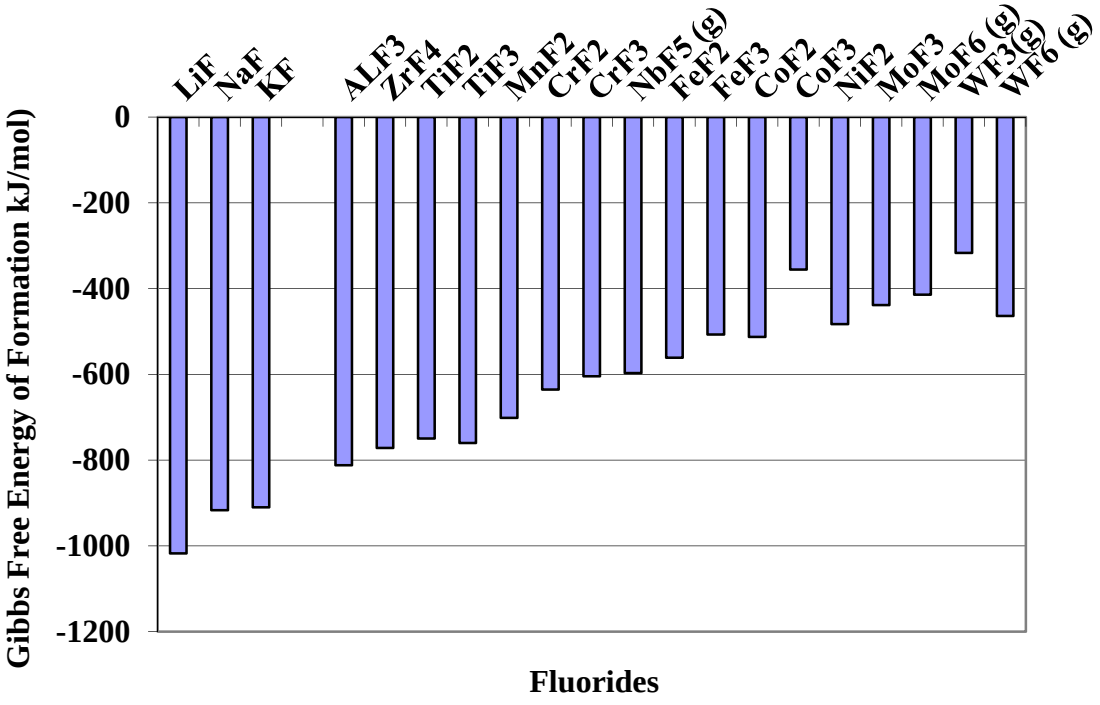

Figure 4.1 Gibbs free energy of fluoride formation per F_2 molecule for salt constituents and the fluorides formed from the tested alloys at 850°C. The more negative the Gibb's free energy of formation an alloy constituent is, the more likely it is to corrode and dissolve in the molten salt. [55]

From previous work **[55]**, it has been observed that Cr is primarily attacked by fluoride based salts due to its higher chemical activity than the other alloy constituent metals. Ni-201 (relatively pure Ni) was selected as a point of comparison with minimal corrosion due the relative stability of Ni in molten fluorides as shown in figure 4.1. In contrast, alloys with higher Cr content are expected to corrode more due to the more negative Gibbs free energy of Cr. Equation 4.1 shows a possible reaction that would result in the removal of Cr from an alloy. If a less active impurity is present in the salt, Cr will form a fluoride compound in its place.

$$Cr + FeF_2 \rightarrow CrF_2 + Fe \qquad \text{Equation 4.1}$$

Currently at the University of Wisconsin-Madison, the molten salt research group has performed static corrosion tests on the alloys listed in table 4.1. The static corrosion tests consist of immersing a 1.25"x 0.5"x 0.06" sample of a given alloy for 500 hours in molten salt at 850 °C. The tests were performed in graphite containers. Weight loss and microstructural changes were evaluated after exposure for each sample. Figure 4.2 shows the weight loss of all but one of the alloys. The only alloy not shown in figure 4.2 is Nb-1Zr. As seen in figure 4.1, Zr is even more active than Cr in FLiNaK (more negative Gibb's free energy), and Nb is embrittled by C used in the containers for the static corrosion tests, causing the samples to break and fall apart giving very high weight loss.

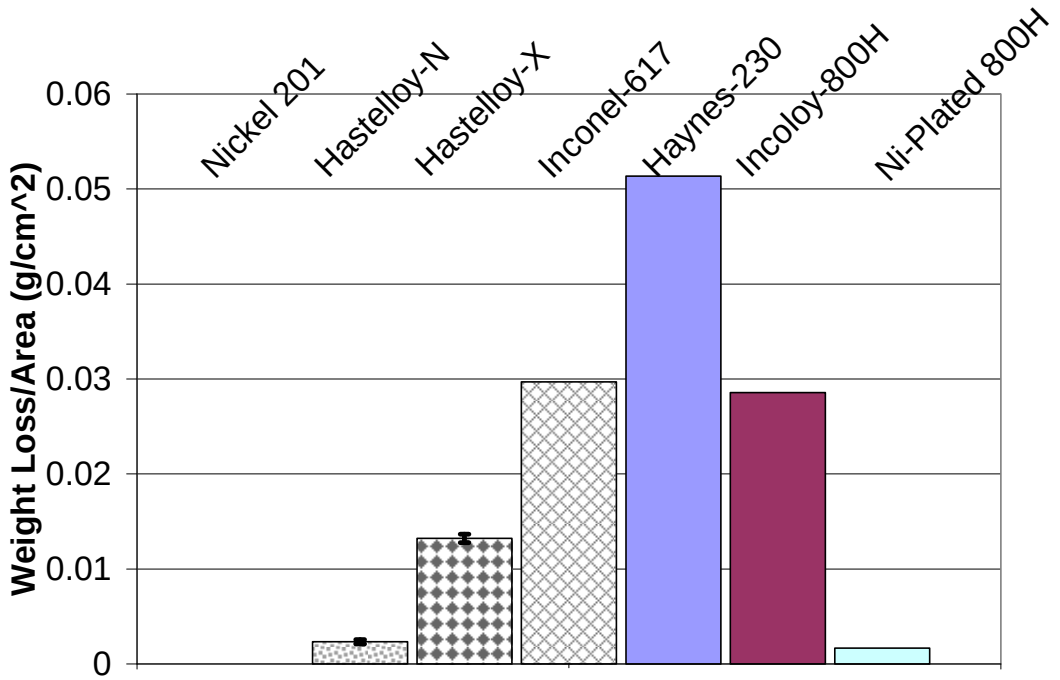

Figure 4.2 Weight loss of each alloy after 500 hour static corrosion test from [55].

Inductively coupled plasma atomic emission spectroscopy (ICP-AES) was performed on the salts after the corrosion tests to determine elemental concentrations of corrosion products. However, results from ICP-AES did not agree with weigh loss data. It is believed that the poor data was obtained because ICP-AES requires a dissolved sample, and FLiNaK was likely not dissolved properly. As a part of this study, NAA was performed on the salts used in the static corrosion tests to determine concentrations of elements that corroded from the alloy into the salt. By knowing the concentrations of each element in the salt, elemental weight loss from the samples can be determined.

Static corrosion tests are also being performed in $MgCl_2$-KCl for 100 h at 850 °C with the alloys listed in table 4.2. Nominal composition of each of the alloys is shown in table 4.2. NAA was used to determine elemental concentrations in these salts after the static corrosion tests.

Table 4.2 Nominal composition of alloys (in wt.%) under investigation in the UW molten salt research program for use in Cl based salts.

Alloy	Cr	Mo	W	Al	Ti	Fe	C	Co	Ni	Mn	Si	P	S	Cu
Inconel-600	15.5					8	0.15		72	1	0.5			0.5
Inconel-617	22.1	9.58		1.05	0.4	1.09	.08	12.4	52.9	.06				
Inconel-625	21.5	9		0.4	0.4	5	0.1	1	58	.5	.5	0.015	0.015	
Haynes-230	22.5	1.2	14.1	0.3		1.8	0.1	0.3	59	0.5				

Hastelloy-X	21.3	8.8	0.4			19.3	.06	1.4	47.5	.54				
Incoloy-800H	20.4			0.5	0.6	42.3	.07		31.6	0.8				
Ni-201					.02	.05	.02	.02	99.4	.19				
316ss	16	2					0.03		12	2	1	0.045	0.03	

4.2 Salts

Molten salts have been proposed for the intermediate heat transfer fluid from the VHTR to a hydrogen production plant due to their excellent heat transfer properties as well as their stability at the high temperatures required for hydrogen production. The two salts studied in this experiment are FLiNaK (46.5 mol% LiF-11.5 mol% NaF-42 mol% KF) and $MgCl_2$-KCl (32 mol% $MgCl_2$-68 mol% KCl) due to their exceptional heat transfer qualities including low vapor pressure, high volumetric heat capacity, and high thermal conductivity. Due to the high volumetric heat capacity and low vapor pressures at the temperatures of interest, smaller heat transfer components would be needed compared to a helium based system. Additionally, molten salts do not react vigorously with air, as an advantage over liquid Na. Table 4.3 shows a comparison of some of the important heat transfer properties of FLiNaK and $MgCl_2$-KCl. Properties of helium and water are included for comparison.

Table 4.3 Comparison of thermophysical properties of FLiNaK and $MgCl_2$-KCl salts at 700 °C, water at 20 °C, and helium at 7.5 MPa [1].

Salt (mol%)	Melting Temperature (°C)	Density (g/cm^3)	Volumetric Heat Capacity (cal/cmºC)	Viscosity (centiPoisse)	Thermal Conductivity (W/mK)
FLiNaK LiF-NaF-KF (46.5%-11.5%-42%)	454	2.02	0.91	2.9	0.92
$MgCl_2$-KCl (32%-68%)	426	1.66	0.46	1.4	0.4
Water (H_2O) @ 20°C	0	1	0.44	1	0.6
He (P=7.5MPa)	N/A	0.0038	0.005	0.042	0.29

Although FLiNaK has superior heat transfer characteristics as compared to $MgCl_2$-KCl, the cost of FLiNaK is nearly six times that of $MgCl_2$-KCl **[1].** However, the cost of procuring a larger heat exchanger for the $MgCl_2$-KCl must be compared against the higher cost of the FLiNaK. Also, corrosion mechanisms differ slightly between the two salts. The chloride based salts may not be as highly corrosive as the fluoride based salts and are generally easier to handle.

FLiNaK salt has been procured from Electrochemical Systems (ECS), Idaho National Lab (INL) and manufactured in house. $MgCl_2$-KCl salt has also been manufactured in house by the University of Wisconsin molten salt research group. Four methods of purification were considered for the production of the $MgCl_2$-KCl salt including bubbling Ar or HCl gas to remove water or oxygen, adding CCl_4 to chemically scavenge impurities, and adding Mg to reduce impurities out of the salt. As part of this study, neutron activation analysis was performed on the salts to determine concentrations of impurities and to help determine which method of purification of $MgCl_2$-KCl is most beneficial in preventing corrosion.

5. Experimental Procedure and Methodology

In this section, a detailed background is given for anodic stripping voltammetry (ASV) and neutron activation analysis (NAA). A description of how each technique was applied to this research is given following each background section.

5.1 Anodic Stripping Voltammetry

5.1.1 Voltammetry Background

Anodic stripping voltammetry (ASV) is an electrochemical technique that allows for determination of concentrations of trace metal cations in a solution. The metal corrosion products that may be detected are any elemental cations that have been dealloyed by reacting with the molten salt. For the alloys tested, this will mostly be Cr and Fe. Each ionic species has its own reduction potential, or half-cell potential, which can be calculated by the Nernst equation, equation 5.1.1.

$$E = E^0 - \frac{2.3RT}{nF} \log \frac{\text{Activity}_{\text{Reactant}}}{\text{Activity}_{\text{Product}}} \qquad \text{Equation 5.1.1}$$

where

E = half cell potential

E_0 = standard half cell potential at 25 °C

R = universal gas constant

T = temperature of the cell

n = number of electrons transferred in the reduction

F = Faraday constant

Activity is defined by the concentration times the gamma value of the given conditions. For low concentrations, the gamma value is one which yields that the activity is equal to the concentration. Concentration effects causing a gamma value not equal to one have been observed when the concentration of the dissolved species reaches 2000 ppm **[13]**. Table 5.1 gives the emf series of several elements of interest in FLiNaK as measured by other researchers **[13, 15, 19, 24, 26].** Temperature and type of reference electrodes (RE) are also given. Quasi-reference electrodes are denoted by QRE.

Table 5.1 Measured reduction potentials in FLiNaK.

Reaction	Reduction Potential (V)	RE	Temperature (C)	Sources
Zr(IV)/Zr	-1.4	Pt-QRE	500	19
Fe(II)-Fe	-0.60	Pt-QRE	500	27
Fe(III)-Fe(II)	-0.5	Pt-QRE	500	24
Ni(II)-Ni	-0.2	Pt-QRE	500	26
Fe(II)-Fe	-0.39	Ni(II)/Ni	500	13
Fe(III)-Fe	-0.2	Ni(II)/Ni	500	13
Ni(II)-Ni	0.0	Ni(II)/Ni	500	13
Al(III)-Al	-1.5	Ni(II)/Ni	750	15

Cr(II)-Cr	-1.13	Ni(II)/Ni	750	15
Cr(III)-Cr(II)	-0.69	Ni(II)/Ni	750	15
Fe(II)-Fe	-0.512	Ni(II)/Ni	750	15
Fe(III)-Fe(II)	-0.21	Ni(II)/Ni	750	15
Ni(II)-Ni	0	Ni(II)/Ni	750	15

ASV, using inert electrodes in molten salts, is a three step process that involves the use of three electrodes. The three electrodes are referred to as the working electrode (WE), the counter electrode (CE), and the reference electrode (RE). ASV is performed in a potentiodynamic cell in which a potential is applied and the resulting current flow is measured. This is different from an electrometric cell, such as those used for pH measurements, where no current flows in the cell and only two electrodes are needed: one for measurement and one for reference. Cells used for ASV require three electrodes to account for the current flow.

When ASV is performed in a potentiodynamic cell, a voltage is applied to the cell to polarize the WE and CE causing a current to flow from the WE to the CE. Since the electrolyte in the cell has a set amount of resistance, there will be a voltage drop across the cell (potential drop (V) = current (i) * solution resistance (R)). Therefore, by using a third electrode (the reference electrode (RE)), with no current flowing between it and the WE, a known potential can be measured between the WE and the RE. Thus, a third electrode must be employed in a potentiodynamic cell to allow for current flow so that the determination of the WE potential will not be affected. Figure 5.1.1 shows the electrical circuit equivalent for current flow and voltage measurements in the electrochemical cell. A very large resistance exists between the WE and RE so minimal current is generated. This keeps the RE unpolarized and at a constant potential throughout all voltammetric measurements. Current should only flow between the WE and CE.

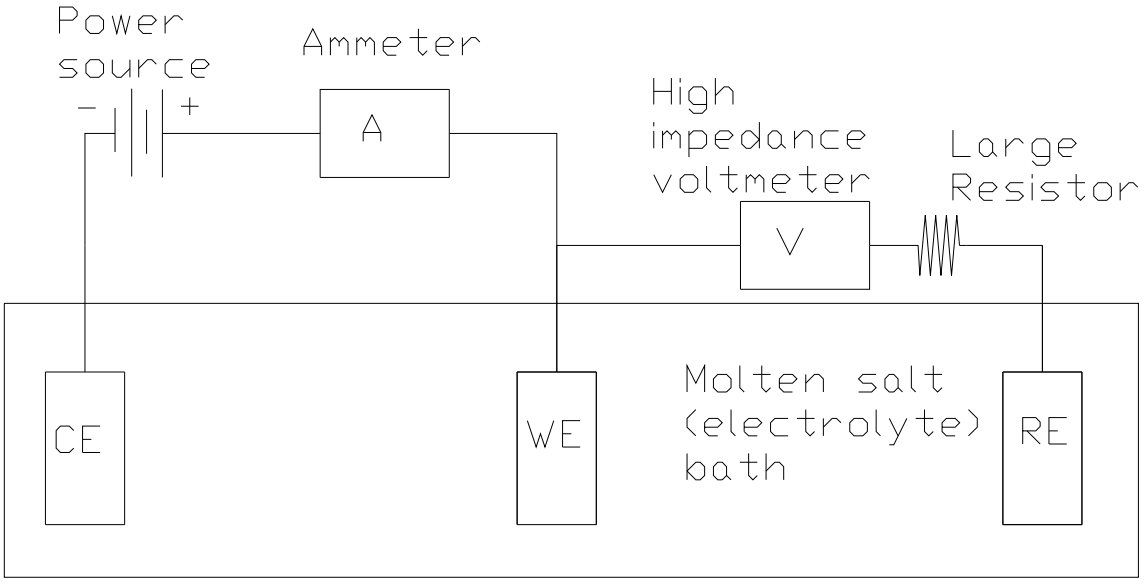

Figure 5.1.1 Equivalent circuit of electrochemical cell.

Figure 5.1.2 shows a typical electrochemical setup. The WE and CE are located in an electrolyte bath with the RE. All three electrodes connect to a potentiostat which is an instrument

that controls the potential between the WE and RE and measures and records the current flowing between the WE and CE and the potential between the WE and RE.

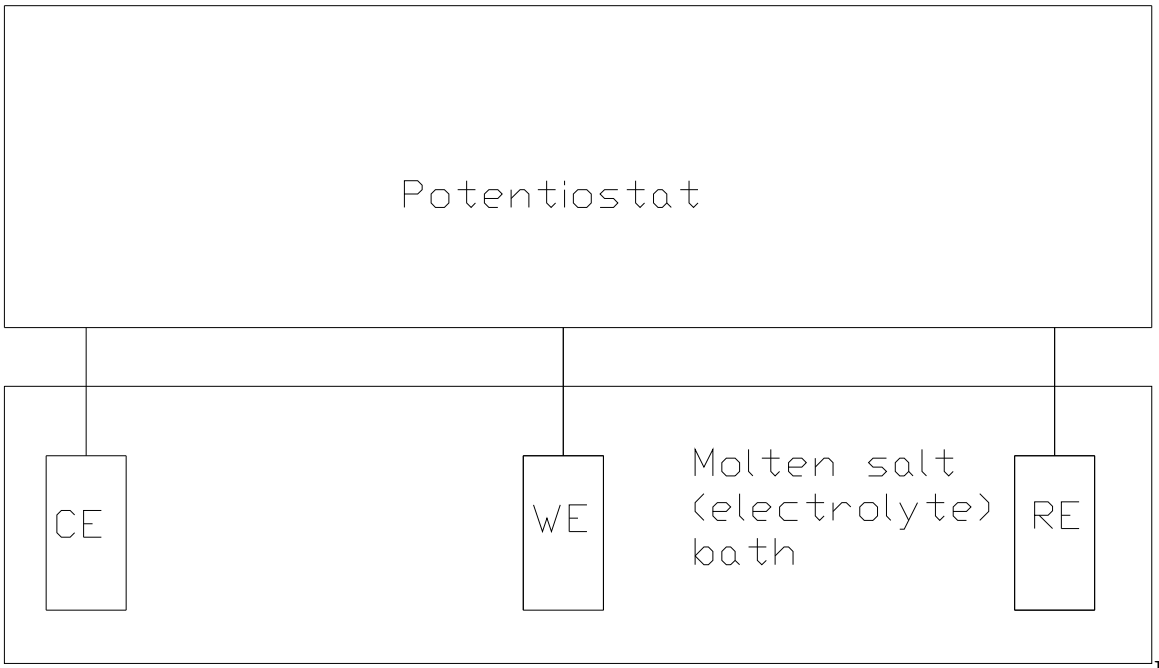

Figure 5.1.2 Basic design of the electrochemical cell used for anodic stripping voltammetry.

The three steps of the ASV technique are the plating step, the stripping step, and the cleaning step. Throughout the process of anodic stripping, all reactions of interest occur at the WE, while the CE is only used as a path to allow current to flow in the solution. The CE is kept at opposite polarity with respect to the WE (as measured against the RE) and has a much larger surface area. The larger area ensures that the CE does not limit the reaction at the WE due to insufficient area to conduct current.

The RE is not absolutely necessary to perform the ASV. However, it is needed to give a reference for comparing the potential of the WE so that repeatable results may be more easily obtained. Current should never be allowed to pass through the RE, and potential should never be forced across it. The RE will never be reduced and should always have a constant potential.

Figures 5.1.3 through 5.1.4 show where voltage is applied, current flows, and voltage is measured in terms of circuits for the plating and stripping steps. The base circuit is the same as figure 5.1.1.

Figure 5.1.3 shows the circuit during the plating process when a voltage is applied between the WE and CE, making the potential of the WE negative compared to the CE. The actual voltage of interest in the cell is measured between the WE and the RE. The potential of the WE, with respect to the RE, must be more negative than the reduction potential of the ionically charged chemical species of interest (hereafter referred to as the analyte) to plate the analyte on the WE. As ions reduce to metal atoms onto the WE, electrons flow from the positive CE to the negative WE. All reactions of interest occur at the WE. When a metal atom reduces onto the WE, an oxidation process must occur at the CE. However, due to the complexity of the system, the oxidation process could be a number of different reactions. Knowing the reaction at the CE is not necessary to

complete the ASV process as long as the reaction at the CE does not limit the reaction occurring at the WE. In the following figures, the processes at the CE are not shown. Only the resulting electron flow is shown.

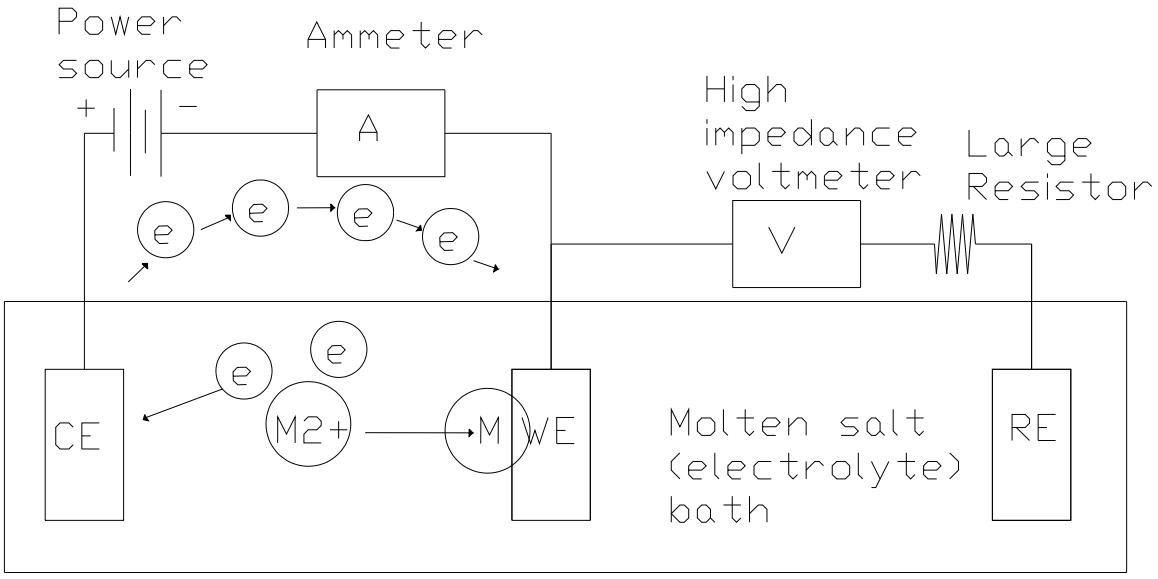

Figure

5.1.3 Detailed experimental system for plating.

Following the plating step, the stripping step oxidizes the accumulated analyte, leading to a reversal of electron flow. This is accomplished by linearly increasing applied voltage between the WE and the CE from the plating potential until the WE is more positive than the reduction potential of the analyte. As the reduction potential of each analyte is passed, the metal atom oxidizes off the electrode surface (deplates) and electrons flow can be measured.

The voltage change and subsequent current measurement is referred to as the stripping step. Figure 5.1.4 shows that during the stripping step, the WE is brought to a more positive potential, and current flows as metal atoms oxidizes into the solution.

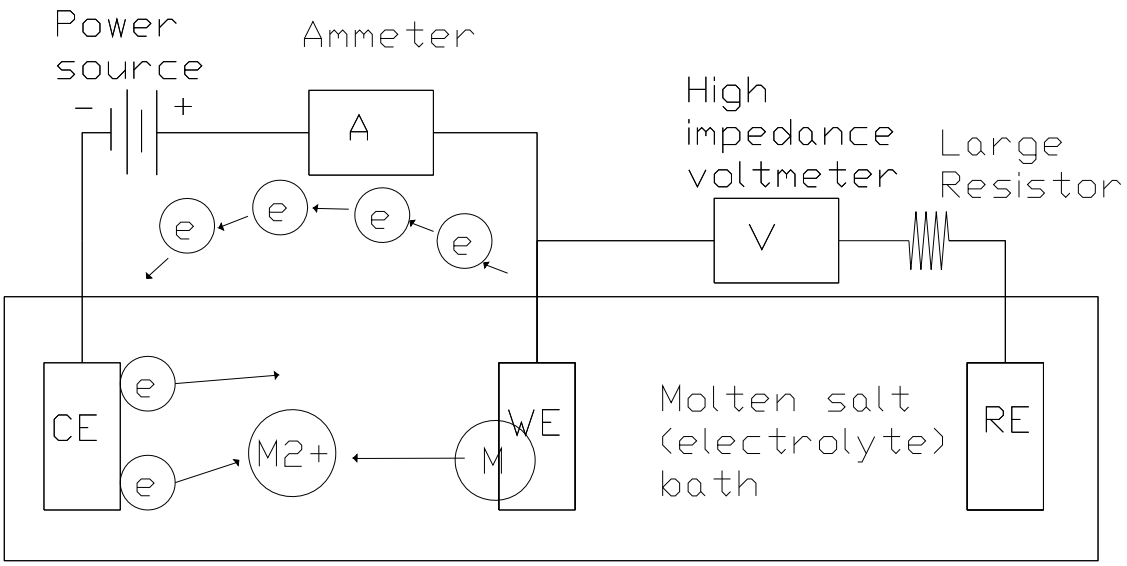

Figure

5.1.4 Current flow during stripping step.

Following the stripping step, a cleaning step is preformed to ensure that all metal ion species that plated initially have been oxidized back into the solution. This is accomplished by holding the potential of the WE greater than the reduction potential of any analyte in solution until the current through the cell reaches a steady value. The cleaning step is generally used with mercury electrodes to force metal ions out of the mercury solution, but the cleaning step has also been performed on metal electrodes **[56]**. Although the cleaning step is not necessary for ASV, it increases repeatability of results by ensuring that the surface of the WE has had the same treatment before each test.

The three steps of the anodic stripping process described in circuit diagrams above can be seen graphically in figure 5.1.5. The three steps are the plating step, the stripping step, and the cleaning step. The initial voltage must be more negative than the reduction potential of the analyte, and the voltage during the stripping step must then pass through the reduction potential of the analyte to detect it.

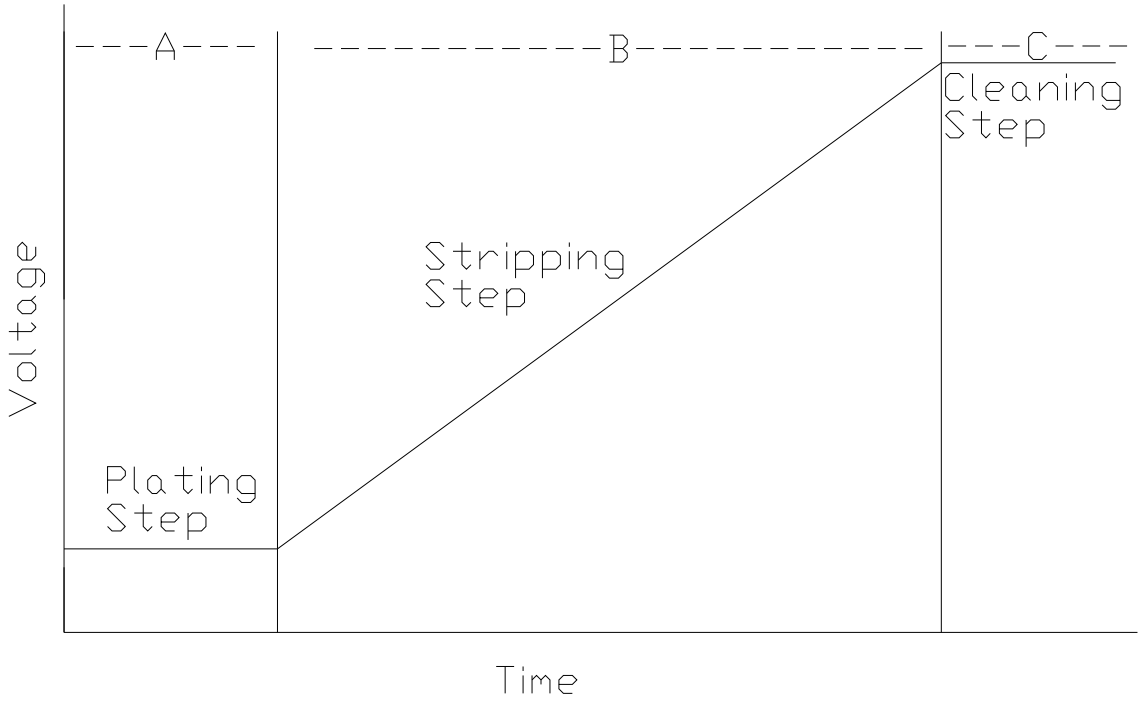

Figure 5.1.5 Potential of the WE as a function of time.

Figures 5.1.6 through 5.1.9 show what happens to the analyte during each step. A detailed description follows. Two different analytes are assumed. Both have different valence states and reduction potentials.

First, the three electrodes are placed in a solution that has a base electrolyte to allow sufficient current to pass between the electrodes. An analyte is then added to the solution as shown in figure 5.1.6.

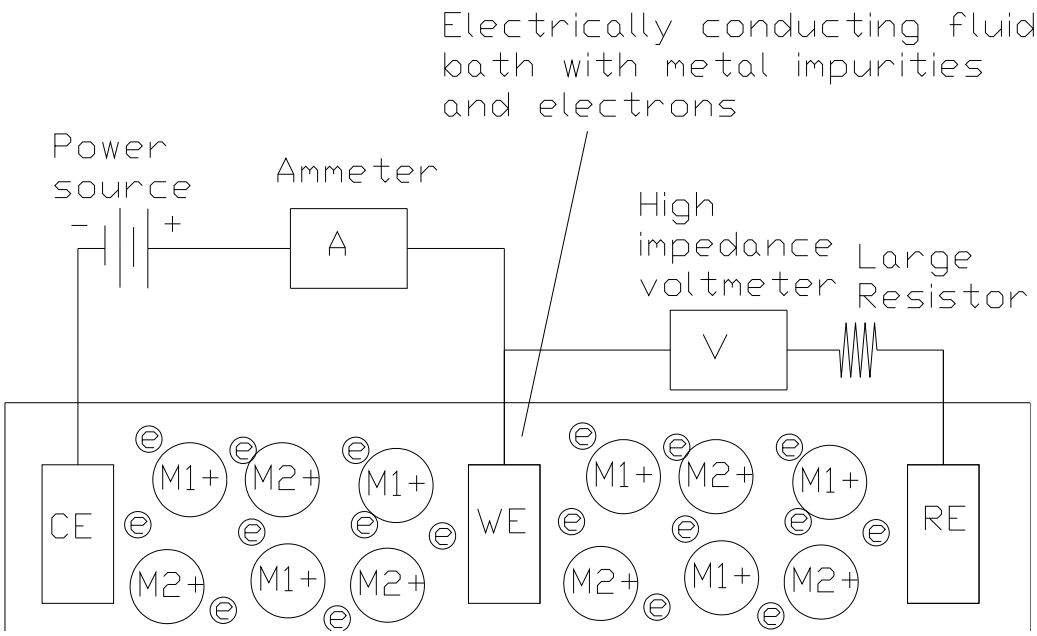

Figure 5.1.6 Three electrodes are placed in an ionically conducting solution with analyte ions with different reduction potentials and valence states.

A voltage is held across the WE and CE to cause the metal cations in the solution to be attracted to the negatively charged WE. The plating potential must be more negative than the reduction potential of the analytes so that the analytes will reduce at the surface of the negatively charged WE. That voltage across the WE and CE is held for a sufficient amount of time to allow for enough analyte in solution to be collected on the WE to give adequate signal to noise ratio during the stripping step. This step is called the plating step as shown in figure 5.1.7.

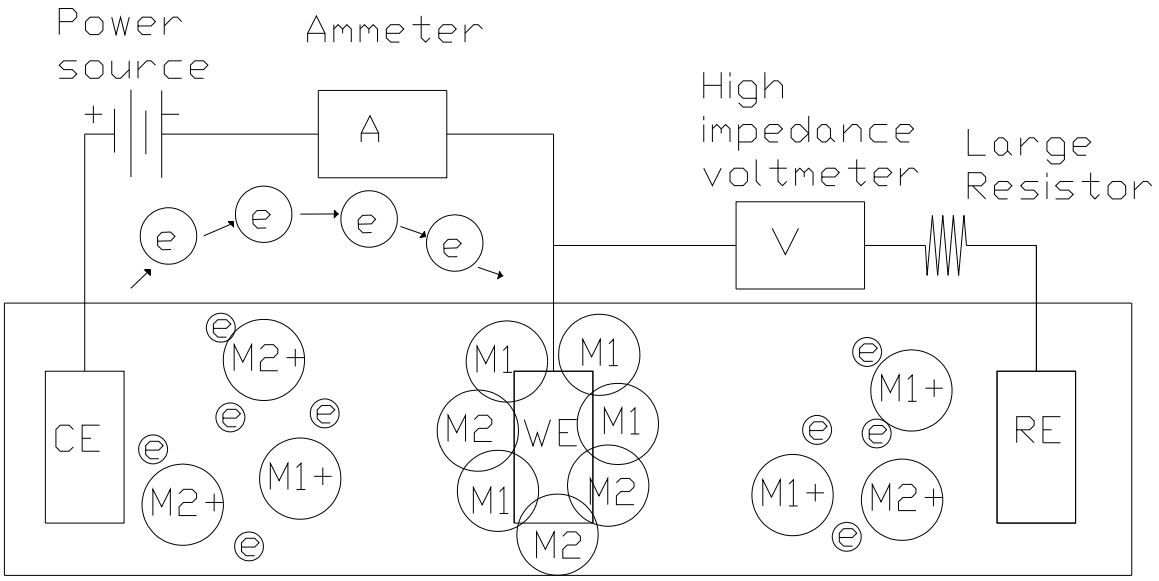

Figure 5.1.7 Plating potential is applied which is more negative than the reduction potential of the two impurity metals causing them to reduce at the WE.

The duration of the plating step depends on the concentration of the analyte in the solution. An acceptable duration will provide an adequate signal-to-noise ratio during the stripping step. One effect that can skew results is that the effective surface area of the WE can change during the plating process. Ideally, the plating step would result in a monolayer of the analyte plating on the WE surface, and no analyte would plate onto the already reduced analyte. If the surface area remains constant during the plating step, a graph of peak current as a function of plating time will result in a straight line. However, if the surface area increases greatly during the plating step, the peak current will deviate from linearity with a larger current than expected. A linear correlation between plating time and peak current was checked for Cr in FLiNaK spanning plating times of 0.3 to 0.8 minutes **[13]** and from 0.25 to 1 minute in this research.

Once a sufficient amount of analyte has been plated on the negatively charged WE, the voltage across the electrodes is made more positive so that the potential on the WE passes the reduction potential of the analyte. When the potential of the WE passes through the reduction potential of the analyte, the analyte oxidizes off of the WE into solution, as shown in figure 5.1.8. When the analyte oxidizes, it becomes a cation, according to its valence state. The introduction of electrons from the oxidation of the analyte causes the current between the WE and CE to increase. Once the potential of the WE passes the reduction potential of the analyte, the electron current then decreases back to the baseline due to depletion of the analyte from the WE. The size of the current peak is proportional to the concentration of the analyte that was plated onto the WE, and thus to the concentration of the analyte in the solution.

Figure 5.1.8 shows the reaction of ionic species as the potential of the WE passes through the reduction potential of metal 1, while figure 5.1.9 shows the same for metal 2.

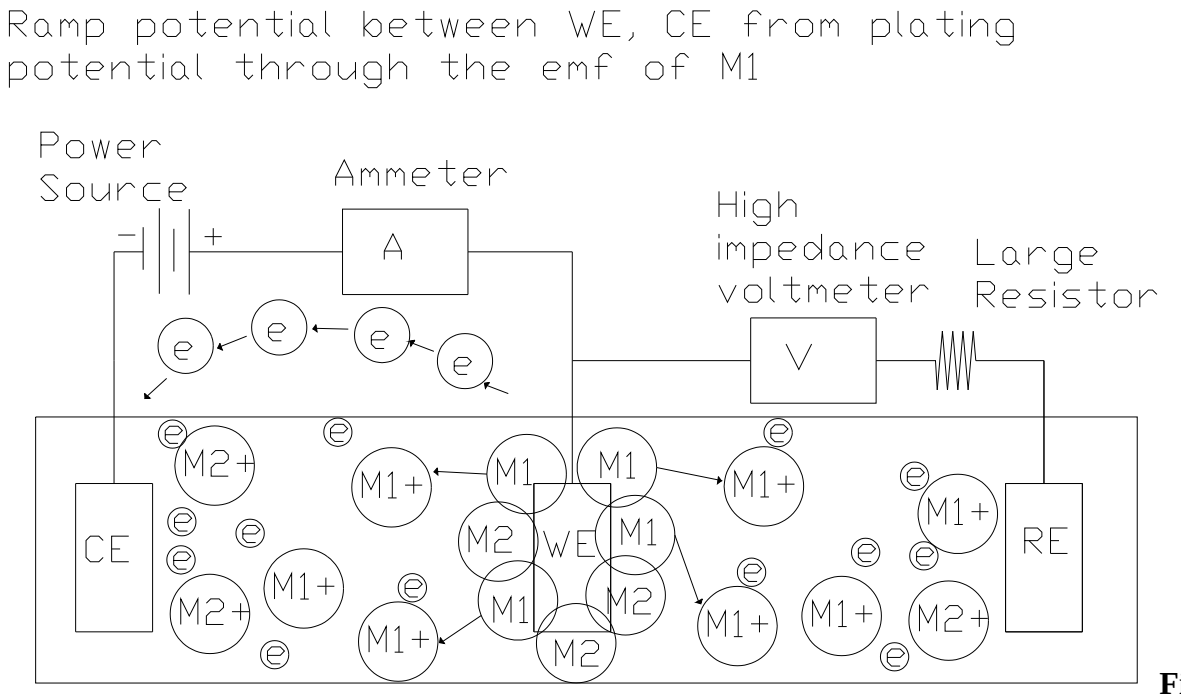

Figure 5.1.8 The stripping step begins as the potential of the WE is varied linearly from a negative value through the reduction potential of metal 1, causing it to oxidize into solution.

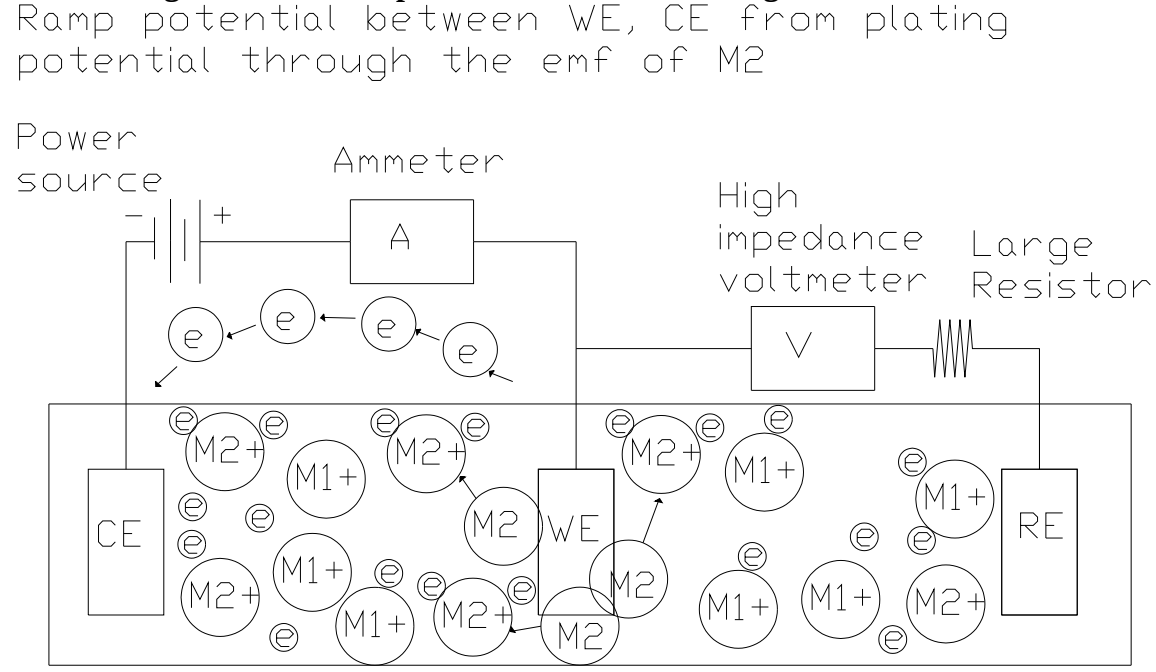

Figure 5.1.9 The stripping step continues as the potential of the WE passes through the reduction potential of the metal 2, causing it to oxidize into solution.

From figures 5.1.7 through 5.1.9, it is observed that the current is the highest when the potential between the WE and CE passes through the reduction potential of one of the plated ions. Figure 5.1.5 (voltage as a function of time) is repeated along with figure 5.1.10 which shows current as a function of time plot. The applied potential of the WE is constant for the plating step.

The current is negative as electrons flow to the CE due to the reduction of metal cations at WE. Then, the WE potential is swept positively and passes through the reduction potential of the two metal cations (similar to figures 5.1.8 and 5.1.9) causing a peak in current as electrons flow from the CE to the WE. The cleaning step holds the potential more positive than the reduction potential of both metal cations to ensure all the metal is oxidized off of the WE. It should last until the current reduces to near zero as the WE and CE are then at equilibrium. Figure 5.1.5 is repeated here along with figure 5.1.10 to show the current response during each voltage step during the anodic stripping process. In figures 5.1.5 and 5.1.10, the area denoted by A is the plating step, B is the stripping step, and C is the cleaning step.

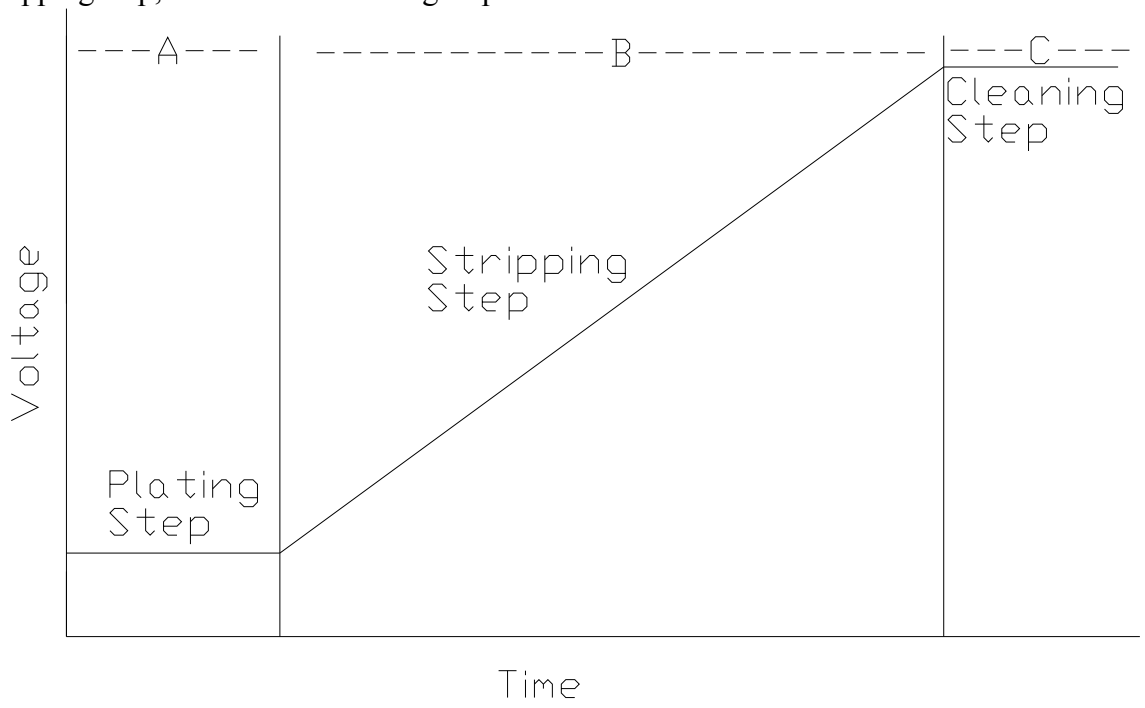

Figure 5.1.5 Applied potential as a function of time for anodic stripping.

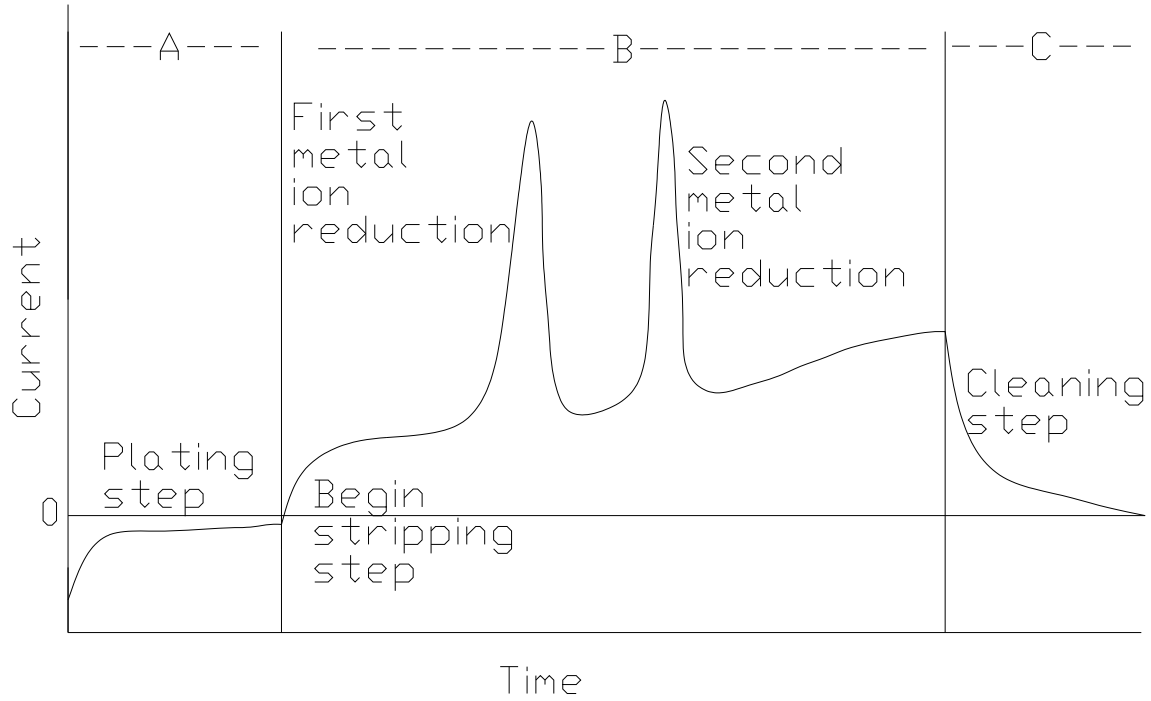

Figure 5.1.10 Following the plating step (A), each metal oxidizes according to its reduction potential during the stripping step (B), more electrons flow, increasing the current in the system; thus, a peak in current is observed at the reduction potential of each metal species. The cleaning step (C) reduces current back to approximately zero.

5.1.2 Materials for Molten Salt Electrochemistry

Pt wires are used for the working electrode (WE), counter electrode (CE), and quasi-reference electrode (QRE), and glassy carbon is used as the container for the melt.

For electrodes to be effective, they must not react with the surrounding environment. All metals will corrode if held at a potential more positive than their reduction potential. During the anodic stripping process, the potential range is determined by the reduction potential of the electrodes and the electrolyte. If the Pt electrodes are held too highly positive, they could be forced to corrode. Pt is one of the most noble metals, allowing for the detection of any metal cation less noble than Pt without oxidizing the Pt electrode. If the electrodes are held to a highly negative potential, the salt will electrolyze at the electrodes and break down.

Keeping the surface area constant between voltammetric measurements increases repeatability. Attempts have been made to hot press boron nitride (an insulator in molten fluorides) along the entire WE length, exposing only the bottom tip to the molten salt. Because hot pressed boron nitride is not electrically insulating above 500 °C in FLiNaK, a mechanical method of obtaining a constant surface area must be used (i.e. the electrode is only dipped a set distance into the melt for each measurement.) This method is not ideal because it can be difficult to determine the surface area precisely. It should be easier to obtain a set surface area for the WE in $MgCl_2$-KCl than in FLiNaK salts because $MgCl_2$-KCl is less oxidizing than the fluoride salt. Alumina (Al_2O_3) can be used to insulate the entire WE, except for the bottom surface that will be polished to a mirror finish, giving an exact surface area of the WE.

5.1.3 Reference Electrodes (RE)

Similar to the WE and CE, the RE should not react with the molten salt. The RE should maintain a constant potential throughout the stripping process. A good RE must also be non-polarizable, reversible, durable, and reusable **[57]**. Electrochemical reversibility refers to an electrode behaving as predicted by the Nernst equation and that it will follow that behavior on a very short time scale.

There are two general designs for obtaining a constant potential for reference: 1) a quasi-reference electrode (QRE) which is placed in the melt along with the WE and CE and 2) an isolated RE connected to the molten salt by an electrically conducting bridge.

The QRE is not as desirable as a true RE because it is not reversible, i.e. there is no way to ensure that the potential of the QRE is stable. Only qualitative information can be gathered from a QRE if the electrolyte composition changes. However, the QRE is more durable and reusable than any true RE currently in use. Figure 5.1.11 shows how the QRE is located with respect to the rest of the electrodes.

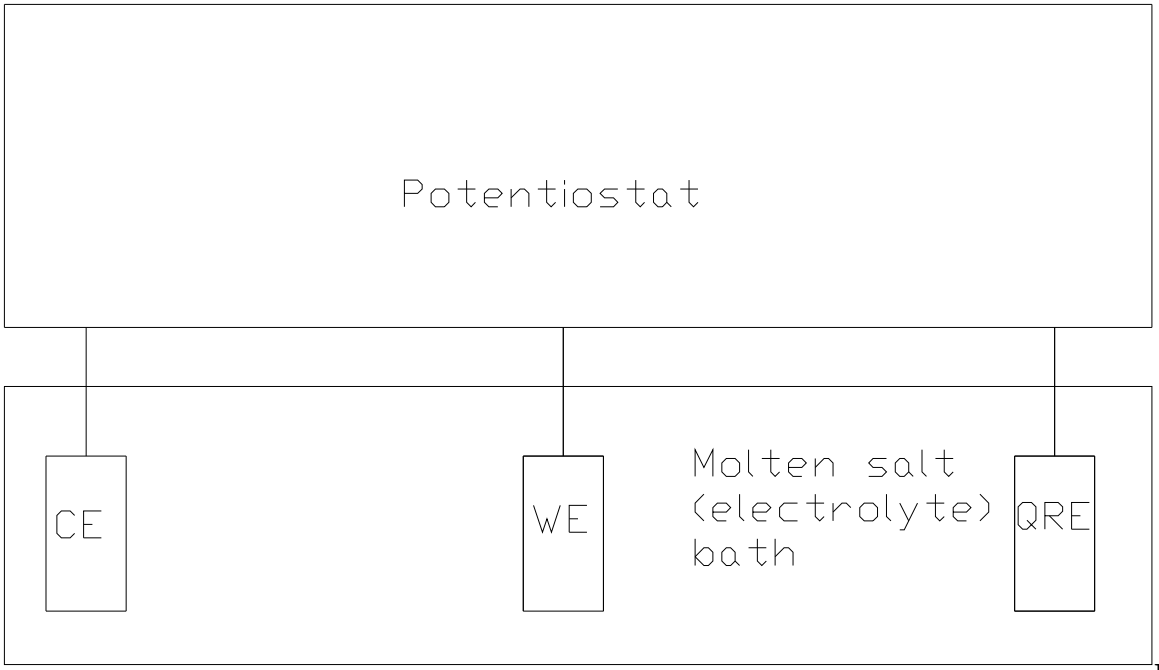

Figure 5.1.11 QRE located in the same melt as WE and CE.

The second type of electrode used to determine a reference potential in molten salts is a true RE. This type of RE maintains a constant potential because it is kept in a solution saturated with an ion corresponding to the composition of the electrode. This creates equilibrium between the electrode and the surrounding solution, preventing the electrode from corroding and keeping the electrode at a constant potential. The RE is contained in a shell that allows charge to pass to the melt solution, but diffusion of species itself is prevented from occurring. This passage can be obtained either by using a salt bridge to connect the RE to the melt or by placing the porous shell of the RE in the melt. If the RE is placed in the melt, care must be taken to ensure that the solution in the RE is prevented from mixing with the solution being analyzed while allowing for charge to pass between the RE and the solution. Figure 5.1.12 shows a true RE setup.

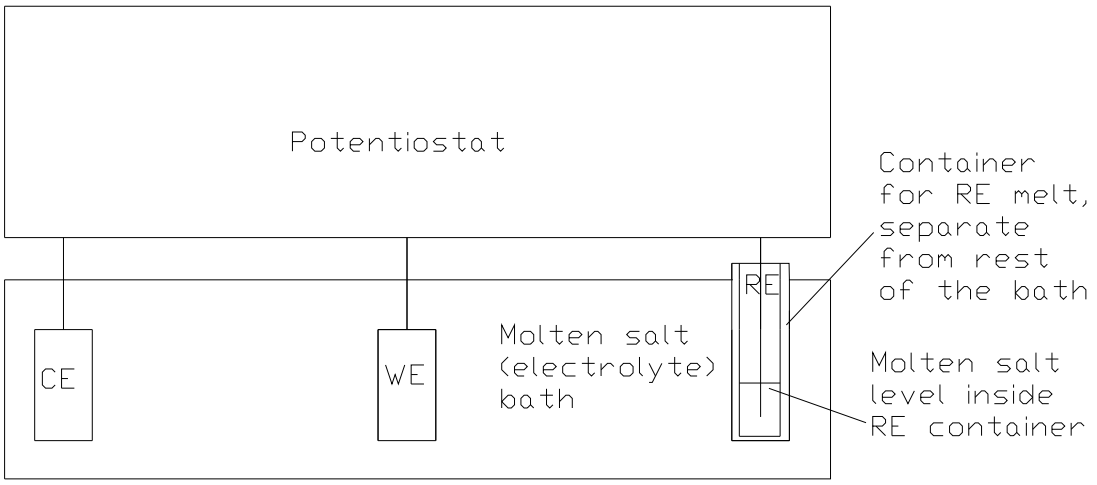

Figure 5.1.12 A true RE is isolated in a container of its own melt but still in ionic contact with the solution.

Instead of keeping the electrode in a container that minimizes species mixing while still allowing charge to pass through, the electrode can be kept in a separate solution which can then be connected by an ionically conducting bridge. Figure 5.1.13 shows how a salt bridge can be used to connect the two melts.

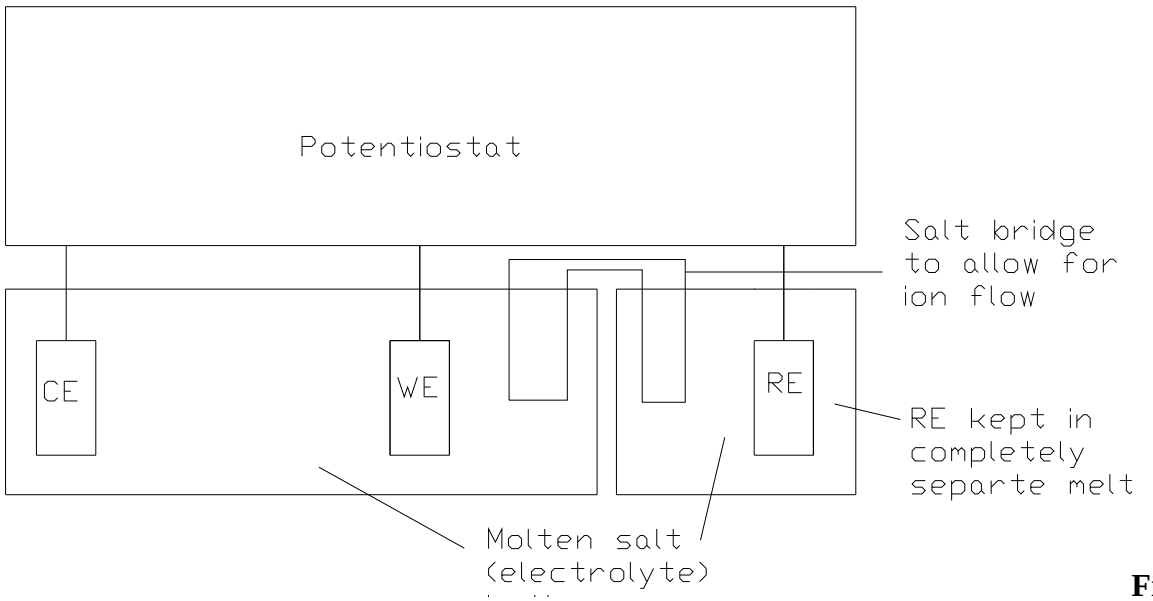

Figure 5.1.13 A salt bridge can be used to keep the ionic species in the RE solution from mixing with the rest of the melt.

When either method is used, a certain time must pass for the salt to impregnate the RE container or the salt bridge. This is referred to as a wetting time. Wetting can be verified by

measuring the potential across two RE. The electrodes are wetted when the potential between the two reaches zero. Once wetting has occurred, it occurs faster each time thereafter.

5.1.4 Cyclic Voltammetry (CV)

While the majority of this research focused on anodic stripping voltammetry (ASV), cyclic voltammetry (CV) can be performed using the same apparatus on a solution to gather other useful knowledge. CV consists of performing the stripping step of ASV, and then reversing the voltage and running the stripping step backwards (making a cycle). Figures 5.1.14 and 5.1.15 show a voltage and current as function of time for CV, and figure 5.1.16 combines the two to show current as a function of potential.

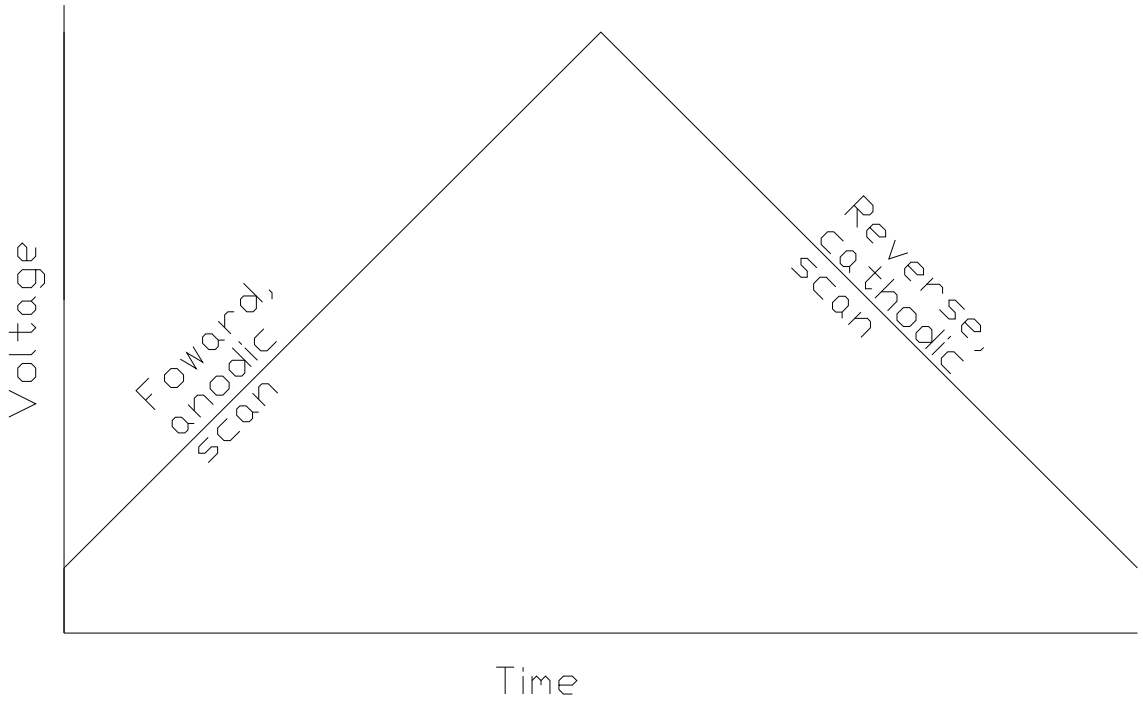

Figure 5.1.14 Voltage as a function of time for CV.

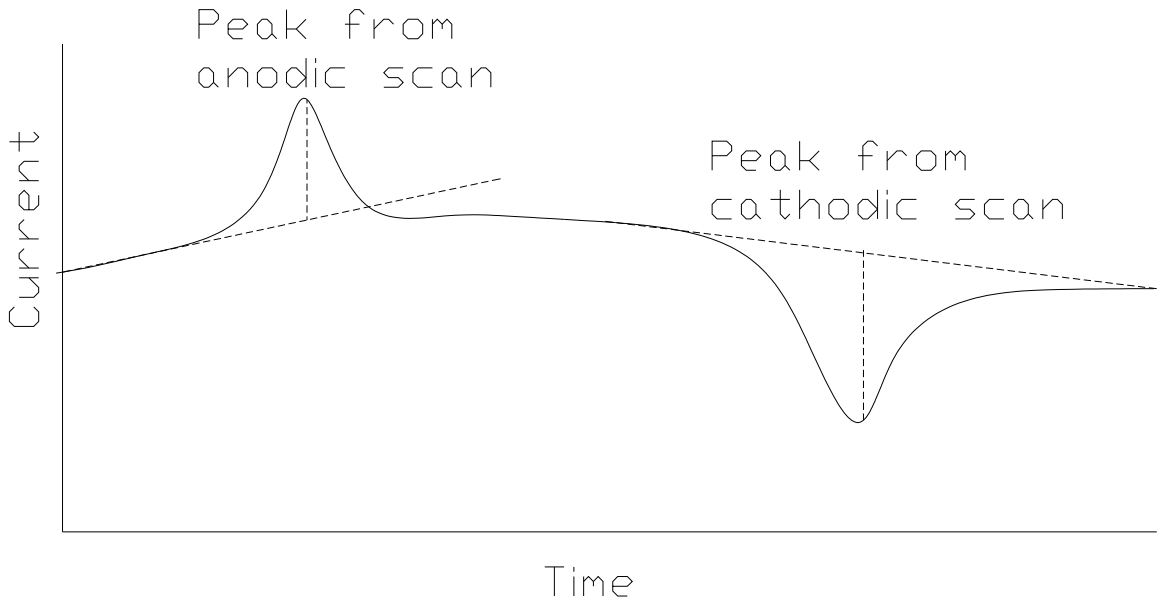

Figure 5.1.15 Current as a function of time for CV.

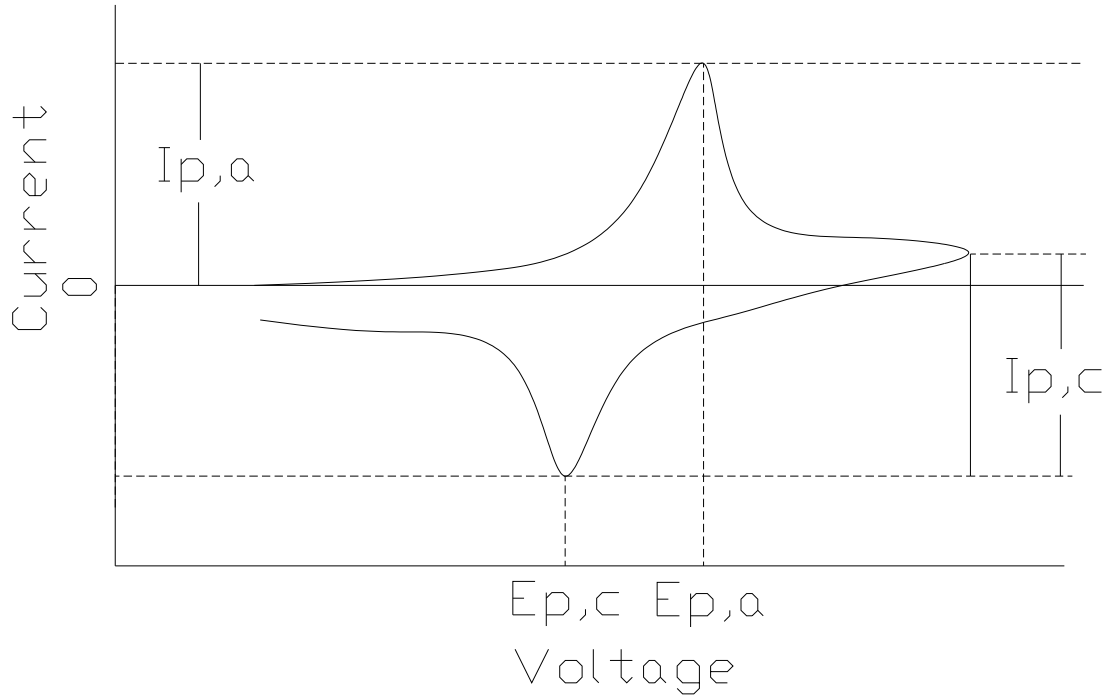

Figure 5.1.16 Current as a function of voltage for CV. Anodic and cathodic peaks are seen at voltages of $E_{p,a}$ and $E_{p,c}$, respectively with currents of $I_{p,a}$ and $I_{p,c}$, respectively.

Several pieces of information can be gathered from a cyclic voltammogram: whether the reaction is reversible, diffusion coefficients of the analyte, number of electrons transferred, and the potential at which the reaction occurs.

A ratio of the peak heights, i_{pa} and i_{pc} should be 1 if the system is reversible (both anodic and cathodic reaction occur on a short enough time scale to always keep the system in equilibrium), and the peak potential will not vary with scan rate. If the system is irreversible, the anodic and cathodic peaks will be widely separated and will not overlap, and the peak potentials will shift with scan rate by the transfer coefficient α. For a totally irreversible system, α can be found by equation 5.1.2.

$$\alpha = \frac{1.857RT}{nF\left(E_p - E_{p/2}\right)} \qquad \text{Equation 5.1.2}$$

where

n = number of electrons transferred

F = Farrady constant

E_p = peak potential

$E_{p/2}$ = half - peak potential

R = universal gas constant

T = temperature

If the system is quasi-reversible (exhibits characteristics of both reversible and irreversible), α is obtained by curve fitting, but is generally approximated as 0.5 **[58]**.

The Randles-Sevick equation (equation 3.1) can be applied to reversible or irreversible systems if the transfer coefficient is included. Equation 3.1, the Randles-Sevick equation for a reversible process at a cylinder electrode, is repeated here for reference. For an irreversible system, the Randles-Sevick equation becomes equation 5.1.3.

$$i_p = \left(0.446 + 0.344\left(r\sqrt{\frac{nFv}{RTD}}\right)^{-0.852}\right) n \cdot F \cdot A \cdot C \cdot \sqrt{\frac{n \cdot F \cdot v \cdot D}{RT}} \qquad \text{Equation 3.1}$$

$$i_p = 1.1\left(0.446 + 0.344\left(r\sqrt{\frac{nFv}{RTD}}\right)^{-0.852}\right) n \cdot F \cdot A \cdot C \cdot \sqrt{\frac{\alpha \cdot n \cdot F \cdot v \cdot D}{RT}} \qquad \text{Equation 5.1.3}$$

where

α = transfer coefficient

n = number of electrons transferred

F = Farrady constant

A = area of the electrode

C = concentration of analyte

D = diffusion constant

v = scan rate

R = universal gas constant

T = temperature

If the analyte reaction is reversible, then the peak current will be linearly proportional to the square root of the scan rate. The diffusion coefficient can also be obtained from the Randles-Sevick equation (equation 3.1) as all other variables are known.

If the system is reversible, the number of electrons transferred in the system can be calculated by equation 5.1.4.

$$E_{p,c} - E_{p,a} = 2\left(1.1\frac{RT}{nF}\right) \qquad \text{Equation 5.1.4}$$

The mid-peak potential is the potential at which point the reaction occurs, shown in equation 5.1.5. This equation holds for reversible, quasi-reversible, and irreversible processes. If the system is reversible, the mid-peak potential is called the formal reduction potential.

$$E_0 = \frac{E_{p,c} + E_{p,a}}{2} \qquad \text{Equation 5.1.5}$$

5.1.5 Molten Salt Cell and Materials Description

All molten salt work was performed under an Ar atmosphere in a glovebox. Materials used in the electrochemical cell are listed in table 5.2.

Table 5.2 Materials used for electrochemical measurements.

Material	Use in experiment	Description (if applicable)	Vendor
CrF_2	Working curve development	Anhydrous, 99% purity	Alfa Aesar
CrF_3	Working curve development	Anhydrous, 99% purity	Alfa Aesar
Cr metal	Working curve development	2-3 mm pieces, 99.995% purity	Alfa Aesar
FeF_2	Working curve development	Anhydrous, 99.9% purity	Alfa Aesar
FeF_3	Working curve development	Anhydrous, 98% purity	Alfa Aesar
Fe wire	Working curve development	1 mm, 99.99% purity	Alfa Aesar
NiF_2	Reference Electrode	Anhydrous, 99% purity	Alfa Aesar
Ni wire	Reference Electrode	2 mm 99.98% purity	Alfa Aesar
Graphite	Reference Electrode	Open porosity:15%, medium pore size:2 μm	SGL Carbon
Graphite	Secondary Container	GR060	Graphite Store
Graphite	NAA sampler	AXZ-5Q	POCO graphite, inc.
Alumina bisque	Electrochemical setup support	Machinable	McMaster
Alumina Paste	Secure alumina	Resbond 989	Cotronics Corporation
Glassy Carbon	Salt container	Sigradur GAT 19	Hochtemperatur-Werkstoffe GmbH (HTW)
FLiNaK Salt	Salt under analysis	(46.5 mol% LiF-11.5 mol% NaF-42 mol% KF)	Electrochemical Systems, Inc.

Figure 5.1.17 shows the initial electrochemical experiment setup with a Pt-QRE.

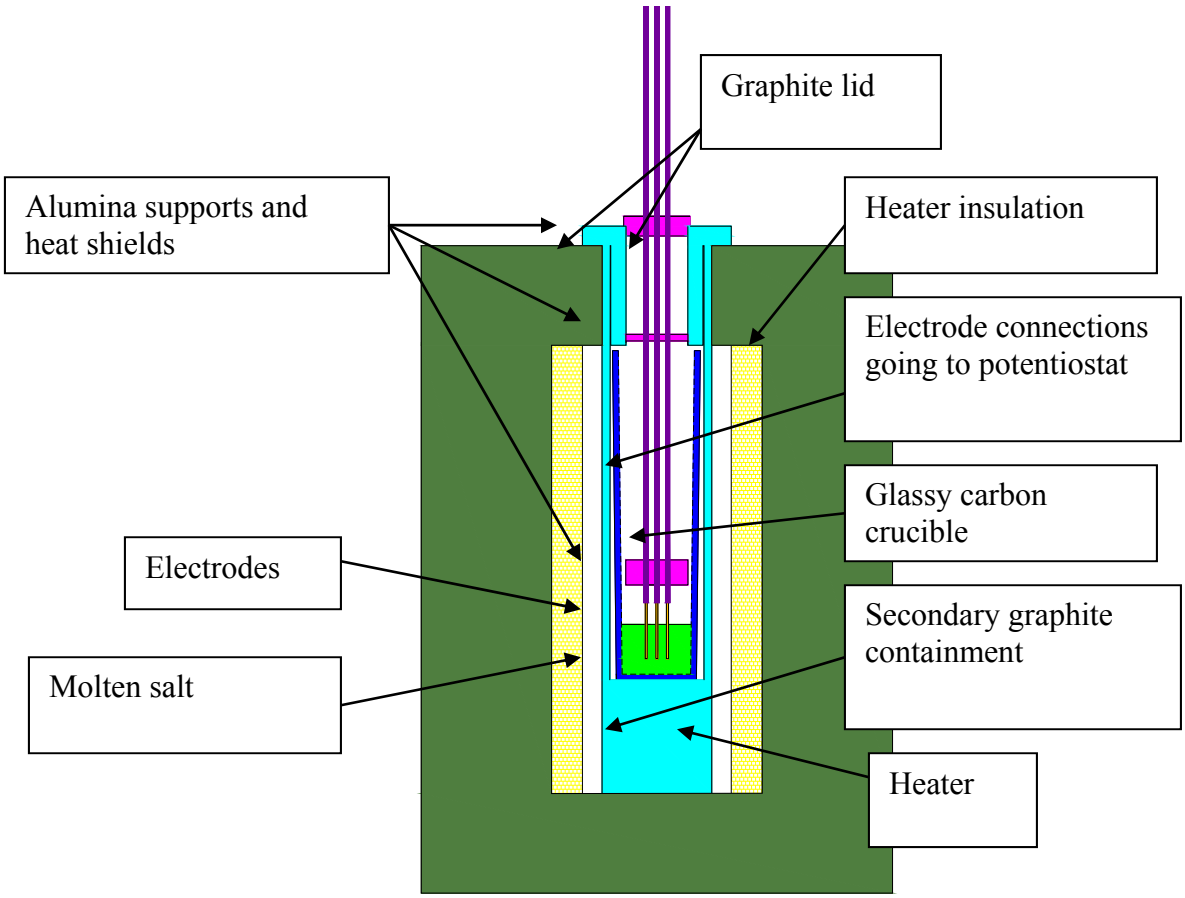

Figure 5.1.17 Schematic of high temperature electrochemical setup.

In the center are the three electrodes used for voltammetry. The bottoms of the electrodes are immersed in molten salt. An alumina apparatus hold the electrodes in place. Figure 5.1.18 shows a picture and a schematic of the alumina apparatus.

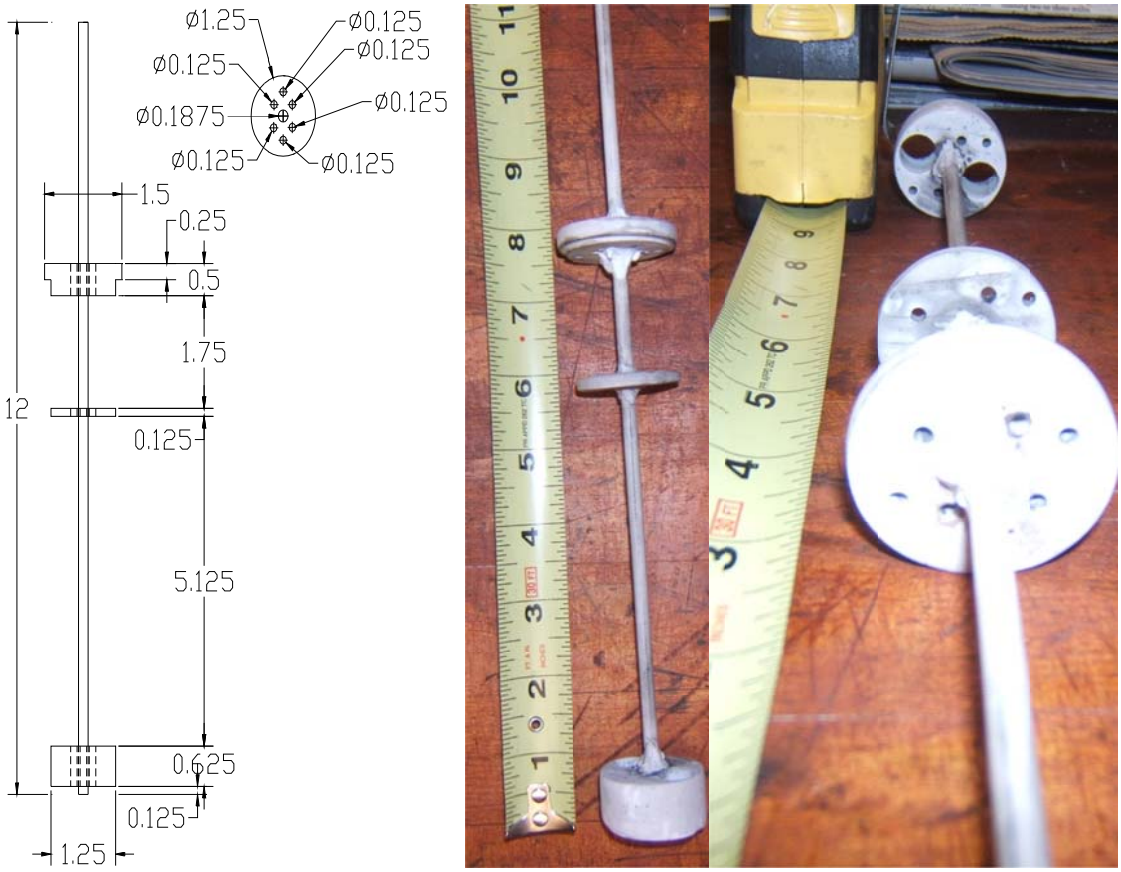

Figure 5.1.18 Alumina apparatus that held electrodes during electrochemical measurements. The larger holes through the bottom piece were drilled when the RE were implemented.

Fired and unfired alumina bisque were tested. Fired alumina bisque was more durable while unfired alumina bisque became embrittled with time. However, the unfired alumina bisque could be machined easily to accommodate updates to experimental hardware such as the addition of a Ni(II)/Ni RE, to be discussed in section 5.1.8.

The molten salt is contained within a 1.4” diameter glassy carbon crucible that rests within a larger graphite crucible. The graphite crucible acts as a secondary containment in case the glassy carbon crucible breaks. A graphite lid and alumina shields help to equalize temperatures. A Thermocraft RH ceramic heater was used in conjunction with LabView for temperature control. A Solartron 1287 potentiostat was used for voltage control and current measurement.

The WE and CE were both 1mm Pt wires. The CE was 0.5” longer than the WE to ensure that it had a larger surface area. A Pt-QRE was used. Figure 5.1.19 shows a picture of the electrode setup. Ni wires were welded to the Pt electrodes to reduce the amount of platinum used in the electrochemical setup (reduce the price of the setup).

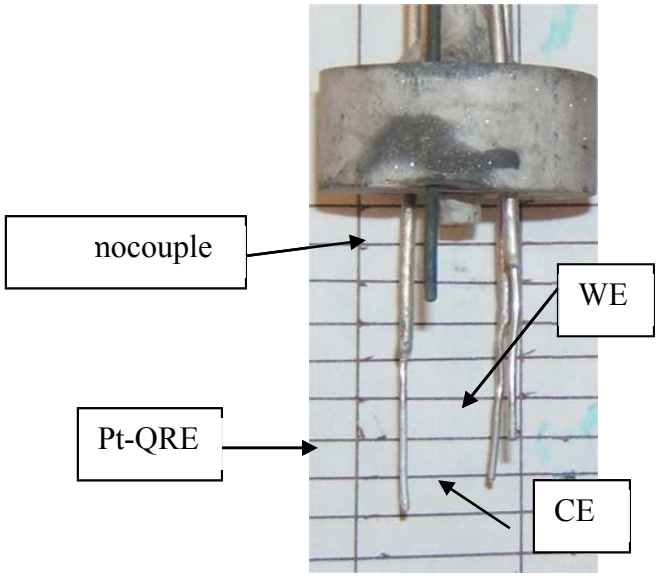

Figure 5.1.19 Electrochemical setup with Pt wires for the WE, CE, and QRE.

5.1.6 Optimizing Electrochemical Parameters

To ensure that no pure salt was wasted while electrochemical parameters were optimized, initial molten salt voltammetric measurements were performed using previously exposed salt from the 500 h static corrosion tests. The salt from the test of Ni-201 showed no weight loss so it was taken as a "pure" salt baseline. To obtain a working curve of peak current as a function of Cr concentration, small portions of salt exposed in the static corrosion test of Haynes-230 (a 22.5 Cr% alloy) were added. This salt was chosen because it had the largest weight loss so it should have contained the most metal ions of any of the salts used in the static corrosion tests. The large concentration of metal ions was desirable as it necessitated less use of the salt exposed to Haynes-230, allowing that salt to be saved for future chemical analysis.

Attempts were initially made to insulate the WE with alumina to provide a constant surface area throughout the breadth of the experiment. The Pt WE was inserted into a small hole drilled in alumina bisque that was subsequently fired at 1700°C. The firing shrunk the alumina around the Pt and reduced the alumina bisque porosity from 20% to near 0. Only the polished bottom of the Pt rod was exposed to the salt. However, alumina proved to be unstable in FLiNaK, and the dissolution of alumina introduced a large concentration of unwanted aluminum ions into the melt. The current peak during the stripping step was large enough that it masked any current peaks of other ions in the solution and was believed to be alumina due to its highly negative emf (see table 5.1). Insulating the WE was summarily abandoned, and the surface area of the WE was calculated by the depth that the WE was immersed in the molten salt. This depth was controlled by bending the Ni wire which connected the Pt electrodes to the potentiostat at a set distance throughout all measurements.

Several parameters were optimized using salts from the static corrosion tests. Acceptable plating times ranged from 15 s to 60 s. 15 s was chosen as optimal to reduce the total time of the electrochemical test as the heater was turned off during testing. A scan rate of 0.1 V/s was used for the stripping step. Scan ranges varied depending on the element of interest during the scan. The cleaning potential was held until the current was less than 0.001 A. A cleaning time of 10 s proved adequate for all measurements. Peaks were detected at -1.1, -0.79, -0.14, and 0.3 V for tests

performed against a Pt-QRE. No conclusive determination was ever made as to which peak corresponded with what element. Peak determination could most likely be completed once working curves for Fe and Ni have been completed as these are the ions, along with Cr, with the largest concentrations in the salts.

5.1.7 Obtaining Working Curves for Cr in FLiNaK using Pt-QRE

In an attempt to determine the Cr peak from the data obtained using salt from the static corrosion tests, an experiment was performed in which approximately equal amounts of CrF_2 and CrF_3 were added to pure FLiNaK. Anodic stripping was performed after each Cr addition with the following parameters: a plating potential of -0.7 V, a scan rate of 0.1 V/s, a final potential of 0V, and a cleaning potential of 0V. 1 mm Pt wires were used as the WE, CE, and QRE. The CE and QRE were inserted 1.5 cm into the melt while the WE was inserted 0.5 cm into the melt.

Concentration of Cr in the solution was estimated by calculation and confirmed by NAA. Samples for NAA were taken using a 3/8" graphite rod with a 1/4" hole drilled into it at an angle. Figure 5.1.20 shows a drawing of the sample removal tool as well as a picture of this tool with and without a small sample of salt in the collection area.

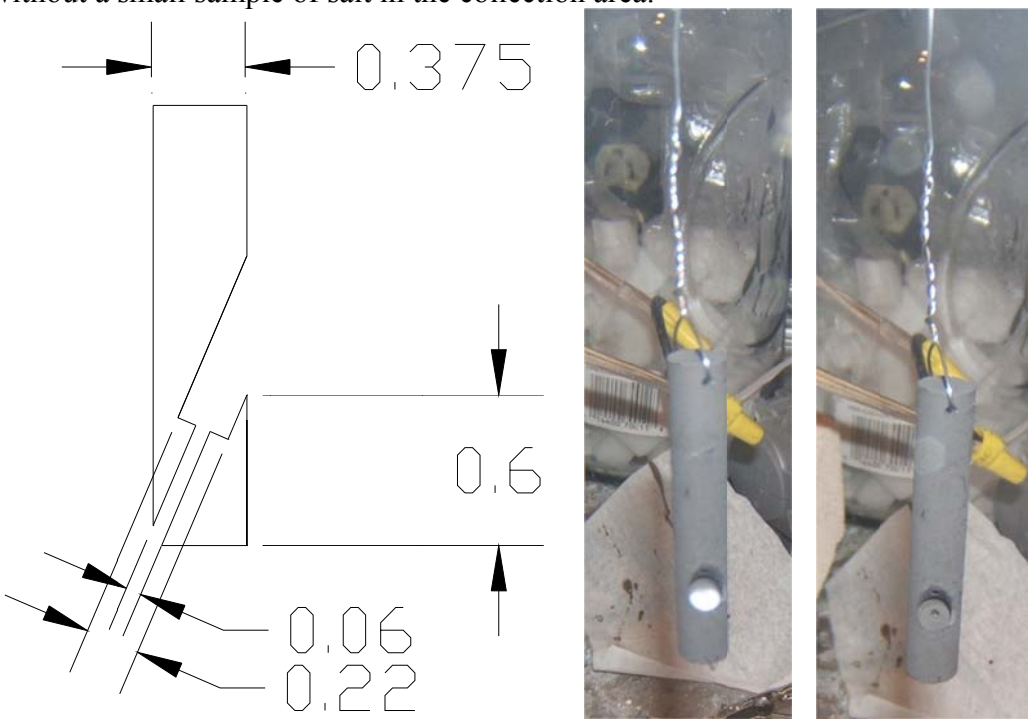

Figure 5.1.20 NAA sample removal tool drawing (left) and pictures with (center) and without (right) a salt sample. The hole through the back can be seen in the picture without the salt sample. Dimensions are in inches.

Two working curves of integrated current as a function of Cr concentration were obtained: one for Cr concentrations ranging from 10-300 PPM, the second for Cr concentrations of 100-900 PPM. To obtain the low concentrations of Cr for the 10-300 working curve, salt from the high Cr concentration (900 PPM) tests was added to pure FLiNaK. Equal portions of salt were removed as added using the NAA sampler to keep the exposed area of the WE constant for all measurements. A 30s plating time was necessary for the lower concentration curve while a 15s plating time was sufficient for the higher concentrations.

The electrodes built up a dark layer on their surfaces over time, necessitating regular cleaning to obtain reproducible data. The layer can be seen in figure 5.1.21. The surfaces near the red lines were above the salt while the surfaces near the black lines were immersed in the salt.

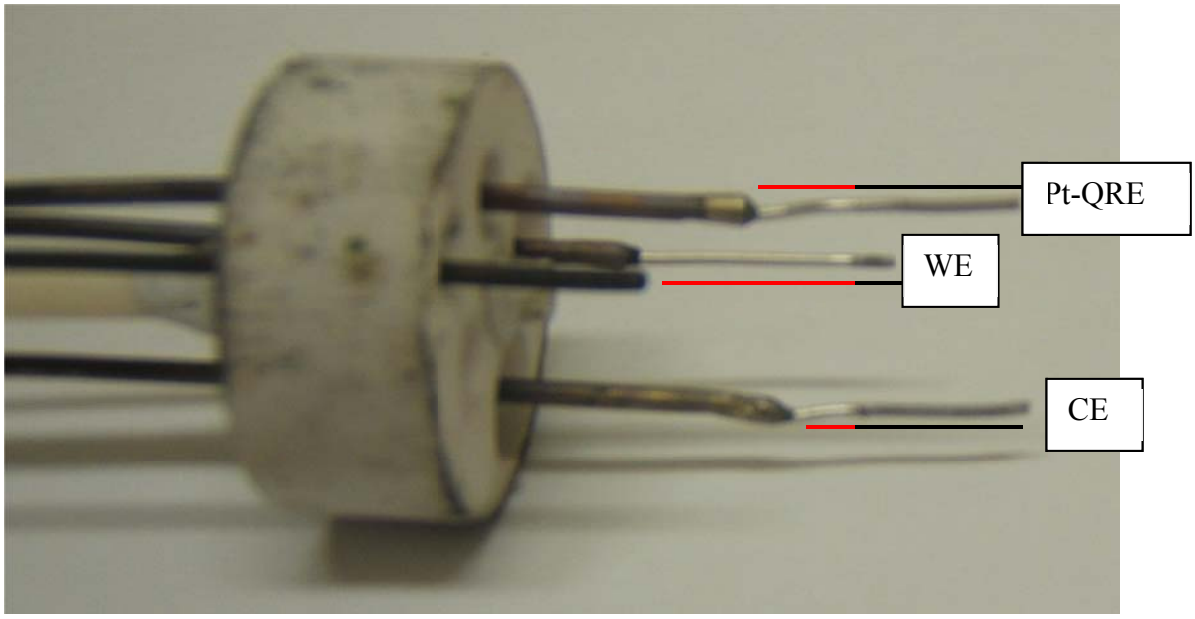

Figure 5.1.21 Film buildup on electrodes is shown near the black lines. The red lines indicate the portion of the electrodes above the salt.

The layer is likely carbon introduced into the salt from the support structure or the glassy carbon. Inspection of the salt after multiple days of taking electrochemical data showed what appeared to be a thin layer of carbon on the surface. The electrodes were cleaned each morning by polishing with 1 micron diamond paste and ultrasonically cleaning for 5 minutes in methanol and distilled water, the suggested method of removing any excess diamond paste.

5.1.8 Obtaining Working Curves for Cr in FLiNaK using Ni(II)/Ni Reference Electrode

Following the development of the working curve using the Pt-QRE, another working curve was obtained using a Ni(II)/Ni RE. While the Pt-QRE was very durable, the Ni(II)/Ni RE was expected to give a more constant potential for comparison. Two 10 mol% Ni(II)/Ni RE were prepared. Mol% is defined by equation 5.1.5a and an example for 10 mol% is shown in equation 5.5b. The RE were contained in graphite with an average grain size of 0.008 in, a bulk density of 1.73 g/cm^3, an open porosity of 15 vol%, and a medium pore size of 0.00008 in. Table 5.3 shows masses used for each reference electrode. Figure 5.1.22 shows a schematic of the Ni(II)/Ni RE.

$$x\ \text{mol\%} = \frac{x\ \text{mol}_{\text{Fraction}}}{100} = \frac{x\ \text{mol}_{\ NiF_2}}{x\ \text{mol}_{\ NiF_2} + (1-x)\text{mol}_{\ FLiNaK}} \qquad \text{Equation 5.1.5a}$$

$$10\ \text{mol\%} = 0.1\ \text{mol}_{\text{Fraction}} = \frac{0.1\ \text{mol}_{\ NiF_2}}{0.1\text{mol}_{\ NiF_2} + 0.9\ \text{mol}_{\ FLiNaK}} \qquad \text{Equation 5.1.5b}$$

Table 5.3 Masses of FLiNaK and NiF_2 used in 10 mol% Ni(II)/Ni RE.

RE 1		
Mass NiF_2 (g)	Mass FLiNaK (g)	Mol%
0.1365	0.5265	9.968
RE 2		
Mass NiF_2 (g)	Mass FLiNaK (g)	Mol%
0.1345	0.5165	10.007

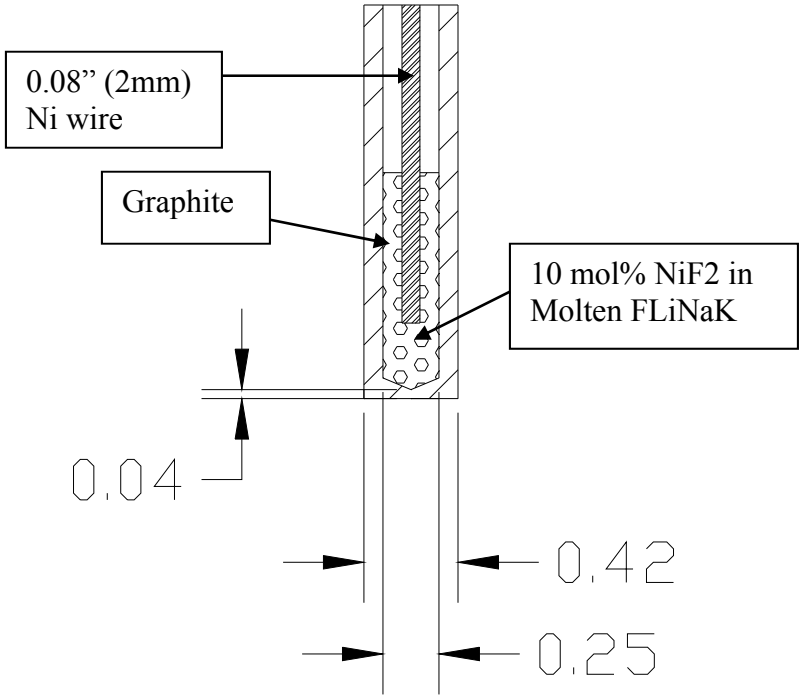

Figure 5.1.22 Schematic of Ni(II)/Ni RE. Dimensions are in inches.

Two RE are necessary to ensure that wetting has occurred and that the RE are stable over time. Checking the open circuit potential between the two reference electrodes gives insight into the condition of the reference electrodes with respect to one another. Figure 5.1.23 shows a schematic of how both RE are used.

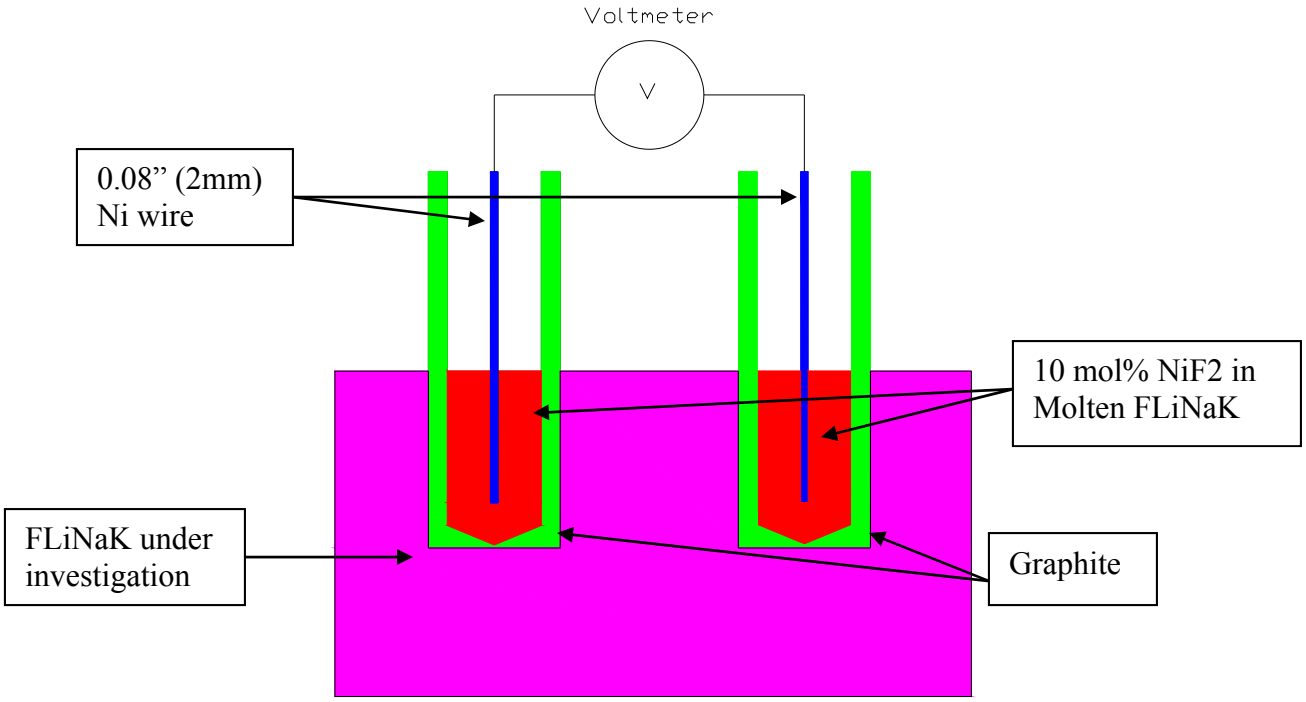

Figure 5.1.23 Two RE are used to determine when wetting has occurred by taking open circuit potential readings between the two RE over time. The potential difference between the two RE is zero when the RE are fully wetted (i.e. no potential drop through either graphite container.)

Holes were drilled into the alumina support structure to allow the RE fit through the alumina but still being held fast. The outer diameter of the RE was 0.42” so the holes were drilled to 0.43”. An alumina adhesive was applied to the outside edge of the top of the RE, making a rim that prevented the RE from sliding through the alumina support. Figure 5.1.24 shows a picture of the electrode setup. A 1 mm Pt wire was the WE and a coiled Pt wire was the CE. Glassy carbon was the salt container. The Ni wires that sit inside the RE were removed for this picture for ease of viewing. Figure 5.1.25 shows a view of the same electrode setup from below with all wires installed.

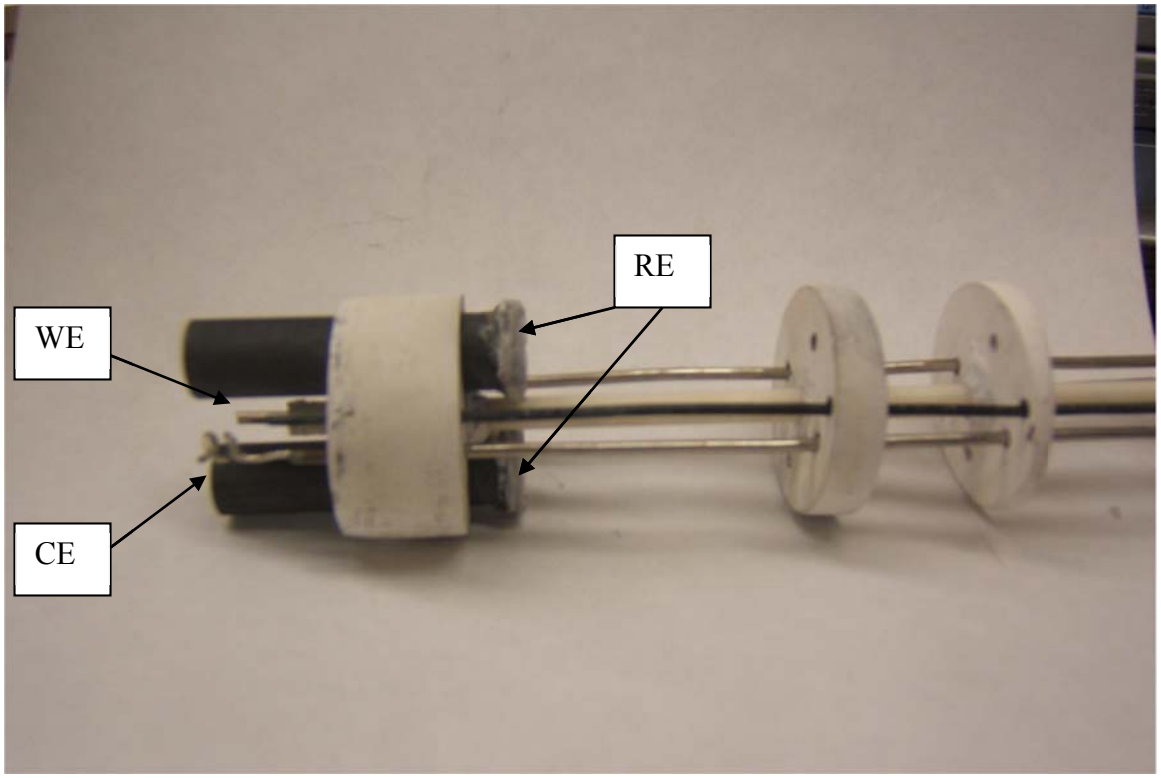

Figure 5.1.24 Side view of electrochemical setup using Ni(II)/Ni RE, a coiled 1mm Pt wire as the CE, and a 1mm Pt wire WE.

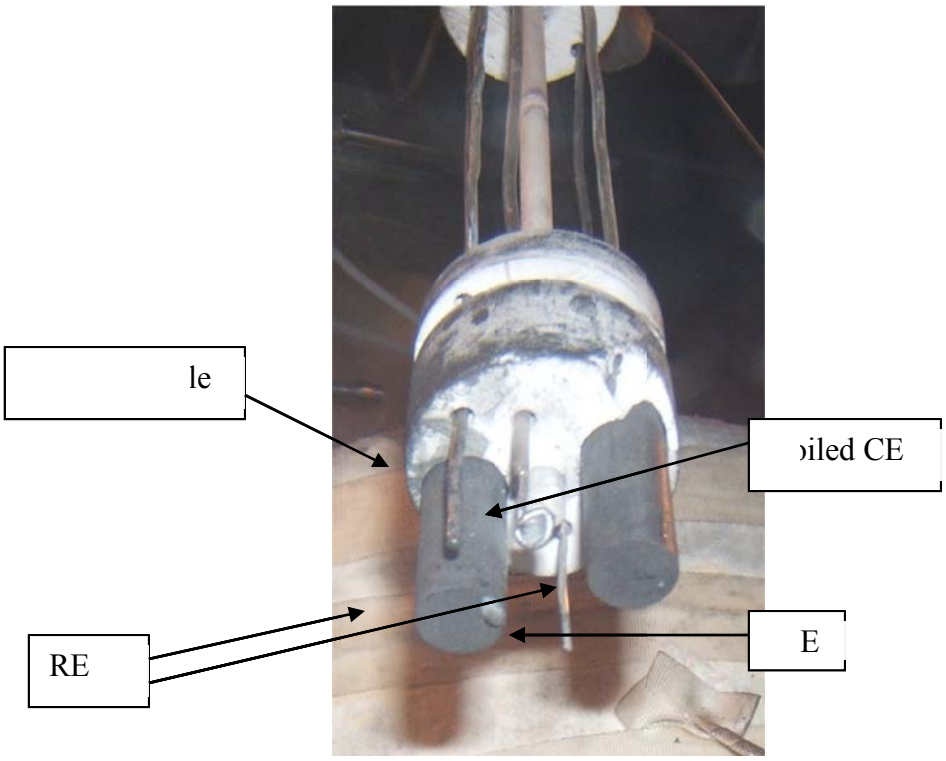

Figure 5.1.25 View of electrochemical setup from beneath using Ni(II)/Ni RE, a coiled 1mm Pt wire CE, and a 1mm Pt wire WE.

Wetting times for the porous graphite membrane (acting to ionically connect the RE to the solution while not allowing species to mix) were determined by monitoring the potential difference between the two identical RE. As described in sections 3.4 and 5.1.3, the RE are deemed wetted and ready for use when the potential difference between the two RE reaches zero. Open circuit potential measurements were taken between the two RE for 60 s intervals periodically while the RE were immersed in the salt. When the two RE were initially immersed in the salt, the potential difference between the two electrodes did not reach zero. Figure 5.1.26 shows the potential difference between the two RE versus time for the first day (using an average value measured for each open circuit potential measurement). A linear approach to zero was expected (similar to figure 3.1), but the unexpected shape of the potential may be due to the mixing of the NiF_2 and FLiNaK inside the RE.

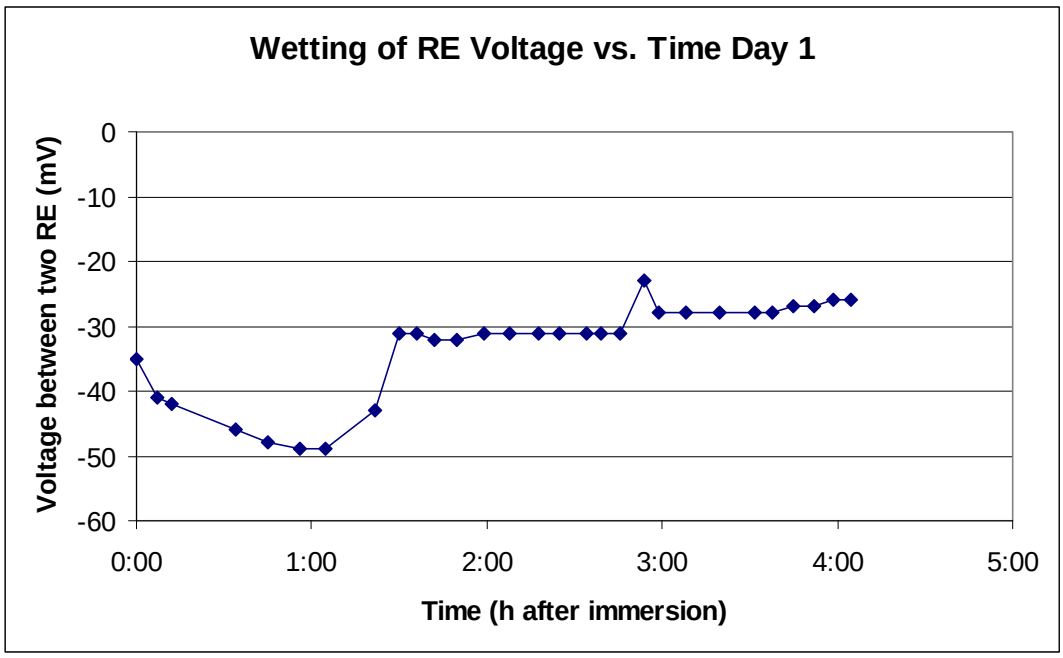

Figure 5.1.26 First immersion of RE in salt showed that wetting had not occurred after 4 hours.

After 24 hours the RE were again immersed in FLiNaK. Figure 5.1.27 shows potential difference as a function of time for the second immersion. The voltage linearly approached zero for ~4hrs. After that, the potential began to approach zero asymptotically.

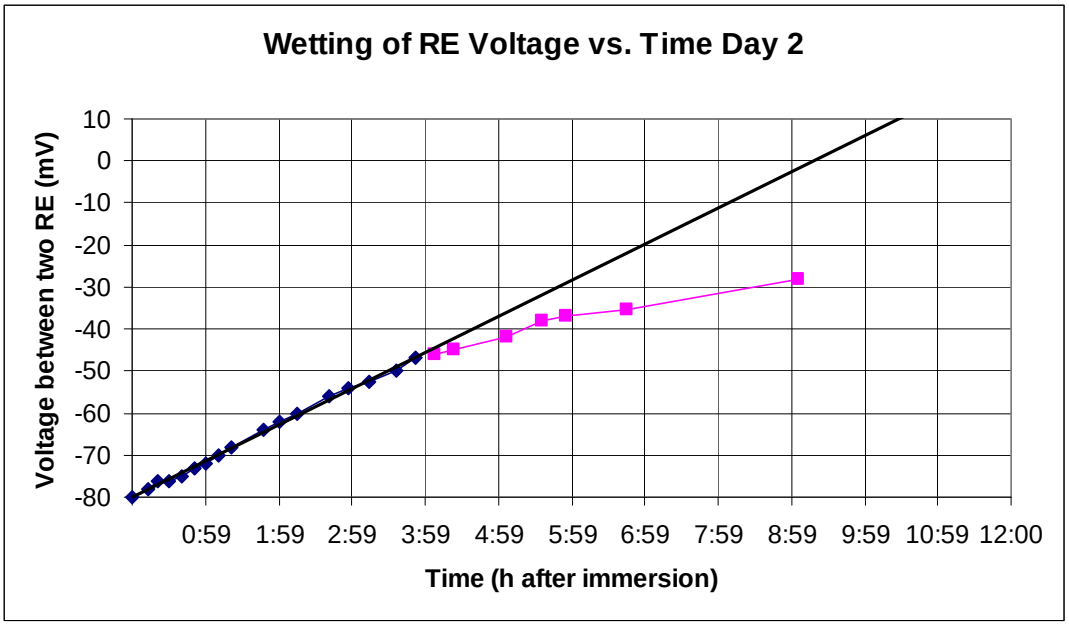

Figure 5.1.27 Potential as a function of time for the second immersion of the two RE in FLiNaK. This is the expected behavior of potential difference when wetting is occurring.

The RE were allowed to freeze overnight outside of the FLiNaK test crucible and were reimmersed the following morning. Figure 5.1.28 shows wetting of the RE.

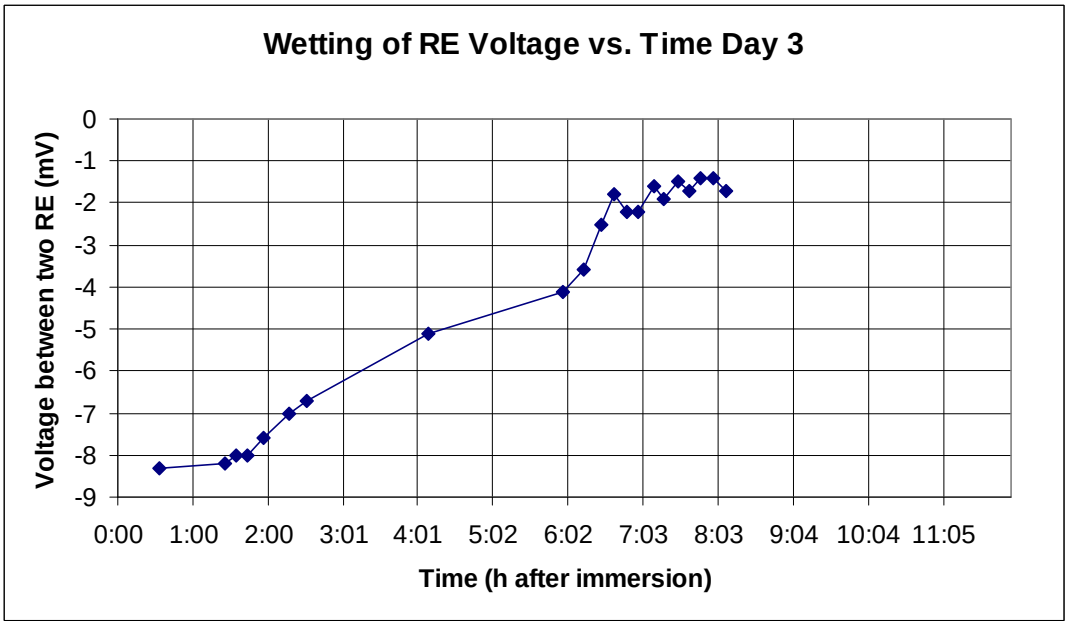

Figure 5.1.28 Wetting of RE occurs after 6.5 hours on the third day, a total of 21 hours after the first immersion.

The potential difference between the two RE never fully reached zero; the 2 mV difference could stem from an error in mass of either the NiF_2 or the FLiNaK inside the RE of less than 1 mg. It was decided to deem wetting had occurred when the potential difference reached a steady value

of ~1.5 mV. Wetting occurred after 6.5 hours on the third day of immersion, that is, after a total of 21 hours after the initial immersion.

The electrodes were again allowed to freeze overnight and wetting of the RE the following day occurred after 3 hours. From this point on, it was determined that the RE were to be kept in the molten FLiNaK to eliminate the need to wait for the RE to wet each morning.

All stripping scans performed when using the Ni(II)/Ni RE had a final potential of 0.3 V, which was then held for 10 s to fully clean the WE. The final voltage of 0.3 V ensured that if any Ni had diffused out of the RE into the FLiNaK, a peak would be detected at 0 V. A peak at 0 V could be determined as Ni because the RE is made from the Ni(II)/Ni couple in FLiNaK. Thus a peak at 0 V vs. the RE would be the same ionic couple as in the RE. If a peak was detected at 0 V, the RE would then be replaced to ensure the purity of the melt. The first set of RE were assumed to be leaking NiF_2 after 300h in the molten FLiNaK when such a peak was found. The RE had been frozen and remelted 12 times.

A second set of RE were made with 1 mol% NiF_2 in FLiNaK as it was determined that both concentrations would saturate the FLiNaK with Ni, necessitating less NiF_2 for each RE preparation. However, these RE were not as steady as the 10 mol% RE. The voltage between the two 1 mol% NiF_2 RE varied ~40mV. It is unclear why the 1 mol% RE were not as stable as the 10 mol% as both should have saturated the solution.

Working curves were developed for Cr concentrations of 10-300 PPM and 100-2000 PPM in the same method as described with the Pt-QRE. Electrochemical parameters were as follows: a plating potential of -0.7 V vs. Ni(II)/Ni RE, a scan rate was 100 mV/s with a scan range of -0.7 to -0.3 V vs. Ni(II)/Ni RE, a cleaning potential of 0.3 V vs. Ni(II)/Ni RE. NAA samples were taken after each addition. The WE was cleaned between each Cr addition using the procedure described previously. A 1/16” Ni tube was placed in the melt to bubble Ar gas for mixing in an attempt to improve repeatability.

5.1.9 Obtaining Working Curves for Cr metal in FLiNaK using Ni(II)/Ni Reference Electrode

Working curves for integrated current as a function of Cr concentration in FLiNaK were attempted by adding 99.999% pure Cr metal to FLiNaK to validate the working curves obtained by adding CrF_2 and CrF_3 to FLiNaK. Anodic stripping scans and NAA samples were taken after each Cr immersion. However, an unexpected large peak was seen at ~-1.1 V. The salt was allowed to freeze once Cr additions were complete in an attempt to determine the source of the large peak, and it was observed that the salt was coated in glassy carbon as shown in figure 5.1.29.

Figure 5.1.29 The salt removed from the glassy carbon crucible for electrochemical measurements after pure Cr metal had been added was covered in glassy carbon.

The salt coated in glassy carbon was replaced with new FLiNaK salt. More Cr metal was added to the clean FLiNaK salt, and the salt was allowed to freeze. After complete freezing had occurred, it was observed that the bottom of the glassy carbon crucible had cracked.

It was thought that this reaction between the glassy carbon and the FLiNaK was due to the FLiNaK becoming more reducing with the addition of Cr metal. The reduced FLiNaK could then wet the glassy carbon, and as the FLiNaK froze, it could grab the glassy carbon and cause it to crack. Wetting of graphite, Cu, and Ni containers using molten FLiBe salt due to the addition of a reducing metal has been observed **[59]**.

5.1.10 Investigation of Cr Metal Interaction with Glassy Carbon

To better understand the reaction between the pure Cr metal and the glassy carbon, it was decided to add a less reducing metal of interest, Fe. Fe was initially added in the form of anhydrous FeF_2 and FeF_3 to determine the potential of Fe reduction. All other experimental parameters were the same as when the working curve using CrF_2 and CrF_3 except that a 1 mol% Ni(II)/Ni RE was used. A range of concentrations of 100-600 ppm was used to make the higher concentration working curve. A lower concentration working was not attempted due to time limitations.

Since Fe(II) and Fe(III) have lower Gibb's free energies than Cr(II) and Cr(III) (see figure 4.1) and from previous work **[60]**, it was expected that the Fe peaks would be more positive than the Cr peaks. Initially, ASV was performed with a plating potential of -0.5 V, but no peaks were seen. The plating potential was then shifted to -1.0 V to ensure that both peaks were detected.

Fe wire (99.99% pure) was inserted into the solution, and ASV was performed over time. However, due to time limitations, the Fe wire was only in the FLiNaK for a total 12 hours. When the FLiNaK froze, no wetting had occurred.

5.2 Neutron Activation Analysis

5.2.1 Neutron Activation Analysis Background

Neutron activation analysis (NAA) is an analytical technique for determining trace impurities by activating a sample via irradiating it with a neutron flux and measuring the resulting gamma radiation of an excited isotope as a function of energy. As an irradiated atom decays from its excited state, it emits radiation to return to its ground state. In many cases, that radiation is in the form of gamma rays. Each radioactive isotope has a characteristic set of gamma ray energies. For example, when naturally occurring Fe is irradiated, one of the radioactive isotopes formed from neutron absorption is Fe-59, which then decays via gamma and beta emission to Co-59. Characteristic gamma rays are emitted at 1099 keV with an intensity of 56% and 1291 keV with an intensity of 43%. Gamma ray intensity is the percent chance that a specific gamma ray is emitted each time that a radioactive particle decays in contrast to the standard definition of intensity being the strength or degree of a measurement. In some decays, no gamma rays are emitted (decay via alpha or beta particles without gamma rays) or multiple gamma rays are emitted. In Fe-59, the gamma ray at 1099 keV is more likely to be emitted than the gamma ray at 1291 keV due to its higher intensity. One can infer the presence of Fe in an irradiated sample if a large number of counts are detected at both energy levels with the correct intensity ratio.

Gamma rays can be detected as a function of energy using a high purity germanium detector. Thus, gamma rays from each isotope can be detected and distinguished from each other. Figure 5.2.1 shows an example spectrum of the detector output after counting a radioactive sample with a high purity germanium detector. This particular spectrum was obtained from an irradiated FLiNaK sample from a 500 h static corrosion test of Hastelloy-X. A high Cr loss was determined for Hastelloy-X from scanning electron microscope (SEM) and energy-dispersive x-ray spectroscopy (EDS). As previously mentioned, radioactive Fe-59 emits gamma rays at 1099 keV and 1291 keV. Both of those peaks can be seen in figure 5.2.1. Note that constituents of the FLiNaK salt (Na, K, Li, and F) are not seen due to the decay time after the irradiation before counting. This will be discussed in greater detail later.

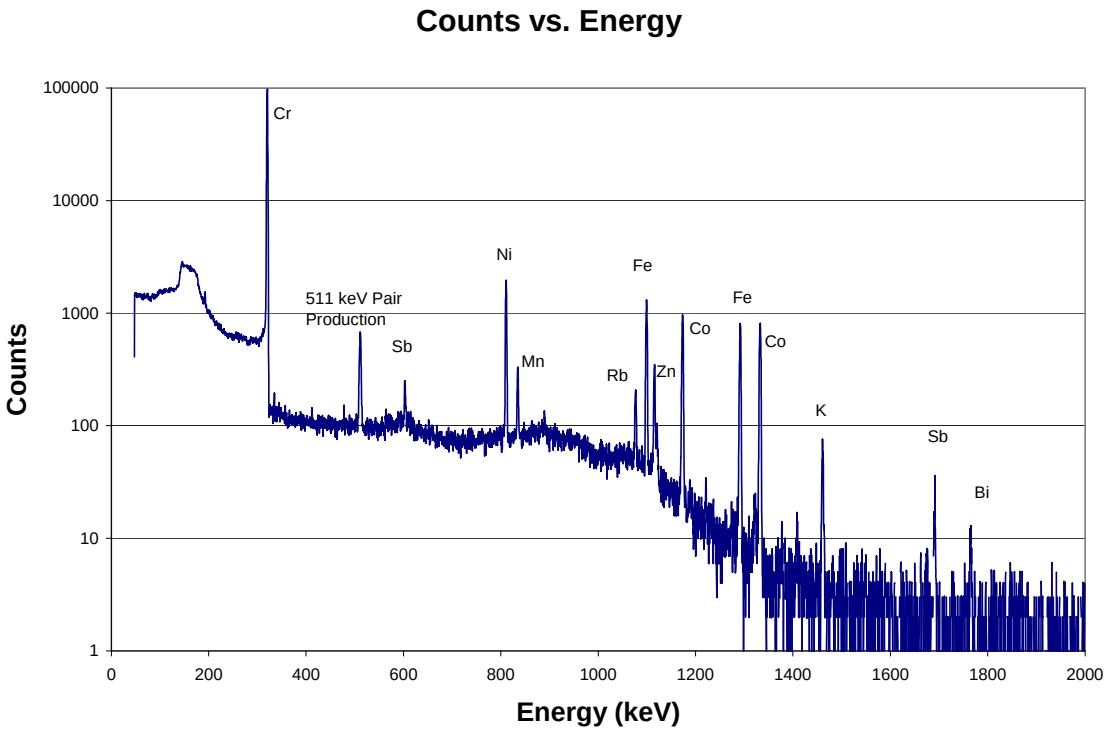

Figure 5.2.1 Typical output when counting a radioactive sample emitting gamma rays on a high purity germanium detector (obtained from a FLiNaK sample from a 500h static corrosion test of Hastelloy-X).

One limitation of this type of measurement is that a radioactive isotope with high activity (a high amount of gamma rays being emitted) can mask the characteristic gamma ray emissions of other isotopes in the spectrum. For example, in figure 5.1, if an element at 400 keV was present but only had 50 counts, it would not be detected. The minimum detectable activity (MDA) is defined by the smallest peak that can be seen above the background spectrum produced from other radioactive elements. The MDA is determined by choosing a region of interest around where a peak is thought to be, and the error is measured for that region. The error in the gross counts is defined as the square root of the number of counts. MDA is then calculated by equation 5.2.1 **[61]**.

$$MDA = 2.71 + 4.66\sigma \qquad \text{Equation 5.2.1}$$

The assumptions in this determination of MDA are that the counting statistics can be described by a Poisson distribution with a large sample size such that they can be considered Gaussian. It is also assumed hypothesis testing has been performed such that two kinds of errors (finding a peak when it is not present and failing to find a peak when it is present) have a 5% probability of occurring. **[62]**

Figure 5.2.2 shows the difference between two different regions where a peak might be suspected. Counts are integrated from the initial energy of the peak to the final energy of the peak and an error is taken for that region. In figure 5.2.2 the initial to final energy range would be from A to B, or from C to D. Peaks are assumed to follow a Gaussian distribution with an uncertainty of the square root of the total counts. A peak is not statistically relevant if the integral of the peak

counts is not greater than the MDA calculated by equation 5.2.1. Highly radioactive isotopes (i.e. large peaks) raise the background of peaks at lower energies due to Compton Scattering near the detector. One must wait for highly radioactive isotopes to decay to decrease the background to detect some less radioactive isotopes. For example in figure 5.2.2, although a peak may exist between energies A and B, the background from the peak between energies C and D will mask the peak between energies A and B. The peak between energies A and B is only statistically relevant when the counts in the energy range of A and B are greater than the counts calculated by equation 5.2.1.

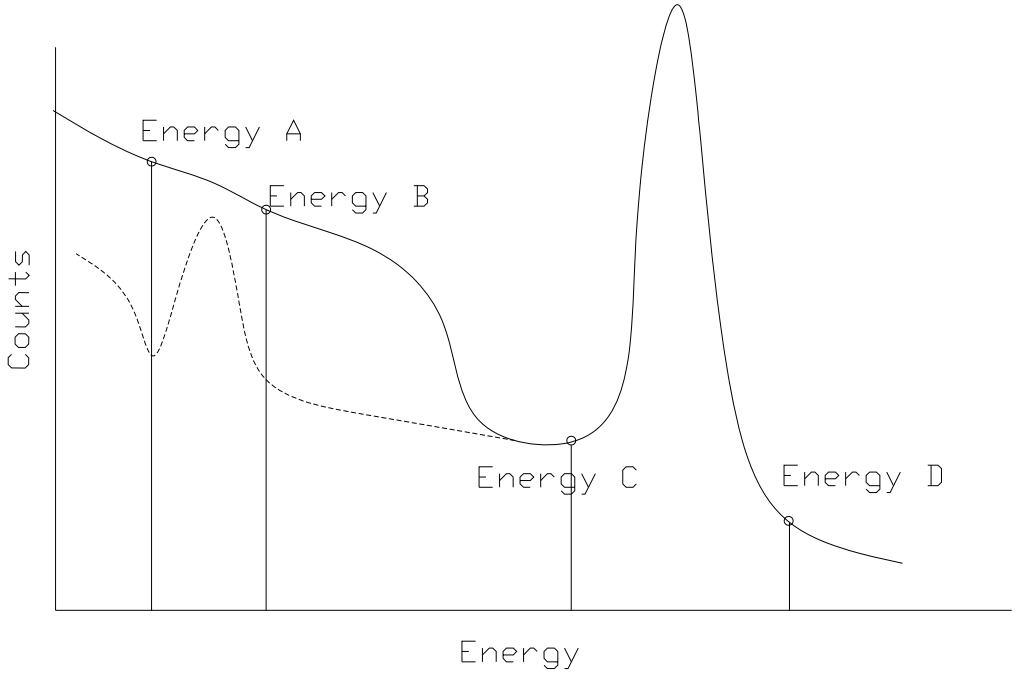

Figure 5.2.2 A sample spectrum with one large peak and a small hidden peak. MDA is determined by the uncertainty associated with the region of interest surrounding a suspected peak. A large peak will cause large MDAs for smaller peaks nearby.

The number of counts in each peak, called the observed activity (A_{OB}), is given by equation 5.2.2a.

$$A_{OB} \approx N\sigma\phi\left(1 - e^{\lambda t_{irr}}\right)e^{\lambda t_{DK}} \qquad \text{Equation 5.2.2a}$$

where

N = number density

σ = probability of absorbing a neutron, also called cross section

λ = the decay constant = $\frac{\ln(2)}{t_{1/2}}$

t_{irr} = the irradiation time

t_{DK} = the decay time

ϕ = the neutron flux of the irradiation facility in use

The University of Wisconsin Nuclear Reactor (UWNR) was used as the neutron source. Irradiation facilities included a tube that propelled samples with air to allow for short irradiations and immediate counting, as well as a submersed tube to allow for longer irradiations and to provide radiation shielding to the operator post-irradiation. Short irradiations (less than one minute) were performed in the air propelled (pneumatic) tube while long irradiations (two hours) were performed in the submersed (whale) tube. Table 5.4 shows conditions used for each type of irradiation and the approximate fluxes in each facility.

Table 5.4 Irradiation details.

Irradiation Facility	Length of Irradiation	Decay Time After Removal from Reactor	Thermal Flux (n/cm^2s)	Epithermal Flux (n/cm^2s)	Fast Flux (n/cm^2s)
Pneumatic Tube	Short (3 sec)	16 minutes	4.44E12	1.28E11	5.87E11
Whale Tube	Long (2 hr)	~2 weeks	7.64E12	3.77E11	1.74E12

Table 5.5 shows the thermal cross section, half life, and the most intense (most likely to be emitted) gamma decay energy of each of the isotopes of interest. Only the thermal cross section is shown as the fast and epithermal cross sections are much smaller and have negligible contribution to the activation. In this application, Cr and Fe halides are the alloy corrosion products of interest that are anticipated to be found in FLiNaK and $MgCl_2$-KCl salt. Halides of the other elements that make up the alloys are of lesser importance for corrosion detection.

Table 5.5 Important nuclear properties of salts and corrosion byproducts.

Isotope	Cr-51	Fe-59	K-42	Na-24	Li-11	F-20	Mg-27	Cl-38
Energy (keV)	320	1099	1524	1368	N/A	1633	843	2167
Half Life	28 d	44 d	12 h	15 h	0.8 s	11 s	9.5 m	37 m
Thermal Cross Section (b)	15.92	1.3	1.46	0.531	0.045	0.009	0.038	0.432

The nuclear properties of FLiNaK affect detection of corrosion byproducts when using NAA. When naturally occurring Li is irradiated, it does not emit a gamma ray when it decays, making it undetectable by NAA. F is hard to detect because it has a short half life, causing most of the radioactive F-20 to decay before a sample can be counted. Since the samples being analyzed are mostly FLiNaK with a small amount of metal impurities, the Na and K counts drown out the rest of the spectrum, making for very high MDA directly after irradiation. To obtain statistically

significant data from Cr and Fe, a two week decay time must pass so that the Na and K in the samples can decay.

The Cl in the $MgCl_2$-KCl salt has a larger cross section and longer half-life than Mg. Additionally, Cl is 67w/o of the salt while Mg is only 18 w/o of the salt. Thus, detecting magnesium is nearly impossible and verification of correct amounts of weight percent of Mg in the salt cannot be found by NAA. The Cl also masks the signal of other elements on a short time scale, making it nearly impossible to detect trace impurities with short half lives. A two week decay time must pass to allow K to decay before detecting any metal impurities since $MgCl_2$-KCl contains K, similar to FLiNaK.

The concentration of the impurity in the sample can be determined two different ways after the activity at a specific energy has been determined. The concentration may be calculated using a known flux profile, sample cross section, sample abundance, radiation intensity, detector efficiency, irradiation time, and decay time. Another method of determining concentration uses a known standard and compares mass and activities via the comparator method.

The first step in performing NAA is counting the sample to determine the activity. The activity of an element in a sample can be calculated by equation 5.2.2b, similar to 5.2.2a with some terms added to show the true equality.

$$A_{OB} = \frac{wa\varepsilon A_v \phi \sigma \left(1 - e^{\lambda t_{irr}}\right) e^{-\lambda t_{DK}}}{A} \qquad \text{Equation 5.2.2b}$$

where

a = atomic abundance

w = weight of the sample

Av = Avogadros Number

φ = flux observed by the sample during irradiation

A = atomic weight of the irradiated element

ε = efficiency of the detector

σ = cross section of the activation in question

t_{IRR} = time of irradiation

t_{DK} = time of decay

λ = decay constant of the radioactive isotope

While the activity can be calculated by equation 5.7b, activity is determined by counting the sample. The uncertainty in the gross activity is taken as the square root of the total counts. Known uncertainties include: half-lives, atomic weights, and atomic abundances, efficiency of the detector, and gamma ray intensity. The neutron flux to which the samples are subjected has been measured previously by the reactor staff. However, the flux values reported have no given uncertainty. Uncertainty in the detector efficiency is measured annually by the UWNR staff as a function of energy. Uncertainty in the sample masses is dependent on the scale used for mass determination,

but this contribution to the total uncertainty is generally smaller than uncertainties previously mentioned. Times of irradiation, decay, and counting are assumed to be correct with no uncertainty. Standard uncertainty propagation **[62]** is assumed throughout the rest of the analysis whenever uncertainty is introduced.

After the sample has been counted and the activity determined, the next step to determining sample concentration is calculation of the sample saturation activity (A_{SAT}) as show in equation 5.2.3.

$$A_{SAT} = A_{OB} \frac{\lambda t_{CNT} e^{\lambda t_{DK}}}{\left(1 - e^{-\lambda t_{IRR}}\right)\left(1 - e^{-\lambda t_{CNT}}\right)} \qquad \text{Equation 5.2.3}$$

where

A_{OB} = observed activity from the detector
t_{IRR} = irradiation time
t_{CNT} = count time
t_{DK} = decay time
λ = decay constant

The thermal flux of each irradiation facility at the UWNR was measured during the initial core measurements in the 1960's and updated in the 1990's. Since the flux can vary during operation, a thermal flux is calculated using an element from a known standard for each irradiation. For long irradiations, the flux is standardized using Fe-59. The flux calculation is performed using equation 5.2.2b as all variables are known except for the flux.

The macroscopic cross section can be calculated using the saturation activity as show in equation 5.2.4.

$$\Sigma = \frac{A_{SAT}}{\phi_{th,M}} \qquad \text{Equation 5.2.4}$$

where

A_{SAT} = saturation activity
$\phi_{th,M}$ = measured thermal flux

The flux averaged microscopic cross-section (σ) can be found using equation 5.2.5. The ratios of each flux value to the thermal flux are assumed to be constant.

$$\sigma = \frac{\sigma_{th}\phi_{th} + \sigma_e\phi_e + \sigma_f\phi_f}{\phi_{th,M}} \qquad \text{Equation 5.2.5}$$

where

$\sigma_{th,e,f}$ = thermal, epithermal, and fast cross sections

$\phi_{th,e,f}$ = thermal, epithermal, and fast fluxes

$\phi_{th,M}$ = measured thermal flux

The mass of the element (m_{ele}) can then be calculated as show in equation 5.2.6.

$$m_{ele} = \frac{\Sigma \cdot MW}{\sigma \cdot Av \cdot A} \cdot 10^{24} \cdot 10^{6} \qquad \text{Equation 5.2.6}$$

where

Σ = macroscopic cross section

σ = flux averaged microscopic cross section

MW = molecular weight of the element

A_v = Avogadros Number

A = naural abundance of the isotope

The natural abundance of an isotope is defined in units of atom percent, i.e. the percentage of the atoms of an element that are of a particular isotope.

Equation 5.2.6 gives the mass of the element in micrograms. The factors of 10^{24} and 10^{6} are for converting from barns to cm^2 and from grams to micrograms. To determine the sample's concentration of an element in units of PPM, the mass of the element (m_{ele}) in units of μg is divided by the total mass of the sample (m_{sam}) in units of g, as shown in equation 5.2.7.

$$\text{PPM} = \frac{m_{ele}\,[\mu g]}{m_{sam}\,[g]} \qquad \text{Equation 5.2.7}$$

A second way of determining the concentration which limits the uncertainty introduced with flux profiles and detector efficiencies is by using the comparator method. In the comparator method a ratio is taken of the activity of an unknown sample to that of an elementally characterized standard. The flux profile during irradiation and time of irradiation must be identical for the sample and the standard. Equation 5.2.8 combines equations 5.2.3 through 5.2.7 to show a ratio of the mass of an element in an unknown sample and in a standard. All variables used in equation 5.13 were described above. Subscripts sam and std represent an unknown sample and a standard, respectively.

$$\frac{m_{ele,sam}}{m_{ele,std}} = \frac{w_{sam}\left(A_{OB}\left(\lambda t_{CNT} e^{\lambda t_{DK}}\right)MW\right)_{sam} \cdot \left(A \cdot A_v\left(1-e^{\lambda t_{IRR}}\right)\left(1-e^{\lambda t_{CNT}}\right)\left(\phi_{th}\sigma_{th}+\phi_e\sigma_e+\phi_f\sigma_f\right)\right)_{std}}{w_{std}\left(A_{OB}\left(\lambda t_{CNT} e^{\lambda t_{DK}}\right)MW\right)_{std} \cdot \left(A \cdot A_v\left(1-e^{\lambda t_{IRR}}\right)\left(1-e^{\lambda t_{CNT}}\right)\left(\phi_{th}\sigma_{th}+\phi_e\sigma_e+\phi_f\sigma_f\right)\right)_{sam}}$$

$$= \frac{\left[wA_{OB}\left(e^{\lambda t_{DK}}\right)\right]_{sam}}{\left[wA_{OB}\left(e^{\lambda t_{DK}}\right)\right]_{std}} \qquad \text{Equation 5.2.8}$$

It can be seen from equation 5.2.8 that all variables cancel except for the weight of each sample, decay time of each sample, and the activity provided the sample and the standard have identical irradiation conditions. Since the decay time, standard concentration (m_{ele}/w), observed activity, and the unknown sample weight are known, one can calculate the mass of the element in the sample and concentration.

5.2.2 Irradiation Facilities for NAA at UWNR

Samples of approximately 200 mg are sealed in 2/5 dram polyethylene vials, shown in figure 5.2.3.

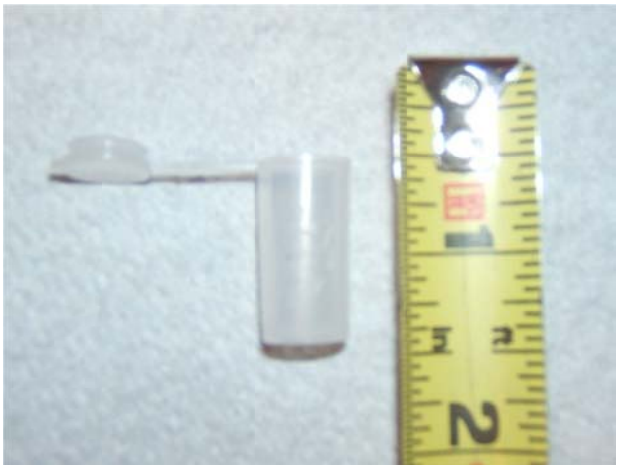

Figure 5.2.3 Unsealed sample vial.

The samples are sealed shut using a friction seal. The 2/5 dram vials are placed into a whale bottle for long irradiations, as shown in figure 5.2.4.

Figure 5.2.4 Sealed sample vials in a whale bottle for long irradiations.

Nine samples can be placed in a circular row in the whale bottle, and four rows can be placed into one whale bottle allowing for 36 samples to be irradiated at one time. The whale is then screwed shut and is ready to be irradiated. The whale tube sample capsule is irradiated for two hours with a thermal flux of $7.64 \cdot 10^{12} \frac{n}{cm^2 \cdot s}$, an epithermal flux of $3.77 \cdot 10^{11} \frac{n}{cm^2 \cdot s}$, and a fast flux of $1.42 \cdot 10^{12} \frac{n}{cm^2 \cdot s}$.

For short irradiations, samples are placed inside a rabbit bottle instead of a whale bottle. The rabbit bottle is shown in figure 5.2.5.

Figure 5.2.5 The first picture is a shows the relative size of the rabbit bottle and the sealed sample. The second and third pictures show a rabbit bottle with and without a sample. A threaded lid (as seen on the bottom of the first picture) screws onto the top of the rabbit to hold the sample in place during irradiation.

One sample is irradiated at a time in a rabbit for 3 seconds with a thermal flux of $7.64 \cdot 10^{12} \frac{n}{cm^2 \cdot s}$, an epithermal flux of $3.77 \cdot 10^{11} \frac{n}{cm^2 \cdot s}$, and a fast flux of $1.42 \cdot 10^{12} \frac{n}{cm^2 \cdot s}$.

After irradiation and sample removal from either system, samples are counted on a high purity germanium detector connected to a mutlichannel analyzer. The Quantum Gold software suite is used for detecting and recording count data. A program developed by the UWNR, NAACalc, is used for determining peak counts and calculating NAA results. Inputs into the program include

masses of samples, identification of standard material, and irradiation conditions. NAACalc then determines whether a peak can be analyzed using the comparator method with the standard or whether concentration must be determined using equations 5.2.1 through 5.1.4.

5.2.3. Initial Irradiations for Neutron Activation Analysis

Initial irradiations were performed to determine approximate sample compositions and appropriate decay and counting times. The salt containing the sample with the highest weight loss (Haynes-230) from the 500 hour static corrosion tests was chosen for the initial irradiations. This salt was chosen because the largest amounts of dissolved cations should be present in the salt, helping define the parameters (such as irradiation time, decay time, count time) that would be necessary to detect the corrosion products. The standard CSSO4 (Canadian soil) was chosen as a standard due to its variety of constituent elements, as shown in Table 5.6 From previous SEM and EDS analysis **[55]**, the main losses from the samples to the salts was Cr and Fe. Nonetheless, the initial analysis was performed to determine what other elements had dissolved from the metals into the salts.

Table 5.6 Elemental composition of standard CSSO4.

Elements in CSSO4 with concentrations above 100 PPM (concentration in PPM):	Elements in CSSO4 with concentrations below 100 PPM:
Al (54,600); Ba (730); C (44,200); Ca (11,200); F (300); Fe (23,700); K (17,300); Mg (5600); Mn (600); N (3800); Na (10,000); P (900); S (595); Si (317,000); Sr (170); Ti (3400); Zr (278).	As, B, Be, Bi, Br, Ce, Ce, Cl, Co, Cr, Cs, Cu, Dy, Er, Eu, Ga, Gd, Ge, Hf, Hg, Ho, I, In , La, Li, Lu, Mo, Nb, Nd, Ni, Pb, Rb, Sb, Sc, Se, Sm, Sn, Sr, Ta , Tb, Th, Tl, Tm, U, V, W, Y, Yb, Zn

To determine the relative masses of the main constituents of FLiNaK, short sample irradiations were performed. As noted in Table 5.9, the half-life of F-19 is 11 seconds, requiring samples to be counted as soon after irradiation as possible. The fastest possible sample changing time was approximately 1 minute, which allowed for the F in the sample to be counted. However, due to the large amounts of Na and K in the sample, almost all other meaningful data were masked. Counting after short irradiations was not useful to detect the elements of interest since all the metals of interest have half-lives on the order of days.

The long irradiations proved adequate for the determination of concentrations of metal cations of interest. Large amounts of activated Na and K were still present in the samples after a decay time of one week, causing high minimum detectable concentrations of metals of interest. Minimum detectable concentrations dropped after a two week decay, allowing for characterization of more impurities including Cr and Fe with minimum detectable concentrations on the order of 100 PPM and 10 PPM, respectively. A three week decay time was considered, but minimum detectable concentration of Cr increased as compared to the two week decay time.

It was determined that all useful data for determining concentrations of corrosion byproducts could be found from long irradiations and counting after a two week decay.

5.2.4. Selection of Standard for Comparator Method

Multiple standards were considered for use in determining concentrations of impurities in the salt samples when using the comparator method mentioned above. Among those considered were four different ferritic rock samples (CSFER1, CSFER2, CSFER3, and CSFER4), stainless steel (NBS 316), and coal ash (NBS 1632A). These standards were chosen due to their high Cr and

Fe concentrations. Table 5.7 shows elemental concentration in PPM of each of the standards. Concentration of Cr and Fe are listed first for ease of comparison.

Table 5.7 Elemental composition (in PPM) of standards for the proposed research.

	Steel	Coal	Fer Rock 1	Fer Rock 2	Fer Rock 3	Fer Rock 4
Cr	6900	34	7	47	6	9
Fe	956000	11000	530000	277000	312000	279000
Al	200	25900	2750	27300	476	
As	170					
Ba			1000	240		
C	3830	660000				
Ca		2400	23600	15700	6000	16000
Cl		760		100		
Co	300					
Cu	420		100			
F			600	400	100	
Ho		380				
K		4120	142	9400	213	2060
Mo	1900					
Mg		1200	1810	12700	6030	8500
Mn	5560		1700	929	620	1470
N		12000				
Na		8200	222	3780	222	371
Ni	20000					
O		155000				
P		2660000	10000	1180	300	570
Pb			5300			
Ru	170					
S		15800	2600	1700	300	1100
Si			79200	230000	250000	23400
Sm	2200					
Sn	100					
Tb	200					
Ti	200		180	1080		420
Tl	200					
V	120					
W	170					
Zn			3500			

Short irradiations were not performed on the standards due to the lack of knowledge gained from the short irradiations on the salts. After a two week decay, spectra from the various standards were compared to spectra from two week decay counts of the initial irradiation. In addition to comparing spectra, densities of the standards were compared to that of the salt samples.

From comparison of the spectra it was determined that the coal ash standard (NBS 1632A) and the steel standard (NBS 316) most appropriately matched the elements of interest. However, the steel standard, on account of its higher density, had nearly triple the mass to obtain approximately the same irradiation volume as a salt sample, a necessity to accurately standardize

using the comparator method. Thus, the coal ash standard (NBS 1632A) was chosen to be the standard for all irradiations in which the elements of interest were Cr and Fe.

5.2.5 NAA Repeatability Tests

Volume Test

Difficulty obtaining a constant irradiation volume for each sample was encountered for the initial FLiNaK samples due to difficulty breaking the frozen salt down into a fine powder. One of the assumptions when a sample is standardized is that the sample and the standard experience the same flux profile due to similar irradiation geometries. The standardization process will be erroneous if the volumes of the samples and the standards are different, due to the difference in the geometry and subsequent flux profile. An experiment was devised to determine the effects of standard volume variance as compared to the sample volume when determining sample composition. As shown in Table 5.8, nine different volumes of standard NBS 1632A were irradiated, and activity per mass was calculated for each. Figure 5.2.6 shows the averaged activity per gram from each of the nine samples of varying volume. Activity per gram decreased linearly with increasing sample volume. The variation of activity as a function of sample was small compared to the variation seen in the initial salt irradiations. A 90% change in volume only changed the activity per mass of the sample by 20%. The volumes of the salts only varied by 40%, and activities varied by greater than 200% during the initial irradiations.

Table 5.8 Masses and volumes used for determining the effects of varying volume in activity determinations.

Mass (g)	Volume (cc)	Percent of Final Volume (%)
0.0425	0.0452	10.35
0.1094	0.1163	26.62
0.1556	0.1655	37.87
0.1979	0.2105	48.16
0.2052	0.2182	49.94
0.2425	0.2579	59.02
0.3087	0.3284	75.15
0.3535	0.3760	86.04
0.4108	0.4370	100.00

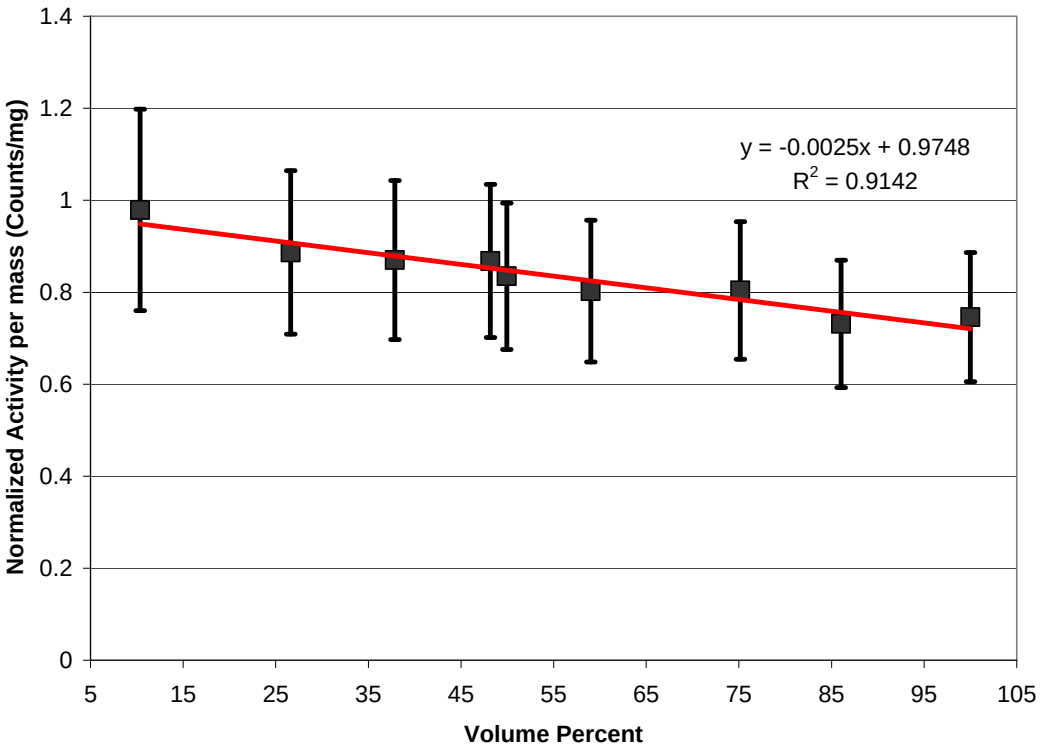

Figure 5.2.6 Activity per mass of different samples of the same material but different volumes.

Row Test

Another experiment was performed to ensure that each sample in a row inside of a whale tube sample bottle was exposed to the same flux as the standard in that row. This experiment also verified repeatability between rows in a whale bottle (see figure 5.2.4 and following for more description) and the NAA calculation methods furnished by the UWNR. The test consisted of irradiating two samples of standard NBS1632A in each of the four rows of a whale bottle. One of the standards was treated as a known standard while the other was treated as an "unknown" sample, and the program furnished by the UWNR was used to calculate the concentrations in the "unknown" sample. Figure 5.2.7 shows normalized concentration for elements with varying percent uncertainty of the counts per second (CPS).

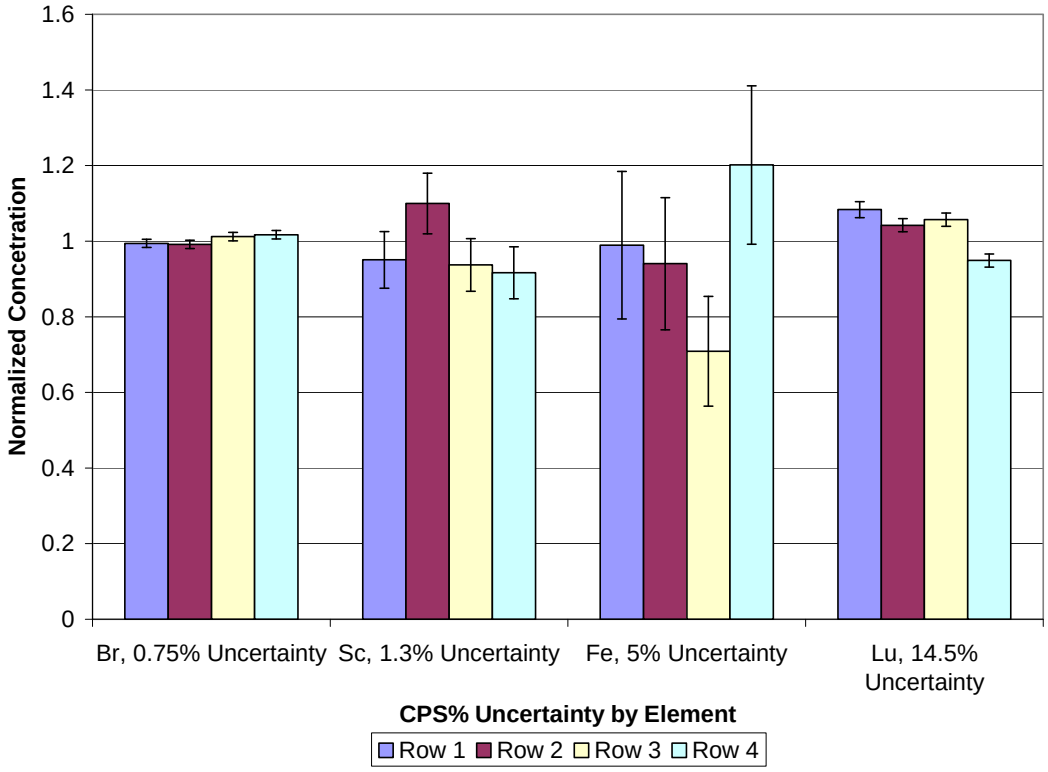

Figure 5.2.7 Comparison of several elements analyzed in the row test.

The NAA calculation program properly analyzed samples if the photopeak count rate had relatively low uncertainty (i.e. high count rate). The precision of NAA decreased as the photopeak uncertainty increased. Repeatability decreased when the uncertainty in the count rate approached 15%.

NAA was performed in search of Cr and other corrosion products when analyzing the salts. With an irradiation time of 2 hrs in the whale tube at the UWNR, a decay time of 2 weeks, and a count time of 1 hour, a FLiNaK sample with 5PPM Cr has a CPS uncertainty of ~7%. The uncertainty in CPS decreases as concentration increases.

5.2.6. Evaluation of Pure Salts and Salts from Static Corrosion Tests

Samples from each of the static corrosion tests, from three FLiNaK preparations (from ECS, Inc., INL, and in-house prepared), and from each of the four $MgCl_2$-KCl purifications were irradiated to determine impurity concentrations. NBS1632A was used as a standard for all irradiations. It was determined that the salt from the static corrosion tests was not homogeneous as

elemental composition results varied depending on where the sample was taken in the crucible. This heterogeneity is assumed to occur during the freezing process as the outside of the crucible would cool faster than the center, causing preferential diffusion of dissolved ions due to the thermal gradients. To account for the heterogeneity of the salt, small portions of each salt were taken from different locations within the crucibles and crushed in a glass mortar and pestle to obtain homogeneous samples. Approximately 300 mg were taken for each sample. The glass mortar and pestle were cleaned with deionized water and ethanol between each sample collection to limit cross contamination when preparing different salts for NAA. The FLiNaK was difficult to crush into a fine powder. In contrast, the $MgCl_2$-KCl was much easier to crush. Short irradiations were forgone due to the anticipation that all meaningful knowledge of metal impurity concentration could be found from long irradiations.

5.2.7 FLiNaK Preparation Test

Concentrations of metals in FLiNaK salt from the static corrosion tests determined by NAA varied significantly greater than the error of the measurement when the samples were prepared by crushing. An experiment was performed to determine if it was possible to obtain more homogeneous samples by crushing the samples into a more homogeneous powder (done outside the glovebox) or by melting the salts, taking samples, and allowing them to freeze (done outside the glovebox). Six samples were irradiated from each preparation (crushing and melting). Table 5.9 shows concentrations determined by NAA from each method of preparation. Taking molten samples was the more repeatable method of the two.

Table 5.9 Results from FLiNaK preparation test. Taking molten samples gave results within error of one another. Crushing had more variation.

	Molten Samples (PPM)	Error (PPM)	Crush outside of Glovebox(PPM)	Error (PPM)
1	81.5	9.1	109.7	11.6
2	90.5	10.1	94.8	10.0
3	73.4	8.5	107.1	11.3
4	78.5	9.0	143.4	15.3
5	76.5	7.8	111.9	12.0
6	83.8	8.4	113.2	12.1

5.2.8 NAA of graphite

Samples of the graphite used in the static corrosion tests were crushed up into a fine powder. NBS 1632A was used for the standard as it matched the density of the graphite reasonably well.

5.2.9 Experimental parameters chosen for NAA of salts

NBS 1632a was the best standard for use in the comparator method for both the FLiNaK and the $MgCl_2$-KCl salt. A homogeneous mixture was obtained by crushing the $MgCl_2$-KCl salt. A mass of approximately 200 mg was collected for each salt sample, and an approximate standard mass 100 mg matched the volume well. For the FLiNaK salt, a homogeneous mixture was obtained by taking molten samples of the salt and allowing them to freeze. Masses of the FLiNaK samples varied due to the geometry of the NAA sampler, but masses were approximately 200 mg. FLiNaK samples with mass greater than 275 mg are discouraged as the increased gamma radiation caused swelling of the sample vials and subsequent jamming in the counting setup. The standard mass for

the FLiNaK salt was chosen to match the approximate volume of the frozen salt sample, which was approximately 150 mg.

All salt samples were irradiated for 2 hrs at 1 MW in the whale tube irradiation facility of the UWNR. An optimal decay time for detecting metals such as Cr and Fe was 2 weeks. Samples were counted on contact of the HPGE detectors at the UWNR for 1 hour.

6. Results and Discussion

6.1 NAA of Salt from 500h Static Corrosion Tests in FLiNaK

Elemental composition of the FLiNaK salt from the static corrosion tests was determined by NAA. Two methods of sample preparation were attempted to obtain homogeneous, representative samples of the entire salt: first, crushing salt to a fine power and, second, melting samples in a glassy carbon crucible, allowing the molten salt to freeze in sizes small enough for irradiation. The second method provided much more repeatable results. Salt samples were melted in a glassy carbon crucible which was ultrasonically cleaned with distilled water and methanol between each melting.

Eight of the salts were analyzed using inductively coupled plasma mass spectrometry (ICP-MS) and inductively coupled plasma atomic emission spectroscopy (ICP-AES). Results are shown where available. Three samples were collected and analyzed for each salt. Figure 6.1 shows the concentrations of Cr and Fe determined by NAA.

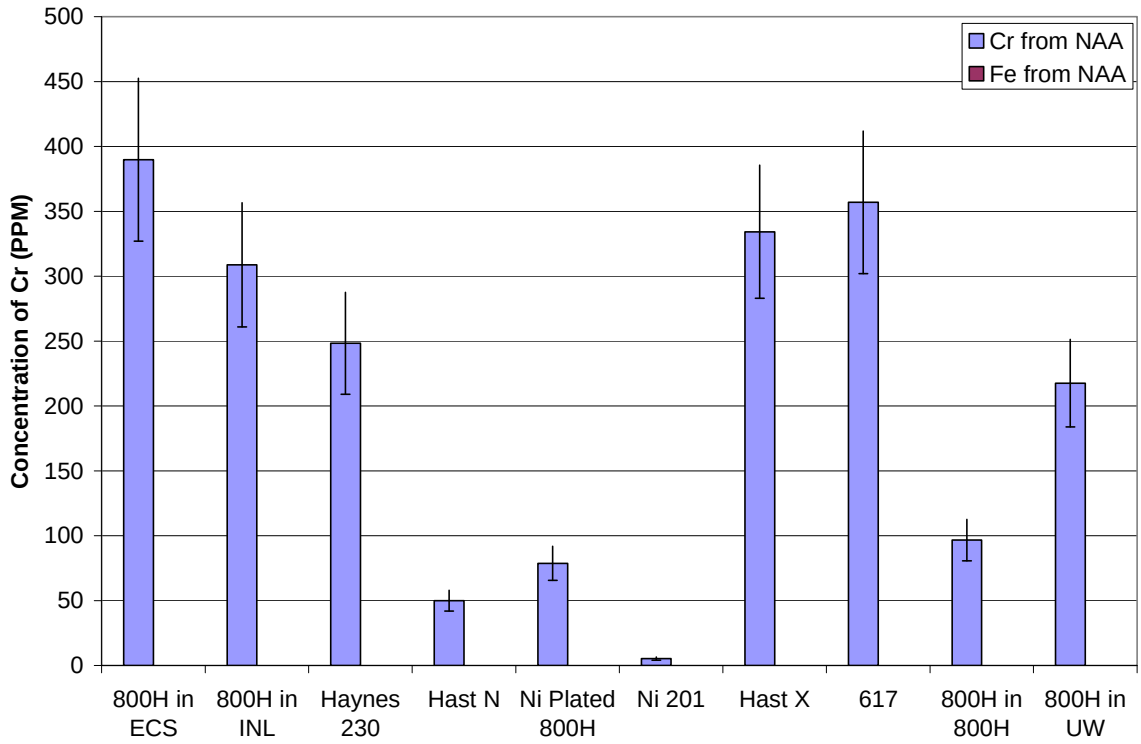

Figure 6.1 Cr and Fe concentration in each of the salts from the static corrosion tests.

NAA shows that 800H in ECS salt had the most elemental Cr and Fe losses, while Ni 201 had the least. Ni-plating of 800H had reduced the dissolved Cr and Fe concentration by a factor of 4. All tests except for the one of the 800H tests were performed in a graphite crucible. The test of 800H in an 800H crucible shows that the graphite container increased the corrosion rate.

Figure 6.2 shows concentration of all impurities for each alloy along with expected results from weight loss and ICP analysis.

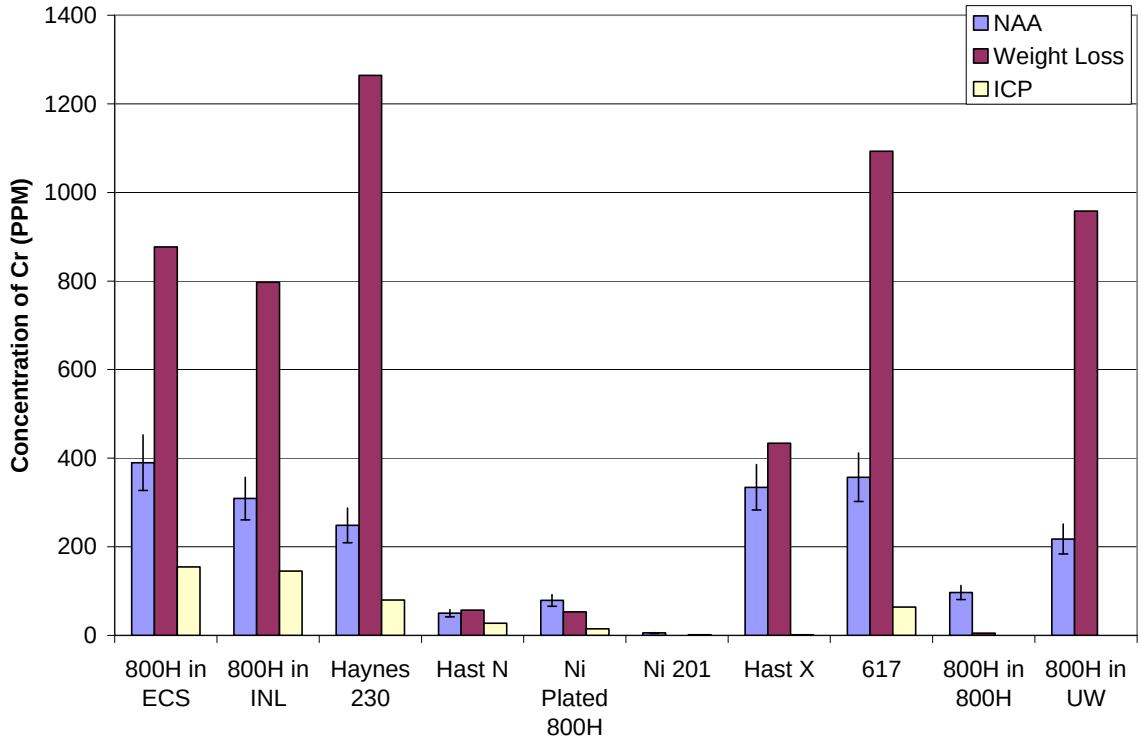

Figure 6.2 Comparison between NAA, weight loss, and ICP results.

The three data sets only agree on alloys with little or no weight loss. NAA shows concentrations of impurities much lower than expected from weight loss, but still higher than concentrations determined by ICP analysis.

6.2 NAA of Pure FLiNaK Salts

Concentrations of impurities in the pure FLiNaK salts were determined using NAA. Table 6.1 shows impurities found in each of the pure FLiNaK salts. Three samples were collected from each salt. Sample collection for the ECS and INL salts was via taking molten samples. However, the UW salt was prepared by crushing due to an insufficient supply from which molten samples could be removed.

Table 6.1 Concentrations of impurities in the pure FLiNaK from the three different sources.

ECS FLiNaK				
Cr				
Fe				
Ni				
INL FLiNaK				
Cr				
Fe				
Ni				
UW FLiNaK				

Cr				
Fe				
Ni				

The salt from ECS was found to have the smallest concentration of impurities, but due the difference in sample preparation methods (UW FLiNaK was crushed instead of melted), there may be an error in the concentrations detected in the UW FLiNaK.

6.3 NAA of $MgCl_2$-KCl Purification Methods

Four methods of purifying the $MgCl_2$-KCl salts were analyzed using NAA. The four methods included bubbling Ar through the melt, bubbling HCl through the melt, adding CCl_4, and adding Mg. A 24 hour static corrosion test was performed using a salt from each preparation by placing a 1.25" x 0.5" x 0.06" sample of 800H in each respective salt. NAA was performed on each salt before and after the static corrosion experiment. Several effects can be seen from the NAA data. First, figure 6.3 shows that the concentrations of Cr and Fe increase significantly after the static corrosion test due to corrosion of the 800H sample.

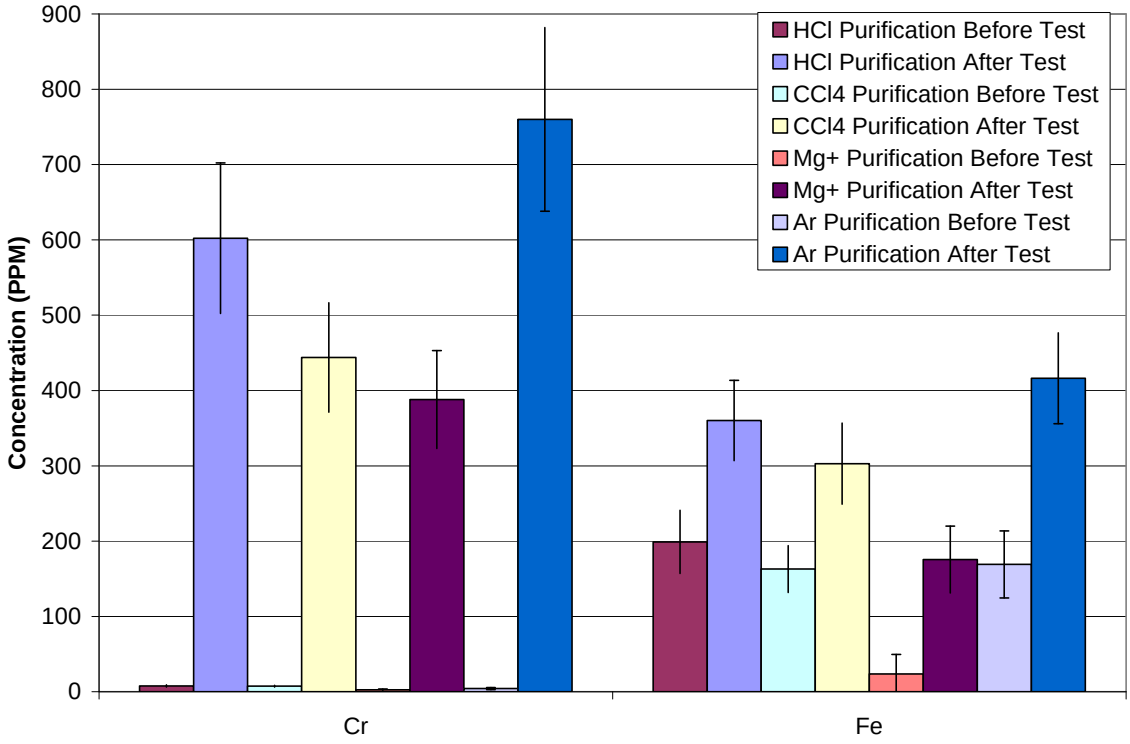

Figure 6.3 Concentrations of Cr and Fe before and after a 24 h static corrosion test of 800H at 850 C.

The concentration of Cr and Fe before the test was approximately 7 ppm and 175 ppm, respectively, for all salts except for the salt purified by the Mg addition where the concentrations of Cr and Fe were 3 ppm and 25 ppm. The best method of purification was determined by two parameters: smallest weight loss during static corrosion test and smallest change in elemental concentration of alloying elements as determined by NAA. The change in

concentration from NAA is shown in figure 6.4. Purifications using CCl_4 and Mg had the smallest weight loss and similar changes in concentrations of Fe and Cr in the salt. Mg addition was chosen to purify the remaining salts as the CCl_4 was more of a health hazard.

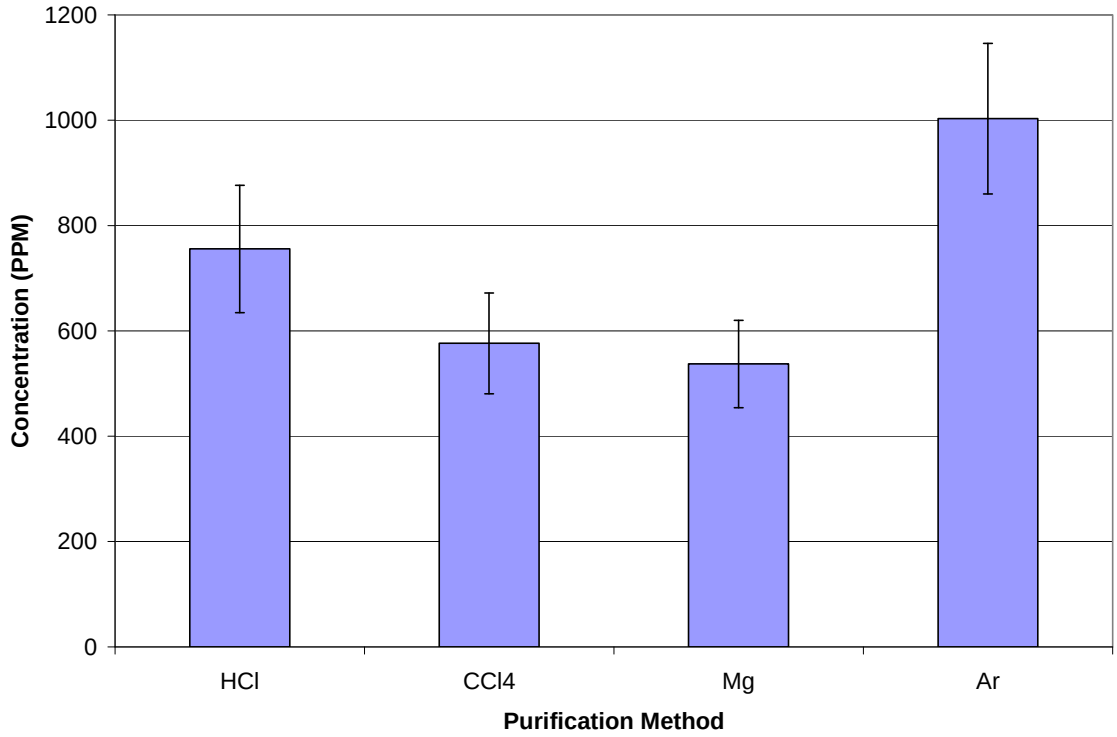

Figure 6.4 Total change in concentration of Cr and Fe between pre and post analysis of the static corrosion tests for each purification method.

Another observation from NAA was that the salts before the static corrosion test showed approximately 100 PPM of Br and 110 PPM of Na, as shown in figure 6.5. These impurities likely came with the Cl and K, respectively, due to their proximity on the periodic table. An increase in the concentration of Na was seen after the static corrosion test which is likely due to handling the samples and introducing salt from unclean hands. After the detection of increased Na concentration, special care was taken to wear gloves at all times when handling samples.

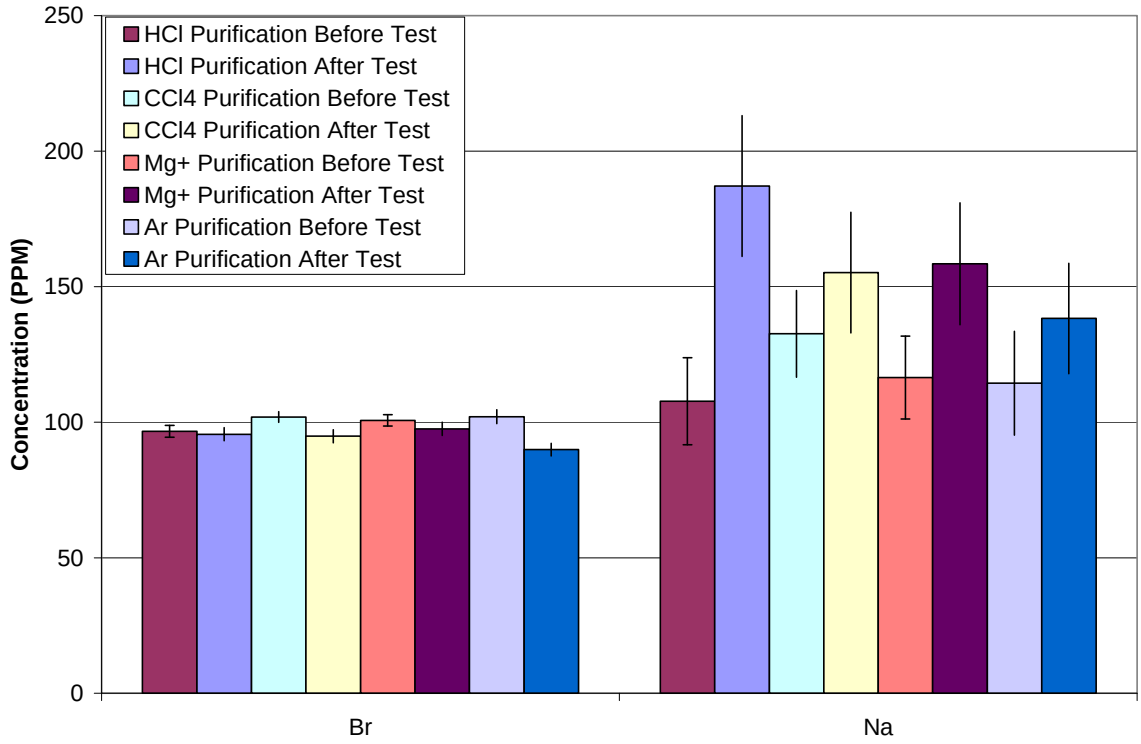

Figure 6.5 Br and Na impurities in the salt present before and after the static corrosion test. The increase in Na is likely due to salt on the exterior of the samples from handling the samples.

For all other tests with $MgCl_2$-KCl, the Mg addition purification method was used, and concentrations of Br of approximately 100 ppm and Na of approximately 150 ppm were expected as known impurities independent of the test being performed.

6.4 NAA of Pure Salt from 100h Static Corrosion Tests in $MgCl_2$-KCl

Static corrosion tests were performed in $MgCl_2$-KCl for 100h at 850 °C using the Mg addition method of purifying the salt. Tests were performed in alumina oxide containers which were cleaned with deionized water and HCl between uses. However, Cr was found by NAA in the static corrosion test of Ni-201 indicating cross contamination from the previous test. Weight loss data was also taken for each alloy. However, some of the samples showed weight gain from an oxide layer. The tests were performed in an Ar atmosphere so there should have been no O present to form an oxide layer. The oxide growth and cross contamination issued led to the determination that the tests ought to be repeated to eliminate cross contamination and the effects of oxide.

6.5 NAA of graphite

NAA was also performed on the grade of graphite that was used in all applications of the experiment including the container material for the static corrosion tests and the NAA sampler. The graphite was analyzed in the as received state before exposure to any heat or salt environment. The only statistically relevant impurity element found in the graphite was Cr. It had a concentration of less than 5 ppm.

6.6 Molten Salt Voltammetry of Cr in FLiNaK

Working curves for Cr concentration as a function of integrated current were obtained by adding CrF_2 and CrF_3. Working curves were obtained using a Pt-QRE as well as a 10 mol% Ni(II)/Ni RE at 650 °C.

The number of electrons transferred (n value) in each peak was identified by cyclic voltammetry (equation 5.1.4). To ensure that the Randles-Sevick equation applied and to check to see if the system was diffusion controlled, CV was performed at several scan rates to ensure that the peak current was linearly proportion to the square root of the scan rate. Figure 6.6 shows a compilation of cyclic voltammograms performed at scan rates of 100, 150, 200, and 300 mV/s. The maximum scan rate was chosen to be 300 mV/s due to data collection rate of the potentiostat limiting the detail of the voltammogram.

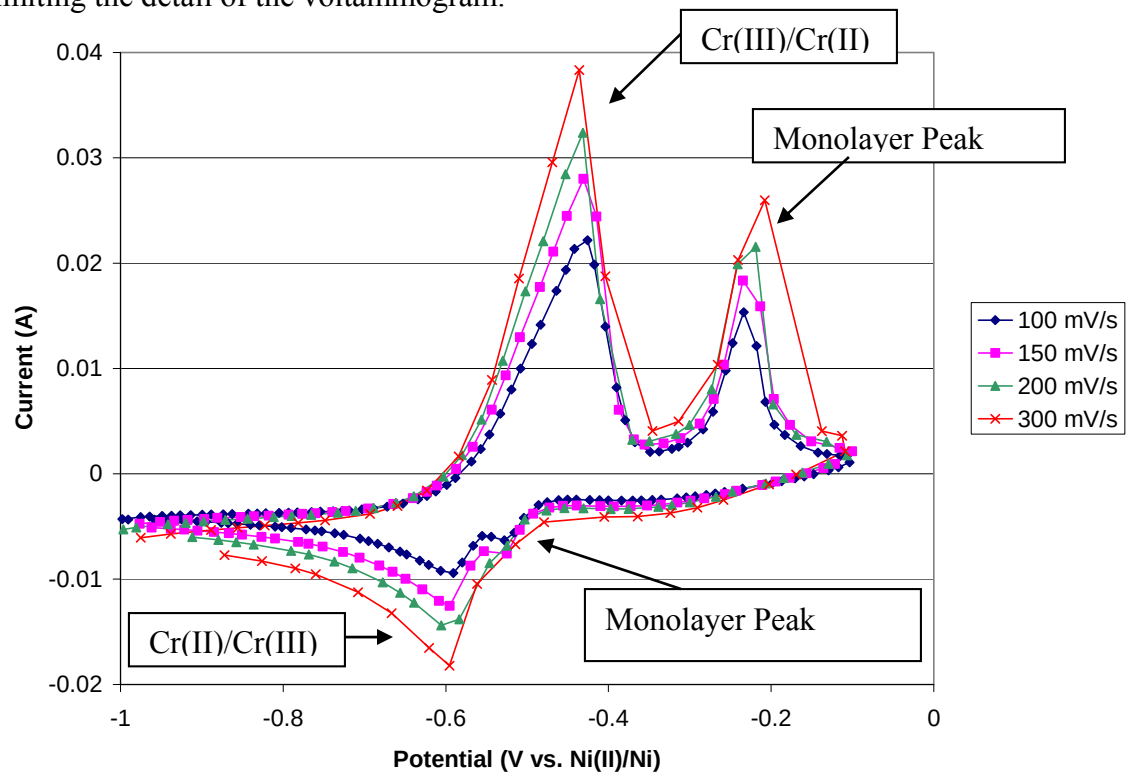

Figure 6.6 Cyclic voltammograms for increasing scan rates. At 300 mV/s, the potentiostat could not collect data fast enough to provide adequate detail for the smaller cathodic peak.

The more negative oxidation/reduction peaks (with a mid-peak potential of approximately -0.51 V) have been deemed a quasi-reversible reduction/oxidation. They do not fit the description of reversible because the anodic peak is larger than the cathodic peak ($i_{pa}/i_{pc} \neq 1$), and they do not fit the description of irreversible because the peak potential does not vary with scan rate and the anodic and cathodic peaks overlap. Previous research has found both Cr(II)/Cr(0) and Cr(III)/Cr(II) to be quasi-reversible reactions **[64]**. The number of electrons transferred in these peaks found by equation 5.1.4 is 1. However, equation 5.1.4 only applies to reversible reactions so the results may be errant as this seems to be a quasi-reversible system. Another way of calculating the number of electrons transferred in the peak is by assuming the system is quasi-reversible and assuming a transfer coefficient of 0.5. The number of electrons transferred calculated by equation 5.1.2 is 2. The disagreement between the two methods of calculating the number of electrons transferred is most likely since the oxidation/reduction couple being considered is quasi-reversible, and the

correlations used are for either reversible or irreversible systems. An n value of two corresponds to the Cr(II)/Cr(0) reduction. This was the most negative peak seen by ASV in a system only containing Cr ions so it should correspond to the Cr(II)/Cr(0), and the transfer coefficient calculation supports this conclusion.

However, previous research at 750 °C has found the reduction of Cr(II)/Cr(0) to occur at -1.13 V vs. Ni(II)/Ni RE **[15]**. The temperature difference of 100 °C (this work being performed at 650 °C) accounts for a shift of 0.2 V, but that still leaves a potential difference of 0.4 V between where Cr(II)/Cr(0) was detected in this research and in **[15]**. Future work should rectify the difference between these two mid-peak potentials.

The anodic and cathodic peaks occurring with a mid-peak potential of -0.35 V vs. Ni(II)/Ni RE do not overlap indicating that the reaction is irreversible. However, the peak potentials do not vary with scan rate, so this reaction may be either irreversible or quasi-reversible. Calculation of the number of electrons transferred by equation 5.1.4 is found to be 0.5 electrons transferred. Once again, equation 5.1.4 is meant to be used for a reversible reaction so the result may be errant. However, it the peaks centered at -0.35 are considered quasi-reversible, the number of electrons transferred can be calculated by equation 5.1.2 if a transfer coefficient of 0.5 is assumed. This results in a 1 electron transfer. An electron transfer of 0.5 does not correspond to any electrochemical reduction, and the oxidation/reduction occurring at -0.35 V is not reversible, so equation 5.1.4 should not be used in this circumstance. A peak of 1 electron transferred would correspond to Cr(III)/Cr(II) oxidation which is expected to be more positive than the Cr(II)/Cr(0) peak due to its less negative Gibb's free energy (see figure 4.1) and from previous research in molten fluoride salts **[13, 15]**.

Analysis of ASV data was performed on the Cr(II)/Cr(0) peak assuming a quasi-reversible behavior.

Figure 6.7 shows a plot of peak current as a function of scan rate for each reduction/oxidation. Since both show a linear relationship between peak current and the square root of scan rate, the Randles-Sevick equation applies, and both processes are diffusion controlled.

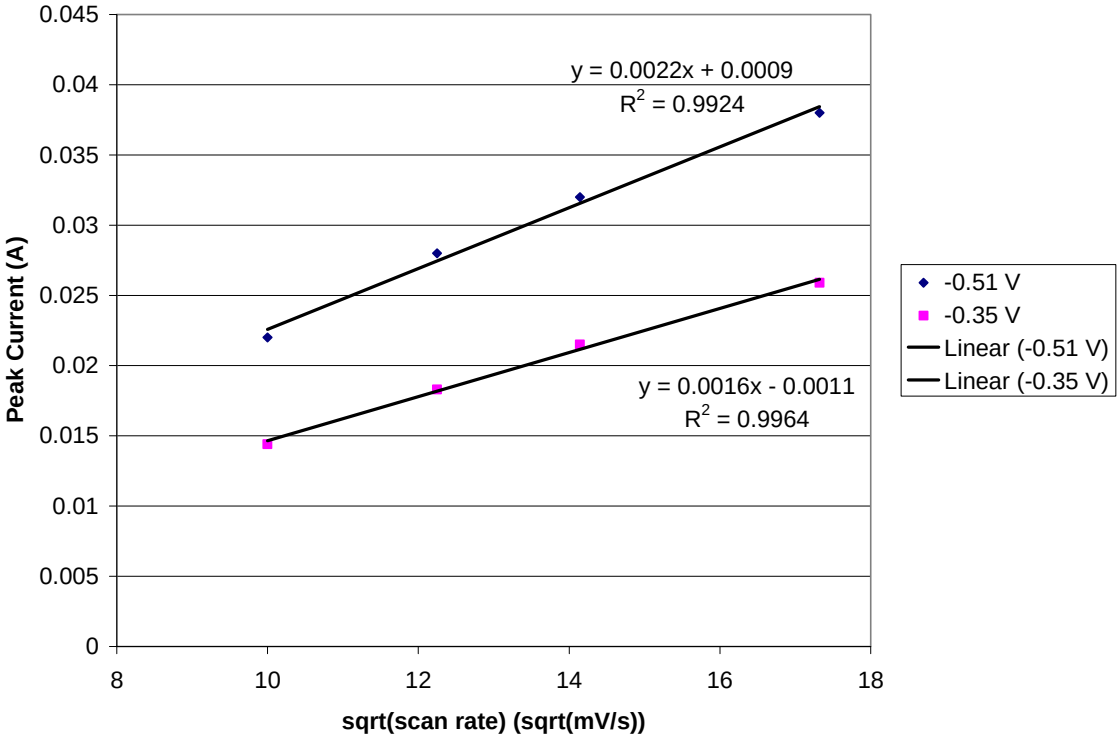

Figure 6.7 Peak current from CV as a function of scan rate for the two sets of oxidation peaks. The first set of peaks had a mid-peak potential of -0.51, and the second set of peaks had a mid-peak potential of -0.35 V. If the Randles-Sevick equation applies and the process is diffusion controlled, the scan rate should be linearly proportional to the peak current.

ASV was performed for development of working curves of integrated current as a function of Cr concentration. All correlations were made from the Cr(III)/Cr(II) as it was better understood and agreed with previous data. Figure 6.8 shows a plating step. Figure 6.9 shows a compilation of stripping steps with increasing Cr concentration in each. Figure 6.10 shows a cleaning step. All of these are representative of other tests performed.

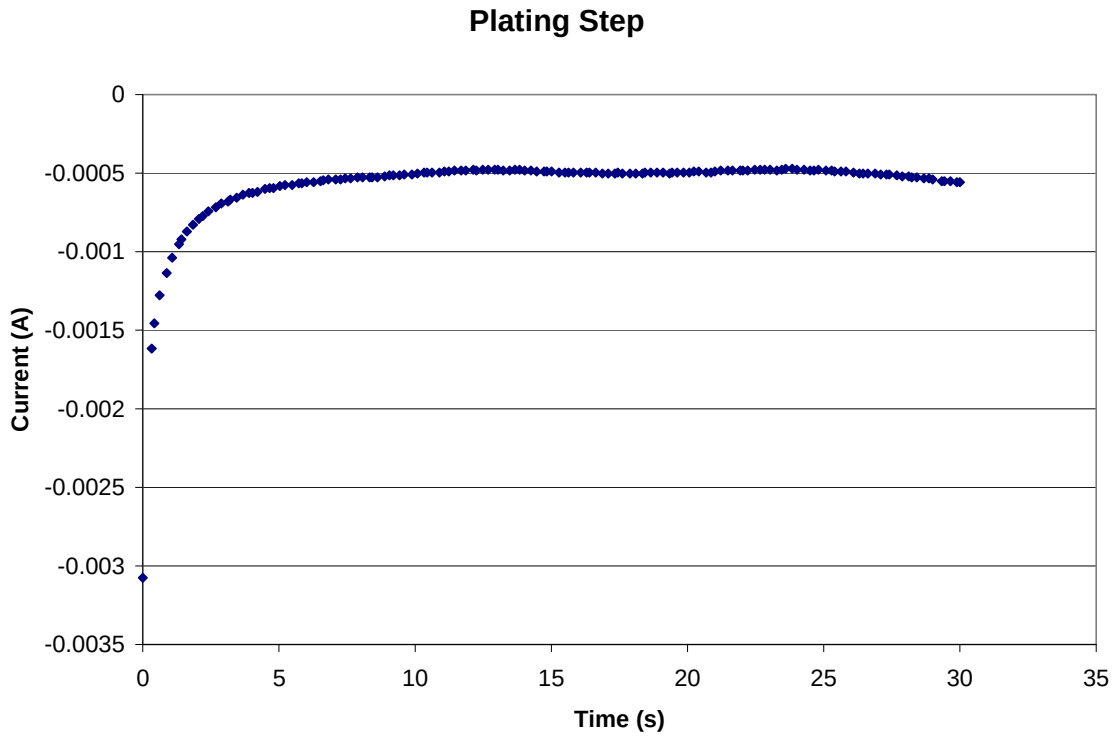

Figure 6.8 The current in the plating step is negative as metal ions are plating on the WE. The current becomes less negative with time as metal cations deplete in the solution.

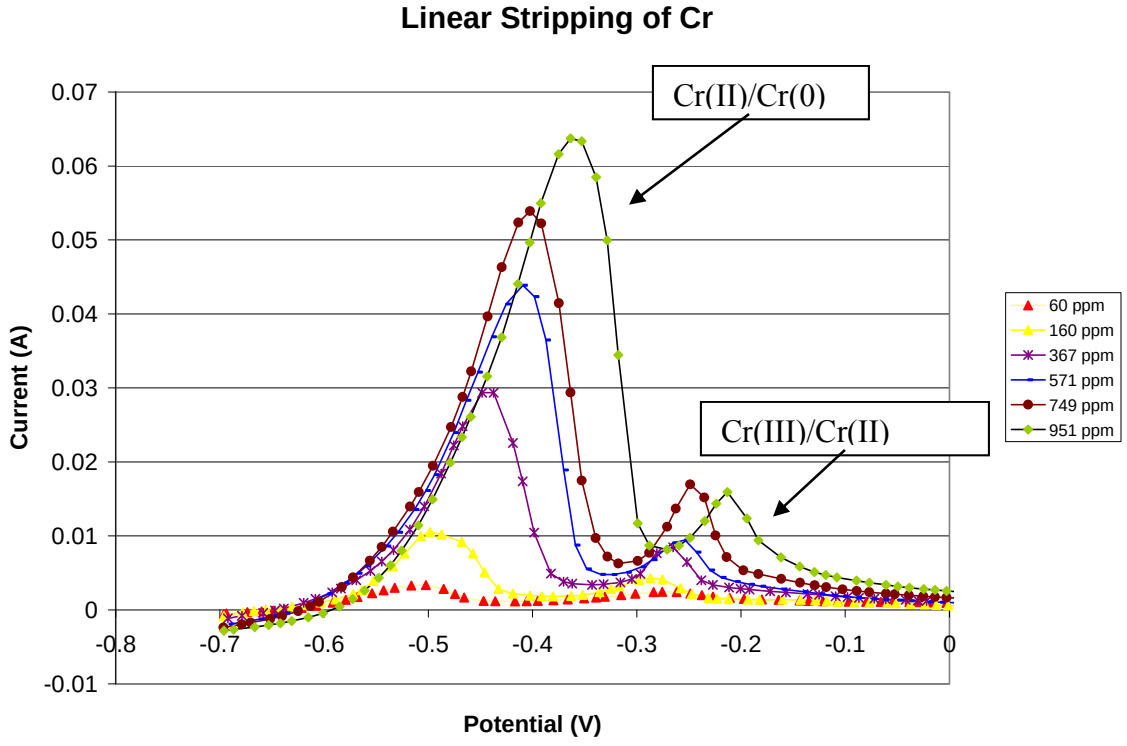

Figure 6.9 The oxidation of Cr from the WE into solution gives a current peak starting at -0.6 V vs. 10 mol% Ni(II)/Ni RE. As the concentration increases, the area under the peak and the peak voltage increase, but the reduction potential (the starting point of the peak) stays constant.

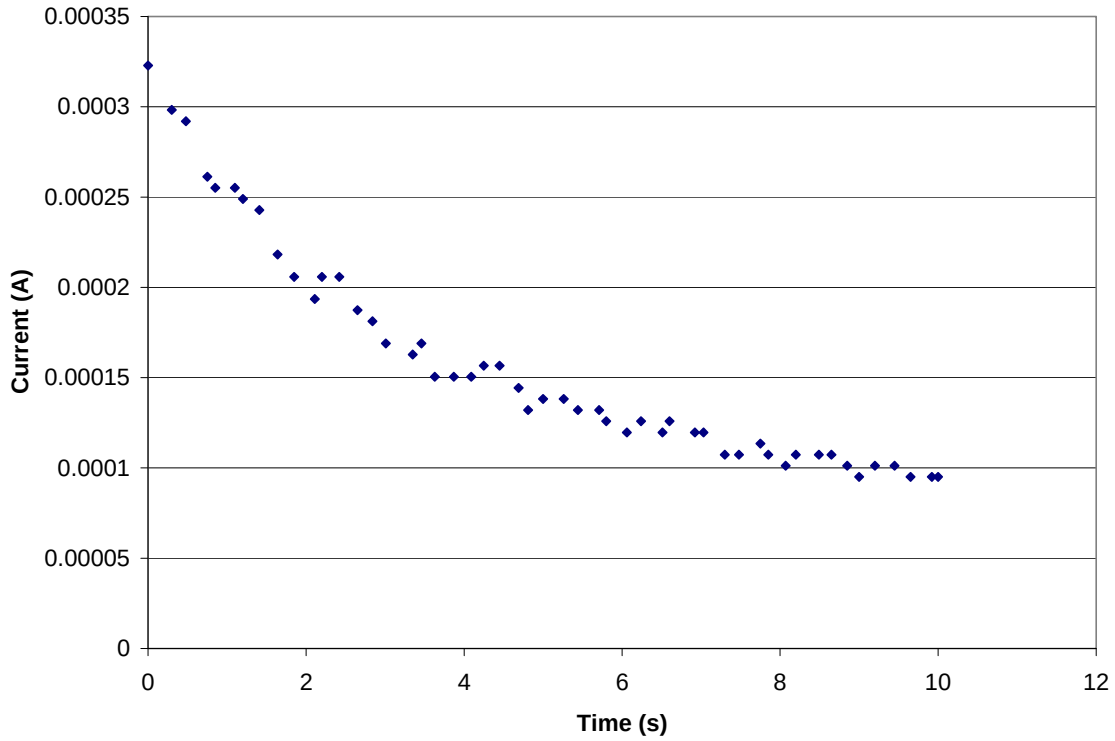

Figure 6.10 The cleaning step after each stripping step reduced the number of ions plated on the WE. Current decreases as there were fewer ions to oxidize into solution. The cleaning time was long enough to reduce the current to 0.001 A.

A working curve of integrated peak current as a function of Cr concentration was developed for high and low concentrations, as shown in figures 6.11 and 6.12. The uncertainties in the following working curves are due to counting statistics from the NAA for determining concentration. The uncertainty of the potentiostat measurements was determined by taking six ASV measurements at each concentration and calculating the spread in the six measurements. It was found that ASV could not accurately determine peaks if less than 30 ppm of Cr was present in the solution. Each working curve shows a linear correlation between current (i) and Cr concentration (C_{Cr}).

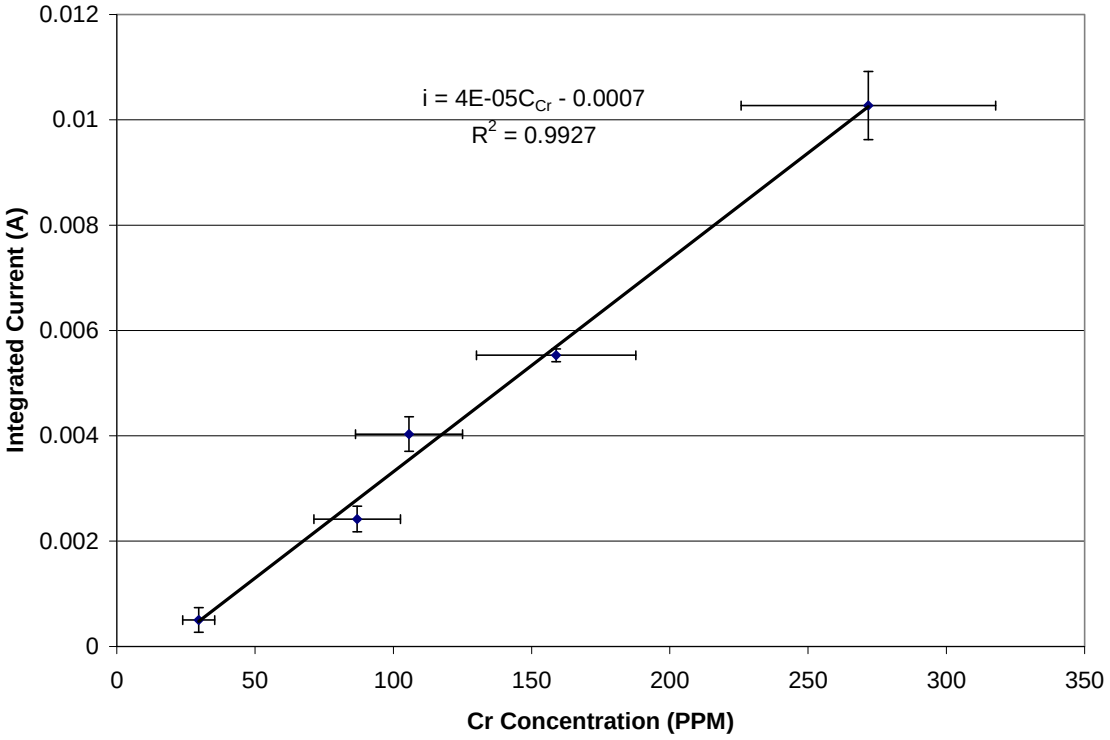

Figure 6.11 Integrated current as a function of Cr concentration below 300 ppm using Pt-QRE.

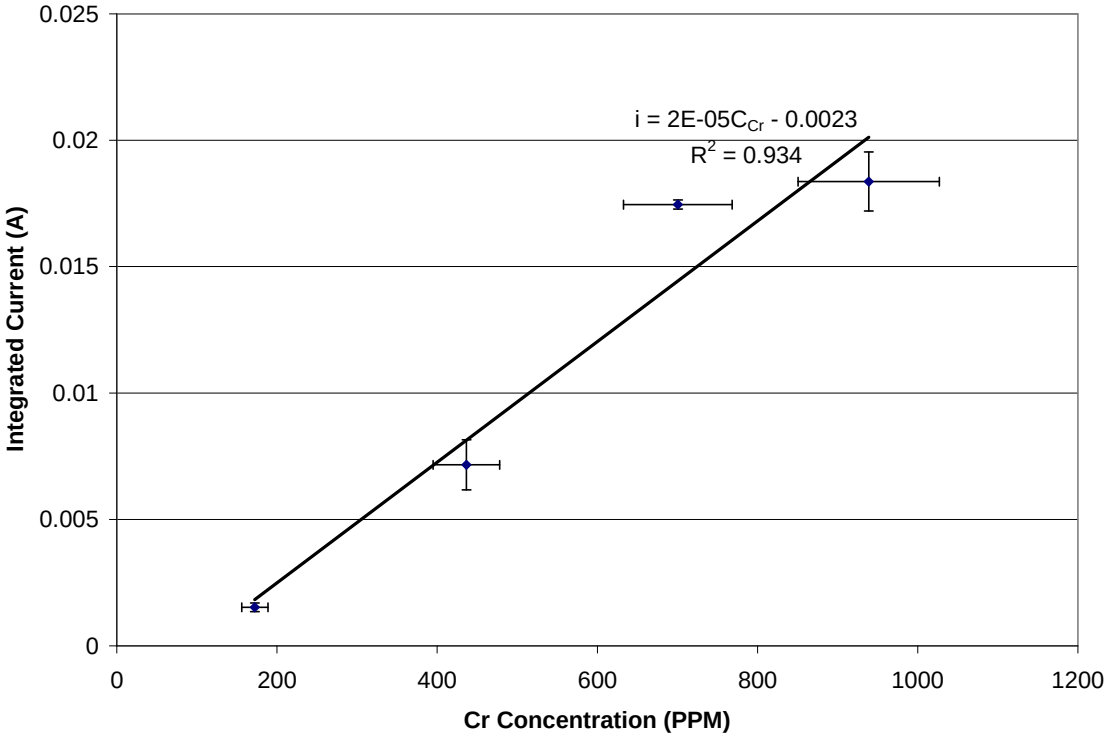

Figure 6.12 Integrated current as a function of Cr concentration below 1000 ppm using Pt-QRE.

Plating times were 30 s at lower concentrations to obtain significant signal to noise ratio and decreased to 15 s at higher concentrations. Since current output from the stripping step is directly proportional to plating time, working curves were made of integrated current divided by plating time so that values could be compared for high and low concentrations. The peak current is also directly proportional to the area of the WE so current densities between measurements with different WE areas can be compared by dividing by the area of the WE. Combining the results from the low and high concentration curves shows that the ASV technique developed in this study is applicable over the entire concentration range. Figure 6.13 shows integrated current density per plating time as a function of Cr concentration over the entire range of Cr concentrations.

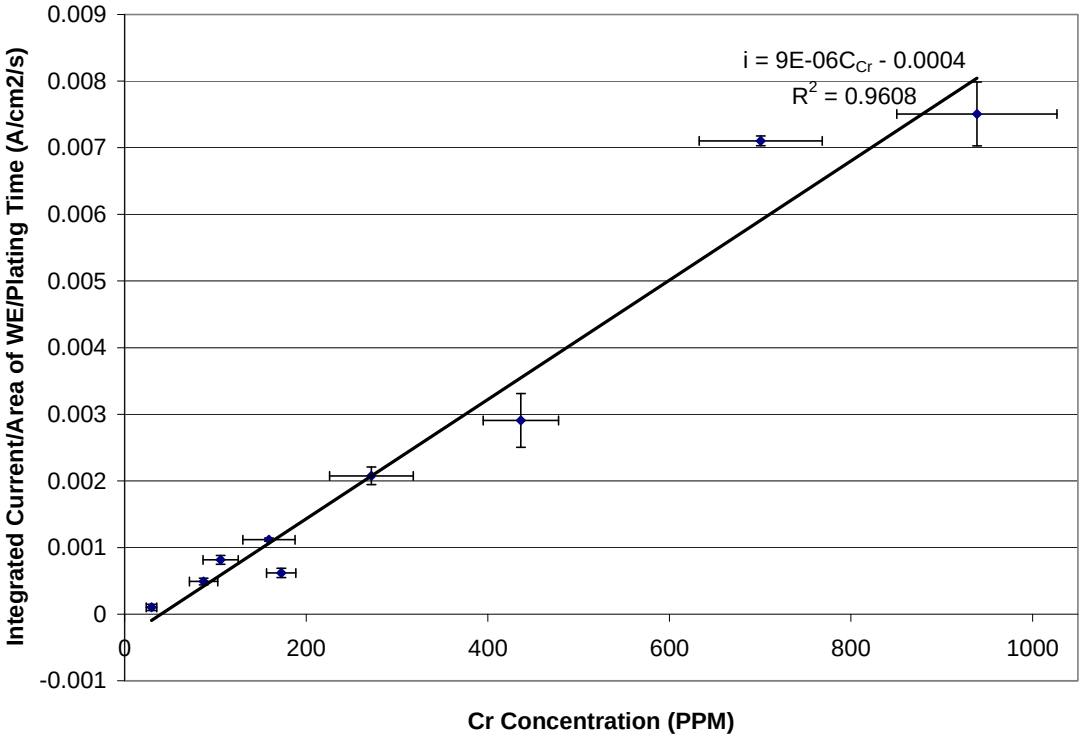

Figure 6.13 Combination of low and high concentrations of Cr working curves using Pt-QRE.

Similar measurements of integrated peak current as a function of Cr concentration were made using a Ni(II)/Ni RE for high and low concentrations. Plating times were increased to 120 s at low concentrations and 30 s at high concentrations in an attempt to decease detection limits, but 30 ppm was still found to be the lower limit of detection. Figures 6.14 and 6.15 show working curves of integrated current as a function of Cr concentration for low and high Cr concentrations, respectively. Figure 6.16 combines the two by dividing by area of the WE and plating time.

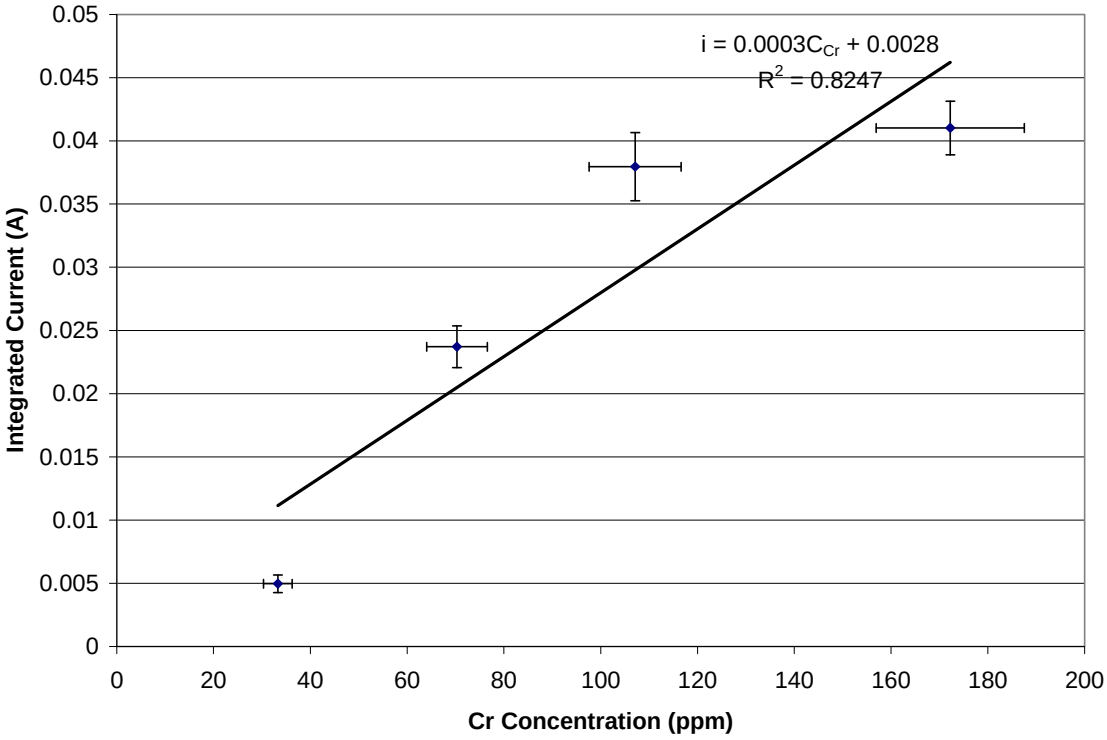

Figure 6.14 Integrated current as a function of Cr concentration below 300 ppm using Ni(II)/Ni RE.

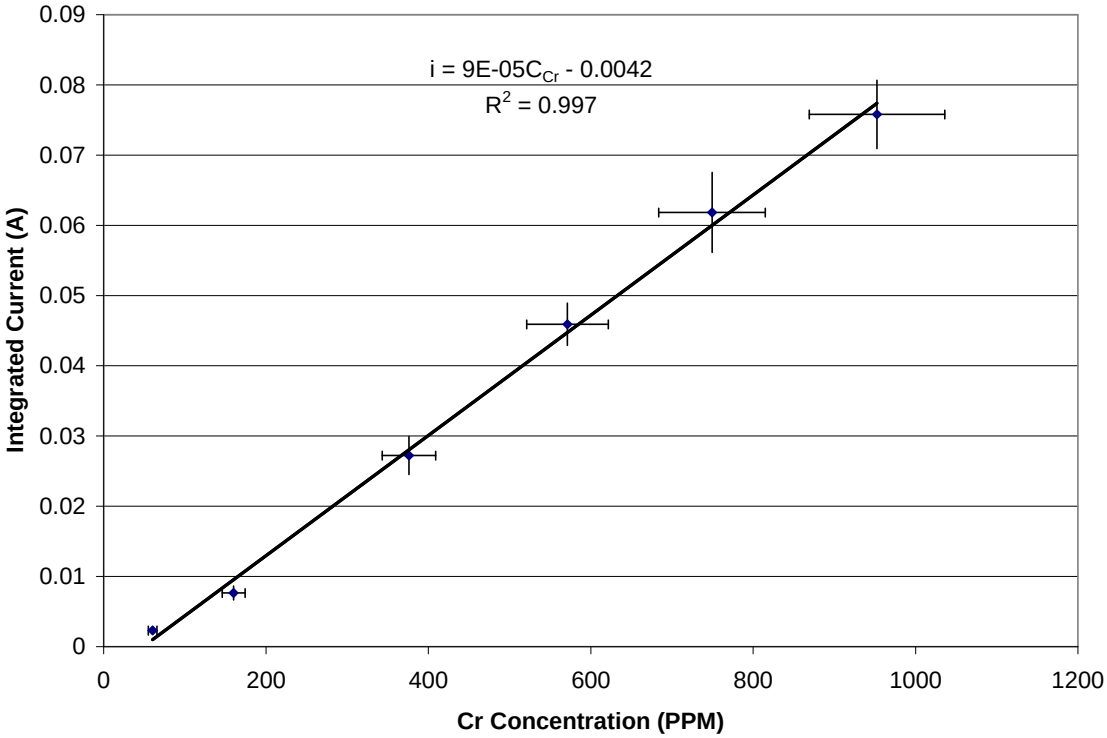

Figure 6.15 Integrated current as a function of Cr concentration below 1000 ppm Ni(II)/Ni RE.

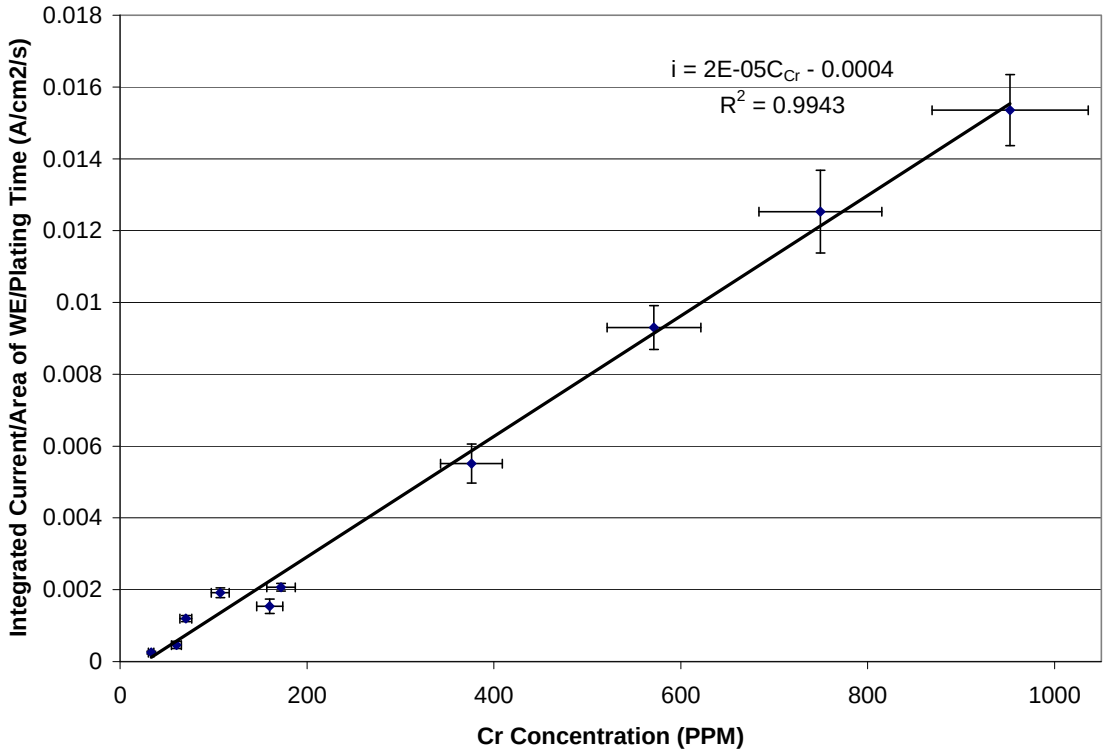

Figure 6.16 Combination of low and high concentrations of Cr working curves using Ni(II)/Ni RE.

An R^2 value of 0.9943 was found when using the Ni(II)/Ni RE, with a slope of 2E-5 $\frac{\frac{A}{cm^2 s}}{ppm\ Cr}$ and an offset of -0.0004 $\frac{\frac{A}{cm^2 s}}{ppm\ Cr}$, which corresponds to zero integrated current at 20 ppm. An R^2 value of 0.9577 was found when using the Pt-QRE, with a slope of 9E-6 $\frac{\frac{A}{cm^2 s}}{ppm\ Cr}$ and an offset of -0.0004 $\frac{\frac{A}{cm^2 s}}{ppm\ Cr}$, which corresponds to zero integrated current at 40 ppm. The difference in values and slopes is most likely due to the use of a Pt-QRE. All experiments used a plating potential of -0.7 V so that comparisons could be made between experiments. However, since there is no way to ensure that the Pt-QRE held a constant potential throughout, the plating potential may have drifted between measurements. In addition, there should be an offset of <30 ppm in the correct working curve since curves were not detected until 30 ppm was added to the solution. The Ni(II)/Ni RE proved to be a better RE than the Pt-QRE as it had a better correlation and had a offset closer to lower than 30 ppm.

6.7 Molten Salt Voltammetry of Fe in FLiNaK

Initial attempts have been made to obtain working curves of integrated current as a function of Fe concentration. However, some aspects of the experiment are still being analyzed. The work reported here is preliminary and many questions still need to be answered. The information below is the current status of ASV of Fe in FLiNaK.

Working curves for Fe concentrations of 80-595 ppm were obtained using the Ni(II)/Ni RE by adding FeF_2 and FeF_3 at 650 °C. At this point, the 1 mol% Ni(II)/Ni RE was employed due to large peak seen at 0 V when using the 10 mol% Ni(II)/Ni RE, as described in section 5.1.8. A plating potential of -0.1 V was held for 30 s for all measurements. The stripping step consisted of a scan rate of 100 mV/s with an initial potential of -1.0 V and a final potential of 0.5 V. The cleaning potential of 0.5V was held for ~10 s following each stripping step. The actual time was varied to allow the current to drop below 0.0001 A.

At lower concentrations two peaks were seen during anodic stripping corresponding to Fe(II)/Fe(0) and Fe(III)/Fe(II), but only one large peak was observed at higher concentrations. This led to the suspicion that the two peaks were overlapping. To generate the working curve, total integrated current was obtained by integrating over both peaks. At lower concentrations, when two peaks were present, current was integrated over both peaks and added together for a total current. At higher concentrations, when only one peak was seen, integrated current was taken over the entire peak. Figure 6.17 shows a compilation of ASV scans from concentrations of 100-600 ppm Fe. Unlike the comparable curve for Cr concentration, the Fe curves do not all have the same starting point which is caused by the variation of the 1 mol% Ni(II)/Ni RE.

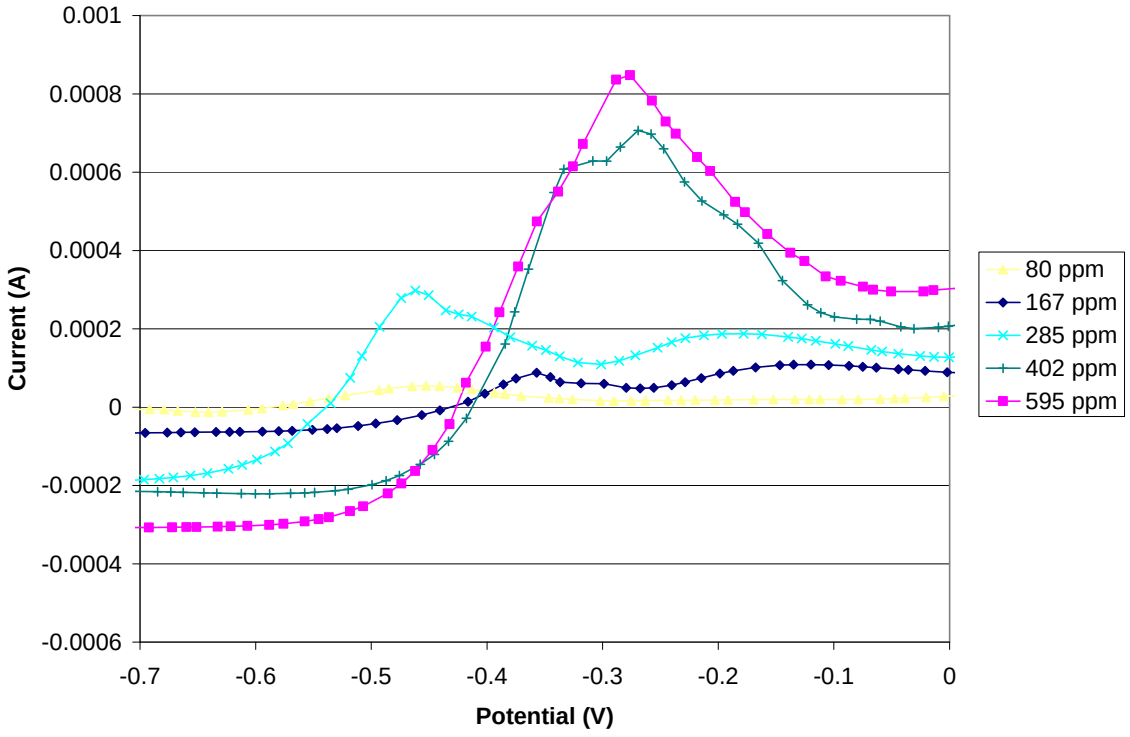

Figure 6.17 ASV of increasing concentrations of Fe in FLiNaK using a 1 mol% Ni(II)/Ni RE.

Figure 6.18 shows a working curve of integrated peak current per area per plating time as a function of Fe concentration. When integrating for the 167 and 285 ppm peaks, the integral was taken under both peaks and added together.

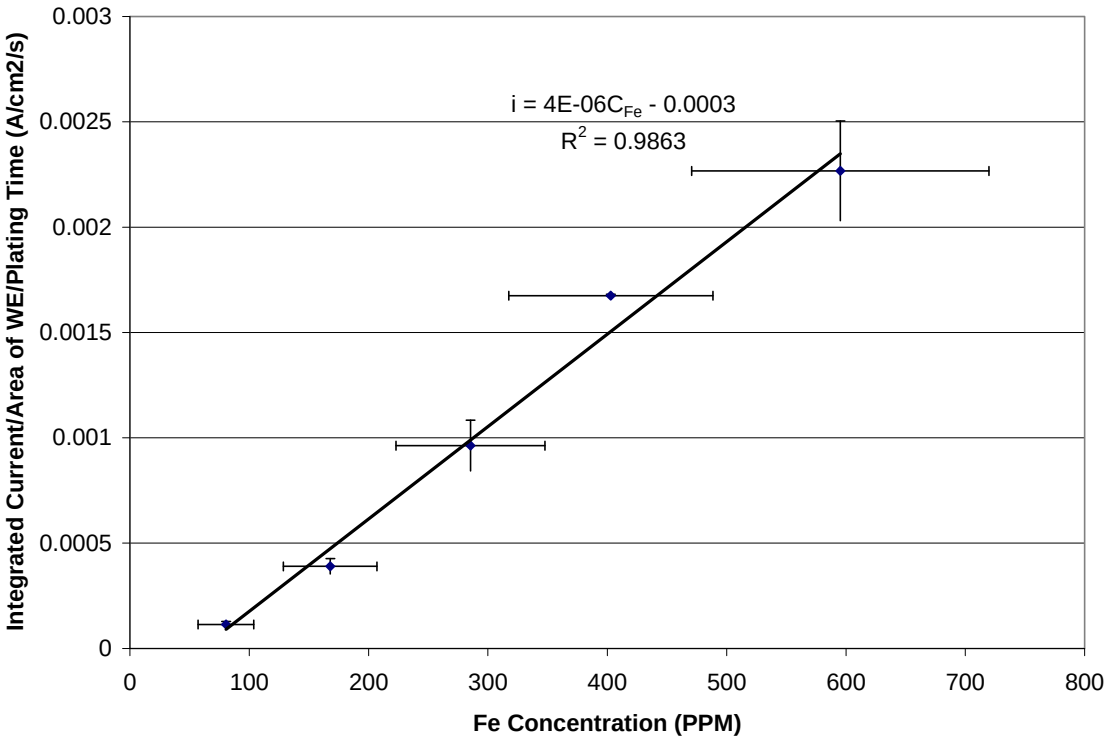

Figure 6.18 Working curve for Fe in FLiNaK.

Cyclic voltammetry was performed for Fe in FLiNaK once the highest concentration was reached. However, electron transfer for each reaction could not determined by this point as only one large peak was observed instead of the two peaks seen at lower concentrations. Figure 6.19 shows a cyclic voltammogram of 600 ppm of Fe in FLiNaK.

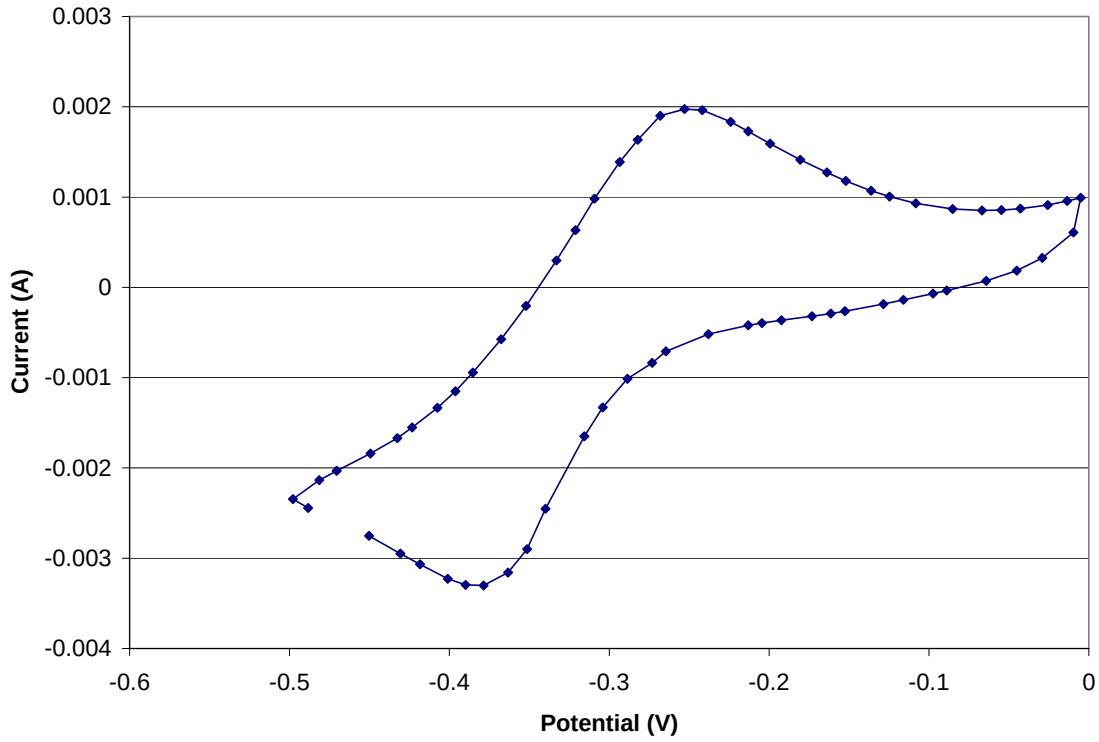

Figure 6.19 Cyclic voltammogram of Fe in FLiNaK using a 1 mol% Ni(II)/Ni RE.

From figure 6.19, it can be seen that the Fe reduction looks much more reversible as the peaks overlap and are approximately the same size. Further analysis should include CV performed at lower concentrations to determine number of electrons transferred in each peak.

Working curves were attempted by dipping a pure Fe wire into the melt. ASV measurements were taken over a 12 hour period with the Fe wire in the melt, but no distinctive peaks were observed during that time period. NAA performed at the end of the experiment revealed that 40 ppm of Fe was present in the solution. The offset of 0.0003 $\frac{\frac{A}{cm^2 s}}{\text{ppm Fe}}$ from the working curve corresponds to a concentration of 75 ppm, which is above the maximum concentration in the Fe wire test but still below the concentration at the first ASV measurement (80 ppm).

6.8 Comparison of adding Cr and Fe Working Curves

From comparing figures 6.14 and 6.15, it can be seen that the slope of the Fe working curve is five times smaller than that of the Cr working curve. The Randles-Sevick equation (equation 3.1) lists variables that can affect the peak height such as area of the WE, temperature of the cell, concentration of the analyte, scan rate of the stripping step, and diffusion coefficient of the analyte. Plating time will also affect the current peak size. Both curves are divided by area of the WE and plating time, so they should be comparable. The concentration ranges were comparable. The scan rate and temperature were constant throughout.

A literature survey of diffusion coefficients of Cr and Fe in FLiNaK and other molten fluoride salts over a temperature range of 500 – 900 °C showed that the diffusion coefficients for both had been calculated using either the Randles-Sevick equation or the Sand equation. The Sand

equation does not apply to this research. The calculated values for both varied between 3.6E-5 cm^2/s and 1.84E-6 cm^2/s **[27, 26, 57, 63, 64]**. Diffusion coefficients for Cr and Fe in FLiNaK from this experiment were calculated from cyclic voltammetry data and using the Randles-Sevick equation, but the calculated diffusion coefficients were much larger than previously reported. The diffusion coefficient for Cr and Fe were found to be 1.5E-3 cm^2/s and 1.9E-4 cm^2/s. The factor of ten in the diffusion coefficient would explain the differences in the working curves, but from the literature, the diffusion coefficients should be the same. It has been noted that diffusion coefficients have been calculated to be much larger than accepted values if an alternate current path existed in the cell **[27]**. Other research has suggested that a large stable anion CrF_6^{3-} could exist in FLiNaK causing smaller diffusion coefficients than generally accepted **[64]**. For future work with this electrochemical setup, it is suggested that the diffusion of Fe be investigated more thoroughly, and steps should be taken to eliminate any alternate current paths if they exist.

6.9 Comparison of adding Cr metal and Fe metal

Cr metal was added by dropping small chunk of pure Cr metal into the melt while Fe metal was added by inserting a 1mm pure Fe metal wire into the melt. When the Cr metal was added, a very large peak was seen at ~1.1 V. When the Fe metal was added, no peaks were observed. NAA showed a concentration of 40 ppm at the end of the Fe metal experiment. NAA was not performed on the salt used for the Cr metal test as it was initially thought that no valuable information could be gained and eventually due to lack of time.

When the salt containing the Cr metal was removed from the glassy carbon crucible, it was coated in glassy carbon (see figure 5.1.25) and caused the glassy carbon crucible to crack. When the salt containing the 40 ppm of Fe from the Fe wire was removed, there was no sign that the glassy carbon crucible had been wetted. The salt looked similar to when the FeF_2 and FeF_3 had been added. This is evidence for the hypothesis that the more reducing Cr would wet the glassy carbon more than the Fe. However, the Cr was added in a chunk that rested on the bottom of the glassy carbon crucible while the Fe wire never contacted the glassy carbon crucible itself. This could be a reason for the difference in the wetting, but the Cr metal was only a small chunk (~0.5 cm diameter) sitting at the bottom of the glassy carbon crucible, and all sides of the salt were covered with glassy carbon, not just the bottom. This could be tested by adding a small chunk of Fe metal to see if it wets the glassy carbon crucible. However, if the Fe does wet the glassy carbon crucible, the glassy carbon crucible will most likely crack and no longer be able to be used for voltammetric measurements.

6.10 Effects of Variations on Electrochemical Cell Parameters

The coiled CE shown in figures 5.1.24 and 5.1.25 was initially used to ensure that the CE had significantly more surface area than the WE without the potential of touching the bottom of the glassy carbon crucible. However, salt often froze within the coil which necessitated regular cleaning to remove the possibility of cross contamination between tests. An improved version of the CE was a Pt wire submerged 1 cm deeper than the WE.

Both fired and bisque-fired alumina were used for the cylindrical support pieces in the tests; fully fired alumina bisque was more durable while bisque-fired alumina became embrittled with time. However, the bisque-fired alumina could be machined and modified to more easily accommodate changes to experimental hardware.

Bubbling was attempted using a 1/16” Ni tube. Since the plating step is diffusion controlled, it was thought that bubbling Ar gas the melt might increase the diffusion of ionic species to the WE. However, bubbling had no effect as repeatable results were obtained independent of whether the melt was being bubbled. Effects of bubbling are shown in figure 6.20.

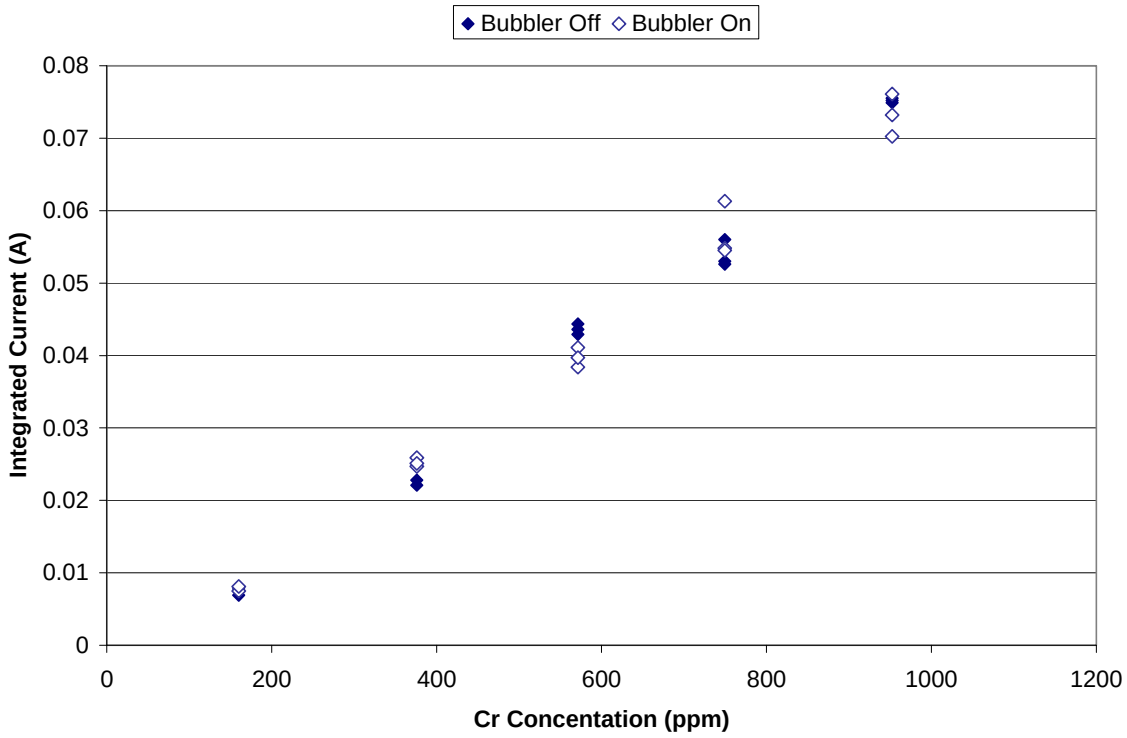

Figure 6.20 Six measurements were taken at each concentration: three with a bubbler on, three with a bubbler off. Bubbling the FLiNaK during ASV did not consistently change current observed during the stripping step.

ASV was performed in glassy carbon, graphite, and Ni 200 crucibles under an Ar atmosphere. Once frozen, the salt slid out of the glassy carbon and graphite containers easily where as the salt would not fall out of the Ni crucible. The salt eventually came out when the crucible was repeatedly tapped with a wrench. ASV measurements were repeatable between all three crucibles.

7. Summary

7.1 Anodic Stripping Voltammetry in Molten FLiNaK Salt

An *in situ* corrosion probe for molten FLiNaK (46.5 mol% LiF-11.5 mol% NaF-42 mol% KF) salt at 650 °C has been developed using anodic stripping voltammetry (ASV). The probe was calibrated for Cr, which was added in the forms of CrF_2 and CrF_3, and Fe, which was added in the forms of FeF_2 and FeF_3. The calibration curves were of integrated peak current per area of the working electrode per plating time as a function of Cr or Fe concentration. The Cr(II)/Cr(0) reduction was integrated for all correlations. Neutron activation analysis (NAA) was used to calibrate the currents detected during ASV to concentrations of metals in the salt. Cyclic voltammetry was performed to determine number of electrons transferred in each peak and to estimate diffusion coefficients using the Randles-Sevick equation. A two electron transfer occurring with a mid-peak potential at -0.51 V vs. 10 mol% Ni(II)/Ni RE was determined to be the Cr(II)/Cr(0) peak. A one electron transfer occurring with a mid-peak potential of -0.35 V vs. 10 mol% Ni(II)/Ni RE was determined to be the Cr(III)/Cr(II) reduction.

A Pt quasi-reference electrode (QRE) and a Ni(II)/Ni reference electrode (RE) contained in a graphite crucible were used. The Ni(II)/Ni RE gave more repeatable results. However, the Ni(II)/Ni RE had a lifetime of ~300 h at which point the graphite container began to leak Ni, as evidenced by a current peak present near 0 V vs. Ni(II)/Ni RE. A 10 mol% Ni(II)/Ni RE was more stable than a 1 mol% Ni(II)/Ni RE. The working electrode, counter electrode, and QRE were made out of Pt. Glassy carbon, graphite, and Ni 200 were used as containers for the molten salt during electrochemistry. The only difference is that the frozen salt fell out of the glassy carbon and graphite crucibles, while it had to be pounded out of the Ni 200 crucible. All tests were performed in a glovebox under an Ar atmosphere. Bubbling Ar gas through the melt did not affect voltammetric measurements.

7.2 Neutron Activation Analysis

Neutron activation analysis (NAA) proved useful for determining elemental concentration from FLiNaK (46.5 mol% LiF-11.5 mol% NaF-42 mol% KF) and $MgCl_2$-KCl (32 mol% $MgCl_2$-68 mol% KCl) salt when homogeneous samples were collected. Homogeneous samples were collected from the $MgCl_2$-KCl salt by crushing to a fine powder in a glass mortar and pestle. Homogeneous samples of FLiNaK salt were collected by removing a small portion of molten FLiNaK in a graphite sampler and allowing it to freeze.

The standard NBS 1632a was adequate for use as a standard for the comparator method of determining sample composition. Standard masses were chosen to match the height of the sample. This led to a range of standard masses of 100-120 mg. Irradiations for NAA were performed for 2 hours in whale tube E8 or C8 at the University of Wisconsin-Madison Nuclear Reactor. An optimal decay time before counting for detecting Cr and Fe was found to be 2 weeks. Counting was performed on contact of the detector.

NAA of 500 h static corrosion tests of selected alloys in FLiNaK performed at UW showed significant concentrations of Cr, which was predicted by scanning electron microscope and energy-dispersive x-ray spectroscopy. Concentrations determined by NAA correlated with those determined by inductively coupled mass spectrometry and inductively coupled auger electron spectrometry measurements, although NAA concentrations were larger by a factor of 2-5. This factor could be attributed to dilution factors used and incomplete dissolving of FLiNaK during measurements using inductively coupled mass spectrometry and inductively coupled auger electron spectrometry.

NAA of $MgCl_2$-KCl purification methods correlated with weight loss data and helped determine which method of purification gave the smallest dissolution of alloys. NAA of 100 h static corrosion tests of selected alloys in $MgCl_2$-KCl confirmed a cross contamination issue and gave unique data as weight loss measurements were affected by formation of oxide layers on the alloys being tested.

8. References

1. Williams, D. F., Toth, L. M., and Clarno, K. "T. Assessment of Candidate Molten Salt Coolants for the Advanced High-Temperature Reactor." *ORNL TM-2006 12*. (2006).
2. Kingsley, et al. "Fused salts in Inconel and Hastelloy B." *ORNL-2106*. (1954): 66
3. Croft, et al. "Dynamic corrosion by fluorides: Corrosion by fluorides in seesaw tests." *ORNL-1294*. (1954): 107-116.
4. http://www.haynesintl.com/pdf/h2052.pdf, accessed 5/5/08
5. MacPherson, H.G. "The molten salt reactor advernture." *Nuclear science and engineering.* 90 (1985): 374-380.
6. Laurenty, B. et al. "Inhibiting corrosion in molten fluoride salts: investigation on FLINAK." *2005 annual meeting and fall showcase 05 AICHE.* Cincinnati, OH. (2005) 7878-7882.
7. Keiser, J.R., DeVan, J. H., and Manning, D.L. "The corrosion resistance of type 316 stainless steel in Li_2BeF_4." *ORNL/TM-5782*. (1977)
8. Williams, D.F. "Additional physical property measurements and assessment of salt compositions proposed for the intermediate heat transfer loop." *ORNL/GEN4/LTR-06-033*
9. Masuko, N., Osaka, T., and Ito, Y. *Electrochemical Technology: Innovation and New Developments.* Kodansha and Gordon and Breach, Tokyo and Amsterdam (1996).
10. Boussier, H. "Pyrometallurgical processing research program (PYROREP) final report." (2003).
11. Tulackova, R et al. "Development of pyrochemical reprocessing of the spent nuclear fuel and prospects of close fuel cycle." *Atom Indonesia*. 1 (2007): 47-59
12. Bailey, R., and Yoko, T. "High-temperature electroplating of chromium from molten FLiNaK." *Journal of Applied Electrochemistry*. 16 (1986): 737-744.
13. Jenkins, H., Mamantov, G., and Manning, D. "Electrode potentials of several redox couples in molten fluorides." *Journal of Electrochemical Society.* 117 (1970): 183-185. (ALSO ORNL-4812)
14. Jenkins, H. W., Mamantov, G., and Manning, D. L. "EMF measurements on the nickel-nickel(II) couple in molten fluorides." *Journal of Electroanalytical Chemistry.* 19 (1968) 385-389.
15. Mellors, G. and Senderoff, S. "Electrode reactions in the electrolysis of fused salts." Applications of fundamental thermodynamics to metallurgical systems. Proceedings of the first conference on the thermodynamic properties of materials held a the University of Pittsburgh. Gordon and Breach Science Publishers. New York. (1969) 81-103.
16. Bailey, R., and Yoko, T. "Electroplating of Chromium in Molten FLINAK." Proceedings of the first international symposium on molten salt chemistry and technology: April 20-22, 1983, Kyoto, Japan. (1983): 115-118.
17. Senderoff, S. and Mellors, G.W. "Electrodeposition of coherent deposits of refractory metals: I: Niobium." *Journal of Electrochemical Society.* 112 (1965): 266-272.
18. Senderoff, S. and Mellors, G.W. "Electrodeposition of coherent deposits of refractory metals: II. The electrode reactions in the deposition of tantalum." *Journal of Electrochemical Society.* 112 (1965): 840-845.
19. Senderoff, S. and Mellors, G.W. "Electrodeposition of coherent deposits of refractory metals: III: Zirconium." *Journal of Electrochemical Society.* 113 (1966): 60-66.

20. Senderoff, S. and Mellors, G.W. “Electrodeposition of coherent deposits of refractory metals: V. Mechanism of deposition of molybdenum from chloride melts.” *Journal of Electrochemical Society.* 114 (1967): 556-560.
21. Manning, D.L., Malone, E.R., and Buhl, R.V. “Electroanalytical studies in molten NaBF4-NaF.” *ORNL-5047.* 1975.
22. Iizuka, M., Inoue, T., Shirai, O., Iwai, T, and Arai, Y. “Application of normal pulse voltammetry to on-line monitoring of actinide concentrations in molten electrolyte salt.” *Journal of Nuclear Materials.* 297 (2001): 43-51.
23. Mamantov, G. and Manning, D. L. “Electoranalytical studies of bismuth in molten LiF-BeF2-ZrF4.” *ORNL-5074* 1975:56-57.
24. Manning, D. “Voltammetry of iron in molten lithium fluoride-potassium fluoride-sodium fluoride.” *Journal of the Electrochemical Society.* 6 (1963): 227-233.
25. Xingdong, W. and Shuzhen, D. “High temperature reference electrodes used in molten fluorides.” *Rare Metals.* 12 (1993).170-174.
26. Manning, D. “Voltammetry of nickel in molten FLiNaK.” *Journal of Electroanalytical Chemistry.* 7 (1964): 302-306.
27. Manning, D. and Mamantov, G. “Rapid scan voltammetry and chronopotentiometric studies of iron in molten fluorides.” *Journal of Electroanalytical Chemistry.* 7 (1964): 102-108.
28. Jenkins, H. W., Manning, D. L., Mamantov, G., and Young, J. P. “EMF, voltammetric and spectrophotometric measurements on the U(IV)/U(III) couple in molten LiF-BeF2-ZF4.” *ORNL-4396. (*1969): 201-202.
29. Manning, D.L. and Borstein, H.R. “Reference electrode studies in molten fluorides.” *ORNL-4548.* 1970:184-185.
30. Polyakova, L.P., Polyakov, E.G., and Bjerrum, N.J. “The study of electrode processes in LIiF-NaF-KF-K2TaF7-KBF4 melt.” *Plasmas and Ions.* 2 (1999): 117-125.
31. Apple, R. F. et al. “In-line analysis of molten MSBR fuel.” *ORNL-5047*. 1975: 52-55.
32. Grimes, W.R. “Chemical research and development for molten salt breeder reactors.” *ORNL-TM-1853*. 1967: 9-11, 107-113.
33. Alabyshev, A.F., Lantratov, M.F., and Morachevskii, A.G. *Reference electrodes for fused salts, The Sigma Press, Publishers, Washington D.C., (1965).*
34. Kontoyannis, C. “Pyrolytic boron nitride coated graphite as a container of reference electrodes for molten fluorides.” *Electrochimica Acta.* 40 (1995): 2547-2551.
35. Wang, J. *Stripping analysis: Principles, instrumentation, and applications.* VCH Publishers, Derrfield Beach, FL, (1985).
36. Scholz, F. *Electroanalytical methods: Guide to experiments and applications.* Springer-Verlag, Berlin, Heidelberg, (2002).
37. Robin, A. and Lepinay, J. “Electrochemical study of the anodic dissolution of iron and nickel in the molten LiF-NaF-KF eutectic at 600 C using convolution voltammetry.” *Electrochemica Acta.* 37 (1992): 2433-2436.
38. Meyer, A.S. “Analytical developments for the molten-salt reactor program.” *ORNL-4930.* (1973).
39. Guar, H. C. and Behl, W.K. “Electrode potentials in fused magnesium chloride-sodium chloride-potassium chloride eutectic.” *Electrochemica Acta*. 8 (1963):107-104.
40. Guar, H. C. and Jindal, H. L. “Standard electrode potentials in molten chlorides-II.” *Electrochemica Acta*. 15 (1970):1113-1126.

41. Guar, H. C. and Jindal, H. L. “Polarography in molten magnesium chloride-potassium chloride as solvent.” *Electroanalytical chemistry and interfacial electrochemistry*. 23 (1969): 298-303.
42. Guar, H. C. and Jindal, H. L. “Standard electrode potentials in molten chlorides.” *Electrochemica Acta*. 13 (1968):835-842.
43. Guar, H. C. and Behl, W.K. “Polarograhic studies in molten magnesium chloride-sodium chloride-potassium chloride eutectic.” *Journal of Electroanalytical Chemistry*. 5 (1963): 261-269.
44. Guar, H. C. and Jindal, H. L. “On the use of Pt Foil as reference electrode in molten salts.” *Current Science*. 2 (1968) 49-50.
45. Bayes, C. F., and Hitch, B. F. “An EMF study of LiF-BeF_2.” *ORNL-5257*. 1968
46. Bayes, C.F. “Thermodynamics of molten LiF-BeF2 solutions.” *ORNL-3913*. 1965 (21-24).
47. MacPherson, H.G. “Molten salt reactor program quarterly progress report.” *ORNL-2626.* 1959 (vi-viii).
48. Uchida, I., Niki, K., and Laitinen, H. A. “Some redox reactions on semiconducting tin oxide electrodes in molten LiCl-KCl eutectic at 450 C.” *Journal of the electrochemical society.* 11 (1978): 1759-1764.
49. 45)empty
50. Jindal, H.L. and Guar, H. C. “Voltammetric study of palladium chloride in molten ternary eutectic, magnesium chloride-sodium chloride-potassium chloride.” *Indian Journal of Chemistry.* 5 (1967): 624-626.
51. Hill, G.J., and Johnson, K.E. “Impedance phenomena in molten salts.” *Journal of the Electrochemical Society*. 11 (1961): 1013-1018
52. Broadhead, K.G., et al. “Fast-neutron activation analysis in molten salt electrometallurgical research.” *Modern trends in activation analysis*. (1965) 39-43.
53. Peng, Y.-K.M. et al. “Spherical Tokamak (ST) transmutation of nuclear wastes.” *16th IEEE/NPSS Symposium Fusion Engineering.* 1995.
54. Ingersoll, D. T., et. al. “Status of preconceptual design of the advanced high temperature reactor (AHTR). *ORNL/TM-2004/104* (2004): 52-54.
55. Olson, L., et al. “Materials Corrosion in Molten LiF-NaF-KF Salt.” *Journal of Fluorine Chemistry*. Article in press (2008).
56. Cauchi, M. “Data analysis tools for safe drinking water production.” PhD Thesis (2006).
57. Chryssoulakis, J, Bouteillon, J., and Poignet, J.C. “Electrochemical behavior of pure iron in the aluminum refining electrolyte.” *Journal of applied electrochemistry*. 8 (1978) 103-108.
58. Wang, J. *Analytical electrochemistry*. Wiley-VCH, New York. (2000).
59. Yong, J.P., et al. “Effect of reductants on metal-fluoride-salt wetting behavior.” *ORNL 4396*. (1969) 205-206.
60. http://www.canberra.com/literature/935.asp, accessed 5/16/08
61. Curre, L. “Limits for qualitative detection and quantitative determination.” *Analytical chemistry*. 40 (1968): 586-593.
62. Knoll, G. *Radiation detection and measurement*. John Wiley and Sons, New York (2000).
63. Haarber, G.M., Kvalheim, E., and Rolseth, S. “Electrochemical behavior of dissolved iron species in molten salts.” *Electrochemical Society Proceedings Volume 2004-24*. 24 (2004): 990-998.
64. Yoko, T. and Bailey, R. “Electrochemical studies of chromium in molten FLINAK.” *Journal of the Electrochemical Society.* 131 (1984): 2590-2595.

Task 2: Molten Chloride Heat Transfer in Nuclear Systems

A forced convection loop was designed and constructed to examine the thermal-hydraulic performance of molten KCl-$MgCl_2$ (68-32 at %) salt for use in nuclear co-generation facilities. As part of this research, methods for prediction of the thermo-physical properties of salt mixtures for selection of the coolant salt were studied. In addition, corrosion studies of 10 different alloys were exposed to the KCl-$MgCl_2$ to determine a suitable construction material for the loop.

Using experimental data found in literature for unary and binary salt systems, models were found, or developed to extrapolate the available experimental data to unstudied salt systems. These property models were then used to investigate the thermo-physical properties of the $LiNO_3$-$NaNO_3$-KNO_3-$Ca(NO_3)_2$ system used in solar energy applications. Using these models, the density, viscosity, adiabatic compressibility, thermal conductivity, heat capacity, and melting temperatures of higher order systems can be approximated. These models may be applied to other molten salt systems.

Coupons of 10 different alloys were exposed to the chloride salt for 100 hours at 850°C was undertaken to help determine with which alloy to construct the loop. Of the alloys exposed, Haynes 230 had the least amount of weight loss per area. Nickel and Hastelloy N performed best based on maximum depth of attack. Inconel 625 and 718 had a nearly uniform depletion of Cr from the surface of the sample. All other alloys tested had depletion of Cr along the grain boundaries. The Nb in Inconel 625 and 718 changed the way the Cr is depleted in these alloys. Grain-boundary engineering (GBE) of Incoloy 800H improved the corrosion resistance (weight loss and maximum depth of attack) by nearly 50% as compared to the as-received Incoloy 800H sample.

A high temperature pump, thermal flow meter, and pressure differential device was designed, constructed, and tested for use in the loop. The heat transfer of the molten chloride salt was found to follow general correlations used to estimate the Nusselt number for water in both the forced convection laminar regime and in the mixed convection regime.

A principal goal of Generation IV nuclear power plants is to utilize the high temperature process heat generated in a reactor for the operation of chemical processing plants. The first such plant designed to showcase this capability is the Next Generation Nuclear Power Plant (NGNP), a Very High Temperature Reactor (VHTR). The NGNP-VHTR will use a portion of the heat from the nuclear reactor to produce hydrogen from water using either a sulfur-iodide (SI) cycle, or high temperature electrolysis (HTE). The efficiency of both the SI and HTE processes increase with an increase in temperature. This results in a need to run the chemical processes at temperature in excess of $800^{O}C$. Other chemical industries with varying optimal high temperature requirements such as water desalination plants and oil shale extraction plants are also being considered. At these high temperatures, the materials available for structural components and heat transfer fluids are limited. For example, three alloys are being considered for the structural materials in the intermediate heat exchanger: Inconel 617, Haynes 230, and Incoloy 800H due to their high temperature creep rupture strength and oxidation resistance at these temperatures. For heat transfer fluids, there are three main choices are high pressure He, liquid fluoride salt, and liquid chloride salt. Of the two classes of molten salts, one eutectic mixture from each anion type, FLiNaK (LiF-NaF-KF 46.5-11.5-42 at %) and KCl-$MgCl_2$ (68-32 at %), have been identified in previous studies as possible candidates for use in the NGNP/IHX Loop intermediate loop.

The present work seeks to explore the use of these molten salts in consideration of their applications in intermediate heat exchanger (IHX) design and other heat transfer components. Heat transfer mechanisms of these molten salts will be studied over the forced and mixed convection regions for heat transfer. A forced convective loop has been constructed to measure heat transfer coefficients, friction factors and corrosion rates in different diameter tubes in a vertical up flow configuration in the laminar flow regime. Equipment and instrumentation for the forced convective loop has been designed, constructed, and tested. These include a high temperature centrifugal pump, mass flow meter, and di_erential pressure sensing capabilities to an uncertainty of < 2 Pa. The heat transfer coefficient for the KCl-MgCl2 salt has been measured in two different diameter channels (0.083‘ and 0.370” D). In the 0.083” D channel, the experimental heat transfer coefficient has been found to agree with values obtained from heat transfer correlations used for water. In the 0.370” D channel, the experimental heat transfer coe_cient data was found to be predicted by either a correlation for mixed convection, or forced convection depending on the value of Gr^{*}/Re.

In the design of the loop, it was necessary to select a material to contain the KCl-$MgCl_2$ salt. The corrosion of 10 di_erent alloys was studied by static corrosion tests with the alloys exposed to the KCl-$MgCl_2$ salt for 100 hours at 850_C to help in selection of an alloy. Initial tests were conducted to determine a method for purification of KCl-$MgCl_2$. Four methods were evaluated by corrosion testing Incoloy 800H for 24 hours at $850^{O}C$ in this salt. Reduction of the salt by Mg contact produced the best results for purification of the KCl-$MgCl_2$ salt. Using this purification technique, the 10 alloys were screened for their corrosion performance in KCl-$MgCl_2$. Of the alloys exposed, Haynes 230 had the least amount of weight loss per unit area. The metals were corroded by removal of the Cr from the alloy. Nickel and Hastelloy N had the least amount of attack based on maximum depth of attack. This is due to the minimal amount of Cr in Nickel 201 and Hastelloy N. Of the higher Cr containing alloys, Inconel 625 and 718 were corroded by a nearly uniform depletion of Cr from the surface of the sample. All other alloys tested were attacked by Cr depletion along the grain boundaries. The uniform depletion of Inconel 625 and 718 resulted in a

smaller depth of attack from the alloy. The change in the mode of Cr depletion is believed to have changed due to the Nb content in these two alloys. In addition, grain-boundary engineering (GBE) of Incoloy 800H improved the corrosion resistance (as measured by weight loss and maximum depth of attack) by nearly 50% as compared to the as-received Incoloy 800H sample.

Since most of the complexity involved with use of molten salts in large scale applications is due to their high melting temperatures, methods for predicting a range of properties for molten salt systems was also studied. Limited experimental data on the thermal physical properties of salt mixtures is found in literature for systems with more than two components. Using the experimental data available for unary and binary salt systems, parameters for models found in literature were fit to predict melting temperature, heat capacity, density, and viscosity. Adiabatic compressibility and thermal conductivity models were developed to predict the thermal conductivity of these salt mixtures. These property models were then used to investigate the thermo-physical properties of the $LiNO_3$-$NaNO_3$-KNO_3-$Ca(NO_3)_2$ system used in solar energy applications. Using this approach, the density, viscosity, adiabatic compressibility, thermal conductivity, heat capacity, and phase diagrams for higher order systems can be approximated. These values were then applied to a solar parabolic trough system to show how the models can be utilized to select a salt for use in a solar plant. This approach can then be extended to other molten salt systems.

Nomenclature

	Constants	
F	Faraday's constant	9.6485×10^{4} J V^{-1}
g	gravitational constant	9.81 m s^{-2}
h	Planck's constant	6.626×10^{-34} J s
k_B	Boltzmann's constant	1.381×10^{-23} J K^{-1}
N_A	Avogadro's constant	6.022×10^{23} mol^{-1}
R	universal gas constant	8.314 J mol^{-1} K^{-1}
π		3.1416
	Symbols	
a_i	activity of i	
A	area	m^2
A_0	viscosity pre-exponential	kg m^{-1} s^{-1}
at %	atomic percent	
c	speed of sound	m s^{-1}
C_P	constant pressure heat capacity	J kg^{-1} K^{-1}
C_V	constant volume heat capacity	
D	tube diameter	m
e^-	electron	
E	energy	J
E	potential	V
E^O	standard potential	V
E_A	activation energy	J mol^{-1}
F	frequency	s^{-1}
F	friction coefficient	
F	view factor	
G	Gibbs Energy	J mol^{-1}
G	mass flux	kg m^{-2} s^{-1}
G	modulus of rigidity	Pa
G^*	Total activation energy	J mol^{-1}
G^*_{ij}	activation energy for ij pair	J mol^{-1}
G^{Exc}	excess Gibbs energy	J mol^{-1}
G^{Idl}	ideal Gibbs energy	J mol^{-1}
Gr	Grashof number	
Gz	Graetz number	
h	convection coefficient	W m^{-2} K^{-1}
H	enthalpy	J mol^{-1}
I	current	amps
k	thermal conductivity	W m^{-1} K^{-1}
K	form loss coefficient	
L	length	m
LMTD	log mean temperature difference	^oC or K
m	mass of standard unit	kg SU^{-1}
$\dot{m}$	mass flow rate	kg s^{-1}
M_i	molecular weight of i	g mol^{-1}
n	number of electrons	
n	moles of components	mol
N_i	number of moles of i	mol

n_{ij}	number of moles of ij pairs	mol
Nu	Nusselt number	
P	pressure	Pa
P	power	W
Pr	Prandtl number	
q	energy	W
q"	heat flux	W m^{-2}
Q	volumetric flow rate	m^3 sec^{-1}
r	radius	m
Ra	Rayleigh number	
Re	Reynolds number	
S	entropy	J mol^{-1} K^{-1}
t	time	s
T	temperature	^oC or K
$\overline{T}$	average temperature	^oC or K
T_M	melting temperature	K
T_0	reference temperature	^oC or K
U	internal energy	J mol^{-1}
V	velocity	m s^{-1}
V	volts	V
V_i	molar volume of i	m^3 mol^{-1}
V_M	molar volume	m^3 mol^{-1}
W	pumping power	W
X_i	mole fraction of i	
X_{ij}	site fraction of ij pairs	
Y_i	coordination equivalent site fraction of i	
z	axial distance from entrance	
z	height	m
Z_i	coordination number of component i	

Greek symbols

α	thermal expansion coefficient	K^{-1}
α	constant	
β	fitted constant	
χ	fitted constant	
ΔE_η	energy of vaporization	J mol^{-1}
ΔG_{AB}	Gibbs energy of cation exchange	J mol^{-1} K^{-1}
ΔG_F	Gibbs energy of fusion	J mol^{-1}
ΔG_F	Gibbs energy of formation	J mol^{-1}
ΔG^M	Gibbs energy difference between two phases	J mol^{-1} K^{-1}
ΔH_F	enthalpy of fusion	J mol^{-1}
ΔP	pressure drop	Pa
ΔS^{config}	configurational entropy	J mol^{-1} K^{-1}
ΔS_F	entropy of fusion	J mol^{-1} K^{-1}
ε	emissivity	
γ	coefficient	
Γ	torsional stress	Pa
κ_S	adiabatic compressibility	
κ_T	isothermal compressibility	
Λ	Wilson coefficient	

μ	dynamic viscosity	kg m^{-1} s^{-1}
μ	chemical potential	
η	volume of standard unit	m^3 SU^{-1}
η	kinematic viscosity	m^2 s^{-1}
ω	angular frequency	s^{-1}
Θ	electrical resistance	ohms
\upsilon	fitted constant	
ρ \rho	density	kg m^{-3}
σ	uncertainty	

Subscripts

\infty	value at free stream
a	constant
A	component A
C	cold
CAN	pressure can
CMN	common
Con	contraction
Exp	expansion
Exp	experimental
f	fluid
FC	forced convection value
H	hot
i	inside
i	inlet
M	value at melting
ms	molten salt
NC	natural convection
o	outlet
o	outside
R	radiation
Ref	reference value
s	surface
s	solid
sf	simulant fluid
SU	standard unit
The	theoritical value
TS	test section
W	wall

Superscripts

Exc	excess property
Idl	ideal value
l	liquid
O	standard state value
P	pressure dependent
s	surface

Calculus and Algebra

$\int$	integral
∂X_A	derivative with respect to X_A
Σ	summed over all values

Introduction

Generation IV type nuclear reactors are being researched and designed to reduce the risk of proliferation and increase the efficiency of the nuclear fuel cycle. Several different reactor designs are being examined: Supercritical Water (SCWR), Molten Salt (MSR), Advanced Gas (AGR), Very High Temperature (VHTR), and Sodium Cooled (SCR) reactors. In addition to the previous design goals, it is desired to be able to use the heat from Generation IV type reactors for purposes other than electricity production. One of the main interests is using nuclear heat in chemical processes that currently require fossil fuels for heat production.

Of particular interest in the United States is a variant of the VHTR called the Next Generation Nuclear Plant (NGNP). The NGNP is a commercial demonstration plant that will couple a 500 MWt helium cooled reactor to a chemical plant to utilize nuclear energy to create process heat. The process heat can be used in chemical processes that require large amounts of energy at elevated temperatures; e.g. hydrogen production, oil extraction, water desalination, and steam generation. The heat that is transported to the chemical plant is in addition to the reactor power that will be utilized to produce electrical energy. Initial plans for the NGNP are to couple a chemical plant and nuclear plant together to utilize 50 MWt of the reactor 500 MWt for production of process heat for the chemical plant [10]. That is the heat generated from the nuclear fission will be transported to a chemical plant where hydrogen can be produced, water desalinated, shale oil heated, etc. Instead of producing the heat using natural gas or other petroleum distillates. This is also beneficial in that the hydrogen is produced from water and not from steam-reforming of natural gas.

Two different methods are currently being examined for the production of hydrogen: high temperature electrolysis (HTE) and a thermo chemical cycle utilizing sulfur and iodide (S-I). Since the efficiency and size of both components scale with temperature, it is economically favorable to operate the hydrogen production process at the highest possible temperature. Initial review and calculations call for the operating temperature at the hydrogen production facility to be at least 850°C. The resulting problem is finding a way to couple the thermal energy between the nuclear and chemical plants so that the total process is efficient to maximize profitability. This coupling is made more difficult by licensing restrictions of the nuclear reactor. The licensing requirements for the nuclear facility will make it necessary to separate the chemical and nuclear plants. This separation distance between the chemical and nuclear facilities is likely to require a minimum separation distance of 90 m [11]. It is necessary to find a heat transfer fluid that will allow the movement of the thermal energy at the high temperature of the process.

In selecting a heat transfer fluid, it is necessary to have a fluid that is stable at the maximum possible outlet temperature of the reactor, 850°C and be stable in radiation fields. At this temperature and with radiation, coolants that contain molecular bonds break down due to the energy imparted to the atoms. The conditions of the reactor thus restricts the heat transfer fluid to simple fluids, such as noble gases, alkali and alkaline-earth halide salts, carbonate salts, and liquid metals. Most industrial liquid metals: sodium and NaK, have a high vapor pressure at these elevated temperature and are not considered for application in the NGNP. Of the noble gases, helium is the best heat transfer fluid possessing the best thermal conductivity and specific heat of all gases except hydrogen. Of the halide salts, fluoride salts and chloride salts are both stable and

have low vapor pressures over the proposed operating temperature range for the NGNP (700-900°C).

Liquid salts are excellent candidates as a heat transfer fluid for the NGNP application because of their thermo-physical properties. Liquid halide salts generally possess high boiling points, low vapor pressure, large specific heat and thermal conductivity, chemical stability at high temperatures and in radiation fields, and high density at low pressures [9]. These characteristics make liquid salts excellent candidates for heat transfer media to transfer thermal energy from the nuclear to chemical facility. The high volumetric heat capacity, ρC_P, of the salts allow for large amounts of energy to be stored in small amounts of volume. This reduces the volume of heat transfer equipment. In addition, the low vapor pressures (<5 Pa @ 900°C) of molten salts reduces the stress requirements in the piping, also allowing for smaller piping. The fact that the liquid salts are liquid at operating temperature greatly reduces the pressure drop of the heat transfer fluid in the piping between the nuclear and chemical islands.

This reduction in the pumping power needed to overcome the frictional pressure drop in the fluid is one reason that molten salts are advantageous over helium as a heat transfer fluid. The use of salts as heat transfer fluid, instead of He, improves the efficiency of the whole NGNP reactor system, electric and hydrogen production, by up to 0.6% [12]. This is if 50 MWt of the 600 MWt is transported to the chemical island with FLiNaK, the total efficiency of the plant increases by 0.6%, or 3.6 MW. For comparison, it requires a 100°C temperature increase in the reactor outlet temperature to increase the efficiency of the whole plant, electrical and chemical, by 1.1%. This increase in efficiency from the use of salts, then increases the economic viability of the NGNP.

One of the major research areas for use of molten salts in the NGNP is the intermediate heat exchanger (IHX). In the IHX, heat is transferred from the helium reactor coolant to the molten salt. The molten salt then transfers the heat to the chemical process fluid at the secondary heat exchanger (SHX). In the IHX, the helium reactor pressure is designed to operate at 7 MPa while the pressure in the salt is expected to be slightly above atmospheric pressure. Although the pressure of the molten salt can be tailored to produce the best results in both the IHX and the SHX. Due to large pressure differences between the two fluids (He and molten salt), a large stress will be imposed on the structural material of the IHX. To reduce the stress due to the pressure differences, one current design for the IHX calls for capillary tube, shell and tube heat exchanger [13]. The salt flows through the capillary tubes, with the helium on the shell side of the heat exchanger. To reduce the pressure drop of the salt through the capillary tubes, the salt is expected to flow through the capillary tubes in the laminar regime.

This research looks at the use of molten salts for the NGNP and other reactor applications. Specifically, methods for prediction of salt thermo-physical properties for selection of a molten salt coolant. Corrosion of container materials by molten salts and possible methods for corrosion mitigation. Finally, the thermal-hydraulic performance of molten salts through small diameter channels is also investigated to characterize heat transfer and friction coefficients of KCl-$MgCl_2$ (68-32 at %) salt flowing through small channels.

One of the main challenges in the experimental design of the forced convective loop is equipment to operate in flow conditions necessary, high temperatures and low flow rates. This difficulty is

due to the high melting point of the molten salt (426OC). It would be desirable to reduce the melting temperature of the molten salt for IHX design to reduce these difficulties. This is accomplished by moving to ternary and higher order salt systems. However, not much experimental data exists in literature for salt mixtures with more than two components. Methods for predicting a range of properties for molten salt systems has been studied.

The cost to build and operate the IHX loop depends to a great extent on the materials for fabrication, the selection of which depends on the corrosion performance of the metals in molten salt at high temperatures. Therefore, this study also investigates the corrosion performance of various candidate materials in chloride salts, particularly KCl-$MgCl_2$ in static environments. Therefore, static corrosion tests of multiple alloys were performed at 850°C for 100 hrs in quartz crucibles. In addition, a few tests were conducted with SS-316 and 800H samples in crucibles of the same material at 850°C for 500 and 1000 hours, respectively.

A forced convection loop was constructed to examine small channel flow typical of the proposed IHX design. Convection coefficients were measured in both forced and mixed convection heat transfer regimes for the KCl-$MgCl_2$ salt.

History of Molten Salt

Molten salts have a wide and diverse use in many industrial processes. One of the first commercial uses of liquid halide salts was in the Hall-Heroult process to reduce AlF_3 in cryolite ($NaF\text{-}AlF_3$) to Al metal. Since that time, many industrial processes have used molten salts in some aspect. Four main areas of interest in molten salts have been in their use as heat treating media, heat transfer agents, thermal storage material, and nuclear reactor fuel and coolants. Since the 1920's, molten salts have been used as media for heat treatment of steel parts, ranging from tools to automobile components. Heat transfer salt (HTS) ($NaNO_3\text{-}KNO_3\text{-}NaNO_2$) has been utilized for many years as a heat transfer fluid and is stable to temperatures below 538°C. More recently (1980's), molten salts have been used as a thermal storage material, which capture energy and store in receptacles for later use, e.g. solar towers and satellites. The large latent heat, or volumetric heat capacity, is the most important property in this application. The use of salts in the nuclear industry as reactor coolants and fuel started around 1950. All four above mentioned processes take advantage of the large volumetric heat capacity of these salts along with their high temperature stability.

The use of molten salts in the nuclear industry started with the Aircraft Reactor Experiment (ARE) at ORNL (1949-1956). The ARE was commissioned in 1949 to determine the feasibility of using nuclear power to propel an airplane. The use of nuclear power to propel an airplane required a large power density in the reactor core. Initial concept with sodium coolant could not remove enough heat to keep the temperature of the fuel rods at a reasonable operating temperature. To increase the power density in the reactor core, the ARE utilized a fuel bearing salt $NaF\text{-}ZrF_4\text{-}UF_3$ salt in the reactor core that allowed power densities to reach higher levels than those in sodium cooled reactors. A large experimental programs was associated with this project to study phase diagrams, physical properties, corrosion, chemistry, and analysis techniques of fluoride based salts. After termination of the ARE, ORNL applied the ARE technology to commercial power reactors under the Molten Salt Reactor Experiment (MSRE). The MSRE (1956-1969) was an 8 MW reactor that contained a fuel bearing salt of $LiF\text{-}BeF_2\text{-}UF_3\text{-}ThF_4$. The reactor went critical in June 1965 and subsequently led to many valuable experiments. In conjunction with this effort, molten salt research was continued in support of the MSRE program at ORNL. After the MSRE, work at ORNL with molten salts was at a much smaller scale than during the ARE and MSRE. The one project of note is the Molten Salt Breeder Reactor (MSBR). The MSBR was a funded program for 3-5 years in the early 1970's.

Nuclear applications of chloride based molten salts have also been studied since the days of the ARE. At the same time as the ARE, a Liquid Metal Fuel Reactor (LMFR) was investigated at Brookhaven National Laboratory (BNL). In order to remove fission products from the molten bismuth coolant, it was to be contacted with a eutectic mixture of $NaCl\text{-}KCl\text{-}MgCl_2$ (30-20-50, T_M=385°C). This molten salt research as part of the LMFR took place at Brookhaven National Laboratory (BNL) and was terminated in 1960. A major portion of this research program involved the examination of corrosion of various alloys in this ternary molten salt and the effect of impurities in the salt on corrosion[14, 15]. Other nuclear applications of molten chloride salts, involve using fuel bearing salts in a fast reactor design, similar to the MSRE [16 - 18].

Current commercial applications that have interest in molten salts as coolants or thermal storage media include: the Advanced High Temperature Reactor (AHTR), NGNP, and solar power applications [9, 19 - 21].

Many institutions and organizations have researched different aspects of molten salts, either in conjunction with these nuclear projects, or separately. A summary of major results related to the application of molten salts will be summarized. This summary will be broken down into three areas: Thermo-Physical Properties of Salts (Experimental and Models), Corrosion, and Heat Transfer.

Salt Properties

3.1 Salt Selection

Many different criteria are involved in the selection of a molten salt for a particular process. Some of these criteria include, but are not limited to: operating temperature range of the process, chemical properties of the molten salt, thermo-physical properties of the salt, and cost of the salt. These different aspects of the process all need to be accounted for during the selection of a salt for use in a desired application. It is desired to find a salt which will provide the best thermo-physical and chemical properties relative to the cost of the salt and containment material.

Applications utilizing molten salts as a heat transfer fluid are mostly interested in the properties of the salts that are directly related to the ability of the salt to transfer heat and to store that energy. Other processes such as heat treating baths, chemical separation processes, or thermal storage units, other properties may be of interest. For example in applications of in-core reactor cooling, such as the MSRE and the AHTR, the neutron absorption and radioactive half-life of possible isotopes are an essential consideration in the selection of the salt. For fuel bearing salts (salts with fissile material dissolved in the coolant salt), the solubility of the fissile material, i.e. salts of uranium, plutonium, and thorium, are an important consideration in the selection of the salt. For thermal storage applications, the heat of fusion of the salt along with the temperature at which the heat is produced is important to understand. Chemical properties of these salts, mainly corrosion, are also important and more about this selection criteria will be discussed in the next chapter. This chapter will focus more on thermo-physical and transport properties of molten salts. The nuclear properties of these molten salts will not be discussed at all. For more information regarding nuclear properties of molten salt systems, several authors discuss the use of salts in reactor applications [22, 23].

The physical properties of a salt, or salt mixture, determine which salt mixture is selected for a particular process. As such, much effort has gone into experimentally determining the thermodynamic and thermo-physical properties of pure salts and different salt compositions for many different systems. A majority of these salt properties have been compiled into databases and published [24, 25]. More recently, a review of different salts, including their physical properties, was undertaken to determine candidate salts for NGNP and AHTR applications [9, 20, 26, 27].

The physical properties of interest for applications utilizing liquid salts as coolants include the melting temperature, heat capacity, viscosity, density, and thermal conductivity of the fluid. A summary of some properties of molten salts and other common heat transfer fluids is presented in

Table 3.1. In particular, the relevant thermo-physical properties for fluoride and chloride salts at 700^{o}C and for nitrate salts at 400^{o}C are listed along with other coolants at specified temperatures or pressures.

Table 3.1: Thermo physical Properties of Different Molten Salts at 700°C and 1 atm unless noted.

Fluid	Formula Weight	Melting Point	900°C Vapor Pressure	ρ Density	C_P Heat Capacity	μ Viscosity	k Thermal Conductivity
	(g/mole)	°C	mm Hg	kg/m^3	J/kg-K	cP	W/m-K
LiF-NaF-KF 46.5-11.5-42	41.3	454	~0.7	2020	1881	2.9	0.92
KCl-$MgCl_2$ 68-32	73.7	426	<2.5	1556	1150	1.44	0.40
Li_2CO_3-Na_2CO_3-K_2CO_3 43.5-31.5-25 800°C	100.1	397	30	1.93	1935	2.2 600°C	--
$NaNO_3$-KNO_3 49-41 400°C	93.2	223	---	1840	1500	1.80	0.55
H_2O 20°C	18	0	--	3.8	4160	0.8	0.63
Na 500°C	23	98		780	1230	0.18	60
He 7.5 MPa	4		--	3.8	4160	0.042	0.29
Parathern NF 100°C	350	-43	---	840	2180	4.0	0.13
Drakesol 260 100°C	230	-2.8	---	770	2000	1.2	0.098

From examination of Table 3.1, the thermo-physical properties of molten salts are comparable to the thermo-physical properties of water at room temperature. Further examination of the properties in Table 3.1 show that for general comparisons, fluoride salts have the highest volumetric heat capacity, ρC_P, and thermal conductivity among the three different types of salts listed (fluoride, chloride, and nitrate). However, the melting temperature and viscosity of the fluoride salts are the highest of all of the salts listed. Chloride salts have the lowest viscosity, but also the lowest thermal conductivity, and volumetric heat capacity of the molten salts. The chloride salts do have a lower melting point than the fluorides, while being able to go to higher temperatures than the nitrate salts. The thermal conductivity, viscosity, and volumetric heat capacity of the nitrate salts is intermediate when compared against fluoride and chloride salts. The operating temperature range for these salts is less than for the fluoride and chloride salts, in both melting and maximum temperature of operation.

A straight comparison of the properties such as viscosity and heat capacity will not tell which fluid is superior due to differences in these properties. For example, one fluid, A may have a higher heat capacity, but also higher viscosity than another fluid B. Although A is able to store more heat, the higher cost of pumping could make fluid B more desirable. A ranking system to take into the different effects has been developed by Etherington [28] and applied to molten salts by Williams [9, 20]. The following figures of merit (FOM) have been applied to rank the molten salts:

$$\text{FOM (forced convection, turbulent)} = \frac{\mu^{0.2}}{\rho^2 C_P^{2.8}} \tag{3.1}$$

$$\text{FOM (natural convection, turbulent)} = \left(\frac{\mu^{0.2}}{\alpha\rho^2 C_P^{1.8}}\right)^{0.36} \tag{3.2}$$

$$\text{FOM (natural convection, laminar)} = \left(\frac{\mu^{0.2}}{\alpha\rho^2 C_P}\right)^{0.5} \tag{3.3}$$

A final FOM was proposed by Sanders at ORNL based on surface area of a heat exchanger [9]

$$\text{FOM (heat exchanger area)} = \left(\frac{\mu^{0.2}}{\rho^{0.3} C_P^{0.6} k^{0.6}}\right)^{0.5} \tag{3.4}$$

These FOM's allow for comparison of the different coolant salts to compare which salt is better from an overall total operational standpoint.

In addition to these physical properties, the operating range of the molten salt needs to be compared to the operating range of the process. Ideally the salt would be liquid at room temperature, while also remaining in the liquid state to temperatures exceeding 1000°C. However, a salt mixture with these unique temperature properties has not currently been found. In most applications, the melting point of a salt mixture sets the lower temperature limit on an application utilizing molten salts. In the NGNP application, it is desired to get the melting temperature of the salt mixture to as low as possible while maintaining thermal stability of the salt at temperatures > 1000°C.

One way to lower the melting point of a salt is to combine multiple salts together to form a salt of eutectic composition. These eutectic compositions have a much lower melting temperature than the individual salt components and are characterized by a single melting point. For example, for the ternary system of LiF, NaF, and KF, the individual constituents have melting point of 830°C, 880°C, and 912°C, respectively. The binary systems, LiF-NaF, LiF-KF, and NaF-KF have their lowest melting temperatures at 649°C, 492°C, and 718°C, respectively. When all three components are combined, the eutectic composition, FLiNaK, is formed with reduction of the melting point to 454°C. These deep-well eutectic compositions are commonly formed in mixtures of salt components. However, most ternary and higher order systems of salt mixtures have limited experimental data available for the thermo physical properties of the salts, e.g. density, viscosity, thermal conductivity, etc...

The use of correlations and other engineering practices for designing heat transfer equipment, e.g. heat exchanger area, pipe size, and pump size, are dependent on accurate knowledge of the thermo-physical and transport properties of the salt. In the selection of salts for the NGNP IHX loop, a thorough review of the properties of multiple molten salts (fluorides, chlorides, and fluoroborates) that are of interest for reactor cooling and heat transport loops has been reported on by Williams at ORNL [9, 20, 26]. In addition, Janz produced a database that contains the relevant properties for molten salts in energy applications [24, 25]. These databases are thorough and complete, however they do not contain data for any salt system that has not been experimentally determined. An integral part of molten salt technology is to identify new salt compositions with lower melting points and higher operational temperatures, and improved physical properties.

In the approach for determining new salts for evaluation in processes, it would be beneficial to have a way to predict properties of these higher order salt systems to narrow down potential salts and their compositions of interest for applications without needing to experimentally determine values for the possible composition space. There has been some work on the prediction on all of these salt properties, by either empirical models or more systematic modeling. It has been noticed from analysis of liquid salts from x-ray spectroscopy and neutron diffraction [29] that molten salts maintain a short range order (SRO) in the liquid phase. A lattice type model can then be used to determine the local structure of these liquid salts because the ionic charge maintains the local structure.

The maintaining of SRO in the molten salts in the liquid phase is due to the ionic nature of these salts, e.g. the positive and negative charged ions [30]. Previous work has applied this knowledge of the SRO of salt systems to model the density and viscosity of these salt mixtures [6, 31]. In quantifying and predicting properties, it would be beneficial to define a deviation in a salt property from ideal mixing based off a change in the local environment of the salt mixture. Then if the local environment of the salt is known, the properties of the salt mixture can be determined.

In this section, work that has been done to model the thermo-physical properties of molten fluoride, chloride, and or nitrate salts will be discussed in each of the sections. As will be discussed, several different empirical models exist to predict the properties of molten salt systems based off of either a potential functions or theoretical models fit to experimental data. One such approach uses the quasi-chemical model (QCM) to model phase diagrams of salt systems and can be used to extrapolate phase diagrams of higher order systems. In addition, quasi-chemical models have been

developed by others for prediction of density and viscosity of salt systems [6, 31, 32]. These models work due to the fact that molten salts still possess short range order in the liquid phase, as has been discussed previously.

Molten nitrate salts are of interest to the solar industry for the same reason that chloride and fluoride based salts are of interest to the nuclear industry: high volumetric heat capacity, liquid phase in desired operating temperature, large thermal stability region. Due to the lower operating temperature of the system, the solar industry is interested in liquid nitrate salts. Sandia National Laboratory (SNL) has been working with nitrate based salts as part of the solar tower projects [8], [33]. New salt mixtures have been examined and the physical properties are being measured for Li,Na,K,Ca//NO_3 salts. However little work has been done on the modeling of these salts. To highlight how these models can be used, the physical properties of this quaternary system will be determined and compared to experimental values. These models can be readily extended to the development of high temperature salts for use in nuclear co-generation applications.

3.2 Salt Properties

The thermo-physical properties of all substances are directly related to the thermodynamic properties of the system, specifically the Gibbs Energy of the system. This makes it possible to determine different physical properties of these systems by knowledge of the Gibbs energy of the system. The following sections highlight the relationship between the Gibbs energy of the system and the thermo-physical properties of interest.

3.2.1 Phase Equilibria

The solid - liquid phase equilibria is an important parameter in determining what salts can be used in an operating system. Phase equilibria can be experimentally determined is different ways: differential scanning calorimetry (DSC) and through thermal analysis.

A differential scanning calorimeter is a machine that heats up a sample and a reference pan over a temperature range. The DSC goal is to keep the temperature of the two pans constant over the temperature range by controlling the heat addition to each pan. When a phase change in the system exists, a large amount of energy is absorbed (or released) by the sample and a large peak is seen on the power curves. By analysis of the energy vs temperature, the liquidus temperature of the salt is determined. In addition, the heat of formation of that phase change is also determined by calibration of the instrument.

Thermal analysis is a similar technique but usually contains larger samples that are visually inspected over the temperature range. The temperature is recorded when different phenomena is seen to occur, such as first liquid or first solid in the system. The temperature profile also helps to determine the phase changes that can occur.

Thermodynamic phase equilibriums in a system are determined through examination and modeling of the Gibbs energy of the system. The thermodynamic definition of phase equilibria requires that the partial molar energy of a component be equal in all phases, c.f. Equation 3.5. Thus the melting temperature (T_M) of the system, A & B, is determined by setting the Gibbs energy of A in the liquid

equal to the Gibbs energy of A in the solid, while also setting the Gibbs energy of B in the solid and liquid phases equal. This occurs while maintaining a mass balance on the system such that the amount of A in the solid and liquid phases is equal to A put into the system.

Thermodynamically, for two phases to be in equilibrium, the chemical potential of component, A, must be equal in each phase in equilibrium. This is equivalent to saying that the partial Gibbs energy of component A, in all phases must be equal for all the phases to be in equilibrium.

$$\mu_A^l = \mu_A^s \quad (3.5)$$

$$G_A^l = RT\ln\left(\mu_A^l\right) \quad (3.6)$$

$$G_A^l = G_A^s \quad (3.7)$$

The modeling and calculation of phase diagrams has been applied to many different types of systems: metal, salt, ceramics, etc... The general approach for calculating phase diagrams is well established and is called the CALPHAD (Computer Coupling of Phase Diagrams and Thermo chemistry) method. The CALPHAD approach uses experimental data to fit the parameters of a thermodynamic model, some of these thermodynamic models are discussed later in this chapter, that can be used to model the Gibbs energy of a phase. Experimental data is fit first for unary systems. The unary data is then used to model the binary systems. The data from the binary systems is then used to model the ternary systems. This method is then followed to model X-number of components in a system. At each step, the experimental data is used to obtain model parameters that result in the best fit between model and experimental values. The CALPHAD approach to thermodynamic modeling has even led to a journal with the CALPHAD name.

3.2.2 Density (ρ)

Density of molten salts is an important parameter to measure for molten salt systems. Accurate knowledge of the density versus temperature allows for calculation of the volumetric expansion of the salt. The thermal expansion as a function of temperature also allows for determination of natural circulation flows of the salt system. In addition, pyro-processing applications require an accurate measurement of density to calculate the mass of fissionable substances across the process to ensure that all controlled material is properly monitored.

Density is often measured by an Archimedean type principle, where the change in force of a metal bob is measured from air to immersed in the fluid mixture. This type of system requires accurate knowledge of the volume of the metal bob, which is often determined by calibration of the density system against fluids with known densities [1, 34]. Several other density measurement techniques have also been employed by others [34].

Two techniques are used to predict the density of molten salt systems. Early work at ORNL during the ARE found that the density of a salt mixture could be accurately predicted by summing the molar volumes of each of the salt constituents, weighted by the mole fraction of each constituent, Equation 3.8. More recent work at Sandia National Laboratory (SNL) has also shown that density is accurately determined from addition of molar volumes of the salt components [1]. This basic model is still used today in calculations to estimate the density of molten salt systems.

$$\rho = \frac{\sum X_i M_i}{\sum X_i V_i} \quad (3.8)$$

The molar volumes are calculated from experimental data from the densities of the unary salts. Table 3.2 shows the molar volumes for basic salt components at 700°C for F, Cl, and CO_3 salts and 400°C for NO_3 salts.

Table 3.2: Molar volumes of unary salt components for use in calculating densities of salt mixtures.

	F	Cl	NO_3	CO_3
Li	14.87	29.22	40.57	37.61
Na	20.27	36.53	46.01	48.92
K	30.02	48.74	55.28	48.87
Rb		53.96	61.18	
Cs		62.05	68.97	
Be	24.01			
Mg		56.65		
Ca	27.95	52.90		
Ba				
Sr				

More recently, a model for the prediction of density utilizing the quasi-chemical method was proposed and tested to compute the density of mixtures [6], in particular salt mixtures.

The density of a substance is equal to the molecular weight of a system divided by the molar volume of the same substance. The molar volume is a thermodynamic quantity and is related to the Gibbs energy of the fluid by Equation 3.9,

$$V_M = \left(\frac{\partial G}{\partial P}\right)_{T,n,\ldots} \quad (3.9)$$

Thus the optimization of the Gibbs energy of the system with respect to pressure will also allow for the determination of the density of the substance. This approach has been recently utilized and will be discussed more in Section 3.9.

3.2.3. Heat Capacity (C_P)

Besides melting temperature of a salt mixture, heat capacity is equally important in the selection of a salt mixture. Fundamentally, heat capacity shows how much energy can be stored per unit mass of a substance. More often, it is desired to know how much heat can be stored in an unit volume, thus the volumetric heat capacity, ρC_P, is more often mentioned. A larger volumetric heat capacity results in a smaller volume of salt needed to move the heat from the reactor to the chemical plant with the same temperature rise. This results in smaller heat transfer equipment and smaller inventories of salt.

Experimental techniques to determine the heat capacity are usually done by drop calorimetry, or by using modulated differential scanning calorimeter (MDSC). MDSC involves the superposition of an oscillating sinusoidal function over the normal temperature control (ramp or isothermal). That is the set temperature for the sample and pan are always heating or cooling. This technique allows for determination of the heat capacity (reversible heat capacity signal) of the sample along with the information about chemical reactions (non-reversible heat capacity signal) [35]. The MDSC is calibrated by running the system with a sapphire disc and determining a calibration factor offset in the system as a function of temperature.

Theoretically, heat capacity is a thermodynamic variable and is related to the Gibbs Energy of a fluid by Equation 3.10

$$C_P = -\frac{\partial^2 G}{\partial T^2} \tag{3.10}$$

On an atomic level, the heat capacity of a fluid is dependent on the number of rotations, vibrations, and electronic excitations that are available for a given compound. Different theoretical formulations exist for calculating heat capacity from each of these molecular contributions. The sum of the contributions is then summed to get the heat capacity of the fluid.

One of the empirical models that was recommended by Williams [20] is the Petit model for heat capacity, Equation 3.11. This model gives each atom of the salt component a value of 33.47~J/~^{o}C~mole. Use of this model, assumes that the salts behave in a similar fashion to mono-atomic gases and each atom in the salt mixture assumes this ideal value [36].

$$C_P \left[\frac{J}{g-K}\right] = 33.47\frac{\sum X_i N_i}{\sum X_i M_i} \tag{3.11}$$

where X_i is mole fraction, N_i is the number of atoms, and M_i is the molecular weight of the salt component, (i). For example in 2LiF-BeF_2, X = 2/3, N = 2 and M = 25.94 for LiF and X = 1/3, N = 3 and M = 47.01 for BeF_2.

An empirical equation that has been developed in the Russian molten fluoride salt program shows a direct relation between the heat capacity and the inverse of the molar mass [37]:

$$C_P \left[\frac{J}{g-K}\right] = 0.2916 + 80.2/M \tag{3.12}$$

3.2.4. Volumetric Expansion

Volumetric expansion is important in determining the stresses that are imposed in the system during heating and cooling of the system during start-up and shut-down scenarios. Differences in thermal expansion between structure and salt may lead to unexpected stresses in the system.

Volumetric expansion is also important in heat transfer applications utilizing natural convection of the molten salt. The larger the volumetric expansion results in a smaller temperature differential necessary to produce the same amount of flow and heat removal. This parameter may not be necessary during normal operation for pumped systems.

Volumetric expansion coefficient is normally determined from density data as a function of temperature. The volumetric expansion for a substance can be determined by the following equation:

$$\alpha = -\frac{1}{\rho}\frac{\partial \rho}{\partial T} \tag{3.13}$$

The volumetric expansion coefficient is also a thermodynamic quantity since it is directly related to V (through ρ) and T. The volumetric expansion, α, is a second order derivative of the Gibbs energy with respect to T and V:

$$\alpha = \frac{1}{V}\left(\frac{\partial^2 G}{\partial V \partial T}\right)_n \tag{3.14}$$

3.2.5. Isothermal Compressibility

The adiabatic compressibility (κ_S) of a system has been shown to be related to the transport properties (thermal conductivity and viscosity) of a substance [38 - 40]. From a Gibbs energy standpoint, it is necessary to work with the state variables n, P, and T and so it is more convenient to work with the isothermal compressibility. From experimental data it is easier to obtain the adiabatic compressibility. The adiabatic compressibility of a salt mixture can be determined from the speed of sound in the liquid salt;

$$\kappa_S = \frac{1}{c^2 \rho} \tag{3.15}$$

It is necessary to use a relationship to convert the adiabatic compressibility (experimental data) to the isothermal compressibility (model parameter). The adiabatic compressibility is related to the isothermal compressibility of a fluid by the either of the following equations:

$$\kappa_T = \kappa_S + \frac{\alpha^2 T}{\rho C_P} \tag{3.16}$$

or

$$\kappa_T = \kappa_S \frac{C_P}{C_V} \tag{3.17}$$

Thermodynamically the isothermal and adiabatic compressibility of a material is defined by Equation 3.18 and Equation 3.19, respectively:

$$\kappa_T = -\frac{1}{V}\left(\frac{\partial^2 G}{\partial P^2}\right)_{T,n} \tag{3.18}$$

$$\kappa_S = -\frac{1}{V}\left(\frac{\partial^2 G}{\partial P^2}\right)_{S,n} \tag{3.19}$$

3.2.6 Viscosity

In applications involving the movement of the fluid, the viscosity of a salt is an important part in determining pressure drop, heat transfer rates, and pumping power. The viscosity of a salt mixture is slightly more complicated to measure than the density of a salt mixture.

The most common apparatus for measurement of the viscosity of a molten salt is a damped oscillometer. The rate at which the salt damps out an oscillation of a pendulum is used to determine the viscosity of the salt melt [41, 42]. Other techniques have been applied to molten salts for measuring of viscosity of the melt [34]. For non-glass forming salt melts, the viscosity of the salt melts are fit to an Arrhenius type of equation of the following form:

$$\mu = A_O \exp\left(\frac{E_A}{RT}\right) \tag{3.20}$$

with A_O and E_A determined from the experimental data.

In the cases when the molten salts do exhibit glass forming tendencies, as in the K-Ca//NO_3 binary system, the viscosity of the glasses are described by the Vogel-Fulcher-Tamman-Hesse equation [43], defined by

$$\mu = A_O \exp\left(\frac{E_A}{R(T - T_O)}\right) \tag{3.21}$$

Since the viscosity of a fluid is a transport property, there is no thermodynamic relationship that relates G to μ.

3.2.7. Thermal Conductivity

Thermal conductivity of the fluid is the last parameter that is of interest for the use of molten salts as heat transfer/storage media. The thermal conductivity is an important parameter to help determine the rate at which heat will move through the system due to conduction. The thermal conductivity is important to help understand the rate of heat transfer in forced convection systems.

Experimental determination of thermal conductivity of molten salts is most often measured by using a gap between a hot plate (top) and cold plate (bottom) [44 - 46]. A salt layer is placed between a hot surface (top) and a relatively cold surface (bottom) and the temperature across the salt is measured. A slight modification of this procedure is done by varying the gap between the hot and cold surfaces, variable gap technique. The variable gap technique provides a method for more accurate determination of the thermal conductivity [44]. Other methods have also been employed to determine thermal conductivity: co-axial cylinders, hot wire, and thermal diffusivity measurement [34, 38, 47, 48].

The thermal conductivity of molten salts is extremely difficult to measure due to many uncertainties associated with other modes of heat transfer at high temperatures: radiation heat transfer and natural convection. Pure molten salts are nearly transparent to infrared radiation allowing significant heat transfer to occur by radiation. This transparency coupled with the high temperatures of the salt melts allows for significant radiation heat flux from the hot to cold surface and thus is a significant source of error in the measurement of the thermal conductivity of the salt.

Another effect is the tendency of the salts to naturally convect heat to the cold surface, consequentially increasing the rate of heat transfer from hot to cold regions. These two effects cause a large source of error in the measurement of the thermal conductivity of molten salts.

Two empirical models that are utilized for estimation of the thermal conductivity have been described by Williams [9]. These two models are presented in of a molten salt mixture is shown in Equation 3.23 [37]

$$k = 0.119T_M^{0.5}\frac{\rho^{0.67}}{(M/n)^{1.167}} \quad (3.22)$$

$$k = -0.34+0.5x10^{-3}T+\frac{32.0}{M} \quad (3.23)$$

Different methods for predicting thermal conductivity of fluids have been proposed by relating it to the adiabatic compressibility of a fluid. A predictive equation for the thermal conductivity of alkali-halide salts was proposed by Smirnov [38]. This model for the thermal conductivity of the salts was derived by assuming the heat transfer occurs along polymer like chains of cations and anions. The model for the thermal conductivity is based off of the following equation:

$$k = \frac{\gamma k_B}{\kappa_S \mu}\left(\frac{V_M}{2N_A}\right)^{-1/3} \quad (3.24)$$

3.3 Gibbs Energy

Thermo physical properties of salt systems can be calculated from the Gibbs Energy of the system. The Gibbs energy of a substance is defined as

$$G = U+PV-TS = H-TS \quad (3.25)$$

For pure components, the Gibbs energy is often already determined and found in literature [49], or in databases or computer programs e.g. FactSage and HSC Chemistry. The Gibbs energy is defined at a standard reference state and data for the standard state enthalpy (H^O) and entropy (S^O) are reported. In addition, the coefficients for the heat capacity of the component are reported to fit a linear equation as a function of T:

$$C_P(T) = a+bT+cT^{-2}+dT^2+eT^{-0.5} \quad (3.26)$$

It is then necessary to account for the differences in temperature and pressure from the reference to actual state. These changes for enthalpy and entropy are highlighted in Equations 3.27 and 3.28, respectively.

$$H(T) = H^O+\int C_P dT \quad (3.27)$$

$$S(T) = S^O+\int \frac{C_P}{T}dT \quad (3.28)$$

Combining Equation 3.25 with Equations 3.27 and 3.28, the Gibbs energy of the system is determined by Equation 3.29

$$G(T) = H(T)-TS(T) = H^O-TS^O+\int C_P dT-T\int\frac{C_P}{T}dT \quad (3.29)$$

It is then necessary to determine the Gibbs energy of mixtures. The Gibbs energy of mixtures is broken into two main parts, the Gibbs energy due to ideal mixing and the excess Gibbs energy. Where the Gibbs excess energy of mixing is simply defined as the difference in Gibbs energy of the real system from the Gibbs energy of ideal mixing;

$$G^{Exc} = G - G^{Idl} \tag{3.30}$$

The ideal Gibbs energy is determined by combining the Gibbs energy of each component weighted by the mole fraction in the mixture. In addition, a term is added to account for the ideal mixing of the atoms in the system. Mathematically, this is defined by the following:

$$G^{Idl} = \sum_i X_i G_i + RT \sum_i X_i \ln X_i \tag{3.31}$$

The Gibbs excess energy of the system can then be determined by Equation 3.30. Since experimental data for the system is not continuous, it is convenient to use a model to best fit the excess Gibbs energy in order to produce a continuous function.

3.4 Models for Excess Gibbs Energy

Many models have been proposed for the fitting of the excess Gibbs energy to experimental data. All of these models require the use of fitting constants to produce the best fit to the experimental data. However, the parameters of the system the models are fitted against do change. The parameters of the system could be mole fraction, X_A, charge fraction, Y_A, or site fraction, X_{AA}. Each of these models will be briefly described based on the method for fitting of experimental data.

Polynomial Expansion

One of the simplest forms to fit the excess Gibbs energy of a system to do is a linear expansion of the data multiplied by the mole fraction of the components, similar to the Redlich-Kister method. Also the linear expansions are used to fit against the enthalpy and entropy separately. Then the excess Gibbs Energy then takes a form similar to 3.29

$$H^{Exc} = X_A X_B \left(H_0 + H_1 X_B + H_2 X_B^2\right) \tag{3.32}$$

$$S^{Exc} = X_A X_B \left(S_0 + S_1 X_B + S_2 X_B^2\right) \tag{3.33}$$

$$G^{Exc} = H^{Exc} - TS^{Exc} \tag{3.34}$$

Redlich-Kister

The Redlich-Kister equation for excess Gibbs energy is of the form

$$G^{Exc} = X_A X_B \left(A + B\left(X_A - X_B\right) + C\left(X_A - X_B\right)^2 + \ldots\right) \tag{3.35}$$

The data is then fit by linear regression techniques to obtain the values of A, B, C, etc... that best reproduce the experimental data.

Margules

Margules model for the excess Gibbs energy of a binary mixture contains two variables that are fitted to obtain the best correlation to experimental data:

$$G^{Exc} = X_A X_B \left(A_{AB} X_A + A_{BA} X_B \right) \tag{3.36}$$

Margules model for the excess Gibbs energy contains a form similar to a truncated form of the Redlich-Kister equation. A_{AB} is equal to (A + B) and A_{BA} is equal to (A - B).

Wilson

The Wilson equation is another way to fit experimental data to an equation. The Wilson equation is of the form:

$$G^{Exc} = -X_A \ln\left(X_A + X_B \Lambda_{23}\right) - X_B \ln\left(X_B + X_A \Lambda_{21}\right) \tag{3.37}$$

The Wilson equation for binary systems has two coefficients, Λ_{12} and Λ_{21}, that are fit to reproduce the experimental data [50].

Quasi-Chemical Model

The Quasi-Chemical Model (QCM) is generally used for solid systems of two components in one dimension. The QCM is used to relate the energy of a system by the exchange of unlike atoms in a lattice system. Specifically, the change in the energy of the system is determined from a change in the local structure of the system. In a system composed of A and B atoms, there is a change in the energy of the system when in one case A and B are nearest neighbors the comparison to when A is the nearest neighbor of A or when B is the nearest neighbor of B.

$$A - A + B - B \rightarrow 2 \quad A - B \qquad \Delta G_{AB} \tag{3.38}$$

The same philosophy has been applied to molten salt systems with only a slight modification. In the case where the anion is the same in a mixture of two salt components, the QCM is applied to the change of the second nearest neighbor, or the nearest cation neighbor. In equation form, this is written as

$$A - X - A + B - X - B \rightarrow 2 \quad A - X - B \qquad \Delta G_{AB} \tag{3.39}$$

This change in energy of the system due to mixing of the components can be determined from experimental data where the energy of the system has been measured.

The QCM is a statistical thermodynamic model used to model the thermodynamic properties of mixing [51, 52]. Many authors have theorized and developed this model to show how it is related to more traditional thermodynamic models. One of the main differences is the over prediction of the Gibbs energy due to mixing. To account for this difference, a configurational entropy term S_{Config} is added to the system to correct for this over prediction.

Modified Quasi-Chemical Model

The modified quasi-chemical model (MQCM) was introduced by Chartrand and Pelton [52] to allow for modeling of systems that contain local order. The basis for the model follows closely to the QCM discussed in Section 3.4. The difference lies in the ability to define coordination numbers to account for these regions of local order in the system away from the 1:1 region in the MQCM. For example, KCl-$MgCl_2$ salt system contains a region of high symmetry in the 2 KCl - 1 $MgCl_2$ region. The MQCM allows for coordination numbers to be defined so the MQCM reproduces the local ordering in the system.

Extrapolation to Ternary and Higher Order Systems

Several of the previous models were developed and modeled for binary systems. In order to determine the Gibbs energy of ternary and higher order systems, it is necessary to extrapolate the model of binary systems to higher order systems.

Kohler and Toop Methods

There are multiple geometric models that are available for the extension of the binary data to higher order systems. Two geometric models that have been successful in this process are the Kohler and Toop methods. The Kohler method is recommended for applications when the charge of each of the cations in the system are equal. Thus the system can be called symmetric. The Toop method is used when the charge of one of the cations is different than the other two cations.

For a ternary system of composition P, with salt components A, B, and C, the Kohler method relatively weights the excess Gibbs energy for each of the three binary systems (A-B, A-C, and B-C) by the square of the mole fraction of the salt components in the ternary system:

$$G_P^{Exc} = (1-X_C)^2 G_{AB}^{Exc} + (1-X_B)^2 G_{AC}^{Exc} + (1-X_A)^2 G_{BC}^{Exc} \quad (3.40)$$

The Toop method is a geometric model that treats the two binary sub-systems that contain the non-symmetric component (e.g. C) as constant across the composition range. Thus the equation for the prediction of the ternary parameters varies slightly from those in the Kohler method.

$$G_P^{Exc} = (1-X_C)^2 G_{AB}^{Exc} + \left(\frac{X_B}{X_A+X_B}\right)^2 G_{AC}^{Exc} + \left(\frac{X_A}{X_A+X_B}\right)^2 G_{BC}^{Exc} \quad (3.41)$$

Extension of Kohler and Toop Methods to MQCM

The MQCM also contains methods to extrapolate the data from binary systems to ternary and higher order systems. These methods reduce to the Kohler or Toop method for ternary systems, but contain additional terms that can be used in higher order systems. For further reference, the reader is referred to the following article [53].

3.5 Model Selection for Molten Salt Systems

Successful modeling of many salt systems have been performed using these discussed models. Polynomial expansion has been used to successfully model the binary and ternary systems for the

alkali halides, nitrates, and hydroxide salt systems[54, 55]. Redlich-Kister expansions have also been used to successfully model the LiF-BeF_2 and LiF-BeF_2-ThF_4 systems [56]. Wilson model for excess Gibbs energy has been applied to the Li-Na-K//NO_3 ternary system [57].

The Modified Quasi-Chemical Model has been successfully applied to most salt systems, that accounts for local ordering. Work has been done to model salt systems that are of interest in molten salt reactor applications with fuel bearing salts [16] and in the area of magnesium production [58].

In the following sections, the polynomial expansion is used in the optimization and expansion of the different binary subsystems. The Kohler and Toop approximations are used to extrapolate the excess Gibbs energy for the binary system to the ternary systems.

3.6. Structure of Molten Salts

The root of the quasi-chemical model treats the chemical systems as sitting on a lattice structure. In the solid form, salts form a crystal structure that is interpreted in the quasi-chemical model as a two lattice type system with the cations and anions on different lattice structures. Due to the ionic charge of the salt systems, the cations and anions are always closest. Alkali halide molten salts are unique fluids in such that the ionic nature of the salt is maintained through the melting point. That is the charge of each ion is maintained at temperatures above the melting point of the salt. This ionic nature of the salt helps the liquid atoms to maintain a lattice type structure in the liquid phase in short range. Due to the charge, the cation is still surrounded by a group of anions. This short range order (SRO), in the salts keep the atoms in the system in a set pattern. Experimental and simulation work has shown that the charged ion has a sphere of opposite charge ions around it. With large relaxation times required, to remove an ion from this charged sphere [59].

Earlier experimental studies have been completed showing that this local structure is maintained in the molten salts. X-ray analysis of NaCl at 850^{o}C (T_M = 805°C) showed clearly the structure factors for the Na-Na, Cl-Cl, and Na-Cl interactions with a large amount of structure short distance from an atom. A general review of the structure of liquid molten salts can be found in literature [59].

The quasi-chemical model assumption of local structure in the liquid phase is valid and further shows how the model can be used to help understand the local structure of the system. This local structure can then be utilized in helping to understand the molten salt systems and the deviations that occur during mixing of components.

To apply the use of the local structure of the salt melts, a quasi-chemical approach was taken to determine the thermo-physical properties of the Li,Na,K,Ca//NO_3 system. This nitrate salt system is of importance to the solar industry and application of these models to the binary and ternary sub-systems has not been applied. The same approach that is outlined can be used in determining salt properties of other salt systems, such as chloride and fluoride based systems.

3.7 Thermodynamic Modeling of Phase Diagram

In determining the phase diagram of a salt mixture, it is necessary to know the Gibbs energy of each phase in the system [54, 60]. The Gibbs energy of the system is then used to determine under what conditions can two phases be in equilibrium, see Section 3.2.1.

In order to use Equation 3.5, it is necessary to know how to define the partial Gibbs energy of component A. The partial Gibbs energy due to component A is defined as

$$G_A = G + (1 - X_A)\frac{\partial G}{\partial X_A} \tag{3.42}$$

The total Gibbs energy of a phase is then the sum of the partial Gibbs energies of each component:

$$G = G_A X_A + G_B X_B \tag{3.43}$$

The basic solution for phase equilibrium between two phases, in this case solid and liquid, is then defined as:

$$RT \ln\left(\frac{X_s^A}{X_l^A}\right) - G_s^{E,A} + G_l^{E,A} = -\Delta G_{s\to l}^A \tag{3.44}$$

If the salt systems were to mix ideally, the phase diagrams for the salt mixtures could be determined by applying Equation 3.44 with the excess Gibbs energy equal to zero. Real systems contain some deviation from ideal mixing, and are modeled by using an excess property term equal to the difference between actual and ideal values. Equation 3.44 shows that it is necessary to know the partial Gibbs excess energy of the component in the mixture to predict the phase diagram of a system. In addition, it is necessary to know the change in Gibbs energy between the two phases. With this knowledge, the position of the solidus and liquidus can be determined.

As has been discussed, there are many ways to model the Gibbs excess energy of the fluid. The basic approach is to create a linear equation, based on mole, site, or charge fractions. Experimental data is used to fit the coefficients of the linear equation. The two methods, polynomial expansion and the MQCM will be discussed in more detail since most literature about salt systems utilize either of these two methods.

3.7.1 Polynomial Expansion

The Gibbs energy is related to the enthalpy and entropy as was discussed in Equation 3.25. It was also discussed, how the Gibbs excess energy term is used to model real systems based on experimental deviation from ideal systems. The polynomial method for modeling the Gibbs excess energy models the excess enthalpy and excess entropy terms as linear expansions multiplied by the mole fractions of the salt component in the mixture. This linear expansion is represented mathematically by Equation 3.34

Then using Equation 3.42, the partial Gibbs energy of each component can be calculated according to Equation 3.42. This results in the following equations [54]:

$$H_A^E = X_B^2\left[h_0 + h_1\left(X_B - X_A\right) + h_2\left(X_B^2 - 2X_A X_B^2\right)\right] \quad (3.45)$$

$$H_B^E = X_A^2\left(h_0 + 2h_1 X_B + 3h_2 X_B^2\right) \quad (3.46)$$

The entropy is calculated with the same equations by replacing h_i with s_i. The Gibbs energy of component A is then equal to

$$G_A^E = H_A^E - TS_A^E \quad (3.47)$$

To determine phase equilibria, values from Equation 3.47 is then put into Equation 3.44. The experimentally determined liquidus and solidus data is then used along with other thermodynamic data to find the best fit of the values h_0, h_1, s_0, ... for the polynomial expansion. The excess Gibbs energy for the system is then added to the ideal Gibbs energy to compute the Gibbs energy of the mixture.

3.7.2 Modified Quasi-Chemical Model

The MQCM is a statistical thermodynamic model used to compute the Gibbs excess energy of the system. The MQCM assigns an energy associated with the reaction associated with the exchange of nearest neighbor on a lattice, for salt systems the second nearest neighbor is exchanged, Δg_{AB}. This change in energy associated with mixing is then used to model the excess Gibbs energy of the system, by the following equation:

$$G = \left(n_A G_A^o + n_B G_B^o\right) - T\Delta S^{Config} + \left(\frac{n_{AB}}{2}\right)\Delta G \quad (3.48)$$

where, G^o_A and G^o_B are Gibbs energy of the pure components and the configurational entropy term, ΔS^{config}, for mixing of (A-A), (B-B), and (A-B) pairs, is defined as

$$\Delta S^{Config} = -R\left(n_A X_A + n_B X_B\right) - R\left[n_{AA}\ln\frac{X_{AA}}{Y_A^2} + n_{BB}\ln\frac{X_{BB}}{Y_B^2} + n_{AA}\ln\frac{X_{AB}}{2Y_A Y_B}\right] \quad (3.49)$$

where X_{ij} is the site fractions for components i and j, Y is the coordination fraction, and X_i is the mole fraction. These values are defined respectively as

$$Y_i = X_{ii} + \frac{X_{ij}}{2} \quad (3.50)$$

$$X_i = \frac{n_i}{n_{tot}} \quad (3.51)$$

The pair fractions, or fractions of SNN, for a given Δg_{AB} can be determined by looking at the equilibrium distribution of the salt [52]. The equilibrium distribution is calculated by setting

$$\left(\frac{\partial G}{\partial n_{AB}}\right)_{n_A, n_B} = 0 \quad (3.52)$$

The equilibrium pair fractions then can be computed by the following equations:

$$\frac{X_{AB}^2}{X_{AA}X_{BB}} = 4\exp\left(\frac{-\Delta G_{AB}}{RT}\right) \quad (3.53)$$

$$1 = X_{AA} + X_{BB} + X_{AB} \quad (3.54)$$

$$X_A = \frac{\left(2n_{AA} + n_{AB}\right)/Z_A}{\left(2n_{AA} + n_{AB}\right)/Z_A + \left(2n_{BB} + n_{AB}\right)/Z_B} \quad (3.55)$$

Using the site fractions evaluated from ΔG_{AB}, a linear expansion is used to model ΔG_{AB}. The pair fractions then give the fraction of SNN's based off of a defined composition for the liquid phase. Knowledge of the site fractions of the liquid phase of the salt is then used in modeling other properties.

3.7.3 Determination of Phase Equilibria

Now that the Gibbs energy of the liquid and other phases can be modeled, the phase diagram of the system can be determined by minimizing the Gibbs energy of the mixture. Gibb's minimization is accomplished by determining the Gibbs energy of all phases (solid, liquid, solid-solubility, etc...) in the system that can be in equilibrium. Then a standard state is chosen for each component A and B. The Gibbs energy for each phase is then computed as a difference from the standard state values chosen. Mathematically the difference in the Gibbs energy is computed by the following equation:

$$\Delta G_{\alpha\to\beta}^{M} = X_B G_B - X_A G_A + RT\left(X_A \ln X_A + X_B \ln X_B\right) + X_A \Delta G_{\alpha\to\beta}^{A} + X_B \Delta G_{\alpha\to\beta}^{B} + G_{AB}^{Exc} \quad (3.56)$$

where α and β are phases and A and B are the two components of the binary system. The location of phase equilibrium at each temperature is found by examining the ΔG^M curves at that temperature [61, 62].

To demonstrate the method for determining the location of phase equilibria, the $NaNO_3$ and KNO_3 binary system will be used for an example, Figure 3.1. This binary system contains a solid solution and liquid phase in addition to the standard reference state. The composition of the phase equilibria at each temperature is determined by the following algorithm. The Gibbs energy of each phase is computed over the composition space, $X_{NaNO3} = 0 \rightarrow 1$ at a given T. For simplification, X_{NaNO3} will be denoted as X for this example. The phase with the lowest Gibbs Energy at X = 0 is determined. A tangent line to the G^M curve is drawn from X = 0 for the lowest energy phase to see if an intersection occurs. If an intersection occurs, then the location of the common tangent is set. If no intersection is found, X_{NaNO3} is increased and the process repeated. At some composition X = α, a tangent line is found that intersects another G^M curve at X = β. The points α and β are recorded and X is incremented to β. A tangent line at X = β is then drawn and incremented. This process is repeated for the range of temperature of interest. For a binary system with just a liquid and solid phase, the tangent lines of the G^M curves that pass through 0 at X = 0 and 1 are the only necessary points to determine [62].

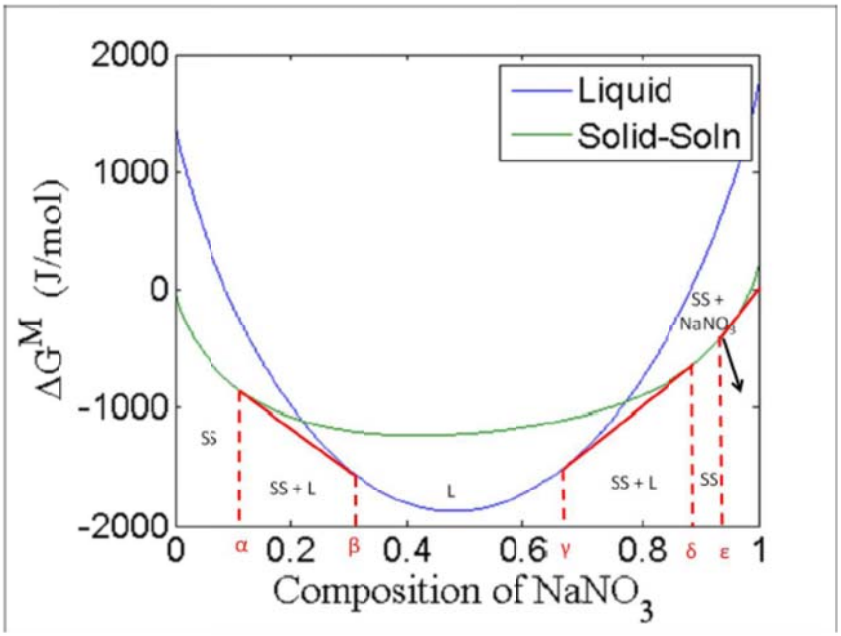

Figure 3.1. The methodology for location of phase equilibria is found by determining common tangent lines between phases.

3.7.4 Phase Diagrams of the Li,Na,K,Ca//NO_3 Systems

Phase diagrams of the binary systems: Li,Na//NO_3, Li,K//NO_3, and Na,K//NO_3, have been modeled previously [55]. No work has been published that models the Li,Ca//NO_3, Na,Ca//NO_3, or K,Ca//NO_3, or the four ternary systems: Li,Na,K//NO_3, Li,Na,Ca//NO_3, Li,K,Ca//NO_3, and Na,K,Ca//NO_3 systems, or the quaternary system Li,Na,K,Ca//NO_3.

The Li,Na//NO_3, Li,K//NO_3, and Na,K//NO_3 systems were modeled again as a comparative measure to ensure that the proper techniques were used in the phase diagram modeling of the systems. The phase diagrams for these three binary systems are not shown in the current work, but are published in literature [55]. The thermodynamic parameters are listed in Table 3.3. As is shown, the parameters for the thermodynamic model match closely to literature values [55].

Thermodynamic data for the three binary systems involving $Ca(NO_3)_2$ were then obtained. The data was then used to fit parameters to the polynomial expansion technique. In determining the phase diagram for these systems, all available thermodynamic data is needed to get the best fit possible. Thermodynamic data for pure liquid $Ca(NO_3)_2$ is not available due to decomposition of $Ca(NO_3)_2$ starting at 400°C, (T_M = 561°C). The heat of fusion, ΔH_F has been approximated from DSC, or mixing calorimetry experiments to be ~23.6 kJ/mol [63, 64]. This value of 23.6 kJ/mol was then used for ΔH_F, while ΔS_F was calculated at the melting point using the difference in Gibbs energy of two phases in equilibrium is zero and Equation 3.25.

Calorimetry data for the mixing of solid calcium nitrate with the three alkali nitrates has been measured by Kleppa, [63]. This partial enthalpy of mixing due the addition of solid Ca(NO3)2 was used to determine the parameters for the enthalpy in Equation 3.34. It was necessary to correct the experimental heat of mixing data by the ΔH_F of $Ca(NO_3)_2$ to get liquid-liquid mixing data to use in

the optimization of the parameters for Equation 3.34 [63]. Experimentally, the phase diagrams of the three binary systems have been investigated by thermal analysis of different compositions of the salt mixture [3 - 5]. This experimental data is used to further fit the parameters for the thermodynamic models for the entropy. The total deviation from model and experimental data is then minimized, which slightly modifies the values determined for enthalpy and entropy determined previously.

Using this method, the parameters for the thermodynamic models for each of the binary systems was computed, Table 3.3. The computed phase diagrams are compared to the experimentally determined phase diagrams for the Li,Ca//NO_3, Na,Ca//NO_3, and K,Ca//NO_3 systems and shown in Figures 3.2a, 3.2b, and 3.2c, respectively. Each of these three binary systems are well modeled using the limited data available. For the binary system, K,Ca//NO_3, a stoichiometric compound, $K_4Ca(NO_3)_6$, is stable at temperatures less than 440 K. The estimated thermodynamic parameters for the $K_4Ca(NO_3)_6$ system are listed in Table 3.3.

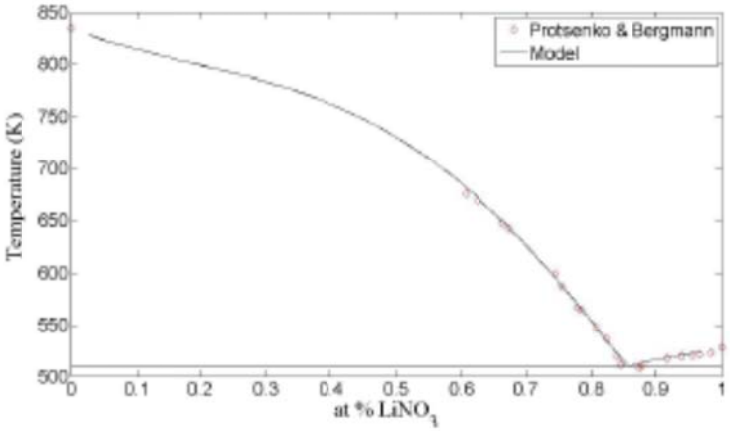

(a) Li,Ca//NO_3

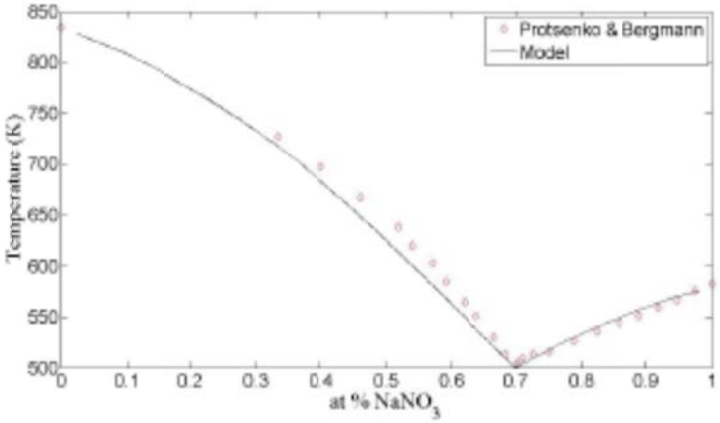

(b) Na,Ca//NO_3

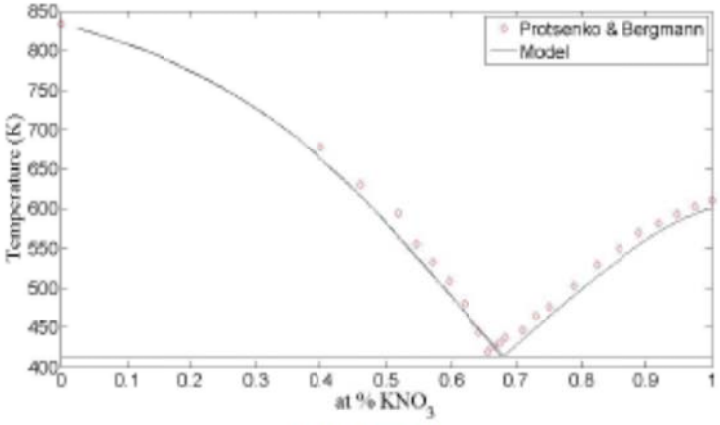

(c) K,Ca//NO_3

Figure 3.2. Phase Diagrams of the (a) Li,Ca//NO_3, (b) Na,Ca//NO_3, and (c) K,Ca//NO_3 systems.

Table 3.3. The optimized parameters for the binary nitrate systems have been computed and compared where possible to experimental data.

Salt System	h_0	h_1	h_2	s_0	s_1	ΔG_{AB}
Li,Na//NO_3	-1989.5	48.11	--	0.781	--	-3412.4 – 208.29 X_{LiLi}
[55]	-1938	64	--	0.874	--	--
Li,K//NO_3	-7360.8	-2299.4	1938.0	5.33	--	-3412.4 – 208.3 X_{LiLi}
[55]	-7360	-2300	1936	5.334	--	--
Li,Ca//NO_3	1047.9	910.0	-710.1	10.10	-15.06	-26.2 – 1712.8 X_{LiLi} + 1466.7 X_{CaCa}
Na,K//NO_3 (l)	-1709.2	-284.5	--	--	--	-556.88 – 90.142 X_{NaNa}
Na,K//NO_3 (s)	-2529	8366	--	-18.241	16.902	
[55]	-1640	-280	--	--	--	--
[55]	-2529	8366	--	-18.241	16.902	
Na,Ca//NO_3	-3055.1	-7256.4	4028.5	9.51	-6.254	-2865.1 – 211.5 X_{NaNa}
K,Ca//NO_3	-12205.6	-8776.5	1399.5	14.70	-22.82	-4339.6 – 2895.8 X_{KK} – 782.9 X_{CaCa}
ΔG_F $K_4Ca(NO_3)_6$ = 3876.6 – 5.761 T(K)						

In order to calculate the ternary phase diagrams, the necessary geometric models need to be used for determining the Gibbs excess energy of the ternary system. For the Li,Na,K//NO_3 system, the Kohler (symmetric) model is used in the prediction scheme. For the Li,Na,Ca//NO_3, Li,K,Ca//NO_3, and Na,K,Ca//NO_3 systems, the Toop model is used to model the ternary phase diagrams. Matlab code has been written to compute the location of phase equilibrium over the temperature and composition space for each of the ternary systems. All four of the ternary systems were modeled without using ternary excess parameters, currently all the systems were modeled with only the parameters for the liquid phases. As such, the Na,K//NO_3 binary system shows a lower eutectic temperature than the binary system. The ability to model other phases, such as solid-solubility as seen in the Na,K//NO_3 system, is currently being added to the code. Regardless, the eutectic temperature and compositions for each of the ternary systems are fairly accurate.

Li,Na,K//NO_3

The ternary phase diagram for the Li,Na,K//NO_3 system has been experimentally investigated by Carveth [2]. This investigation determined a eutectic composition at 30-14-56 wt % $LiNO_3$, $NaNO_3$, and KNO_3, respectively, with a melting temperature of 120°C. The current ternary phase diagram was computed using the symmetric model with no ternary terms added. The result of the ternary model is a eutectic point at 28-13.1-58.9 wt % $LiNO_3$-$NaNO_3$-KNO_3 with a melting temperature of 116.6°C. The calculated phase diagram compared to the experimental phase diagram of Carveth is shown in Figure 3.3

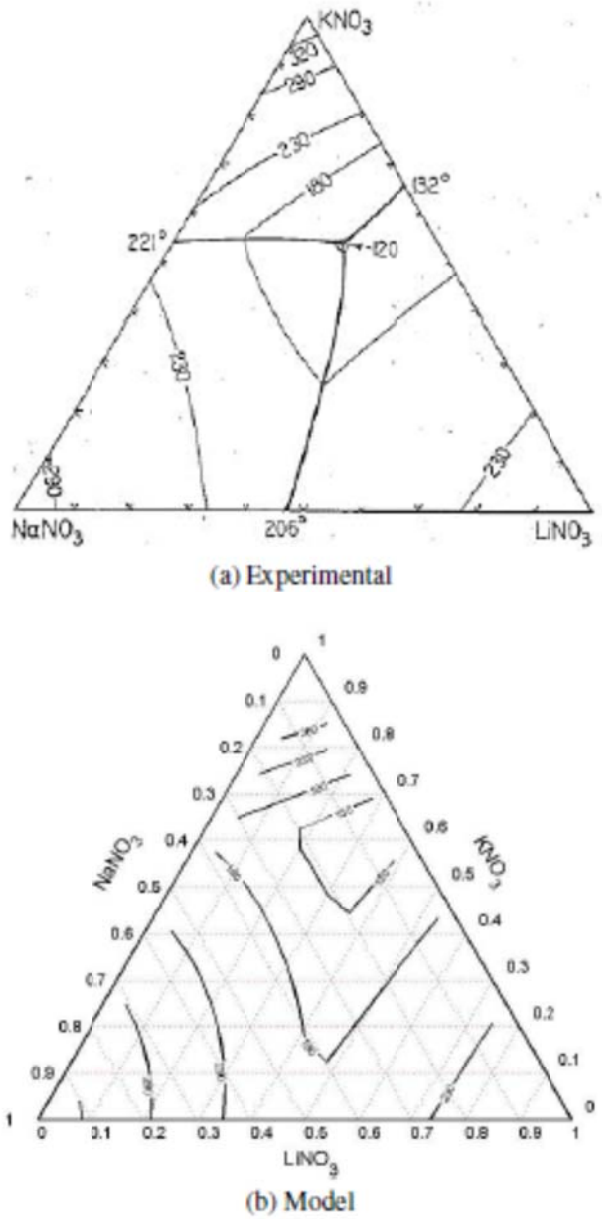

Figure 3.3. Phase Diagrams for the Li,Na,K//NO_3 system (a) experimental phase diagram [2] (b) computed phase diagram.

Li,Na,Ca//NO_3

The ternary phase diagram for the Li,Na,Ca//NO_3 system has been experimentally investigated by Lehrman [3]. This investigation determined a eutectic composition at 40-30.5-29.5 wt % $LiNO_3$, $NaNO_3$, and $Ca(NO_3)_2$, respectively, with a melting temperature of 170.3°C. The current ternary phase diagram was computed using the asymmetric model with no ternary terms added. The result of the ternary model is a eutectic point at 42.8-33.1-24.1 wt % $LiNO_3$-$NaNO_3$-$Ca(NO_3)_2$ with a melting temperature of 174.5°C. The calculated phase diagram compared to the experimental phase diagram of Lehrman is shown in Figure 3.4

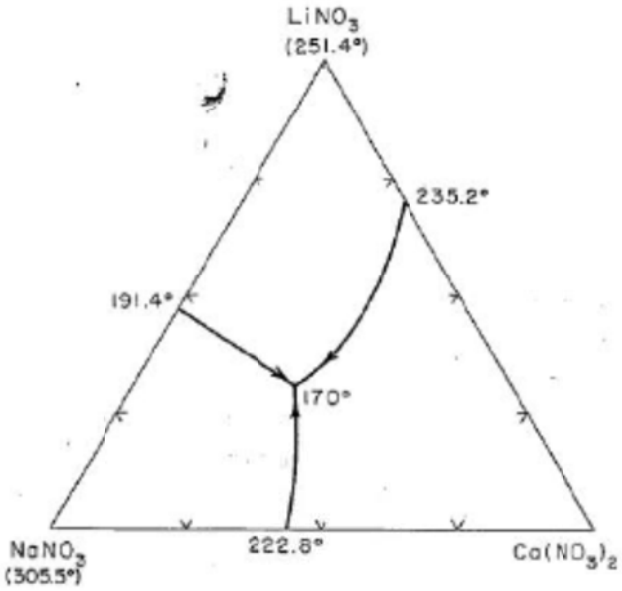

(a) Experimental

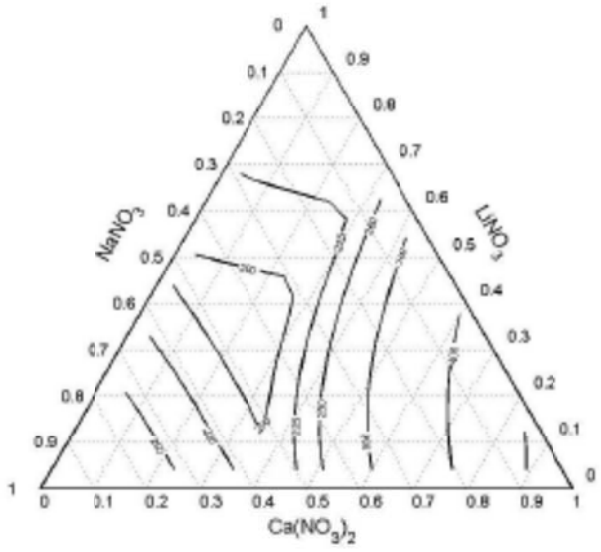

(b) Model

Figure 3.4. Phase Diagrams for the Li,Na,Ca//NO_3 system (a) experimental phase diagram [3] (b) computed phase diagram.

Li,K,Ca//NO_3

The ternary phase diagram for the Li,K,Ca//NO_3 system has been experimentally investigated by Lehrman [4]. This investigation determined a eutectic composition at 23-62-15 wt % $LiNO_3$, KNO_3, and $Ca(NO_3)_2$, respectively, with a melting temperature of 117.4°C. The current ternary phase diagram was computed using the asymmetric model with no ternary terms added. Currently there has been no attempt to account for the $K_4Ca(NO_3)_6$ phase in the model. The result from the

ternary model is a eutectic point at 20.4-58.2-21.4 wt % $LiNO_3$-KNO_3-$Ca(NO_3)_2$ with a melting temperature of 109°C. The calculated phase diagram compared to the experimental phase diagram of Lehrman is shown in Figure 3.5

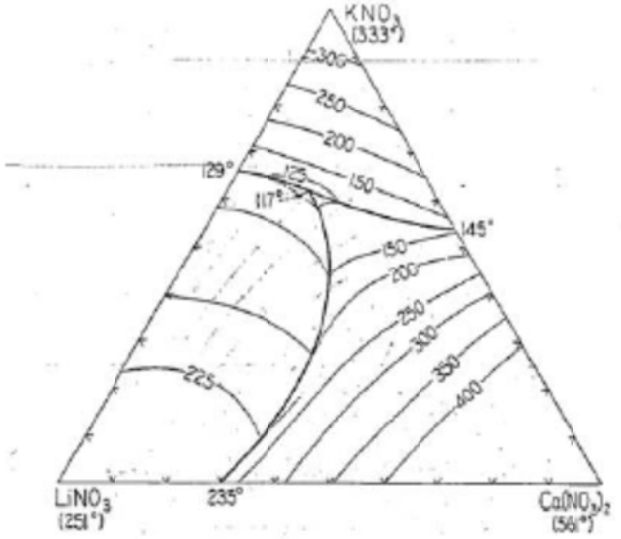

(a) Experimental

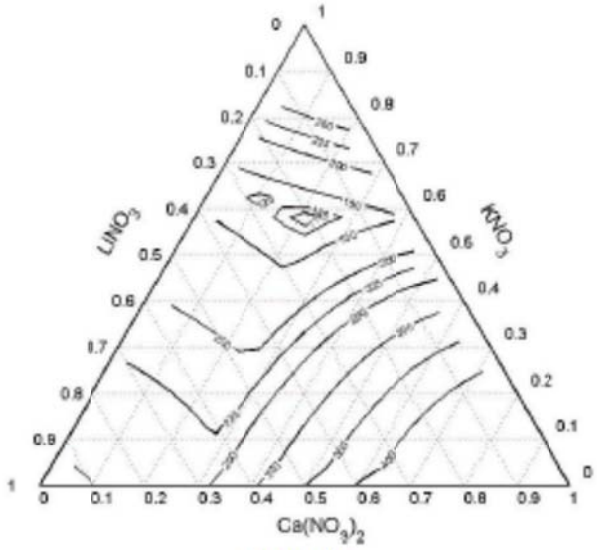

(b) Model

Figure 3.5. Phase Diagrams for the Li,K,Ca//NO_3 system (a) experimental phase diagram [4] (b) computed phase diagram.

Na,K,Ca//NO_3

The ternary phase diagram for the Na,K,Ca//NO_3 system has been experimentally investigated by Protsenko [5]. This investigation determined a eutectic composition at 11.8-39.4-48.8 wt % $NaNO_3$, KNO_3, and $Ca(NO_3)_2$, respectively, with a melting temperature of 133°C. The current

ternary phase diagram was computed using the asymmetric model with no ternary terms added. Again no attempt has been made to model the $K_4Ca(NO_3)_6$ phase. Currently, the model also needs to account for the Na,K//NO_3 solid solution, which will increase the temperature near the Na,K//NO_3 line in the phase diagram, but have little effect on the eutectic composition and temperature. The result of the ternary model is a eutectic point at 14.4-45.6-40.0 wt % $NaNO_3$-KNO_3-$Ca(NO_3)_2$ with a melting temperature of 130.5°C. The calculated phase diagram compared to the experimental phase diagram of Protsenko is shown in Figure 3.6

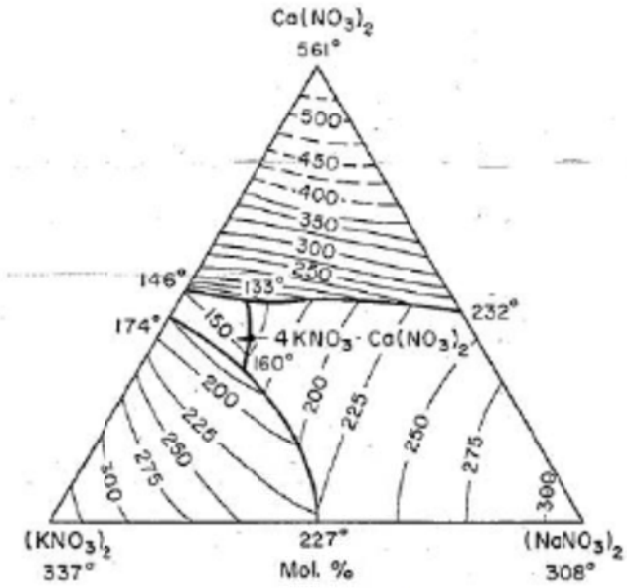

(a) Experimental

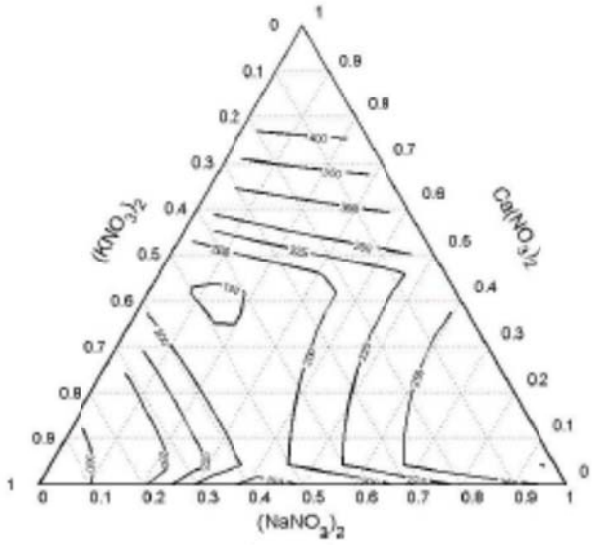

(b) Model

Figure 3.6. Phase Diagrams for the Na,K,Ca//NO_3 system (a) experimental phase diagram [5] (b) computed phase diagram.

Although no attempt has been made to fine tune the ternary systems with the experimental data, it can be seen that only a small excess term would be needed due to good initial agreement in the phase diagrams.

3.8 Heat Capacity

The thermodynamic relation between heat capacity and Gibbs Energy allows for calculation of the heat capacity of the system using Equation 3.10. The heat capacities of solar salt ($NaNO_3$-KNO_3, 52-48 at %) and the $LiNO_3$-$NaNO_3$-KNO_3 eutectic have been investigated using modulated differential scanning calorimetry (MDSC) at the University of Wisconsin-Madison. The values obtained from experimental work are compared to the values obtained from the model in Figure 3.7. The values for the Gibbs energy of the pure salt components as a function of temperature have been tabulated [65].

To calculate the heat capacity of the fluid, the Gibbs energy of the fluid was then determined at the desired composition for a range of temperatures. A numerical derivative of the Gibbs energy was taken in order to determine the heat capacity of the fluid over that temperature range. This procedure produced results within ±5% for the solar salt and Li,Na,K//NO_3 eutectic.

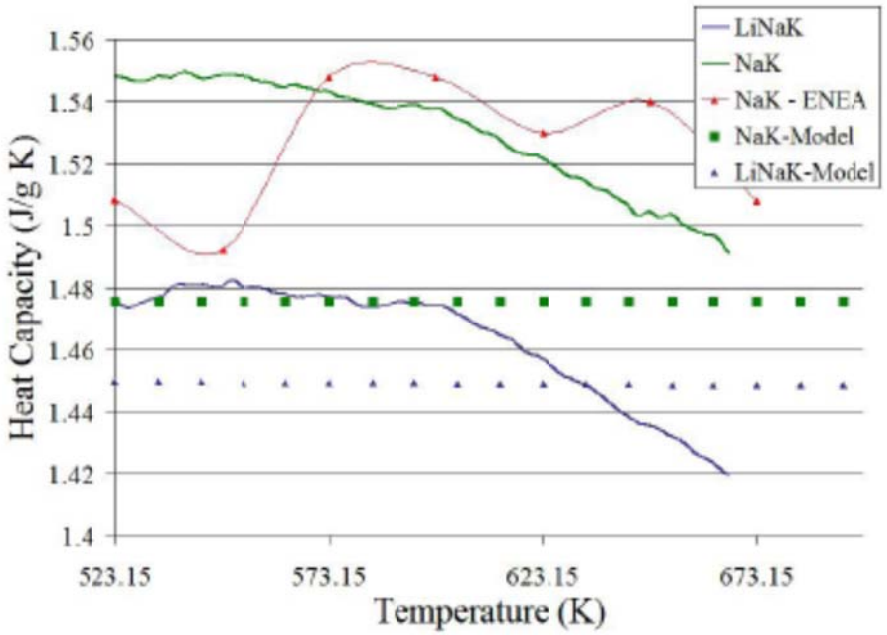

Figure 3.7. The heat capacity of solar salt and the ternary eutectic, LiNaK, are compared to theoretical values obtained from the model.

Heat capacity was also experimentally determined using the MDSC in this current work for KCl-$MgCl_2$ and FLiNaK salts. These measurements and comparison to the theoretical model is found in Appendix A in Section A.2.

3.9 Density

Extensive work on molten salt mixtures of fluoride salts and their physical properties was undertaken at Oak Ridge National Laboratory (ORNL) during the 1950's as part of the Aircraft Reactor Experiment (ARE). The density of molten salt mixtures was soon understood to follow a simple rule for the addition of the molar volume of the salts, see Equation 3.8. However, some deviations from this simple mixing rule do occur. As such a Quasi-Chemical Model for the prediction of the density of the salt mixtures was developed by modeling NaCl-KCl-$MgCl_2$-$CaCl_2$ salt mixtures [6].

The method was tested by the original author to compute densities for the salt mixture of NaCl-KCl-$MgCl_2$-$CaCl_2$. In order to utilize the same extrapolation techniques (Kohler and Toop Methods) that were used in the prediction of the phase diagrams, the molar volume of the salt mixtures is fit to experimental data. Since the molar volume of a substance is related to the Gibbs energy of the fluid by Equation 3.57, the molar volume of mixtures can utilize the same extrapolation techniques that are used for the Gibbs Excess energies in the liquid phase.

$$V = \left(\frac{\partial G}{\partial P}\right)_{T,n,\ldots} \tag{3.57}$$

The experimentally determined density data is changed into a molar volume by using the relationship:

$$V_M = \frac{\sum X_i M_i}{\rho} \tag{3.58}$$

This experimental data is then fit to model parameters for unary and binary systems to obtain the model for the density of the salt mixtures.

Unary Salts

The experimental values for the molecular volumes of the unary salts are determined from the density data. The volume for the unary salt is then fit to the following equation:

$$V(T) = V(T_{Ref})\exp\left(\int_{T_{Ref}}^{T} \alpha(T)dT\right) \tag{3.59}$$

where $\alpha(T)$ is a polynomial representation of the thermal expansion of the salt, given as

$$\alpha(T) = a_0 + a_1 T + a_2 T^{-1} + a_3 T^{-2} \tag{3.60}$$

The natural log of each side of Equation 3.59 to reduce it to a linear equation that is solved for the parameters $V(T_{Ref})$, α_O, α_1, α_2, and α_3.

Binary Salts

The QC density model characterizes the deviations from ideal mixing as a function of the pair fractions. The volume of the salt mixture is computed from experimental data and the ideal volume of the mixture is subtracted;

$$V_{AB}(T) = n_A V_A + n_B V_B + \frac{n_{AB}}{2}\left(\frac{\partial \Delta G_{AB}^{P}}{\partial P}\right)_{T,n,\ldots} \quad (3.61)$$

where ΔG^{P}_{AB} is defined by

$$\Delta G_{AB}^{P} = \beta_0(P-1) + \beta_1 X_{AA}(P-1) + \beta_2 X_{BB}(P-1) \quad (3.62)$$

Additional terms are then added to ΔG_{AB} to have a pressure dependency in the equation for Gibbs excess energy. The excess Gibbs energy of the liquid phase is then described by this general form of the equation:

$$\Delta g_{AB} = \alpha_0 + \alpha_1 X_{AA} + \alpha_2 X_{BB} + \beta_0(P-1) + \beta_1 X_{AA}(P-1) + \beta_2 X_{BB}(P-1) \quad (3.63)$$

The excess Gibbs energy then can be separated into two parts: pressure dependent and pressure independent terms. In [6], it was found that the addition of the pressure dependent terms had negligible effect on the excess Gibbs energy of the liquid phase as determined by modeling the phase diagram.

The density of higher order systems can now be predicted by extrapolation of the binary system data to higher order systems.

In order to apply the previous equations to the optimization of model parameters and prediction of higher order salt systems, a Matlab script was written to analyze experimental data and compute the coefficients for the unary salts. The values that were determined experimentally for the fluorides, chlorides, and nitrates of lithium, sodium, and potassium are listed in Table 3.4. These optimized values were solved using a Matlab script based off of the density equations that were recommended by Janz in NIST publications [24, 25]. The values for NaCl and KCl that were obtained in [6] are also presented to validate the current script versus literature values, Table 3.4 and Figure 3.8. The a_3 term was unnecessary due to rank limitations in the Matlab code. In order to show how the volumes of NaCl and KCl obtained compared to literature, the molar volumes of the NaCl and KCl salts were graphed over the temperature range 25°C to 600°C.

Table 3.4. Model parameters for the molecular volume of single component salts

Fluid	$V(T_{Ref})$	a_0	a_1	a_2	a_3
$LiNO_3$	3.5595	1.5602e-4	1.2814e-7	7.5075e-2	1.2207e1
$NaNO_3$	3.7010	1.3986e-4	1.1314e-7	7.9059e-2	1.3979e1
KNO_3	3.8681	8.4741e-5	1.4958e-7	1.2301e-1	2.2558e1
$Ca(NO_3)_2$*	4.1194	2.9219e-2	-8.5774e-6	-1.6083e1	-2.9576e3
NaCl	3.3689	7.4636e-5	9.3191e-8	7.7993e-2	0
NaCl [6]	3.3864	-9.10e-6	2.118e-7	17.496e-2	-37.278
KCl	3.6303	7.6530e-5	1.2035e-7	7.8969e-2	0
KCl [6]	3.638	-3.428e-5	2.537e-7	19.689e-2	-40.725
* The data for $Ca(NO_3)_2$ was determined from binary data for K,Ca//NO_3 system.					

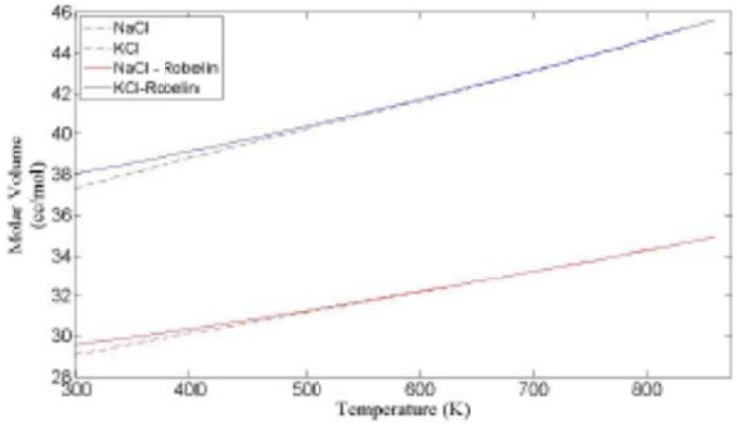

Figure 3.8. Comparison of molar volumes from Matlab script versus literature values for NaCl and KCl [6].

The density of the $Ca(NO_3)_2$ system has not been determined experimentally due to the decomposition of the solid at a temperature of 400°C which is below the melting point of the solid, 561°C. In order to approximate the density of the $Ca(NO_3)_2$ salt, Equation 3.8 was used with the binary density data for the K,Ca//NO_3 system to determine the molar volume for $Ca(NO_3)_2$.

The excess parameters for the volumes of the six binary systems Li,Na,K,Ca//NO_3 were computed as described in Equation 3.61. The excess parameters model the deviation in the binary volumes from the ideal combination of the unary volumes weighted by mole fractions. The values for the excess parameters of these binary systems is listed in Table 3.4.

Table 3.5. The excess parameters for determining the volume of salt mixtures based off of experimental density data.

Salt System	ΔG_{AB}^{P}
Li,Na//NO_3	0.035
Li,K//NO_3	-0.0785 – 0.417 X_{LiLi} + 0.767 X_{KK}
Li,Ca//NO_3	---
Na,K//NO_3	-0.0054
Na,Ca//NO_3	-0.0047
K,Ca//NO_3	0.0002

From examination of Table 3.5 , it can be seen that the deviation from ideal mixing for the mixtures of these binary salt mixtures is small. Thus comparison to the findings at ORNL in the 1950's shows that the density of these salt mixtures is accurately approximated by weighting the molar volumes of the individual components of the mixture by their mole fraction and summing. For a more complete table of excess values for binary salt systems see Appendix A.

Figure 3.9 compares the computed density using the fitted parameters for the binary systems compared to the experimentally determined density of the binary systems computed at 350°C. No experimental data was found for the Li,Ca//NO_3 system and was assumed to behave ideally.

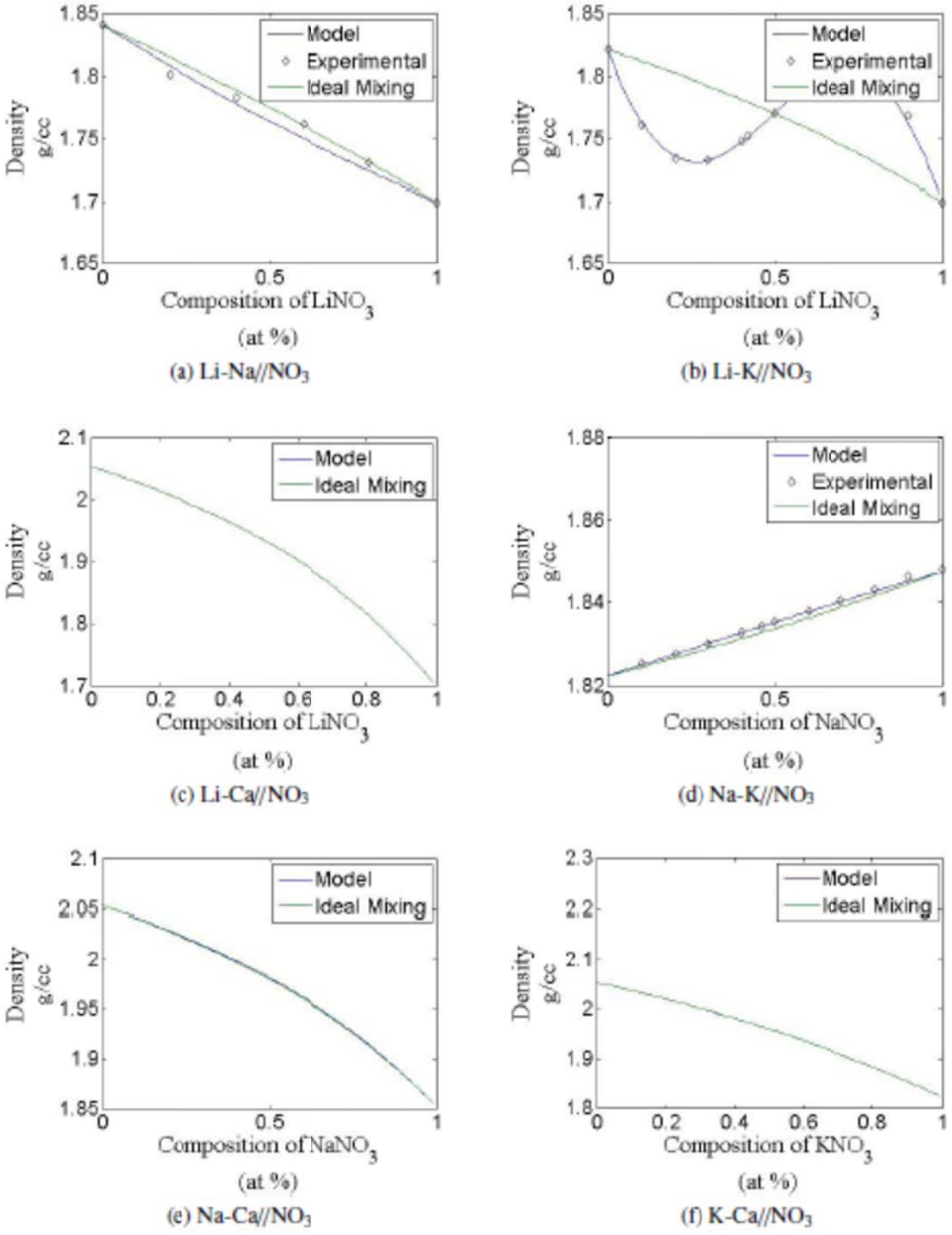

Figure 3.9. Comparison of the density from the MQCM for the binary systems in the quaternary Li,Na,K,Ca//NO_3 salt at 400°C.

Density data for the eutectic composition of Li,Na,K//NO_3 has been found in literature [7]. The comparison of the model density versus the experimental data is shown in Figure 3.10 . The model deviates by ~ 1% over the temperature range of the salt.

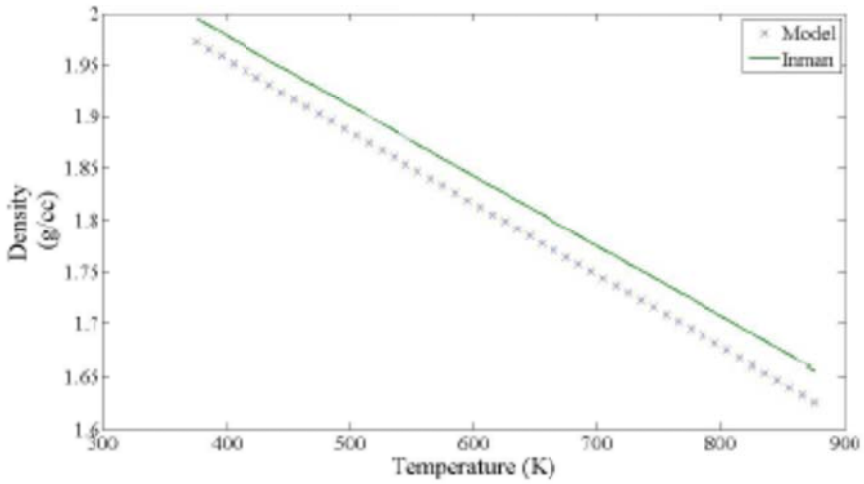

Figure 3.10. The density of the ternary Li,Na,K//NO_3 salt system was predicted using the quasi-chemical density model and deviates by 1% from the equation listed by Inman [7].

Recent work at Sandia National Laboratory measured the density of four different quaternary salt mixtures of the Li,Na,K,Ca//NO_3 system [1]. The experimental data from the report was taken and compared to the QC Density model for the four different quaternary systems Table 3.6.

Table 3.6. The composition of the four quaternary systems and the equation for the density [1]

Salt Name	$LiNO_3$	$NaNO_3$	KNO_3	$Ca(NO_3)_2$	Density (g/cm^3)
A	25	15	45	15	$2.1697 - 8.222 \times 10^{-4}$ T(°C)
B	30	20	38	30	$2.1295 - 7.416 \times 10^{-4}$ T(°C)
C	29	18	45	8	$2.1206 - 7.375 \times 10^{-4}$ T(°C)
D	26	23	46	5	$2.1102 - 7.330 \times 10^{-4}$ T(°C)

The results for the four different quaternary systems listed in Table 3.6 are compared in Figure 3.11. The maximum deviation from experimental values and model is 1.5% for the quaternary system labled A.

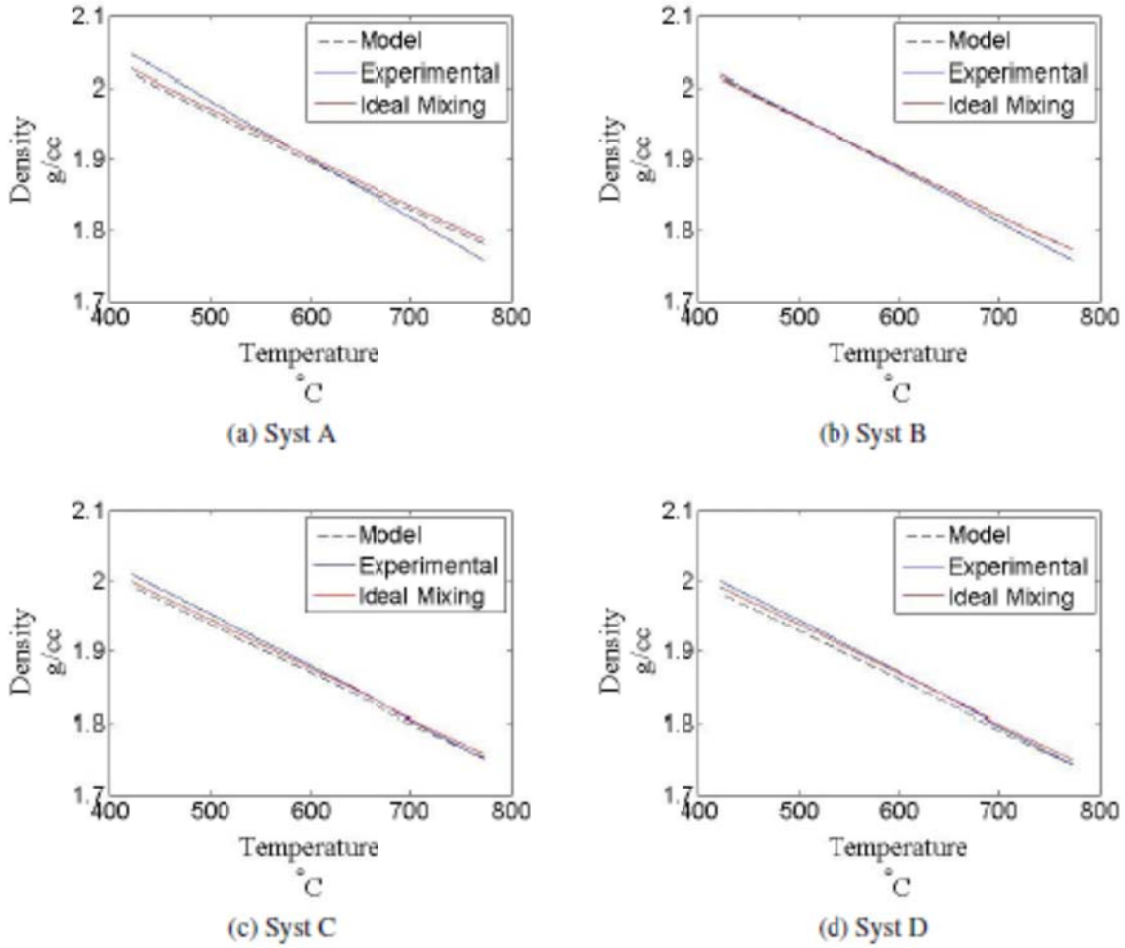

Figure 3.11. Comparison of the density from the MQCM for four different compositions from the quaternary Li,Na,K,Ca//NO_3 salt compared to experimental data obtained at SNL.

3.10 Viscosity

Transport properties of salt mixtures, viscosity and thermal conductivity, are more complicated to predict due to the nature of the properties. However, two models are proposed to model the viscosity using quasi-chemical principles. These models have been found in literature that have been proposed to model viscosity of molten slag systems [32] and molten salt systems [31]. Both viscosity models utilize viscosity equations that are based off of Eyring's kinetic rate theory and have an Arrhenius type form for predicting viscosity, see Equation 3.20.

The first viscosity model was developed for use in predicting the viscosity of molten oxide slags [32] and is given by the following:

$$\mu = \frac{2RT}{\Delta E_v}\frac{(2\pi m_{SU} kT)^{1/2}}{v_{SU}^{2/3}}\exp\left(\frac{E_A}{RT}\right) \tag{3.64}$$

In this model, two terms, ΔE_v and E_A are modeled using a linear expansion based off of the pair fractions of the system. Two other terms, m_{SU} and v_{SU}, the mass and volume of a standard unit,

respectively, are both determined from the site fractions at a given composition, but are not directly fitted to experimental viscosity data.

The terms m_{SU} and ν_{SU} are determined by calculation of the volume and mass of a standard unit. A standard unit is based off of one mole of anion. For the following nearest neighbor systems: K-Cl-Mg, Mg-Cl-Mg, and K-Cl-K, the standard units would be $K_{0.5}Mg_{0.25}Cl$, $Mg_{0.5}Cl$, and KCl, respectively. The m_{SU} is then computed for the given standard units. For the ν_{SU}, it is assumed that the standard unit can be treated as a hard sphere and the volume is calculated from the ionic radius.

The second viscosity model that has been used to model NaCl-KCl-$MgCl_2$-$CaCl_2$ salts uses a slightly different form of Eyring's equation. This viscosity model is given by:

$$\mu = \frac{hN_A}{V_M}\exp\left(\frac{G^*}{RT}\right) \tag{3.65}$$

where, G^* is modeled as a linear expansion

$$G^* = X_{AA}G^*_{AA} + X_{BB}G^*_{BB} + X_{AB}G^*_{AB} + \ldots \tag{3.66}$$

G^*_{AA}, G^*_{BB}, etc... is fit to the unary data and modeled as a linear function w.r.t. temperature:

$$G^*_{AA} = c_{AA} + d_{AA}T_{AA} \tag{3.67}$$

The viscosity data for the binary systems is then used to calculate the values for the G^*_{AB} terms.

The same methodology is employed to determine the viscosity of the salt mixtures as was used in modeling the density and phase diagram. The unary systems were fit to the model first, followed by the binary systems. Once these systems are determined, the viscosity of the binary, ternary, and higher order systems can be determined by using the knowledge of the SRO of the liquid phase that is determined from phase diagram optimization utilizing the MQCM.

The viscosity of the binary and ternary systems have been modeled and compared to experimental values for the different systems. Two models have been used to predict the viscosity based on the quasi-chemical approach, see Equations 3.64 and 3.65. The experimental viscosity data for the unary and binary systems are reported in Refs. [24, 25].

The two different viscosity models have different parameters that need to be determined. The parameters for the viscosity models are listed in Tables 3.7 and 3.8. For Equation 3.64, the volume of the standard unit was determined by using the ionic radius data tabulated by Shannon [66]. For the ionic radius of the nitrate ion, the value of 4.37×10^{-10} m [67]. The volume and mass of the standard units for the nitrate system are presented in Table 3.7.

Table 3.7. The optimized parameters for the mass and volume of the standard unit for Eq 3.64.

Salt	v_{SU} x 10^{29} m^3	m_{SU} x 10^{26} kg
$LiNO_3$	56.55	11.45
$NaNO_3$	65.59	14.11
KNO_3	79.63	16.79
$Ca(NO_3)_2$	48.38	13.62
$LiNaNO_3$	60.96	12.78
$LiKNO_3$	67.44	14.12
$LiCaNO_3$	52.36	12.54
$NaKNO_3$	72.39	21.91
$NaCaNO_3$	56.55	13.87
$KCaNO_3$	85.81	24.58

As has been mentioned in Section 3.9, that no experimental data exists for liquid $Ca(NO_3)_2$. The viscosity of $Ca(NO_3)_2$ was approximated by using the model proposed by Robelin and solving for the viscosity of $Ca(NO_3)_2$ simultaneously with the data for the KNO_3-$Ca(NO_3)_2$ system. The viscosity was then fit to the normal Arrhenius type equation for the other salt systems. The viscosity for the $Ca(NO_3)_2$ system was approximated as

$$\mu = 2.3x10^{-7} \exp\left(\frac{61255}{RT}\right) \tag{3.68}$$

for the temperature range 500-600 K. This viscosity is not realistic since Ca(NO3)2 is solid, but allows for an approximation of the binary systems.

Table 3.8. The optimized parameters for the two viscosity models.

Salt	$\ln(\Delta E_\upsilon)$	E_A	G^*
$LiNO_3$	2.40	23,630	17,410 + 19.7 T(K)
$NaNO_3$	2.40	24,980	15,520 + 21.3 T(K)
KNO_3	2.42	26,780	17,240 + 21.3 T(K)
$Ca(NO_3)_2$	3.12	82,830	60,460 - 62.7 T(K)
$LiNaNO_3$	2.35	22,150	14,900 + 22.4 T(K)
$LiKNO_3$	2.39	23,780	15,180 + 22.5 T(K)
$LiCaNO_3$	3.38 - 7.61 X_{CaCa}	93,430 - 402,900 X_{CaCa}	-116,600 + 315 T(K)
$NaKNO_3$	2.40	24,322	15,690 + 21.4 T(K)
$NaCaNO_3$	2.80 - 4.82 X_{CaCa}	54,212 - 239,600 X_{CaCa}	-111,200 + 234 T(K)
$KCaNO_3$	2.53 + 0.17 X_{CaCa}	35,930 + 29,510 X_{CaCa}	32,470 + 18.0 T(K)

To show how the models compare to the experimental data for the binary systems the comparison of the viscosity at 350°C is presented in Figure 3.12. The binary systems containing $Ca(NO_3)_2$ contain considerable deviations in with current approximations in the model. Regions in the $Ca(NO_3)_2$ systems with < 30% $Ca(NO_3)_2$ are matched to within ±10% with the viscosity model developed by Jak [32].

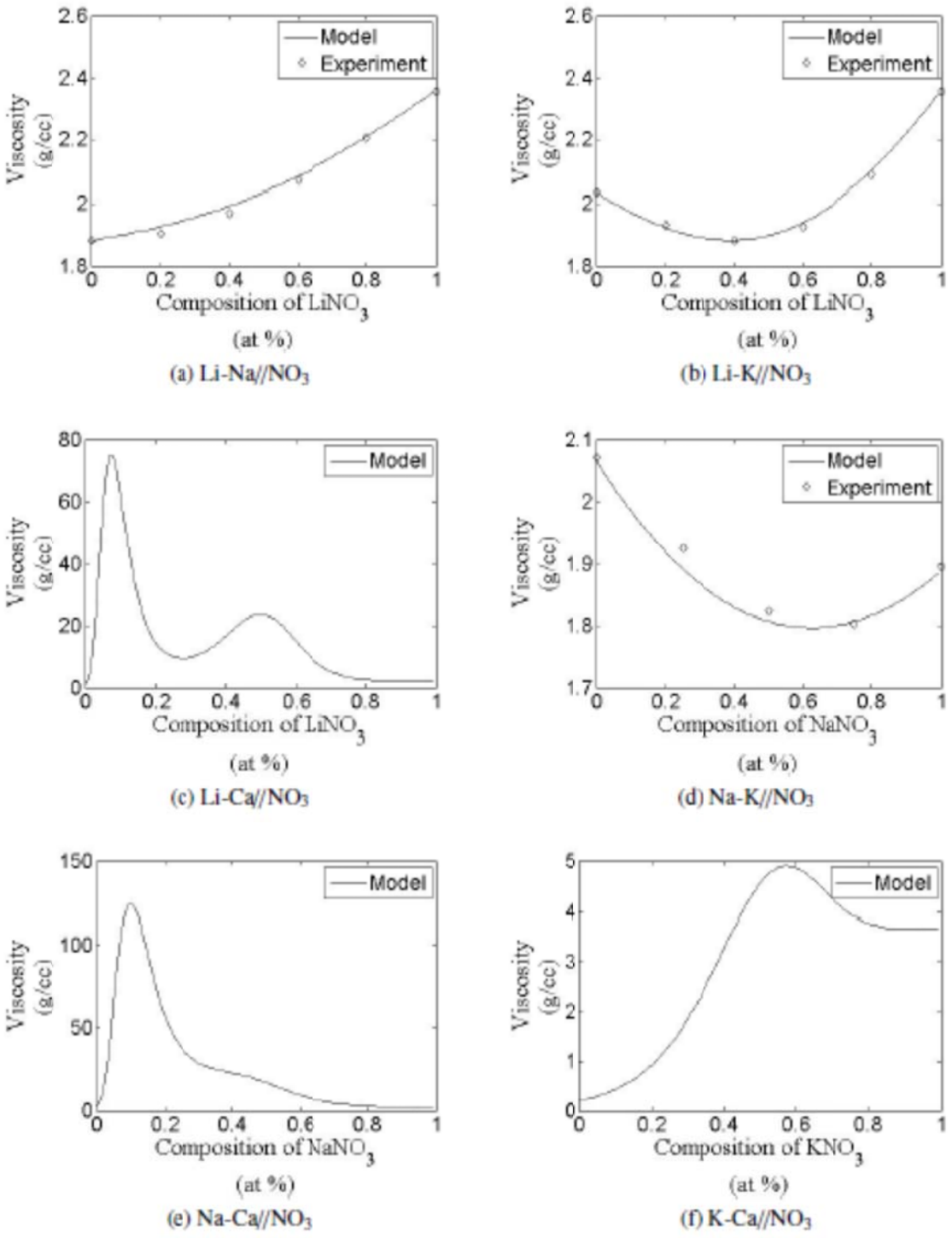

Figure 3.12. Comparison of the viscosity from the MQCM for the binary systems in the quaternary Li,Na,K,Ca//NO_3 salt at 400°C.

The viscosity of the eutectic composition of the ternary system, Li,Na,K//NO_3 has been modeled and compared to experimental values [8]. The data for the binary systems was used along with the site fractions for the eutectic composition and the viscosity modeled, Figure 3.13.

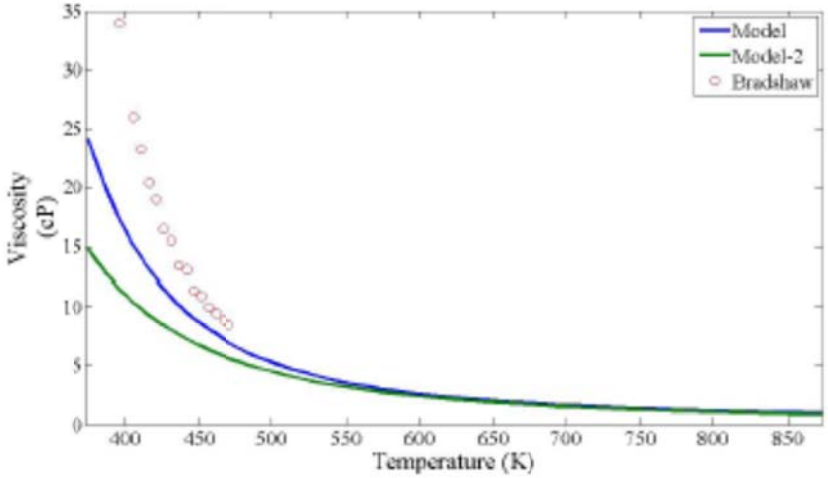

Figure 3.13. The viscosity of the ternary eutectic of LiNaK has been modeled and compared to experimental data for the system [8].

The viscosity of the model is 50% lower than experimental values at the melting point of the eutectic and decreases to 20% at 200°C. As the temperature of the melt increases, it is expected that the viscosity for the ternary system and model to converge to the same values. The reason for this deviation at low temperatures is due to the extrapolation of the viscosity data from temperatures of 400-600°C where the binary salts are liquid.

3.11 Adiabatic Compressibility

The modeling of adiabatic compressibility of the fluid is desired to help with the determination of the thermal conductivity of the liquid salt as discussed in Section 3.2.7. Several different relationships have been proposed to relate the thermal conductivity of a fluid to its adiabatic compressibility [38 - 40]. If it is possible to model the compressibility of a salt mixture, the thermal conductivity of that fluid should also be able to be modeled from the determination of the compressibility.

The adiabatic and isothermal compressibility of a substance are functions of thermodynamic properties. Since the isothermal compressibility of a substance is very similar to the relationship for the molar volume of a substance, both are derivatives of the Gibbs energy [Equations 3.57 and 3.18], a similar approach was taken to model the compressibility of a fluid as was outlined in Section 3.9 for the density model.

In current modeling efforts, it was assumed that the adiabatic compressibility and isothermal compressibility are offset by a constant value. Then the adiabatic compressibility and isothermal compressibility are assumed to behave similarly.

Speed of sound data for unary salts was used in Equation 3.15 to obtain the adiabatic compressibility of the fluid as a function of temperature.

$$\kappa(T) = \kappa(T_{Ref})\exp\left(\int_{T_{Ref}}^{T}\chi(T)dT\right) \quad (3.69)$$

This adiabatic compressibility is then fit to a linear expansion in a similar fashion to Equation 3.60.

$$\chi(T) = \chi_0 + \chi_1 T + \chi_2 T^{=1} + \chi_3 T^{=2} \quad (3.70)$$

The deviation in the adiabatic compressibility of the fluid from ideal mixing was then computed for the binary systems based off of the deviation from ideal mixing.

$$\kappa_{AB}(T) = n_A\kappa_A(T) + n_B\kappa_B(T) + \frac{n_{AB}}{2}\left(\frac{\partial^2 G^P_{AB}}{\partial P^2}\right)_{T,n,\ldots} \quad (3.71)$$

where the following additional terms are added to ΔG^P_{AB} to account for the second order derivative:

$$\Delta G^P_{AB} = \delta(P-1)^2 + \delta_0 X_{AA}(P-1)^2\delta_1 X_{BB}(P-1)^2 \quad (3.72)$$

Using this approach the models accurately reproduce the isothermal compressibility (speed of sound) data from binary experiments.

The adiabatic compressibility of the Li,Na//NO_3 and Na,K//NO_3 systems was modeled in this approach. The fit to the experimental data is seen in Figure 3.14. To extend this approach to the ternary system, the deviation from ideal mixing for the Li,K//NO_3 system was assumed to be the same as the Li,Na//NO_3 system. The speed of sound from the ternary salt (Li,Na,K//NO_3) was then compared to speed of sound data taken at the University of Wisconsin, Figure 3.15. The experimental data used for comparison in Figure 3.15 obtained by the ultra-sonic flowmeters contains a large amount of uncertainty.

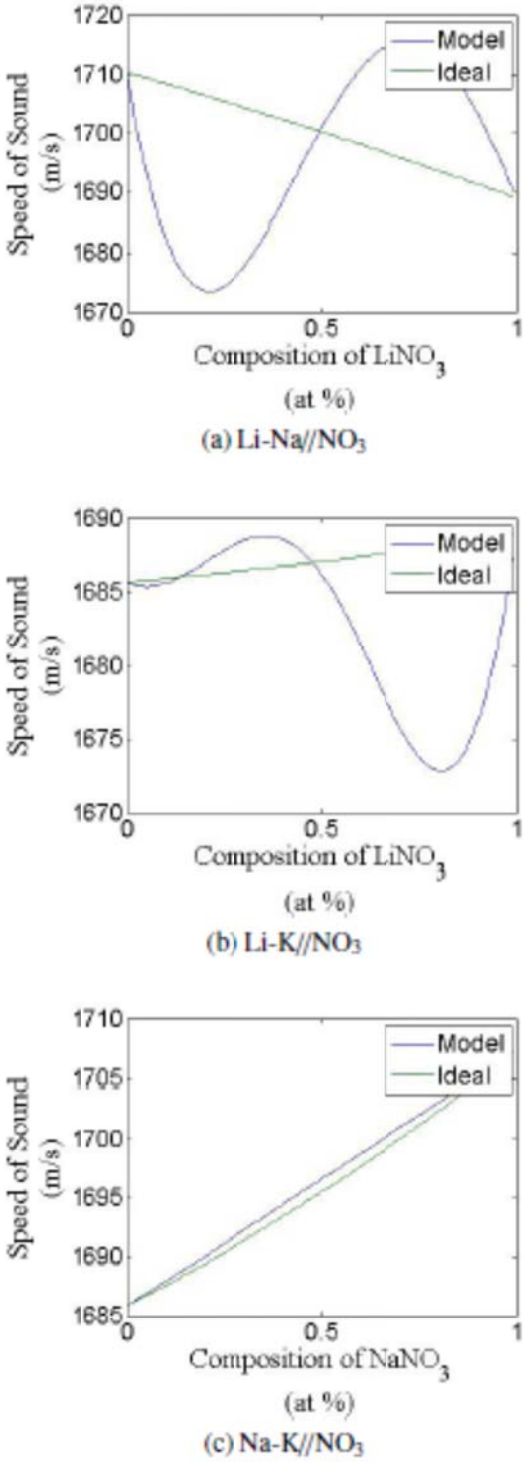

Figure 3.14. Speed of sound for the binary mixtures of Li,Na,K//NO3 extrapolated using the model to 400^{o}C.

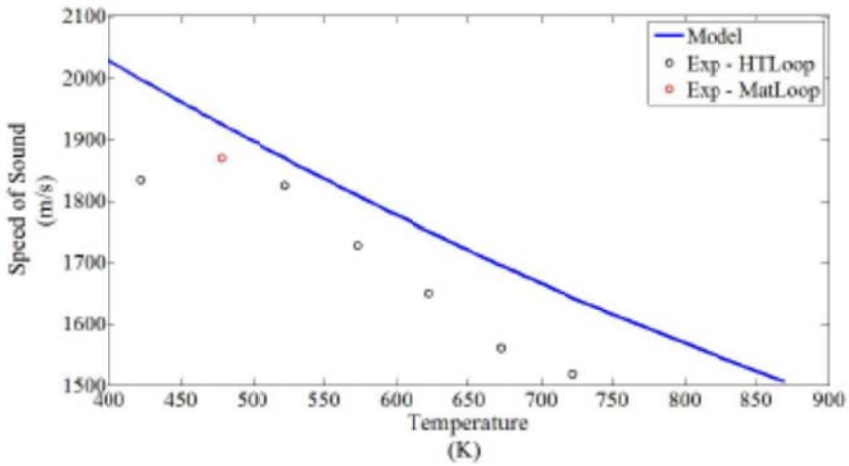

Figure 3.15. The speed of sound of the Li,Na,K//NO_3 eutectic compared to experimental values obtained by ultra-sonic flowmeters.

3.14 Thermal Conductivity

From the previous models, there are quasi-chemical predictive models for the molar volume V_M, viscosity μ, and adiabatic compressibility β_S of salt mixtures. Optimization of Equation 3.24 to model the thermal conductivity of molten salts relies on fitting the coefficient γ to best reproduce experimental data.

The γ term in Equation 3.24 was fit to the unary salts and expanded in a similar manner to the volume and adiabatic compressibility model

$$\ln\gamma = \gamma_0 + \gamma_1\left(T - T_{\text{Ref}}\right) + \gamma_2\left(T^2 - T_{\text{Ref}}^2\right) + \gamma_3 \ln\left(T - T_{\text{Ref}}\right) + \gamma_4\left(\frac{1}{T} - \frac{1}{T_{\text{Ref}}}\right) \tag{3.73}$$

The model then fits the deviation in the thermal conductivity from ideal mixing as a function of the site fractions of the salt system:

$$k_{Mix} = n_A k_A + n_B k_B + 1.5 X_{AB}\left(\varsigma_0 + \varsigma_1 T + \varsigma_2 X_{AA} + \varsigma_3 X_{BB}\right) \tag{3.74}$$

The experimental values for the thermal conductivity of the binary systems were used to fit the parameters of the thermal conductivity model. The values that were obtained for the binary systems of Li,Na,K//NO_3 are shown in Figure 3.16. No experimental values were found for the Li,K//NO_3 system and the values for the Li,Na//NO_3 system was between 530 and 570 K.

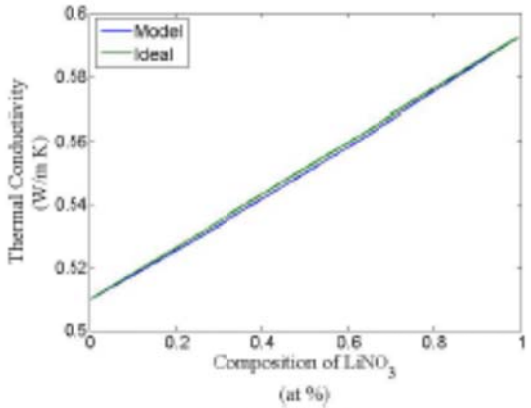

(a) Li-Na//NO_3

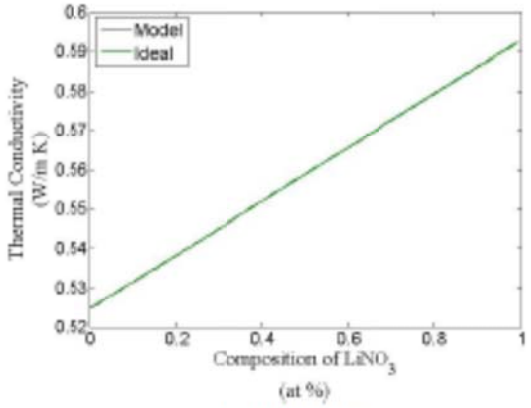

(b) Li-K//NO_3

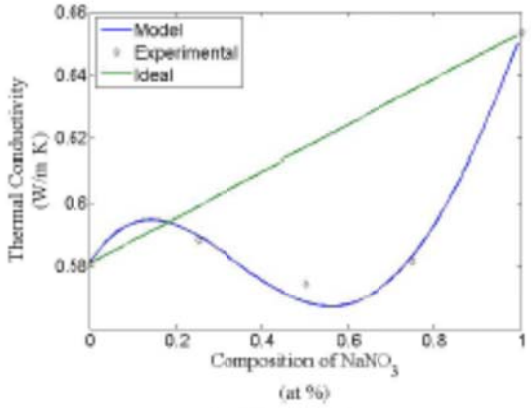

(c) Na-K//NO_3

Figure 3.16. Comparison of the thermal conductivity for the binary mixtures of Li,Na,K//NO_3 at 400^{o}C.

There is no experimental data in literature that has measured the thermal conductivity of any of these ternary and quaternary salt mixtures. The predicted thermal conductivity values for the ternary systems have no experimental data available for comparison against the model. The ideal

value of the thermal conductivity Li,Na,K//NO_3 ternary eutectic based on molar weighted average is compared to the model, Figure 3.17.

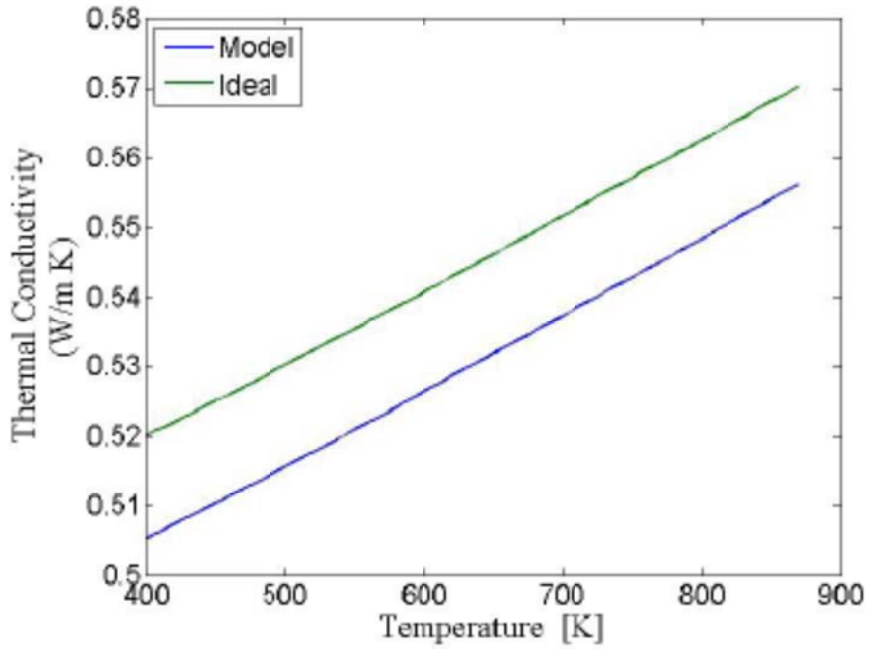

Figure 3.17. Thermal conductivity of the eutectic composition of the LiNaK//NO_3 ternary salt is estimated from the thermal conductivity model and ideal mixing laws.

3.14 Application of Models for Salt Selection

Parabolic trough systems (PTS) pump a fluid through a tube located along the axis of a concentrating solar mirror. Andasol and Nevada Solar One are power plants that operate on this design [68 - 69]. These plants use heat transfer oils for absorbing and transferring the solar energy to produce steam. Andasol also utilizes a molten salt ($NaNO_3$-KNO_3 60-40 wt%) for storage of the solar power for power generation when the sun rays are not present or as strong for up to 6 hours [68]. It would be beneficial to use a molten salt that could both store the energy and transfer the heat. The application of molten salts in these systems is beneficial in that the same fluid used in the parabolic trough system is used for solar storage. Molten salts also allow for higher outlet temperatures from the solar field. Higher temperatures result in higher thermal efficiency for the plant system.

Now that the ability exists for prediction of salt properties, the models are applied to demonstrate the process for selection of a salt for use in a solar plant using parabolic trough system. For example, what if the Nevada Solar One plant is converted to molten salt coolants. Nevada Solar one contains 18,420 4 meter long solar absorption tubes with a output of 64 MW [69 - 70]. Lets assume the only hard criteria for use of a molten salt in the PTS is that the melting temperature is less than 150^{o}C. Some other parameters used in the assumption for the PTS are listed in Table 3.9.

Table 3.9. Parameters used in the evaluation of molten salts for the parabolic trough system.

T_M	150°C
Power	64 MW
ΔT	300 K
Length	73,680 m
Diameter	70 mm
# of sections	10
$T_{Ave,Salt}$	400°C

The four ternary salt systems of the Li,Na,K,Ca//NO_3 systems were examined to determine what compositions meet the melting temperature requirement. Three of the four ternary systems (Li-Na-K, Li-K-Ca, and Na-K-Ca) have compositions with melting points less than 150°C. For simplicity the eutectic composition from these ternary systems are compared. The thermo-physical properties were determined at the average temperature of the fluid (400°C). Three criteria were used in selection of the salt for this purpose, the volumetric heat capacity (thermal storage), pumping power, and cost of the salt mixture. The results from these calculations are presented in Table 3.10.

Table 3.10. Comparison of different nitrate salts for use in PTS.

Salt	Li,Na,K//NO_3	Li,K,Ca//NO_3	Na,K,Ca//NO_3
	(0.38, 0.14, 0.48 at %)	(0.32, 0.59, 0.09 at %)	(0.17, 0.47, 0.36 at %)
T_M (°C)	120	117	133
Cost ($/kg)	18.90	16.10	4.80
ρ (kg/m^3)	1770	1800	1932
C_P (J/kg K)	1424	1332	1581
ρC_P (kJ/m^3 K)	2520	2400	3050
μ (Pa-s)	0.0019	0.0022	0.0069
Reynolds	147,300	132,400	35,700
Pumping Power (kW)	61.6	74.6	53.8

From examination of Table 3.10, the Na,K,Ca//NO3 ternary eutectic has the lowest pumping cost, highest volumetric heat capacity, and lowest cost. The eutectic composition of Na,K,Ca//NO_3 should be examined for use in the PTS systems under the criteria outlined here. Other conditions, such as decomposition temperature and operating conditions may also need to be examined before a final salt is selected. Thermal conductivity of the $Ca(NO_3)_2$ salts are not known. In this analysis, it was assumed that the heat transfer of the fluids are all close enough in forced convection to neglect the effect of the thermal conductivity.

3.14 Summary

Multi-component salt mixtures reduce the melting point of salt systems. The lowering of the melting point, while maintaining the high temperature stability of a salt is a major focus for many different research areas. However, not much is known about the physical properties of most ternary and higher order systems. Methodology and models to predict the thermo-physical properties of salt systems has been developed based on a quasi-chemical approach to allow for an initial screening of these higher order systems. This screening allows for reduction in the amount

of initial screening experiments necessary to select a salt system. These models have been extended to estimate adiabatic compressibility and thermal conductivity of molten salt systems.

The current approach of using a quasi-chemical approach to fit the excess thermo-physical properties of binary salt systems was shown to accurately predict experimental data for ternary and quaternary systems in the Li,Na,K,Ca//NO3 systems. These models can be applied to other anion based salt systems. To show how this approach could be utilized in the selection of a salt system for a desired application, the nitrate salt systems were examined as a potential fluid for solar parabolic trough systems. Of the ternary mixtures compared, the Na,K,Ca//NO3 salt system appears most promising as a heat transfer fluid based on cost of salt, pumping power requirements, and volumetric thermal storage of the salt mixture.

These salt properties are essential knowledge in design and operation of processes that utilize molten salts. This importance can be seen in the early work looking at the heat transfer of FLiNaK salt. Initial experiments found that the heat transfer coefficient was 50% less than the expected values using the Chilton-Colborn correlation, Equation 5.16. Later experiments found that the value for the thermal conductivity used in the analysis of the heat transfer experiments was off by almost a factor of 8. When correct values were used in the data analysis, the heat transfer coefficient was within agreement of the heat transfer correlations [71].

These quasi-chemical models are limited by the accuracy of the experimental data for the unary and binary salt systems to fit the initial parameters. Missing or erroneous data leads to higher uncertainty in the estimated values obtained from these models.

Static Corrosion in KCl-$MgCl_2$

Knowledge of the chemical properties of the salt, mainly corrosion of the container materials, are also necessary in selection of a molten salt for an application. In the corrosion of the alloy, it is important to understand the corrosion rate and mode of attack of the molten salt to the container material. These parameters are necessary inputs to ensure the equipment is designed to have the expected service lifetime.

The importance in understanding the chemistry of the corrosion process and the mode of attack of the salt to the alloy is a major research area involved with the application of molten salts. Large scale testing has greatly increased the understanding of why molten salts are corrosive, how they attack the metals, and ways to increase the corrosion resistance of alloys in these fluids. In this chapter, a review of corrosion in molten salts followed by experiments to investigate methods to prepare KCl-$MgCl_2$ and the corrosion of KCl-$MgCl_2$ on different alloys is presented. A general review of the corrosion process of salts to metal alloys will be discussed in Section 4.1 - 4.5. The following sections discuss preparation of KCl-$MgCl_2$ salt (Section 4.6), corrosion of alloys in KCl-$MgCl_2$ (Section 4.7), and attempts to mitigate the corrosion of two alloys (Sections 4.10.10 & 4.11.2).

4.1 Corrosion in Molten Salts

Corrosion of metals by chloride and fluoride salts is different from corrosion in most other media, including nitrate and carbonate liquid salts. Nitrate and carbonate salts form oxide layers on the surface of the alloys, due to the oxygen that is contained in the anion species. Research involved with corrosion of materials in these salts is to find an alloy that forms a passivating oxide layer to limit the rate of corrosion, or determine what impurities in the initial salt melt will cause failure of the oxide layer (e.g. Cl ions). Thus corrosion in molten nitrate and carbonate salts is very similar to other oxide forming liquids, including water, carbon dioxide, and air. Research on corrosion of materials in these salts is finding the cheapest alloy that will still maintain structural integrity at the operating conditions of interest. Since nitrates and carbonates are not of interest in this study, they will not be discussed further. Chloride and fluoride salts are not known to form passivating oxide layers to limit the rate of corrosion of the alloys. Fluoride salts are good oxide fluxes and remove any oxide originally on the metal surface. Chloride salts are different in that oxides are thermodynamically stable, but do not form a passivating layer to limit the corrosion of the alloy. The normal corrosion product is these salts are metal salts, i.e. CrF_2 or $CrCl_2$, and not metal oxides. These corrosion products do not form passivating layers on the surface, but are readily soluble in the liquid salt leaving the base alloy open for further attack.

Corrosion of metals by fluoride salts has been studied by researchers at ORNL and in Russia as part of research programs for molten salt reactor systems [72 - 75]. The corrosion of alloys in chloride salts has also been studied by many different investigators. In particular, Littlewood studied the thermodynamic driving force for corrosion of metal alloys in molten salts in the 1960's [76 - 78]. Other experiments have also been conducted by others to measure the electrochemical potential at which reduction occurs for many elements in different chloride mixtures at different temperatures [79, 80]. Investigations have also looked at how changing salt baths and cover gas

over these baths change the corrosion rate of pure Fe and Zr [81]. In addition, several different engineering studies on the corrosion of liquid chloride salts have been performed by screening multiple alloys in chloride salt baths. Of particular interest, is a study at Brookhaven National Laboratory (BNL) in the 1950's as part of the Liquid Metal Reactor Experiment (LMR). NaCl-KCl-$MgCl_2$ was to be used in reprocessing of the liquid metal fuel (Bi + U + fission products). In conjunction with this, a large number of corrosion tests were studied examining the corrosion of different alloys in contact with LiCl-KCl, NaCl-KCl-$MgCl_2$, or NaCl-KCl-$MgCl_2$-$BiCl_3$ salt. A more recent investigation by Indacochea examined the corrosion of several alloys in LiCl salts in either reducing or oxidizing environments [82, 83]. Other studies have examined the corrosion of alloys and ceramics exposed to chloride salts [84 - 86]. In addition, there are several bibliographies that summarize the action of molten salts on the corrosion of alloys available in literature [24, 25, 87, 88].

Since fluoride salt corrosion is similar to chloride salt corrosion, a differentiation between the two salt systems will only be mentioned when they differ significantly. As part of an earlier thesis at the University of Wisconsin, a review of corrosion in FLiNaK salt was reviewed and experiments to study the corrosion were completed [89].

4.2 Thermodynamics of Corrosion

Corrosion of metals in most media occur due to electrochemical reactions that take place in the system. An electrochemical process simply means that electrons are transferred during the reaction(s) that cause the corrosion. These chemical reaction(s) can be broken down into two separate reactions, the oxidation and reduction reactions. Often times, the overall reaction is called the RedOx reactions, implying that both reduction and oxidation occur in the system.

For example, a general corrosion process consisting of two metal atoms M and N:

$$M + \frac{m}{n} N^{n+} \quad = \quad M^{m+} + \frac{m}{n} N \tag{4.1}$$

Then Equation 4.1 can be separated into two half reactions: the oxidation and reduction reactions:

$$M \quad = \quad M^{m+} + me^{-} \tag{4.2}$$

$$N^{n+} + ne^{-} \quad = \quad N \tag{4.3}$$

$$M + \frac{m}{n} N^{n+} \quad = \quad M^{m+} + \frac{m}{n} N \tag{4.4}$$

where M is being oxidized (gives electrons), and N is being reduced (accepts electrons). The direction of Reaction 4.1 is determined by looking at the thermodynamic potential of each half cell reaction. The thermodynamic potential of each half cell reaction is usually listed as a reduction potential and is tabulated for standard state conditions. That is the potential that is given is the potential for the reduction reaction at a standard reference state. The potential for Reaction 4.1 is determined by adding the half-cell potentials together, making sure to switch the polarity of the potential for the oxidation reaction. In order for the reaction to be spontaneous, the potential of the reaction must be greater than zero.

This thermodynamic driving force for the reaction is verified by looking at the Gibbs energy of the reaction. The Gibbs energy of formation is related to the potential of the reaction by

$$\Delta G_F = -nFE^o \quad (4.5)$$

Since Gibbs free energy of formation (ΔG_F) is negative for a spontaneous reaction, this confirms that a positive value for E^O results in a thermodynamic potential driving the reaction to the right.

The standard reduction potential of multiple elements has been determined experimentally for many different systems. Table 4.1 lists these potentials for aqueous systems [90] and several molten chloride salt systems [79, 80, 91 - 93]. Although Table 4.1 is useful for standard conditions, rarely do reactions occur under standard conditions when the activity of the species is equal to one. That is the concentration of constituents is usually not equal to a unit molar concentration, or if a gaseous species, have a pressure of one atmosphere. Under these conditions the values in Table 4.1 need to be adjusted for the specific conditions of the environment.

Table 4.1. EMF data for various elements in different liquid media

	Apparent Standard Electrode Potentials				Standard Electrode
	H_2O	NaCl-KCl-$MgCl_2$	KCl-$MgCl_2$	LiCl-KCl	Potential (Calculated)
	V [90]	V [91]	V [80, 92]	V [70. 93]	
System	25°C	475°C	475°C	450°C	
Au(I)/Au(O)	0.140	0.201	0.0431	0.095	--
Cl_2/Cl^-	0.000	0.000	0.000	0.000	0.000
Pt(II)/Pt(O)	-0.160	-0.076	-0.2286	-0.216	-0.284
Pd(II)/Pd(O)	--	-0.281	0.4421	-0.430	-0.472
Ag(I)/Ag(O)	-0.560	-0.756	-0.8088	-0.853	-0.903
Sb(III)/Sb(O)	==	-0.849	-0.8682	-0.886	
Cu(I)/Cu(O)	-0.939	-0.9583	-1.067	-1.030	
Ni(II)/Ni(O)	-1.610	-0.868	-0.9761	-1.011	-1.087
Co(II)/Co(O)		-1.046	-1.1689	-1.207	-1.156
Pb(II)/Pb(O)		-1.247	-1.2868	-1.317	-1.289
Sn(II)/Sn(O)		-1.223	-1.2924	-1.298	-1.333
Fe(II)/Fe(O)	-1.804	-1.259	-1.3452	-1.387	-1.282
Cr(II)/Cr(O)		-1.472	-1.4634	-1.641	-1.553
Cd(II)/Cd(O)		-1.388	-1.5256	-1.532	-1.423
Tl(I)/Tl(O)			-1.5642	-1.586	-1.618
Zn(II)/Zn(O)	-2.123	-1.626	-1.7350	-1.782	-1.616
Mn(II)/Mn(O)	-2.54	-1.870	-2.0166	-2.065	-1.983
Mg(II)/Mg(O)	-3.730	-2.722	-2.7301	-2.796	-2.700

For the general reaction

$$aA + bB = cC + dD \quad (4.6)$$

the relative effects of environment (non-standard state conditions) are accounted for by using the Nernst Equation to account for variations in the activity of the system:

$$E = E^o - \frac{RT}{nF}\ln\left(\frac{a_C a_D}{a_A a_B}\right) \quad (4.7)$$

where $\underline{a_i}$ is referring to the activity of species *i* in the solution. The activity of the species is often assumed to be equal to the molar concentration of the species. Knowledge of the redox reaction and chemical compositions allows for calculation of the Gibbs energy of formation, or potential, for a reaction.

A more general view of the reduction potentials listed in Table 4.1 is to estimate the potential for corrosion based on the reduction potential. The more negative the standard potential of an element, the more this element will be corroded. For example, Cr will corrode more than Fe which will corrode more than Ni in the same salt bath, e.g. LiCl. In addition, it also follows that the lower the redox potential is for the cation of a salt, that salt is less corrosive than a salt with a cation with a higher redox potential, e.g. NaCl will be less corrosive than $MgCl_2$. These rules are general and do vary from salt mixture to salt mixture. This is due to the difficulty in preparing salt melts free from contaminants. This effect is seen when looking at the corrosion of LiCl versus NaCl. It is more difficult to remove water impurities from LiCl than it is NaCl. This increased difficulty in cleaning LiCl leads to an increase in the impurity levels in the salt causing more corrosion of the structural material than NaCl [94, 95].

From Table 4.1 other trends may also be noted: first the standard reduction potential of an atom between like valence states does not change significantly between different media. For example, the Cr atom likes to lose two electrons in the first oxidation state going from Cr → Cr^{2+}. The amount of energy to remove these two electrons is nearly identical. This nearly identical potential is due to the same amount of energy being needed to remove these electrons from the outer electron shell of the Cr atom nearly independent of the media. Second, the different media provide stability of different valence states for each element, mainly transition metals. This allows for differences in corrosion based on which oxidation state is stable in the molten salt. The ability to form different valence states is necessary in some corrosion processes, namely thermal gradient corrosion.

Another way to look at the data from Table 4.1, is to plot the Gibbs free energy of formation as a function of temperature. The resulting figure is called an Ellingham Diagram. This Ellingham Diagram for chloride salts was prepared by looking at the Gibbs energy of formation for each compound per mole of chlorine atom. Gibbs energy of formation as a function of temperature was computed using HSC Chemistry. The Gibbs energy for different metals as a function of temperature is presented in Figure 4.1.

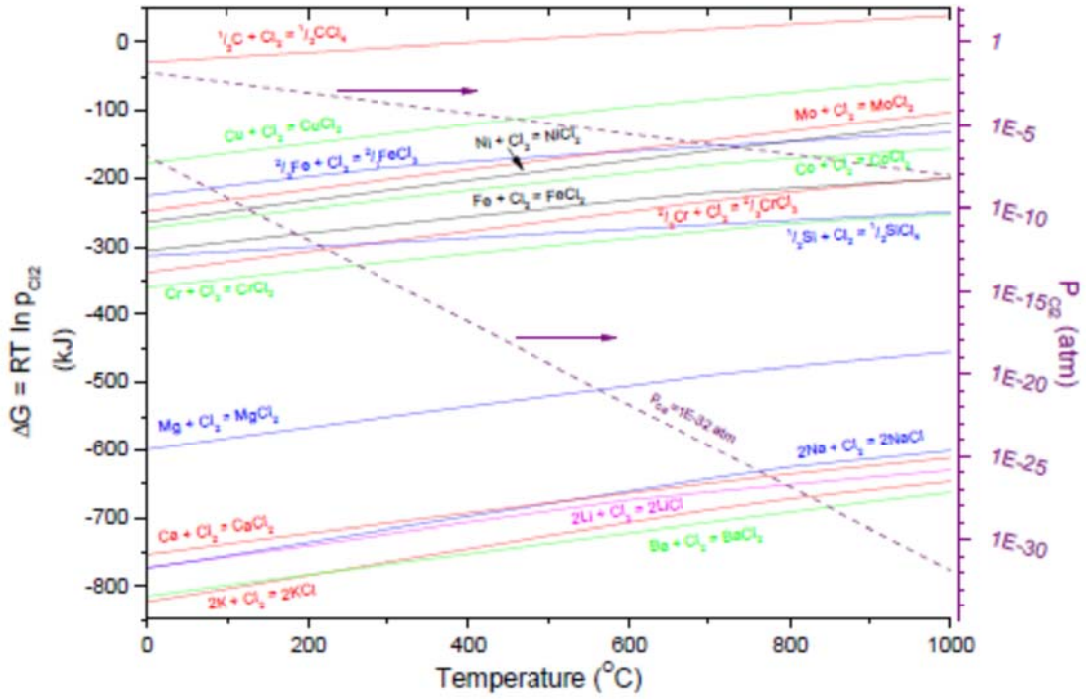

Figure 4.1. Ellingham Diagram for chloride salt systems shows the relative stability of metal chloride compounds.

The Ellingham diagram for the metal/chloride system, Figure 4.1, shows the same trends in stability of salts and metals as was seen from Table 4.1 as is expected based off of Equation 4.5.

From Figure 4.1, it is seen that the salts, alkali-halides and alkaline earth-halides, are more thermodynamically favored than the transition metal chlorides. It is then expected that little corrosion should occur when metals and salts are in contact, since it is thermodynamically unfavorable. The corrosion that occurs in the system must be driven by the impurities in the system. The corrosion process in these molten salts is driven by the amount of impurities that are in the melt, namely O^{2-}, or H^{+} [96 - 98].

However, the corrosion process between fluoride and chloride salts is also different. This difference is due to the relative stabilities of oxide layers in the two salts. In fluoride based salts, the metal fluoride is thermodynamically favored over the metal oxide. In the chloride salts, the oxides are thermodynamically favored, although the ability to form a stable passivating oxide layer on the metal has been proven to be a much more difficult task than oxidizing environments and aqueous solutions [77]. The stability of metal oxides in chloride salts suggests that oxide ceramics are stable in molten chloride salts while the ceramics would corrode in fluoride salts.

4.2.1 Thermodynamic Equilibrium

Corrosion of a metal in a fused salt melt will continue until a thermodynamic equilibrium is established between the metal and the melt. That is until the redox potential of the melt and the metal are equal. The equalization of potentials thus eliminates the thermodynamic driving force for corrosion. At this equilibration of potentials, the metal is said to become "immune" to further corrosion [77].

This ability to acquire immunity of the container metal by the accumulation of corrosion products in the salt melt is often not able to be accomplished in an actual process environment. Multiple sinks often exist for the corrosion products that move the system away from equilibrium resulting in a continuous attack of the metal by the molten salts. Some possible sinks that occur are temperature differentials in the system, formation of gaseous corrosion products, and activity differentials in the system.

Temperature differentials in the system cause a shift of the equilibrium between the metal and the salt. Temperature differentials cause corrosion of the container metal in the hot section and deposit corrosion products in the cold side. This mass transfer of the metal from hot to cold results in continuous attack of the alloy, although at a slower rate than is seen due to initial impurities in the melt [99].

4.2.2 Corrosion of Alloys

Pure metals provide for a good understanding of the corrosion process, but are seldom used as structural materials. Alloys of many different metals are used in most engineering applications due to more desirable physical and mechanical properties of the alloy created by addition of many elements, e.g. tensile strength, creep rupture strength, and corrosion resistance are properties that are improved by alloying. Since alloys are of the most interest in the design of equipment, the corrosion characteristics of these alloys also must be known. Corrosion research in molten salts has been studied by many different investigators. A wide range of research on molten salts has been done to study corrosion of salts used in heat transfer baths. In addition, a large amount of corrosion research has been done at ORNL with fluoride salts. Since the corrosion mechanisms are similar, this data will also be mentioned.

From the discussion of corrosion in molten salts, Section 4.1, it is known that the more active metals are more likely to be corroded. The metal corrosion products formed, i.e. $CrCl_2$ or CrF_2, are soluble in the salt melt and are removed from the alloy. The fact that the products are highly soluble prevents the formation of a passive layer on the surface of the alloy to limit the rate of corrosion of the metal. This is extremely different than corrosion in aqueous solutions. The goal of corrosion prevention in aqueous solutions, or high temperature oxidative environments is to find an element that will oxidize and create a passive layer that reduces the rate of corrosion. The main example of this is Cr which is added to high temperature metals to produce an oxide layer that passivates the surface, reducing corrosion of the base material. This passivation also occurs by additions of Al and Ti. Al and Ti form a thin, highly passivating oxide surface on the metal. This passive layer allows for alloys with these active metals to be used in many high temperature

applications. Many high temperature alloys contain approximately 20% of Cr to form a passive oxide layer during use at elevated temperatures.

Some of the first corrosion work in chloride salts occurred as part of a study to determine the best material to contain salts for use in heat treatment baths. This work examined the corrosion of different Fe-Cr-Ni alloys in four different compositions of baths containing two or more of these elements NaCl-KCl-$CaCl_2$-$BaCl_2$ [100]. It was determined that Cr is the most readily attacked element. It was also determined that for alloys with similar chemical compositions, corrosion increased as the concentration of C in the alloy increased. Experimentally it was determined that reduction of C in addition to additions of C getters such as Nb and Ta, reduced the rate of inter granular corrosion in the Fe-Ni-Cr alloys by a factor of 2.

Corrosion research using fluoride based salts was studied at ORNL in in support of the ARE and MSRE programs. Multiple isothermal and natural convection loops were run to examine the corrosion of different metals with different fluoride salt mixtures [73]. The general trend of these corrosion studies was the finding that the more active a metal is, the more that element is leached from the alloy into the salt. This early corrosion work at ORNL showed that high Ni alloys were the best at resisting corrosion to molten halide salts. From Table 4.1 and Figure 4.1, it can be seen that Ni is more noble than Fe and Cr and should have less corrosion than Fe and Cr. In the ARE, Inconel 600 (a nickel based alloy) was used as the material of construction for the ARE. The corrosion of Inconel 600 was still a concern and as part of the ARE project an alloy was developed that has superior corrosion resistance in molten salts, INOR-8 [72]. INOR-8 is better known today as Hastelloy-N and was used in subsequent experiments at ORNL involving molten salt reactors. For a more detailed assembly of some of the corrosion work at ORNL during the ARE and MSRE, the reader is referred to these recent reports [9, 20].

At the same time as the ARE work at ORNL, chloride salts were of interest to researchers at BNL as part of the Liquid Metal Fuel Reactor (LMFRE) Experiment. Many different materials, including iron based, nickel based, refractory metals, and some ceramics were tested as part of their research program. These metals were exposed to fused chloride salt mixtures of LiCl-KCl (59-41 at %, T_M = 351°C) and/or NaCl-KCl-$MgCl_2$ (30-20-50 at %, T_M= 396°C) at temperatures of 500°C. It was found that 'little corrosion' occurred due to the NaCl-KCl-$MgCl_2$ salts in most alloys. In chemical analysis of the salt after testing, it was found that the concentration of Ni was much lower than the concentration of Fe and Cr. However the corrosion rate of steels was low such that 347 SS was selected for the structural material. 347 stainless steel has similar compositions of Fe, Ni, and Cr as 316 stainless steel. 347 is alloyed with Nb to act as a C getter, while 316 is alloyed with Mo [14].

From these previous experiments, it was found that the elements in an alloy are preferentially attacked based off of the nobility of the metal. The more active an element is the more it will be corroded and removed from the alloy, thus the ranking for attack is Cr, Fe, and Ni. From these programs, it was also determined that the amount of impurities in the molten salt drive the corrosion process. The effect of impurities in the salt mixture causing corrosion has been shown in many studies [83, 101, 102]. As part of the MSRE and LMFRE, methods for preparing and handling of molten salts was taken to ensure that a 'clean' salt was to be used in the experiments.

4.2.3. Corrosion of Ceramics

Studies of the corrosion of ceramic materials has also been investigated for use with Cl salts. Metal oxides are thermodynamically stable compared to the metal chlorides. This makes the oxide ceramics stable in these systems. In the studies at BNL, it was found that the ceramic, Al_2O_3, showed good corrosion resistance in the chloride salts [14]. A wider range of experiments investigating the effect of chloride salts on ceramics has been conducted [84]. The corrosion rate of Al_2O_3 and other ceramics was found to be low (< 0.03 mm/yr) in NaCl-KCl at 750°C.

4.3. Rate Limiting Steps

Thermodynamics is useful in determining the equilibrium state of the system, however it does not give any information regarding the kinetics of the corrosion process. The kinetics of the reaction determine the rate at which the process will occur. This rate is important in the corrosion process as it determines if the lifetime of the designed system will be sufficient for the desired application.

The kinetics of chemical processes (of which corrosion is one) is often limited by one step in the process. This rate limiting step is either beneficial, or detrimental, depending on the process of interest. In corrosion, it is desired to limit the corrosion and thus have a limiting step that reduces the corrosion to a negligible value. The passivation of alloys in oxidizing atmospheres is one such condition.

The corrosion process of the metal by the salt consists of several different steps. First, the atoms being reduced and oxidized need to diffuse to the salt-metal interface. Second the electrons need to be transferred from the oxidizer to the metal atom. Next the halide ions diffuse from the reduced species to the oxidized species. Finally, the corrosion product must diffuse from the surface to the bulk of the fluid. From earlier studies on the corrosion of Hastelloy-N, it was determined that the rate limiting step of the corrosion process is the diffusion of Cr through the alloy to the surface [72, 103]. Detailed mathematical development and analysis of corrosion experiments is developed for fluoride corrosion in Hastelloy N [103]. The model shows the limiting corrosion step in the poly-thermal system was the rate at which Cr diffuses to the surface. Thus attempts to reduce the corrosion of an alloy by rate control, would be aimed at reducing the diffusion rate of Cr in the alloy.

4.4 Corrosion Testing Methods

Three main types of corrosion experiments are usually performed on metals in molten halide salts: isothermal tests, see-saw tests, and poly-thermal loops (forced or natural convection). The first test to check compatibility between an alloy and a salt is an isothermal exposure of the metal to the salt. Metal samples are placed into a crucible and salt is added to the crucible. The time and temperature of the exposure are recorded and the samples analyzed. This isothermal test is done to determine which alloys perform best and should be tested further. Most corrosion tests found in literature are isothermal capsule tests.

The second test that is sometimes used is a see-saw test. A see-saw test is normally done by partially filling a tube with the molten salt. The ends of the tube are kept at different temperatures.

The tube is then rocked back and forth, like a see-saw, at a given frequency to move the salt between the cold and hot ends. The different temperatures at the ends of the tube impose a thermal potential for the corrosion experiment that is not available in the isothermal tests.

The third test involves the construction of a poly-thermal loop, forced or natural-convection, that is closer to the ideal conditions for application [14, 104]. The corrosion in an actual flowing loop allows for experimental determination of thermal gradient effects on the system. This type of test is the most complicated and is usually only done once an acceptable alloy is determined from isothermal tests.

4.5 Methods for Corrosion Mitigation

From the theoretical and experimental work described previously, it is seen that the thermodynamic force behind corrosion of metals is due to differences in the alloy and salt chemistry. The kinetic component of corrosion of alloys is limited by the diffusion of the Cr from the bulk of the alloy to the surface. Thus methods to limit the corrosion of metals in contact with these systems should be aimed at controlling either salt chemistry, alloy chemistry, or finding methods to reduce the diffusion coefficient of Cr in an alloy. Each of these methods will be discussed briefly to highlight previous experimental work. Then will be followed by the experimental results and discussion.

4.5.1 Salt Chemistry

The salt chemistry is controlled by proper purification and handling to reduce cationic and anionic impurities in the salt system. In addition, chemistry control can be achieved by contacting of the molten salt by an active metal. In LiCl salts, the addition of Li metal was effective in lowering the redox potential of the salt and mitigated the corrosion of the test coupons [82]. This process of redox lowering by addition of an active metal has also been shown with Be contact of molten FLiBe (LiF – BeF_2 66.7-33.3 at %) [105].

Initial removal of impurities in fluoride salts involves a process of reduction and fluorination steps to reduce metal fluorides to metal and remove anion impurities [106]. The fluorination step has typically been accomplished by bubbling through the salt with a H_2:HF gas mixture in an inert gas. The H_2 is at a concentration of 10x the value of HF to ensure that the Ni containment vessel is not attacked by the HF gas.

For chloride salts, many different methods have been examined. As part of the experiments at BNL for the LMFRE, the chloride salts were heated at 500°C in vacuum until the pressure of the vessel was < 20 μm Hg. This proved sufficient for their experiments. Other methods have been used to remove impurities from salt mixtures include: chlorinating the salt using either HCl, CCl_4, NCl_3, or other chlorinating compounds, reduction of the salt using active metals such as Mg, or electrochemically purifying the salts [14, 9, 107, 108].

4.5.2 Alloy Chemistry

The alloy chemistry can be controlled by varying composition of the alloying elements. Another method to change the chemistry is to coat the surface of an alloy with noble metals. Both of these

processes have been studied as methods to reduce the corrosion of alloys in molten salts. Alloy chemistry control was used in the development of Hastelloy N to develop an alloy with good corrosion resistance to both molten fluoride salt and to air. Platings have been also studied as part of the MSRE program at ORNL. However more recent work at the University of Wisconsin has looked at the effectiveness of Ni as a coating material for 800H in FLiNaK salt [89].

4.5.2 Alloy Modification

Another method to limit corrosion of alloys in molten salts is to decrease the rate limiting step of the corrosion process. For molten salts, this is done by decreasing the rate of diffusion from the bulk to the surface of the alloy. Coatings can be used to limit the rate of diffusion. Another method that can be used to limit the diffusion is through grain boundary engineering (GBE).

Grain boundary engineering of alloys is a process of mechanical deformation followed by heat treatments. This process creates a large number of low energy boundaries [109, 110]. These low energy boundaries have special characteristics that improve corrosion resistance and mechanical properties of the alloy [111, 112]. One of the benefits of these special grain boundaries is the reduction of the diffusion rate of elements along the grain boundary to approximately the rate of diffusion through the bulk crystal [112, 113]. This ability to reduce the diffusion rate of elements along the grain boundaries should improve the corrosion resistance of GBE alloys in molten salts by reducing the depth of attack of an alloy in the molten salt.

4.6 Selection of Purification Method: KCl-$MgCl_2$

The first step in the production of molten salts for corrosion testing was to determine the most effective way to purify the salts so as to limit the corrosion of the alloys. Many different methods exist for purifying salts for use in testing as was briefly discussed in Section 4.5.1. Four methods were examined in the current study for preparing KCl-$MgCl_2$ salt: bubbling through the salt with Ar gas, bubbling through the salt with Ar/HCl/H_2 gas mixture [98], bubbling with CCl_4 [20], and contacting the salt with metal Mg [107]. All salts were prepared in an Al_2O_3 crucible and stored in an inert atmosphere glove box, Figure 4.2.

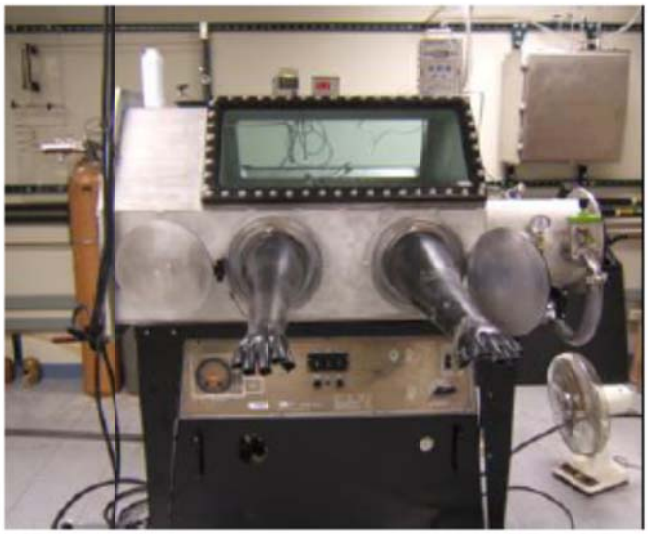

Figure 4.2. The inert atmosphere glove box that was used during the molten salt work with KCl-$MgCl_2$ salts.

The KCl and $MgCl_2$ salt components were purchased from Alfa-Aeser product numbers 11595 & 12315, respectively. The salt components were weighed and placed into an alumina crucible (4" OD, 0.125" wall) inside the glove box. The alumina crucible was then placed into a SS-304 pressure boundary to allow for control of the environment over the salt relative to the rest of the glove box. Ultra high purity (UHP) argon gas was bubbled through the salt by flowing through an Inconel 600 dip tube. The UHP argon gas contains less than 0.2 ppm O_2 and less than 0.05 ppm H_2O was used to limit the amount of impurities introduced into the salt from the gas stream. The exiting gas stream is scrubbed by bubbling through 1M NaOH solution, Figure 4.3, to remove any contaminants from the gas stream before it is vented to the atmosphere. The temperature of the salt melt was also measured and recorded with an alumina clad K-type thermocouple.

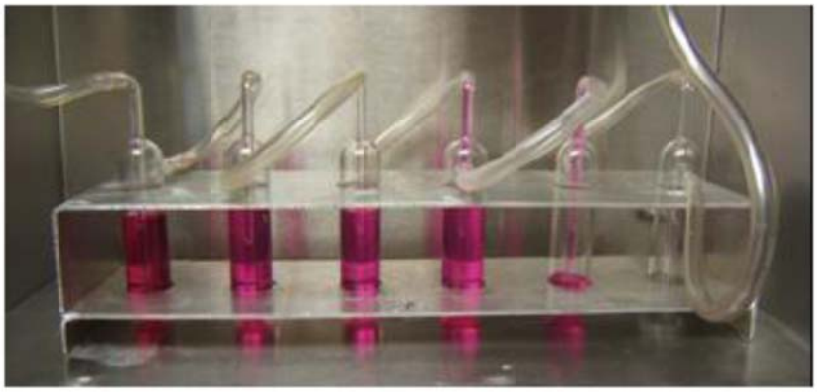

Figure 4.3. The effluent stream from the purification process was directed through these bubblers filled with 1 N NaOH solution along with phenolphthalein pH indicator.

One large batch of KCl-$MgCl_2$ salt was made by slowly heating the system in a step-wise fashion, while continuously bubbling with the salt mixture with argon. The final temperature was 550°C for

a hold time of 16 hours. The general salt composition was verified by examining the cooling curve for the system, Figure 4.4. The temperature of the KCl-$MgCl_2$ salt plateaus at 430°C which corresponds to the liquid solid transition temperature. The expected temperature for this transition is 426°C [20].

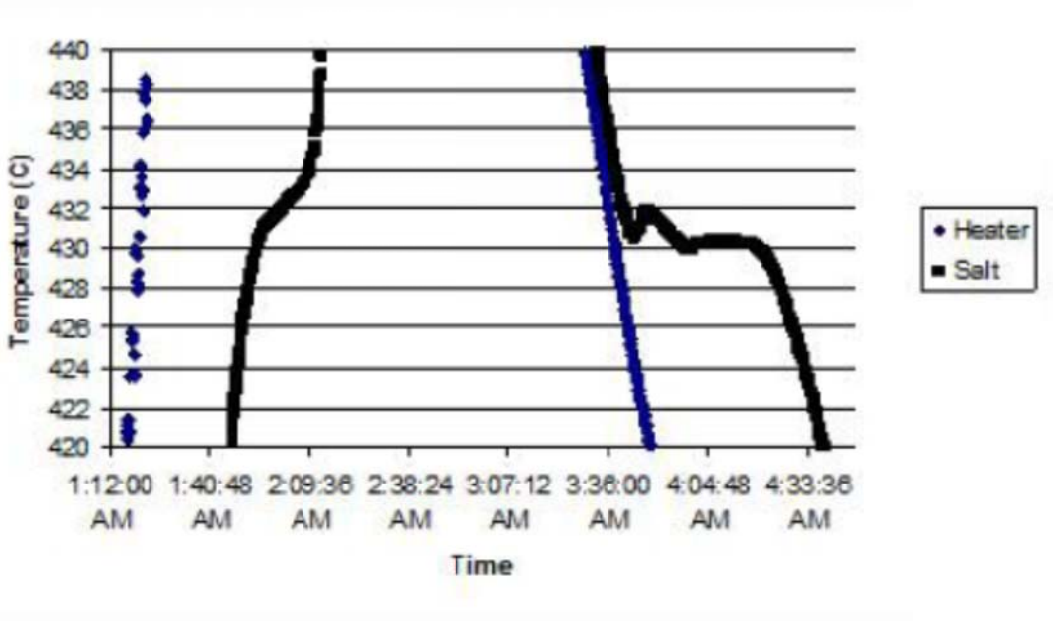

Figure 4.4. The thermal history of the KCl-$MgCl_2$ salts after making the first batch.

This salt was then removed from the crucible and broken into pieces using a quartz mortar and pestle. The Ar purified salt was then further purified by either HCl bubbling (12 hours at 550°C), CCl_4 bubbling (30 min at 550°C), or Mg contact(10 hours at 550°C). Salt samples from each of the purification steps were then used to expose Incoloy 800H coupons (0.5" x 1.25") in the salt at 850°C for 24 hours. The corrosion rate of 800H was then used to relate the effectiveness of the purification process.

800H coupons were placed into individual alumina crucible with 18.7 g of KCl-$MgCl_2$ salt and run in the SS-304 pressure vessel used in the purification steps in the glove box. The purification processes were ranked by weight change of the Incoloy 800H samples, metal concentration in the salt, and SEM analysis of the corrosion sample. Gravimetric measurements showed the CCl_4 and Mg treatments to provide the least amount of corrosion, with HCl next, with Ar purification having the largest corrosion, Figure 4.5a. Metal concentration analysis, done by neutron activation analysis (NAA) and ion-coupled plasma optical emission spectroscopy (ICP-OES), show the same trend, Figure 4.5b.

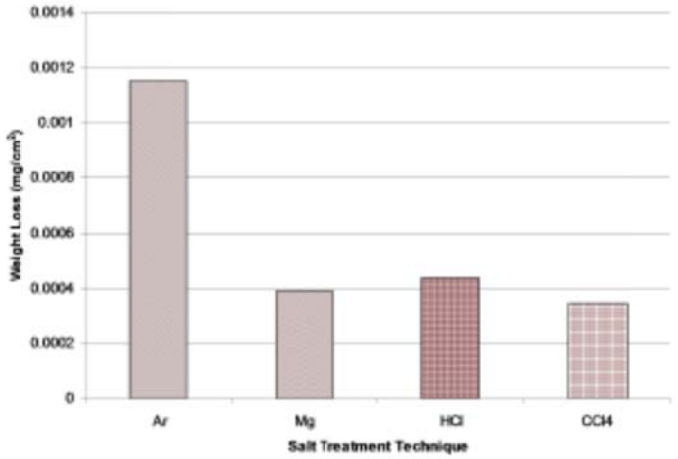

(a) Weight Loss

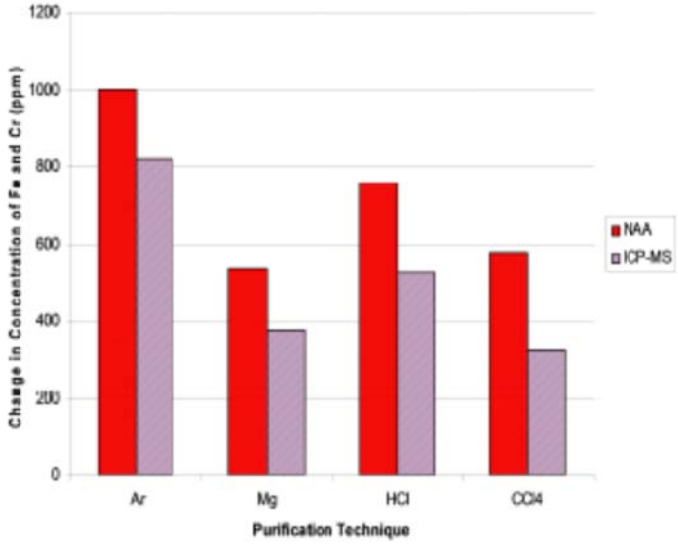

(b) Salt Analysis

Figure 4.5. The different methods for salt purification were analyzed by weight loss (a) and corrosion products in the salt (b). Mg and CCl_4 both produced the best salt for use in future applications.

The ranking of the purification processes is expected. The use of CCl_4 has been shown to effectively remove oxygen impurities in the salt to reduce the redox potential of the salt [114]. The use of Mg, an active metal, will reduce any impurities in the salt melt, metal or oxides, and cause these metals to sink to the bottom of the salt [107]. The explanation that HCl purification caused slightly more corrosion than the Mg and CCl_4 is due to retention of a small amount of HCl in the salt [98]. The hydrogen in the HCl retained in the salt is reduced causing attack on the metal samples when the salt is melted. The use of argon was the least effective purification method studied as no chemical processes were attempted to remove impurities in the system besides removal of water from the system before salt hydrolysis occurs.

Cross-section analysis of the 800H coupons were analyzed under a field-emission LEO SEM. The results show that the Cr is depleted along the grain boundaries of the sample along with a uniform attack along the surface. The depth of attack along the grain boundary is approximately five times greater than the uniform attack. This results in a larger thickness of metal being affected by the salt corrosion than if the alloy was attacked uniformly along the surface. SEM image of the 800H samples exposed to the Mg, HCl, and CCl_4 purified salts along with Cr EDS map is shown in Figure 4.6.

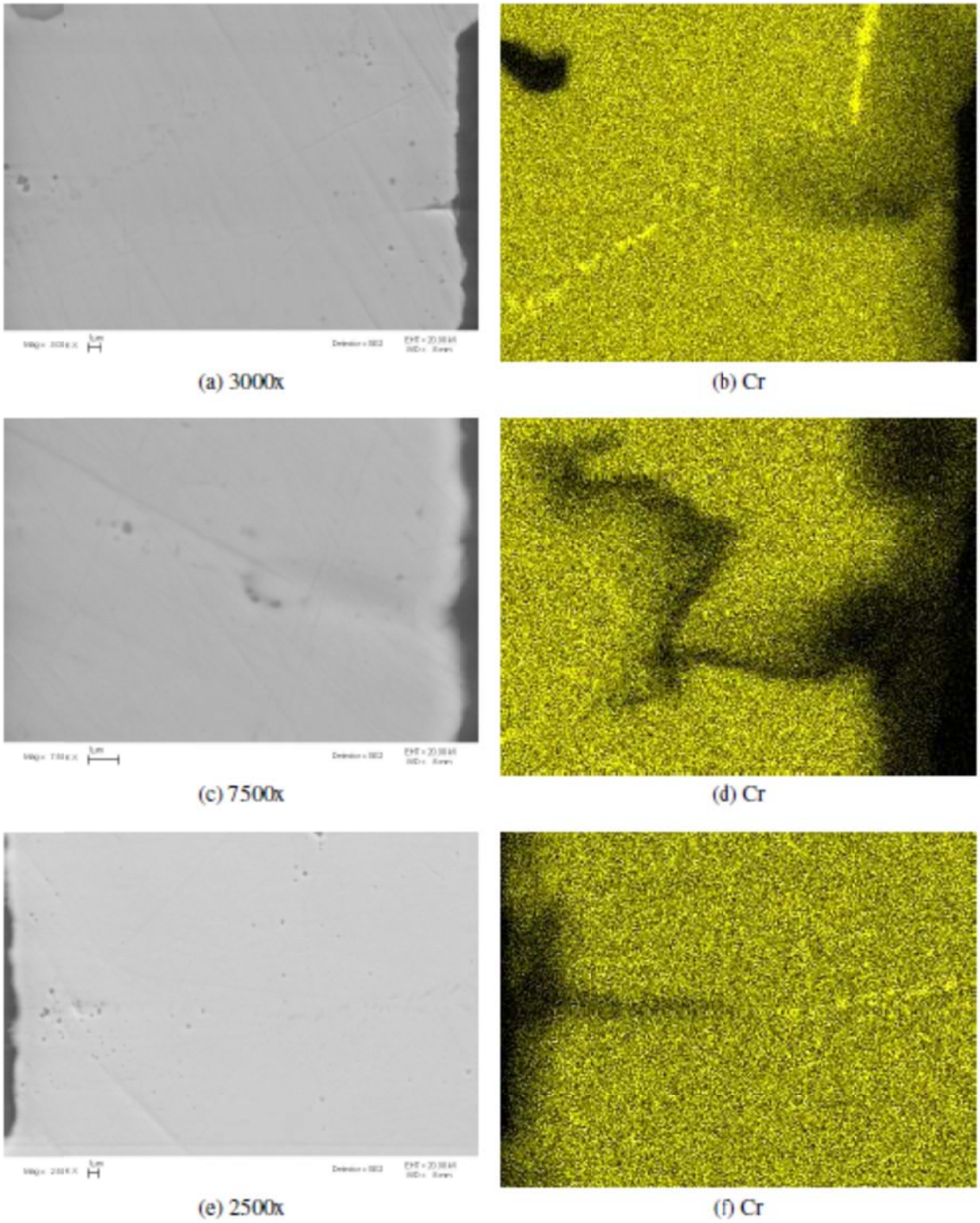

Figure 4.6. SEM image and Cr EDS map of Incoloy 800H samples exposed to KCl-$MgCl_2$ salts prepared by top to bottom: Mg contacting (a & b), CCl_4 (c & d), and HCl (e & f). The depth of attack based on Cr depletion from the surface is 16, 14, & 22 μm, respectively.

The results of this initial screening determined that Mg contact, or bubbling with CCl_4 produced the lowest redox potentials in the salt. Since CCl_4 is a carcinogenic material and produces Cl_2 gas when heated, Mg contact was the chosen method for future preparation of KCl-$MgCl_2$ salts.

4.7 Alloy Selection for Corrosion Tests

To further understand and characterize the corrosion mechanism of KCl-$MgCl_2$ salts, different alloys were tested by exposure to salt for 100 hours at 850°C. Multiple alloys were selected for the corrosion screening tests. The different alloys exposed to KCl-$MgCl_2$ for 100 hrs at 850°C are Inconel 600, 617, 625, and 718, Incoloy 800H, Haynes 230, Hastelloy N and X, Nickel 201, and Stainless Steel 316. This group of alloys was selected due to interest in NGNP applications, their code certification status, forced convective loop construction, or previous history of use in liquid salts.

For the NGNP applications, where the creep rupture strength of the alloys will limit the service lifetime of the materials, Inconel 617, 625, and 718 in addition to Haynes 230 and Hastelloy X are being investigated. For a reactor outlet temperature of 850°C, it has been proposed that Haynes 230 and Inconel 617 are the main candidate materials for IHX construction [115]. However as the expected reactor outlet temperature has decreased, more alloys, including, Incoloy 800H, Inconel 625, Hastelloy X, and 718 are possible candidate materials with 800H being [116]. Nickel 201 is of interest due to the knowledge that nickel is a relatively noble metal for salt applications, but it lacks high temperature mechanical strength. Hastelloy N was developed at Oak Ridge National Laboratory (ORNL) under the name INOR-8 for use in the ARE [72]. Inconel 600 and SS-316 are both candidate materials for construction of the forced convection loop. As such both of these alloys were added to the list of materials studied. A comparison of the strength of these alloys, the 10,000 hr creep rupture strength of these alloys is presented in Figure 4.7.

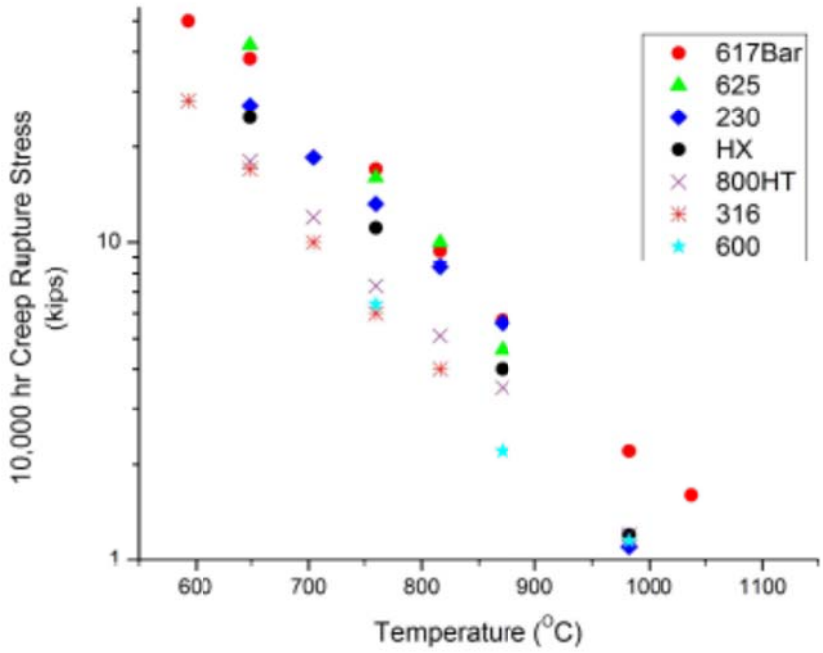

Figure 4.7. Stress necessary to produce creep rupture of the materials at 10,000 hours.

The compositions of the different alloys tested are presented in Table 4.2. In certain alloys where the exact composition of the heat was unknown, the nominal composition for the alloys is presented in its place. In addition, diamond like carbon (DLC) coated 800H samples were also tested in addition to grain boundary engineered (GBE) 800H samples [110].

Table 4.2. Alloy Composition of metals tested in static corrosion tests.

Alloy	Ni	Fe	Cr	Mo	Ti	Al	Co	Mn	C	Other
316	12.0	60.0	18.0	6.0				0.3	0.03	
600	76.0	8.0	15.5						0.15 (max)	
617	52.9	1.09	22.1	9.58	0.4	1.05	12.4	0.06	0.08	
625	62	2.5	21.5	9	0.4 (max)	0.4 (max)			0.10 (max)	Nb - 3.6
718	52.5	19	19	3.1	0.9	0.5	1.0 (max)			Nb – 5.1
X	47.5	19.3	21.3	8.8			1.4	0.54	0.06	W – 0.4
N	72.2	4.03	6.31	16.1			0.15	0.53	0.03	W – 0.06
230	59	1.8	22.5	1.2		0.3	0.3	0.5	0.07	W – 14.1
800H	30.7	45.8	20.8		0.56	0.52		0.96	0.07	
201	99.4	0.05			0.02		0.02	0.19	0.02	

GBE 800H was chosen for further study due to earlier work in the corrosion of 800H alloys in molten salt. It had been seen in testing in FLiNaK and initial testing in KCl-$MgCl_2$, that the corrosion process resulted in a reduction of Cr along the grain boundaries of the alloy to depths of attack much higher than expected based off of weight loss calculations. GBE of 800H has been shown to reduce the diffusion coefficient along the grain boundaries of the alloys during testing of this alloy in super-critical water [109 - 111]. It has also been shown that the thermal stability of the cold-working and annealing process has proven sufficient after exposure at 850^{o}C for 500 hrs [110].

Each alloy has a particular composition that makes the alloy behave in desired ways. The history and applications of these different alloys show how these alloys may be used in applications involving molten salts.

Stainless Steel 316

316 stainless steel is an iron-based austenitic alloy that contains 18 at∴% and 10 at∴% of Cr and Ni, respectively and a small Mo addition. Iron based alloys (347 SS) have been found to be a suitable container material for use in NaCl-KCl-$MgCl_2$ salts at 575°C [14]. 316 is slightly different from 347 in that Nb is replaced by Mo in the alloy.

Inconel 800H

Alloy 800H is an iron-nickel-chromium based steel. The use of Fe in the alloy results in a cheaper material for used with construction. Alloy 800H has higher amounts of Cr and Ni than 316 stainless steel to improve on the high temperature creep rupture strength and high temperature oxidation resistance. 800H is of value to the NGNP and FHR projects due to the alloy being nuclear code certified to 750^{o}C.

Nickel 201

Nickel 201 is a commercial form of pure nickel. Nickel 201 has a very small amount of Fe allowed in the alloy along with several other elements. Out of Fe, Ni, and Cr, nickel is the most noble and should be the most resilient to attack by the molten salt systems. Unfortunately, nickel does not have the high temperature strength necessary for use at temperatures greater than 650^{o}C [117]. However, nickel coatings have been examined for use on structural materials in applications involving molten fluoride salts [89].

Inconel 600

Alloy 600 is a nickel based alloy with chromium and iron additions. The chromium addition to Alloy 600 is to increase the oxidation resistance of the alloy compared to pure nickel. Inconel 600 also has the advantage in that it has higher creep rupture strength at elevated temperatures compared to Ni 201. 600 was the construction material of choice for the ARE at ORNL and so a large amount of corrosion data is available for this alloy.

Inconel 617

Alloy 617 is a nickel super alloy with small amounts of refractory elements. Inconel 617 is of interest for use with molten salts because it possesses excellent high temperature creep rupture strength. Inconel 617 is a nickel based alloy that contains 22 at ∴% Cr and 10 ∴% Mo with minimal amounts of other elements. Since there is large amounts of Cr in the alloy, it is expected that Cr will be readily attacked with the rest of the alloy matrix largely unaffected by exposure to the KCl-$MgCl_2$ salt.

Inconel 625

Alloy 625 is a nickel-chromium alloy that contains additions of Nb and Mo. 625 possesses high temperature creep rupture strength similar to the Inc 718, Hastelloy X and other high temperature alloys.

Inconel 718

Inconel 718 is a nickel-chromium alloy with additions of Nb, Ta, Mo, and Co. 718 also contains small amounts of Ti and Al which provide increased strength by formation of gamma prime and gamma double prime phases (precipitation hardening).

Hastelloy X

Hastelloy X is a nickel super alloy that also contains iron, chromium, and molybdenum. Hastelloy X also has small additions of Co and W. Hastelloy X has been studied previously against corrosion in molten NaCl-KCl-$NdCl_3$ salt mixtures at temperatures from 550-800°C [86]. This alloy is of interest due to the high temperature strength of the alloy.

Hastelloy N

Hastelloy N is a high nickel alloy that contains significant amounts of Mo. Hastelloy N was developed at ORNL as part of the ARE and was originally called INOR-8. Hastelloy N has shown good corrosion resistance to fluoride salts and was used as the structural material for the MSRE at ORNL [72, 99, 118, 119]. Hastelloy N has lower creep rupture strength properties than those desired for the NGNP-IHX with a reactor outlet temperature greater than 750^{o}C ∴[11].

Haynes 230

Haynes 230 is also a high temperature super alloy that is being considered for application for use with the NGNP-IHX secondary loop. Haynes 230 is a nickel based alloy that contains large amounts of W, 14 at∴%. W and other refractory alloys have been found to reduce the rate of corrosion by molten NaCl salts [120].

4.8 Alloy Modifications

Different approaches exist for modification of current alloys that would allow an alloy to operate at high temperatures in molten salt environment. Modifications that can improve the alloy are based on creating a barrier to prevent alloy and salt interactions. These barriers need to be inert to the salt environment and also serve as a barrier to diffusion of Cr from the alloy to the salt. The other approach is to create a large number of special boundaries in the alloy to limit the rate of corrosion along grain boundary networks by GBE.

Diamond Like Carbon (DLC) Coating

Carbon is a noble element and has been proven to be highly resistant to attack by molten salts. Application of diamond like carbon (DLC) coatings is used on different alloy surfaces to increase wear resistance. The use of carbon as a coating was investigated to look at how DLC could be used as a corrosion barrier in molten salt applications.

Grain Boundary Engineering

Two alloys, 800H and 316SS were grain boundary engineered and exposed to the molten salt to examine the effect of GBE on the corrosion of these alloys in KCl-$MgCl_2$ salt.

An effective recipe for grain boundary engineering of Incoloy 800H has been experimentally determined by Tan [109]. The 800H samples were cold worked 6.5 ± 0.6% followed by a heat treatment at 1050ºC for 30 minutes followed by a water quench. The production of these low energy boundaries is found to be significant even after heat treatment of 800H for 500 hours at 850°C [111].

The stainless steel was obtained from a 3.5" D solid round and cut into pieces 1" x 0.5" x 0.10". The cut samples were annealed at 1100°C for 30 minutes immediately followed by a water quench to remove effects of cold working and heat effects in the alloy coupons. Half of the fourteen samples were then rolled to cold-work the samples to 3.1-3.5%. The cold-worked samples were then heat treated at 967°C for 72 hours followed by a water quench. This procedure is outlined in literature to produce a high frequency (86%) of low energy boundaries in SS-316 [112].

4.9 Alloy Testing

After determining that KCl-$MgCl_2$ salt would be purified by contacting the salt with Mg metal to reduce any metal and oxygen impurities in the salt, multiple alloys were selected and tested in the KCl-$MgCl_2$ salt. Three different alloy tests were performed on the metals in the molten salts. The first test was similar to the corrosion test for determining salt purification. Alloy coupons were placed in Al_2O_3 crucibles with 60 g of KCl-$MgCl_2$ salt. The samples were then exposed to the salt for 100 hours at 850^{o}C. The second tests consisted of encapsulating metal samples along with salt in quartz. The encapsulated samples were heated and held at 850^{o}C for 100 hours. The third alloy test involved testing SS-316 in a SS-316 crucible. Two crucibles were prepared to test AR and GBE 316 samples.

The first test was run in the glove box in a similar fashion to the corrosion test for salt processing. A polished coupon (1.25" x 0.5") was placed into an Al_2O_3 crucible along with 60 g of KCl-$MgCl_2$ salt. The samples were set into a SS can and placed in the center of a radiant heater. The samples were exposed to the salt at 850°C for 100 hours. This testing method was abandoned after heat and insulation resulted in failure of the recirculation fan on the glove box due to plugging of several filters. The results from the initial tests will be discussed briefly in Section 4.12 when comparing the effect of crucible material on the corrosion rate of the samples.

The testing in the glove box proved difficult. Quartz is stable to the attack of molten chloride salt and was decided to encapsulate the salt and sample in quartz tubing for corrosion testing. 6 kg of KCl-$MgCl_2$ salt was prepared in a SS-316 vessel by heating the salt while contacting the salt with Mg metal. After cooling, the salt was removed from the crucible and stored in an inert atmosphere glove box. The metal coupons were ground progressively and polished with 1 μm colloidal silica paste and then ultrasonically washed with acetone followed by water. The metal corrosion samples (~ 0.25" x 0.50") were then weighed and encapsulated into the quartz with 10 g of KCl-$MgCl_2$ salt. The size of the samples and salt volume were chosen to keep the ratio of the salt mass to coupon surface area constant between the first and second test. The metal samples, 3 samples of each alloy, were tested by placing one coupon into the 16 mm D quartz tube, moving salt from the glove box to the tube, placing under vacuum, and backfilling with He. Once the tube was back-filled with He, the quartz was heated and sealed to encapsulate the metal coupon and salt with a He environment. During the encapsulation process, a damp cloth was kept over the salt to ensure the salt did not melt during sealing of the quartz rod. After the sample was sealed, the quartz was placed in a water bath to ensure that there were no leaks in the seal.

(a) Quartz before testing (b) Quartz after 100 hrs at 850°C.

Figure 4.8. The quartz encapsulated samples were run for 100 hours at 850°C in the box furnace. Some of the samples corrosion produced salts of different color.

The encapsulated samples were then placed into a box furnace, Figure 4.8a, where the temperature of the heater was held at 850°C for 100 hours. Industrial grade nitrogen gas was passed through the furnace over the course of the run to provide a secondary barrier to possible contamination. After the furnace cooled down Figure 4.8b, the samples were removed from the quartz ampules and cleaned (ultra-sonic bath in de-ionized water, two times 5 minutes each time). Each of the samples

were weighed to determine the gravimetric weight loss for all samples. The weight change data for the samples is presented in Figure 4.9.

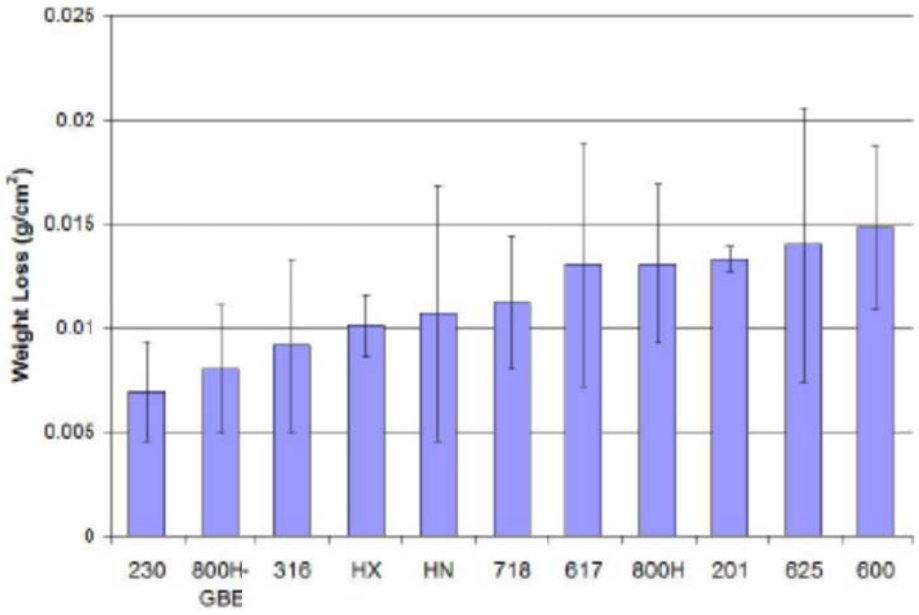

Figure 4.9. Average weight loss of the three samples tested in KCl-$MgCl_2$ salts at 850°C for 100 hours.

The weight loss data is extremely variable between the three samples. This is likely due to differences in the gas composition in the quartz. Each sample was treated the same, however during encapsulation micro cracks in the necked region may have formed. These small cracks could then allow the gas composition to vary among the different tests. The differences in impurities in the gas would then lead to differences in corrosion and in oxide formation on the surface of the metal specimens. As has been mentioned, some metal oxides, including chromium oxide, have a lower Gibbs energy of formation than the equivalent metal chloride. Despite these difficulties, there are some interesting observations to note from the weight loss data of the samples. Haynes 230 outperformed all of the alloys tested in the salt and 800H-GBE had ~ ½ the weight loss as compared to the as-received 800H sample, Figure 4.10. In addition, Ni-201 was not as corrosion resistant as was seen in previous FLiNaK tests [89] based off of weight loss.

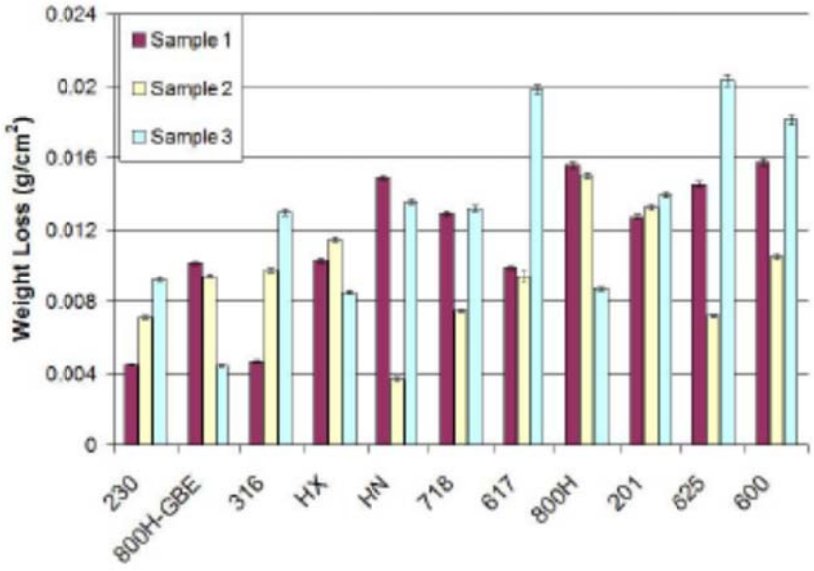

Figure 4.10. The weight loss of each of the samples exposed to KCl-$MgCl_2$ salt. The large deviations between individual alloys is believed to be because of differences in oxide formation on the surface of the alloy.

To get a better understanding and ranking of the corrosion of each alloy exposed to KCl-$MgCl_2$, the samples were analyzed in a SEM in plan and cross-sectional view. To rank each of the alloys, a depth of attack of the alloys was determined by analyzing the Cr concentration of the alloys from the surface. One sample of each alloy was examined, usually the worst performer from the data in Figure 4.10. The exceptions were the Inconel 617 and 625 samples. The 617 alloy sample number 3 broke while removing the salt from the sample due to the sample being too thin (~ 50 μm). The 625 sample number 3 was examined initially, but the depth of corrosion attack went through the thickness of the sample and sample number 1 will be examined instead. The results from the different alloys are presented below.

The final test consisted of exposing SS-316 samples in the as received (AR) and GBE state in a stainless steel crucible. This was due to the differences in corrosion that was seen in the 800H AR and GBE samples run in the quartz test. The crucibles were constructed from 2.5" schedule 40 pipe, 6" tall with 2.875" D discs (1/4" thick) for the end caps, Figure 4.11. The samples were attached to the 1/4" D fixturing rod with 316Si wire. All metal parts (except corrosion samples) were baked in Oakite 33 at 55°C for 12 hours. The parts including samples were then washed in acetone, ethanol, and de-ionized water. The samples were attached to the fixturing rod and placed in the crucible. 400 g of KCl-$MgCl_2$ salt was added to each crucible. The top lid of the crucible was then welded onto the crucible in the inert atmosphere glove box. A small pinhole (0.080" D) was machined into the lid of the crucible to limit pressure buildup during welding. The crucibles were heated to 600°C and the pinhole was sealed. The crucibles were then run in the box furnace at 850°C for 500 hours.

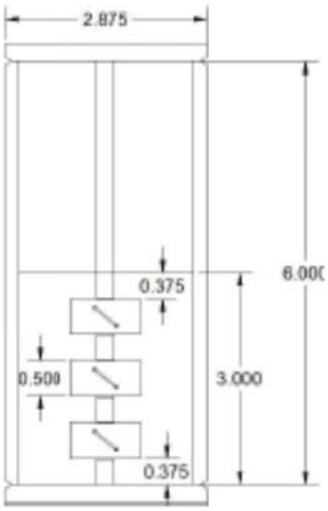

Figure 4.11. Schematic of Crucible Setup for the SS-316 in SS-316 crucible setup.

4.10 Alloy Characterization

A sample from each alloy was analyzed using a field-emission scanning electron microscope (SEM) equipped with energy dispersive X-ray spectroscopy (EDS). The samples were examined in plan and cross-sectional views to characterize the modes of attack in the alloys.

4.10.1 Nickel 201

Nickel is the most noble metal alloying element used in most commercial alloys. Alloy 201 is a nearly pure nickel with small amounts of trace impurities. The exposure to the KCl-$MgCl_2$ salt resulted in etching of the grain boundaries on the surface. This is clearly seen in the plan view image of the sample, Figure 4.12. Small trace amounts of Al and O were also seen on the surface. The oxygen levels increase slightly on the section that appears to be scaling from the surface of the sample.

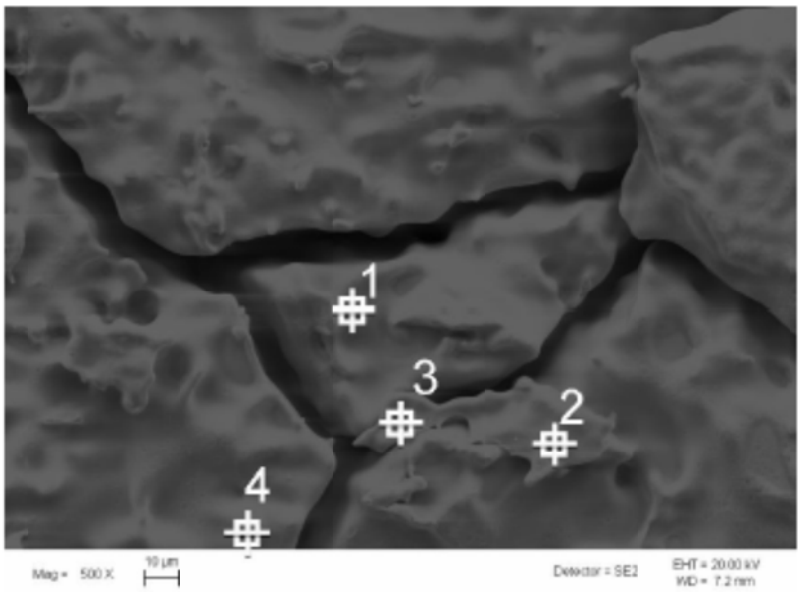

(a) Nickel 201 Plan

Point	Ni	O	Al	Fe
nominal	99.4			0.05
1	96.3	3.4	0.4	
2	95.9	3.6	0.4	
3	92.6	6.6	0.8	

(b) EDS Data - atomic %

Figure 4.12. Plan View of Nickel 201 with point scan data in atomic percent.

Cross sectional analysis of the sample also show the preferential attack along the grain boundaries. The maximum depth of attack of the salt was 50 µm. From EDS map of the cross section, it is noted that an increase in oxygen is associated with the grain boundary attacks, Figure 4.13. Oxygen in the system with the KCl-$MgCl_2$ salt is the source of the corrosion in Alloy 201.

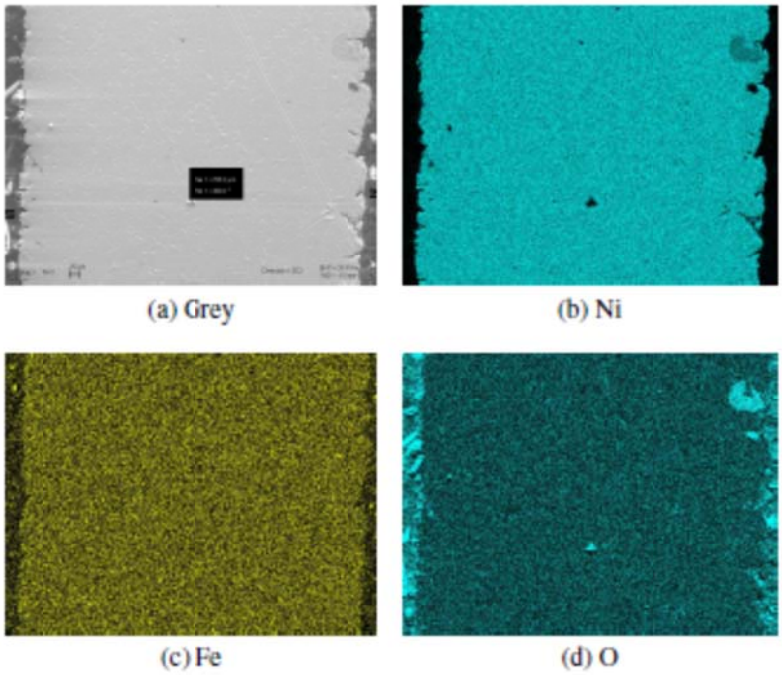

Figure 4.13. EDS maps of Ni-201 alloy show a small amount of oxygen into the alloy along the top right of the figure. The depth of attack from the surface was 50 μm from the surface of the sample.

4.10.2 Hastelloy N

Plan and cross-section views of Hastelloy N, Figures 4.14 and 4.15, respectively, indicate similar corrosion results as Ni-201. From the plan view of the sample, the Fe and Cr concentrations at the surface decreased to about 1 at % from the nominal composition of 6 at %. The attack at the surface left behind small Mo enriched nodules. From Figure 4.1, Mo has almost the same ΔG_F as Ni. As such, Mo should behave similarly in the KCl-$MgCl_2$ salt.

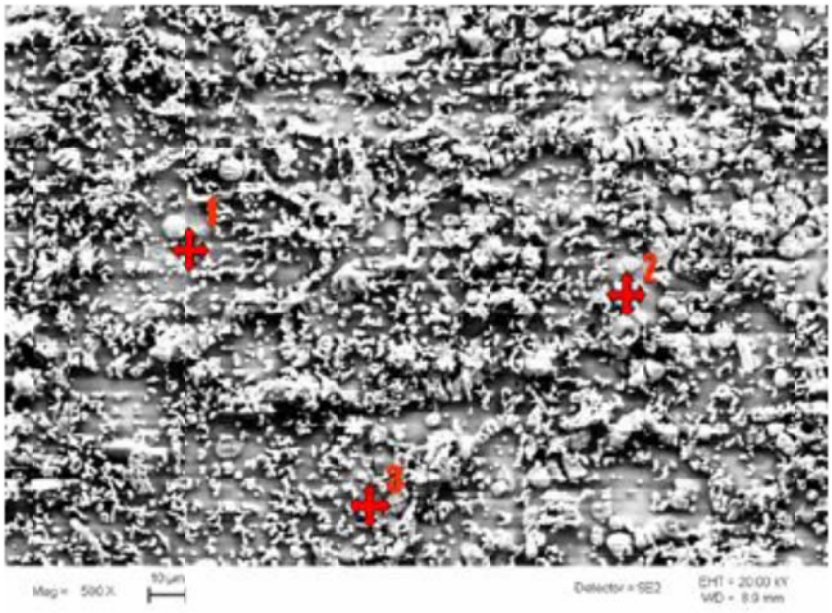

(a) Hast N Plan

Point	Fe	Ni	Cr	Mo	Co	Al	Si	O	Mg	Mn	C	W
nominal	4.03	72.2	6.31	16	0.15					0.53	0.03	0.06
1	0.58	81.09	0.99	14.63		0.15	0.17	1.24	0.11			
2	0.11	28.65	0.23	67.54		0.20	1.17	–	0.24			
3	0.73	81.91	1.33	14.24		0.15	0.16	1.27	0.20			

(b) EDS Data - atomic %

Figure 4.14. Plan View of Hastelloy N with point scan data in atomic percent.

The cross sectional analysis and Cr concentration vs depth analysis of the Hastelloy N sample showed the Cr concentration quickly reached the nominal composition within 25 μm. The Cr EDS map for the cross sectional view does not show segregation of Cr to the grain boundaries, Figure 4.15. The Mo EDS map show significant segregation of the Mo to the grain boundaries of Hastelloy N.

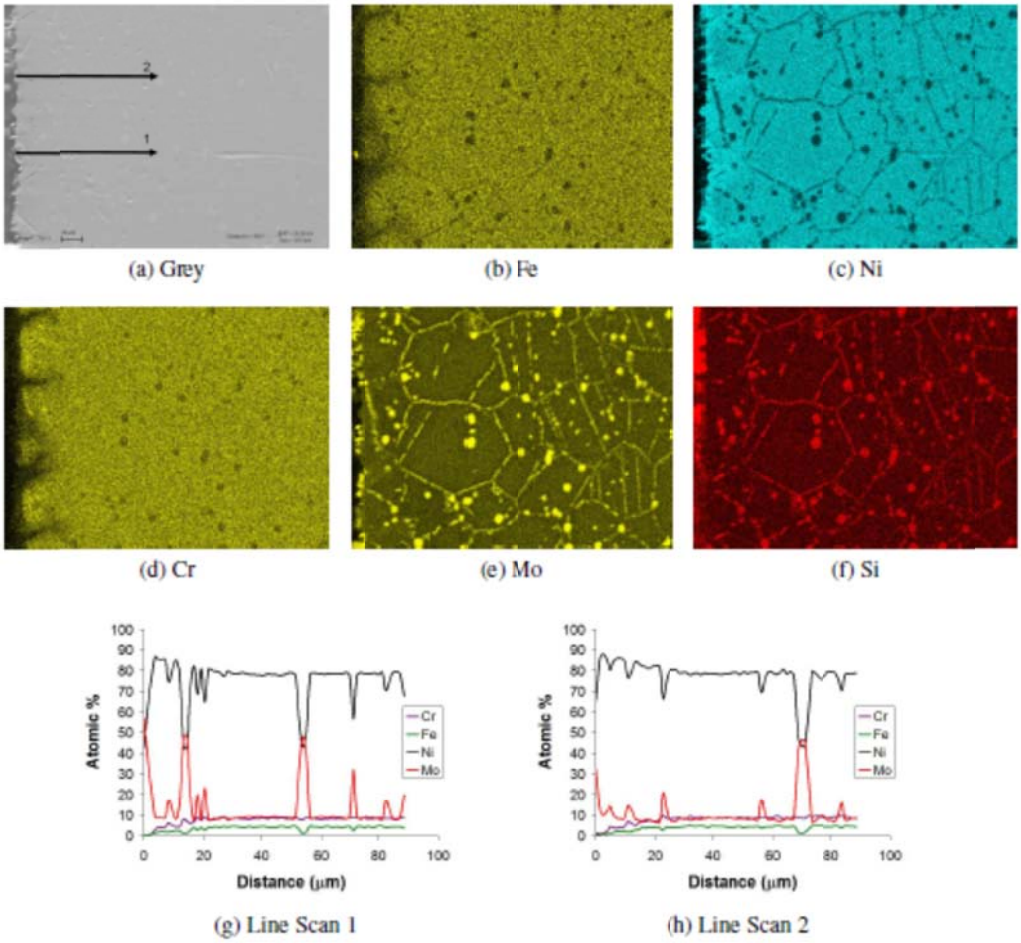

Figure 4.15. Cr and Mo EDS map of Hastelloy N along with two line scans from the surface into the bulk. The depth of attack from the surface was 30 μm from the surface of the sample.

4.10.3 Inconel 617

The removal of Cr from the alloy by the molten salt is seen in Figure 4.16. The concentration of Cr at the surface of the sample is reduced to 4-7 at % compared to the nominal value of 22 at%.

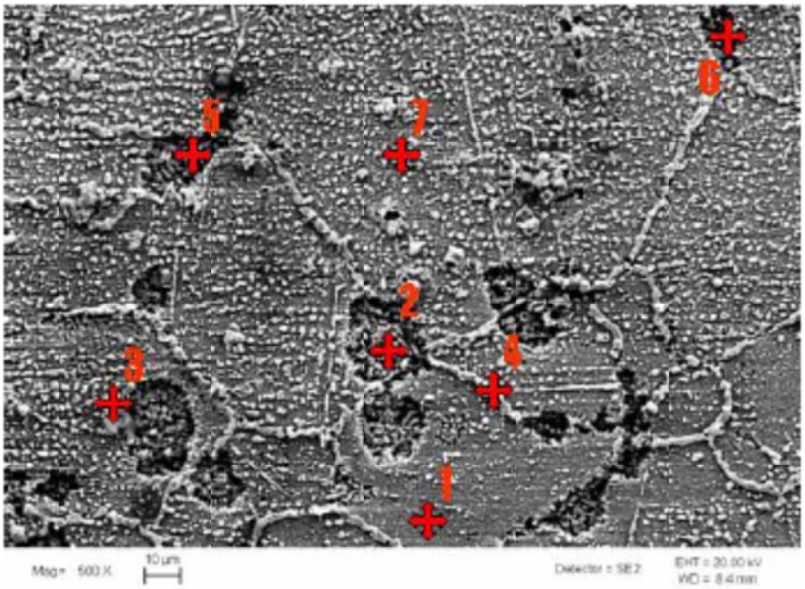

(a) Inc 617 Plan

Point	Fe	Ni	Cr	Mo	Co	Ti	Al	Si	Mg	K	Cl	O	Mn
nominal	1.09	52.9	22.1	9.58		0.4	1.05						0.06
1	1.32	82.46	3.87	4.67	10.23	0.56	10.82	0.85	7.83	0.01	0.23	31.15	
2	1.79	37.37	5.43	4.71	14.09	1.37	8.40	0.95	5.93	0.09	0.47	19.40	
3	0.98	19.83	3.43	4.40	7.54	1.45	7.98	3.60	5.90	0.11	0.67	44.10	
4	2.09	40.13	6.35	5.29	14.75	8.74	5.37	3.04	3.77	0.18	0.76	9.52	
5	2.94	64.08	7.24	0.35	22.03	1.86	0.44	0.14	0.25	0.05	0.08	0.55	
6	2.05	40.29	5.99	3.64	14.58	2.70	7.71	0.48	5.60	0.04	0.09	16.84	
7	2.19	44.79	6.58	6.74	17.12	1.13	2.31	2.95	1.75	0.09	0.00	14.34	

(b) EDS Data - atomic %

Figure 4.16. Plan View of Inconel 617 with point scan data in atomic percent.

A Cr EDS map for the cross-sectional view of the Inc-617 sample is shown in Figure 4.17. In addition, line scans are also presented to highlight the regions of attack in the alloy. From this Cr map and line scans, it is seen that the Cr is reduced along the grain boundaries of the sample. Reduction of the Cr concentration is also seen at the surface of the sample, but again only to small depths compared to the depth of attack along the grain boundaries. The total attack of the salt along the grain boundaries is ~225 μm.

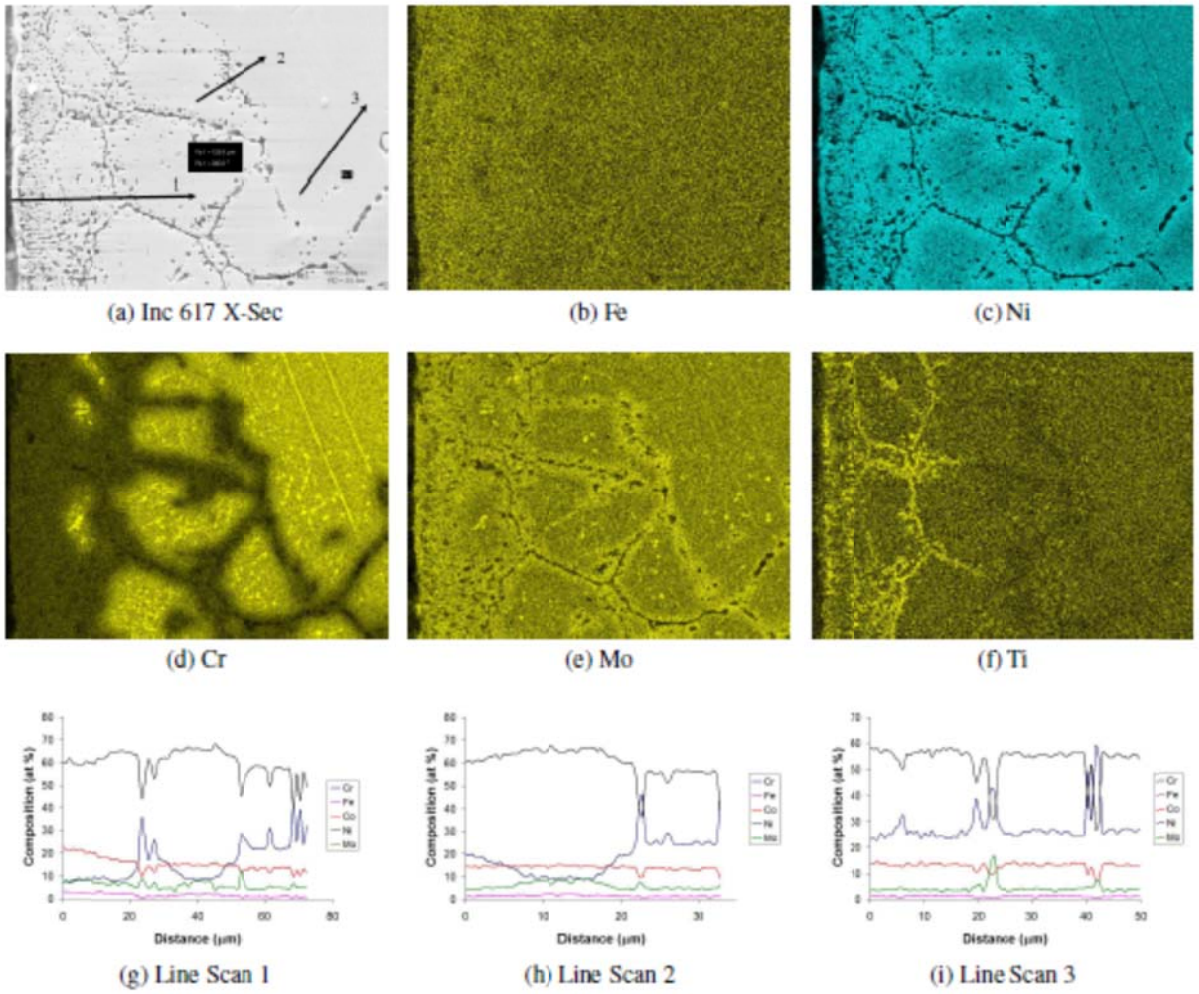

Figure 4.17. EDS maps of Inconel 617 x-section (c) shows attack occurs along the grain boundaries by removal of Cr. The Cr was depleted along the grain boundaries to a depth of 225 μm.

4.10.4 Inconel 625

The worst performing sample out of Inconel 625 was sample 5-3. The inter granular corrosion in this sample was continuous through the entire sample thickness. This sample was analyzed in plan view, while sample 5-1 was used to look at the cross-sectional analysis of the sample. The surface of sample 5-3 contained two different surface textures, Figure 4.18. Where one of the textures appeared to be lifted from the surface of the alloy. A line scan over these two features determined that the elevated texture to be rich in Nb. The lower surface layer was closer to the nominal composition of the alloy with the exception of Cr depletion. The Cr was depleted at the surface to less than 1 wt %.

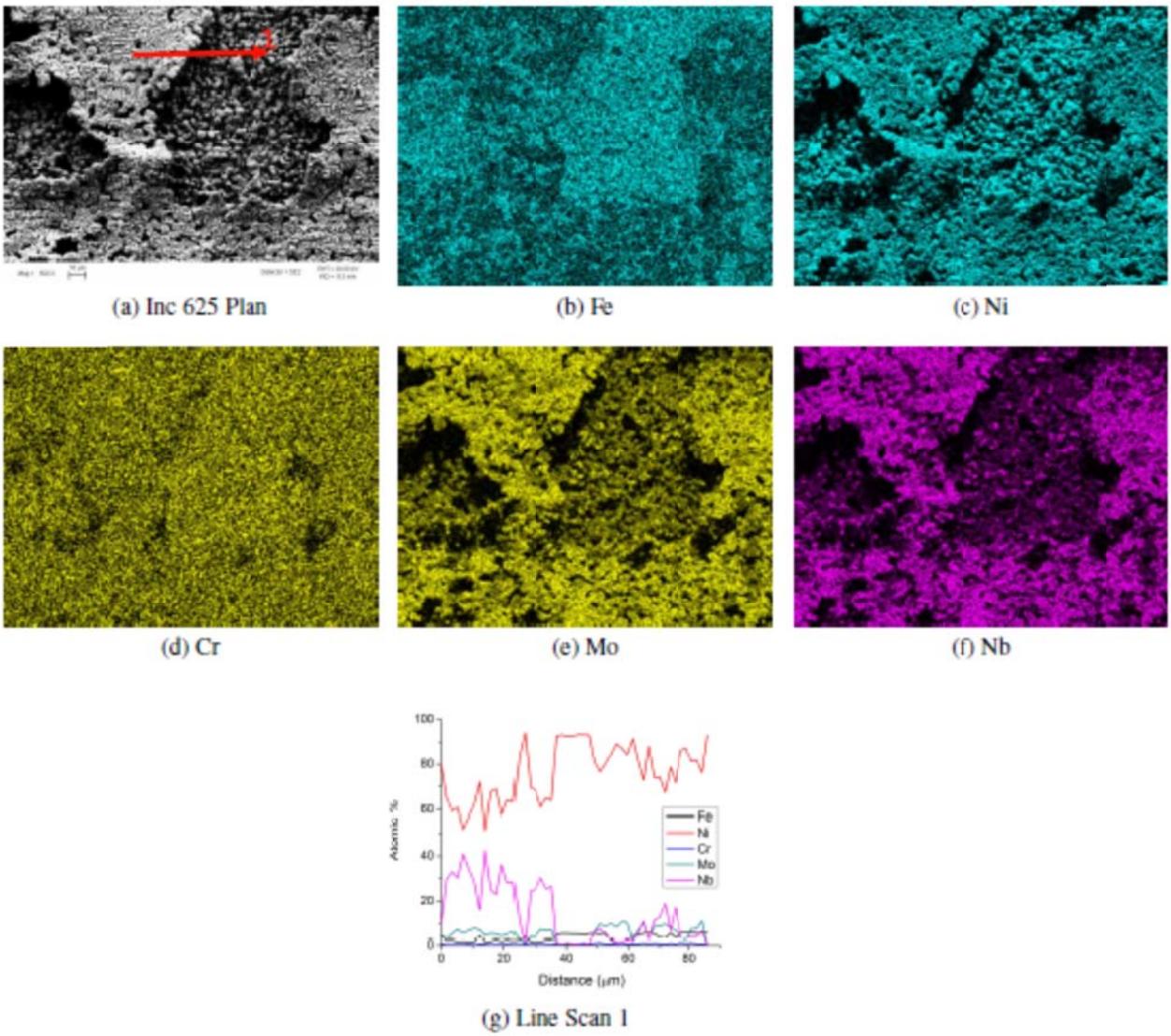

Figure 4.18. The EDS maps of Inc 625 from the surface show two distinct regions. The elevated region (upper left & bottom) is enriched in Nb while the lower region is base alloy minus Cr.

The Cr EDS map for the cross section of sample 5-3 shows a continuous network of corrosion in the sample, Figure 4.19. This is due to sample being thin ~ 270 μm. The depth of attack into the alloy surface was > 135 μm.

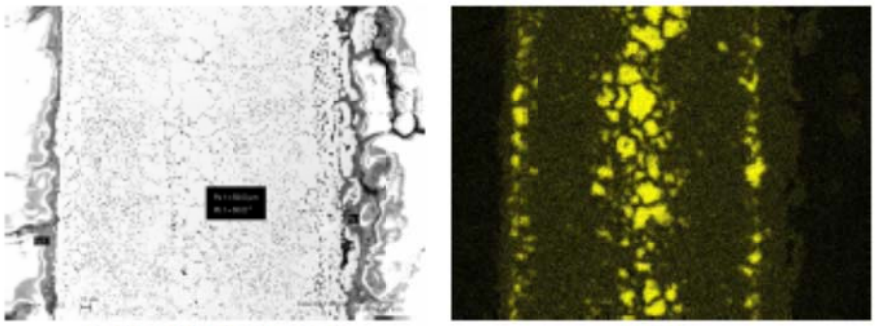

(a) Inc 625 X-Sec (5-3) (b) Cr

Figure 4.19. Cr EDS map of Inconel 625 x-section (c) showing attack through the entire thickness of the sample (270 μm thick).

The next worst performing sample of Alloy 625, Figure 4.9, sample 5-1 was analyzed. Cross sectional view of Inconel 625 shows a nearly uniform chromium depletion layer into the alloy from the surface. This depth of chromium depletion was 120 μm deep. This is slightly less than the value seen in sample 5-3. The Mo and Nb both start to enrich locally in the structure at a depth of 80 μm from the surface, Figure 4.20.

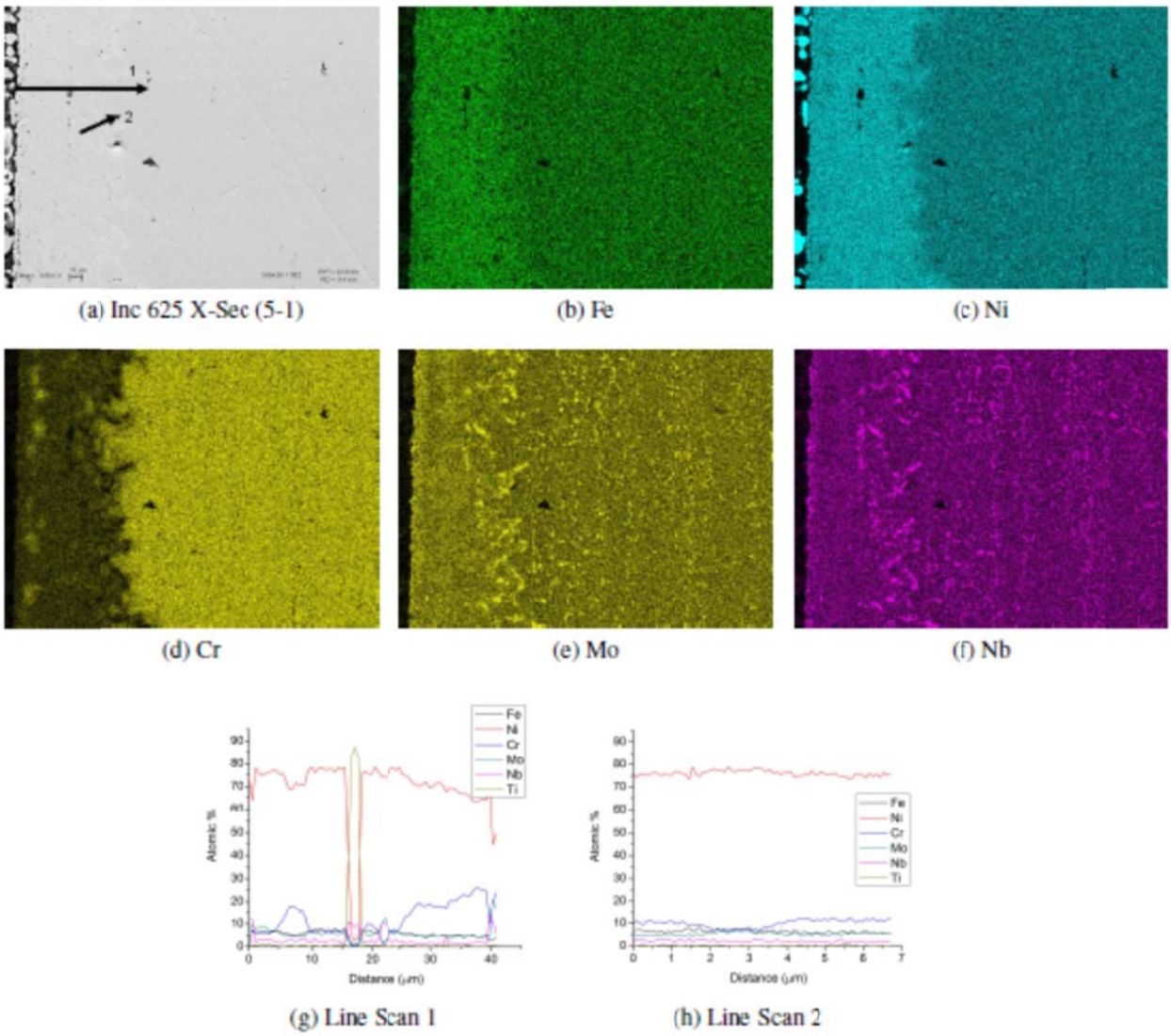

Figure 4.20. EDS maps of Inconel 625 x-section (c) shows the Cr depletion to be nearly uniform through the thickness of the sample. The Cr was depleted to a depth of 120 μm.

4.10.5 Inconel 718

Inconel 718 is compositionally very similar to Inconel 625 with slight compositional changes in the alloying elements. 718 contains increased amounts of Al, Ti, and Nb which are used for age hardening of the alloy [121]. This similarity in the compositions produces similar corrosion behavior in KCl-$MgCl_2$. Plan view analysis of the sample shows regions of increased Nb content up to 30 wt% for regions, Figure 4.21.

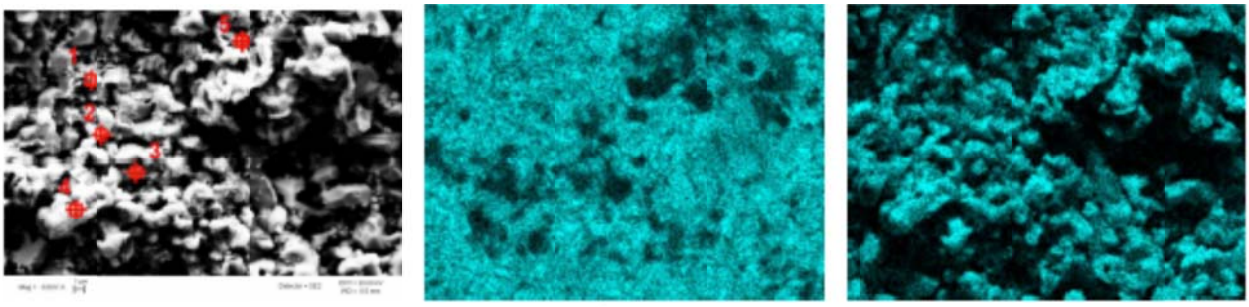

(a) Inc 718 Plan

(b) Fe

(c) Ni

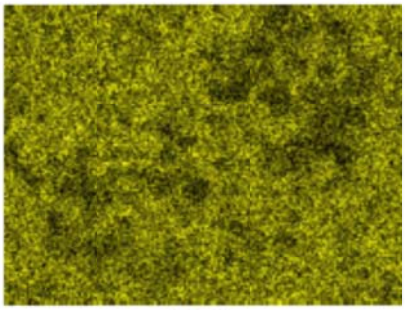

(d) Cr

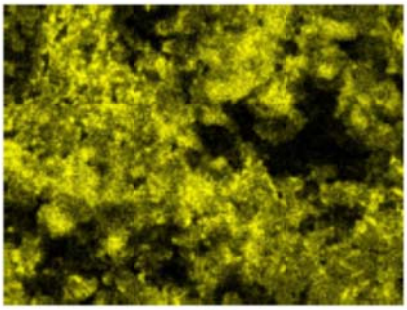

(e) Mo

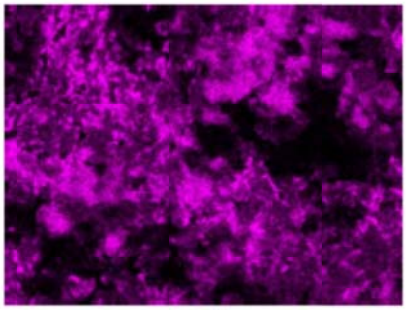

(f) Nb

Point	Fe	Ni	Cr	Mo	Nb	Ti	Al	Si	Mg	O	N
nominal	18.5	52.5	19	3	5.1	0.9	0.5				
1	21.8	39.8	2.4	1.5	13.0	8.5	0.7	0.8	1.6	10.0	
2	25.4	49.8	2.7	1.2	4.8	8.0	0.8	1.6	1.0	4.7	
3	9.5	38.5	0.9	0.4	11.4	4.3	0.5	9.7	0.4	6.6	17.8
4	22.3	49.2	2.6	1.0	4.5	9.4	0.7	1.9	1.2	7.2	
5	11.3	25.4	1.3	0.7	16.6	12.8	0.4	3.4	1.3	12.7	12.8

(g) EDS Data - atomic %

Figure 4.21. Plan View of Inconel 718 with point scan data in atomic percent.

A view of the cross section shows the Cr depletion through the alloy to be nearly uniform with a maximum depth of attack of 125 μm, Figure 4.22d. Examination of the Nb EDS map shows several unique layers, Figure 4.22f. The first layer is 10 μm thick and is nearly void of Nb. The second layer is Nb enriched and is approximately 15 μm thick. The third layer is similar to the base composition and is 25 μm thick. The final layer before the base alloy contains an increase in Nb enriched regions. This layer is 90 μm thick.

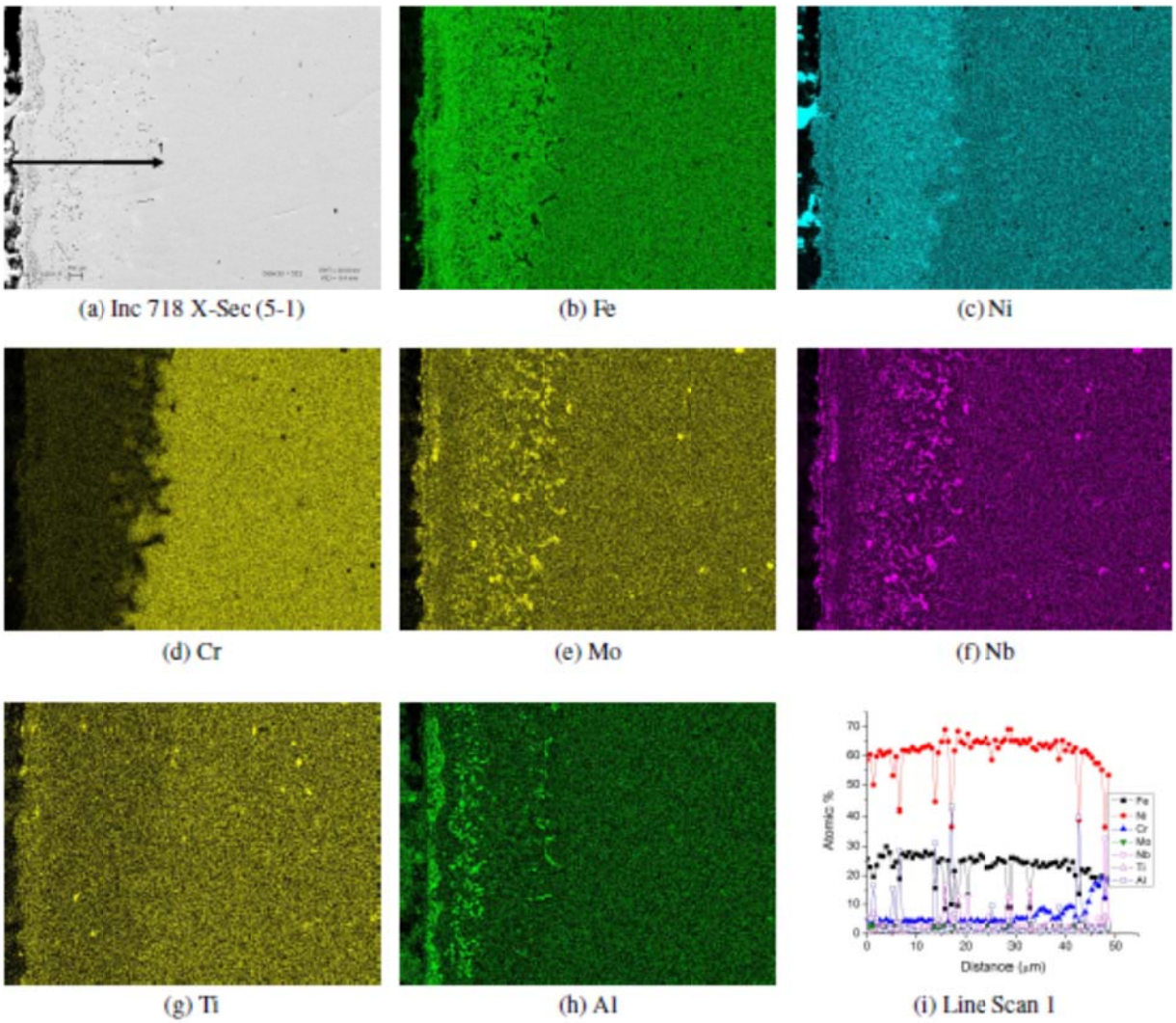

Figure 4.22. EDS maps of Inconel 718 x-section (c) shows the Cr depletion to be nearly uniform. The Nb map (f) shows the formation of three layers on top of the base alloy. Cr was depleted to a depth of 125 μm.

4.10.6 Hastelloy X

The corrosion of Hastelloy X in the quartz crucibles occurred along the grain boundaries of the system. This is evident from the plan view of the sample, Figure 4.23. The grain boundaries are clearly evident in this figure. The Cr levels on the surface of the alloy were depleted to 2.6 wt %.

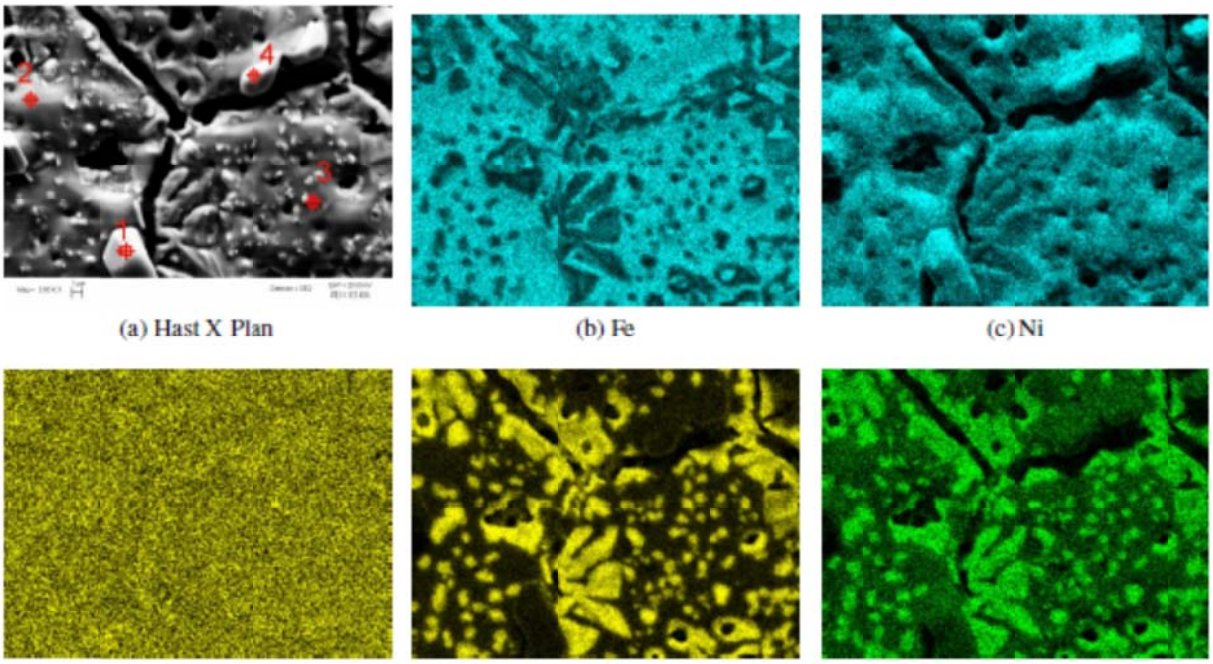

(a) Hast X Plan (b) Fe (c) Ni

(d) Cr (e) Mo (f) W

Point	Fe	Ni	Cr	Mo	W	Si	Mg
nominal							
1	34.3	57.5	1.8	0.6	0.03	2.8	0.3
2	33.3	54.4	1.6	1.4	0.13	1.5	0.0
3	10.7	27.2	2.4	20.9	0.17	9.9	0.0
4	32.7	54.7	1.7	0.9	0.15	2.7	0.4

(g) EDS Data - atomic %

Figure 4.23. Plan View of Hastelloy X with point scan data in atomic percent.

The cross section of the Hastelloy X sample and EDS maps are presented in Figure 4.24. The Cr is removed from the near surface of the alloy to a depth of 20 μm. This is immediately followed by an equal depth of Cr enrichment, attacked near the surface and along the grain boundaries. The maximum depth of attack in the alloy is to a depth of 160 μm. The Cr is depleted a uniform width across the grain boundary until the regions where two or more grain boundaries meet. At these locations, the Cr depletion is wider than along the grain boundary to this point.

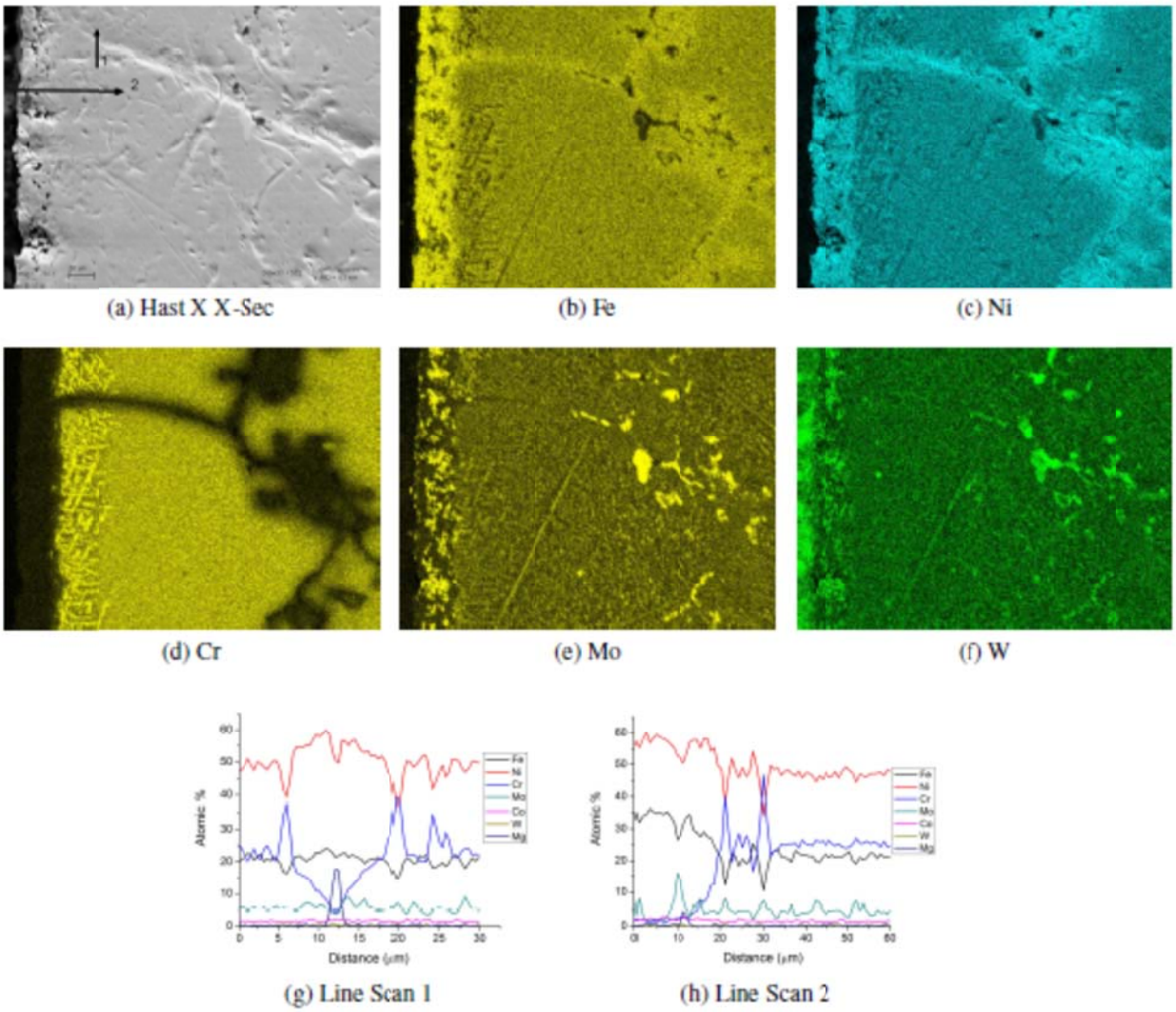

Figure 4.24. Cross-sectional view of Hastelloy X with element EDS maps show Cr depletion to a depth of 160 μm.

4.10.7 Haynes 230

Haynes 230 had the best results of the alloys tested based on gravimetric analysis. Examination of the plan view of the Haynes 230 alloy showed the Cr concentration to be 11-11.5 at%, half of what it is in the as-received sample. This large amount of Cr in the near surface region of the alloy is much higher than the next closest alloy, Inc 617 (4-7 at%).

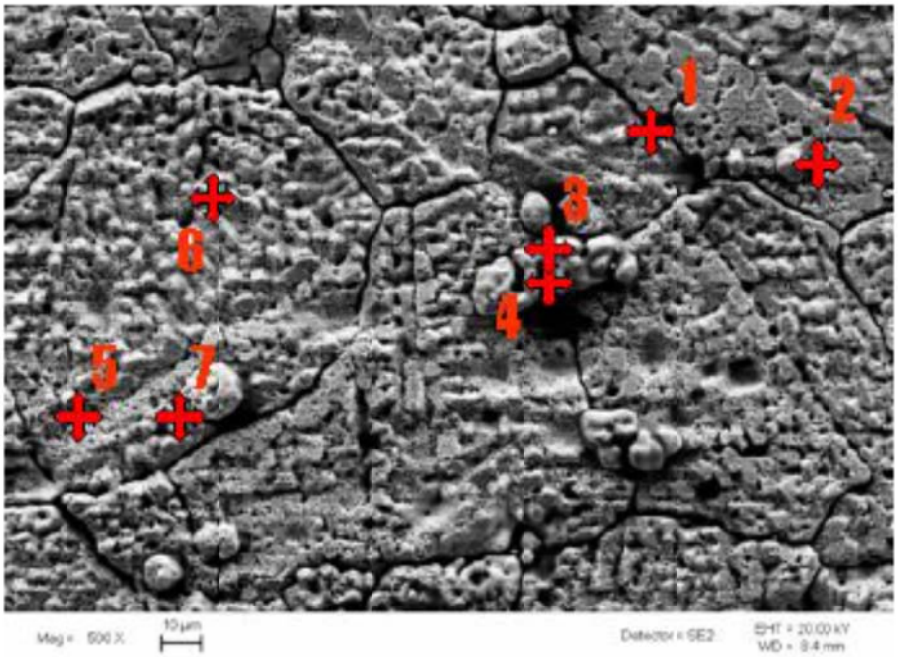

(a) Haynes 230 Plan

Point	Fe	Ni	Cr	Mo	W	Al	Mg	Co	Mn	C
nominal	1.8	59	22.5	1.2	14.1	0.3		0.3	0.5	0.07
1	4.23	73.76	11.13	1.46	6.64	1.09	0.90			
2	4.62	74.61	11.38	0.93	6.24	0.93	0.61			
3	4.50	75.63	10.99	0.76	6.31	0.88	0.35			
4	4.71	74.84	11.15	1.01	6.27	0.77	0.40			
5	4.11	72.59	10.74	1.07	6.82	2.26	1.78			
6	4.15	76.40	10.94	0.22	6.16	0.84	0.65			
7	4.32	74.95	11.48	1.24	6.18	0.71	0.34			

(b) EDS Data - atomic %

Figure 4.25. Plan View of Haynes 230 with point scan data in atomic percent.

A Cr EDS map for the cross-sectional view of the Haynes 230 sample is shown in Figure 4.26. In addition, line scans are also presented to highlight the regions of attack in the alloy. From this Cr map and line scans, two layers seem to exist in the alloy. The first layer is 50 µm deep, while the second layer is 180 µm deep. In the 2nd region, the Cr concentration along the GB, the local minima, is still 17 at%.

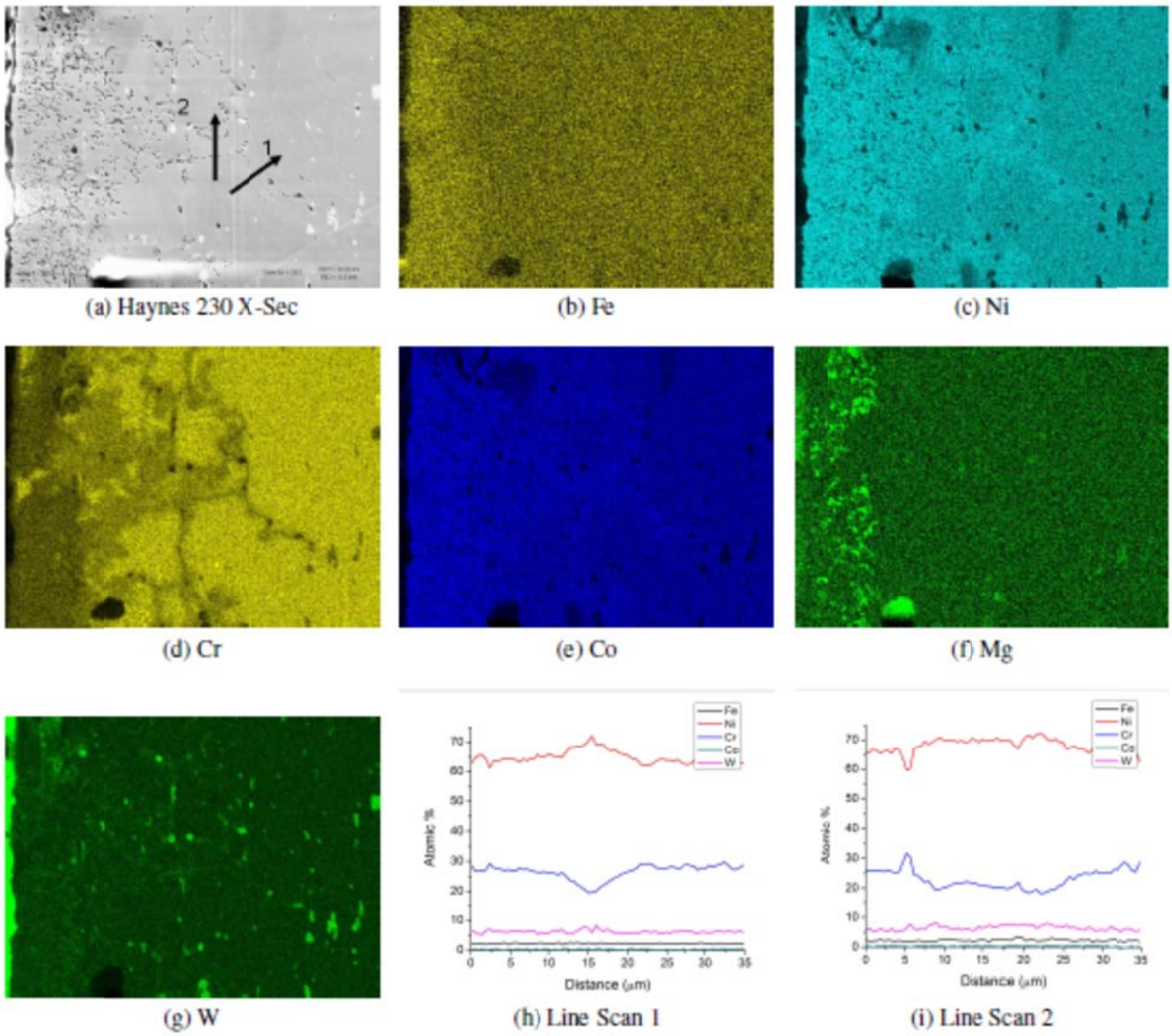

Figure 4.26. Cr EDS map of Haynes 230 alloy shows two regions of depletion. The first region of attack occurs to a depth of 50 μm with the second region occurs to depths of 180 μm from the surface.

4.10.8 SS-316

Plan view of the exposed SS-316 is shown in Figure 4.27 along with point scan data. From this data, it is noted that the surface concentration of Cr is reduced to approximately 1 at%. The surface of the alloy is also 'etched' along the grain boundaries.

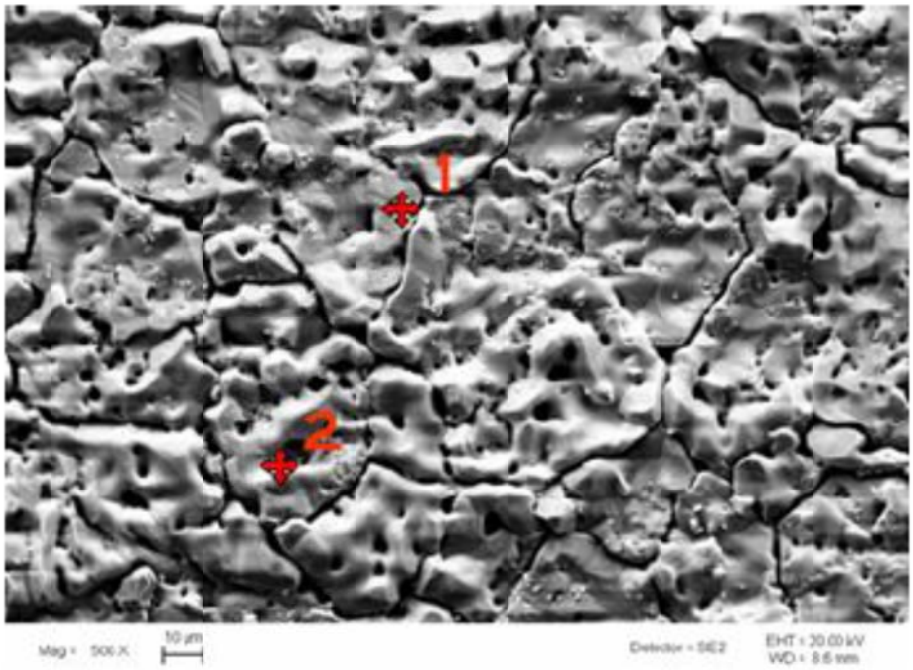

(a) SS 316 Plan

Point	Fe	Ni	Cr	Mo	O	Al	Si	Mn	C
nominal	60.0	12.0	18.0	6.0				0.3	0.03
1	80.20	11.06	1.19	0.80	0.58	0.28	4.39	1.50	
2	79.26	11.18	1.15	0.94	0.00	0.40	5.43	1.64	

(b) EDS Data - atomic %

Figure 4.27. Plan View of SS - 316 with point scan data in atomic percent.

A Cr EDS map and line scans for a cross-sectional view of the SS-316 sample is shown in Figure 4.28. From the data, it is seen that the Cr is reduced along the grain boundaries of the sample. The width of Cr depletion along a grain boundary is relatively thin, only 10 μm across the sample. From the sample surface into the alloy, the depth of Cr depletion is ~ 300 μm.

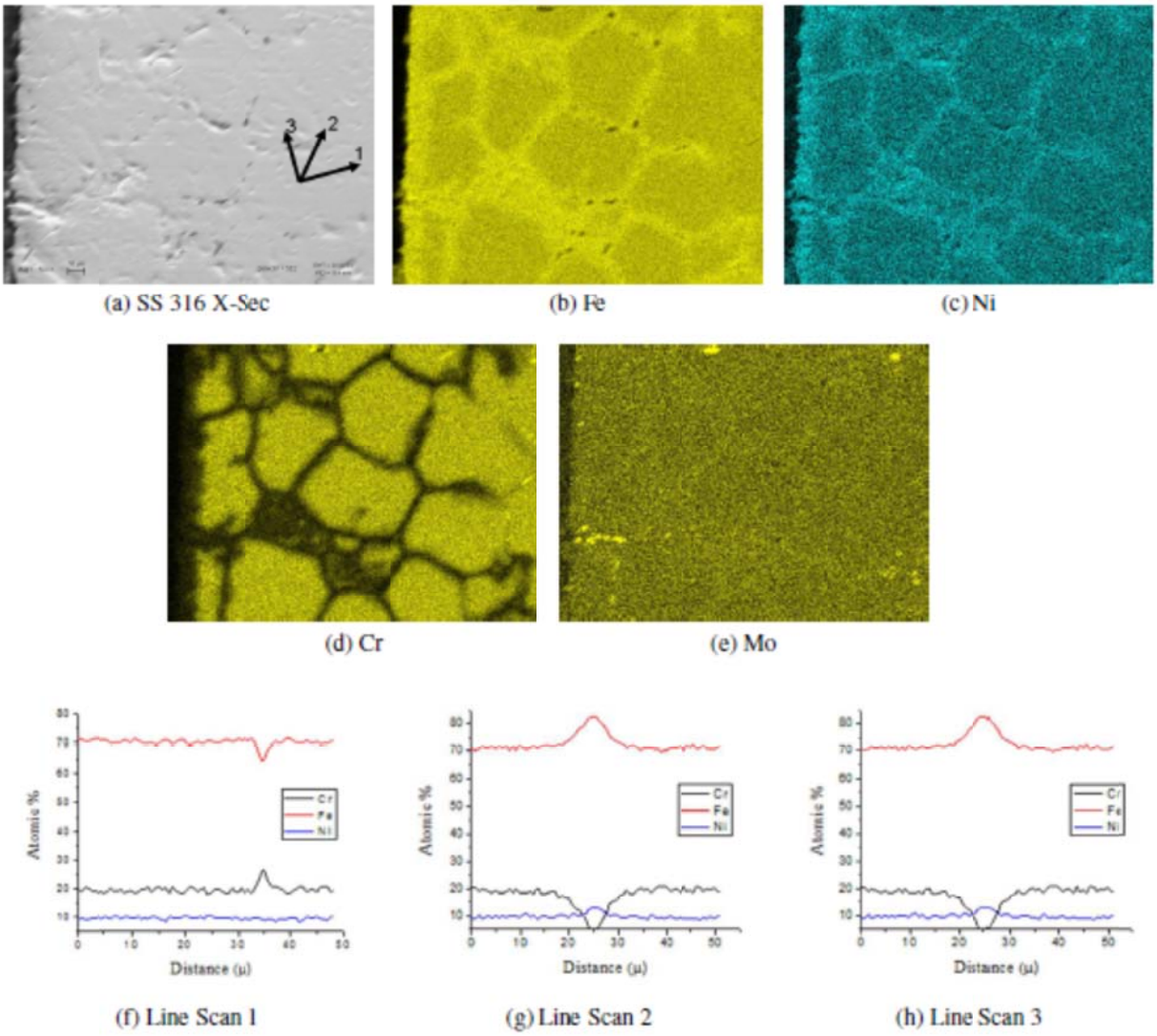

Figure 4.28. Cr EDS map of 316 stainless steel shows the depletion of Cr from the grain boundaries of the sample. This depletion zone is approximately 10 μm wide uniformly across the sample with penetrations along the grain boundary to 300 μm normal to the surface of the sample.

4.10.9 Incoloy 800H

316 stainless steel and Incoloy 800H are slightly different than all other alloys looked at because they are Fe based alloys. Although 800H is an iron based alloy, the corrosion of Incoloy 800H follows trends similar to the Ni-Cr alloys examined. The Cr concentration near the surface of the sample decreased dramatically. This decrease is noted by looking at the Fe/Cr ratios in Figure 4.29. The Fe/Cr ratio increased from 2 to 8 after exposure to KCl-$MgCl_2$ salt, Figure 4.29.

(a) Inc 800H Plan

Point	Fe	Ni	Cr	Ti	Al	Mn	V	Mg	O	Si	K	Cl	N	C
nominal	42.3	31.6	20.4	0.6	0.5	0.8								0.03
1	25.0	17.3	3.2	4.3	2.8	0.0	0.2	19.7	27.1	0.3	0.1	0.1	0.1	
2	27.7	17.3	4.4	8.9	2.0	0.04	0.3	19.1	19.7	0.3	0.2	0.1	0.1	
3	7.6	4.6	0.9	13.7	1.1	0.0	0.2	14.4	54.1	1.2	0.03	0	2.3	

(b) EDS Data - atomic %

Figure 4.29. Plan View of Inconel 800H with point scan data in atomic percent.

Examination of the cross-section of the alloy shows similar results to the previous alloys. Cr was depleted along the grain boundaries of the samples. This Cr depletion occurred to depths of 250 μm from the surface of the sample.

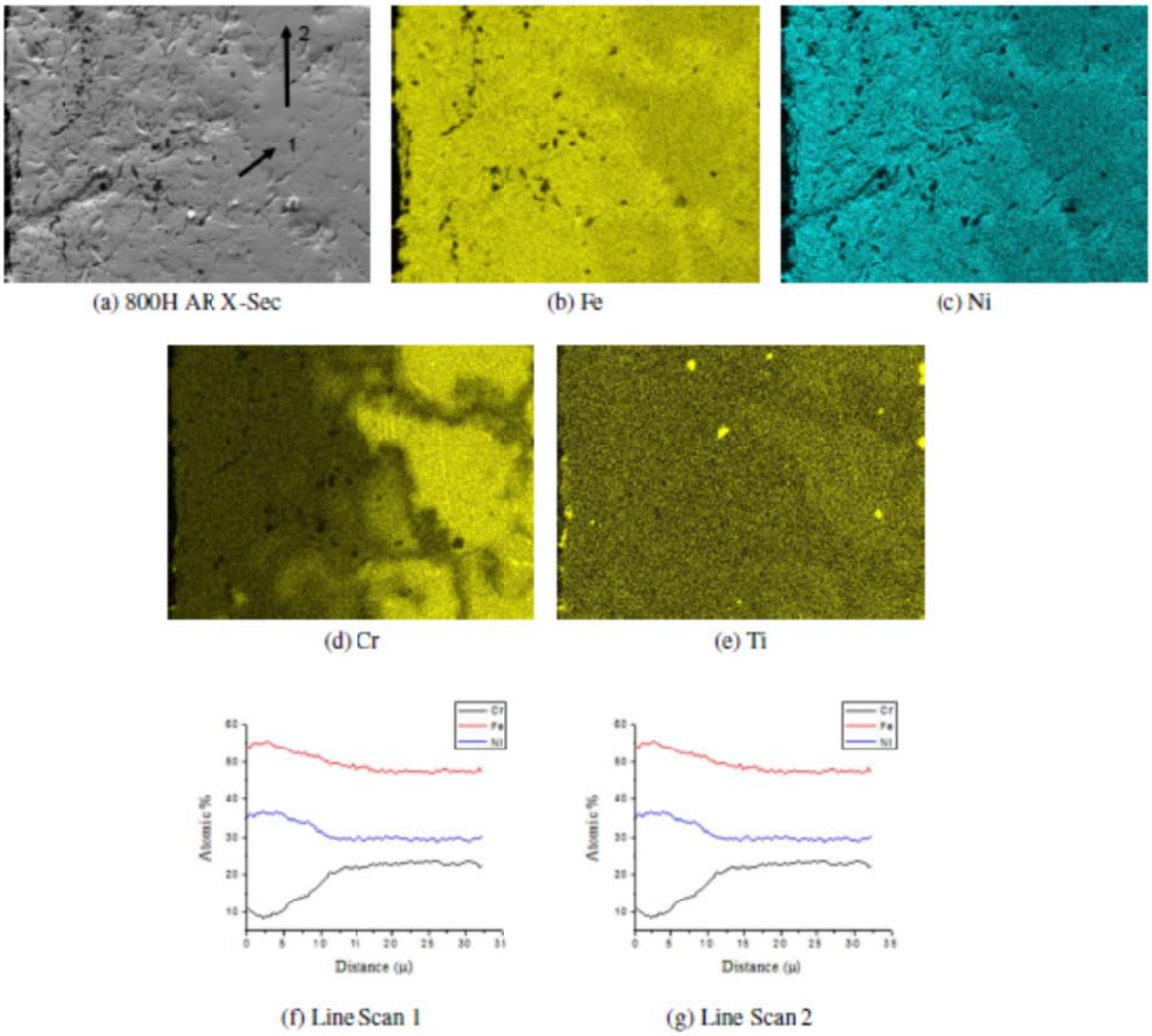

Figure 4.30. Cr EDS map of Incoloy 800H alloy with line shows two distinct affected regions.

4.10.10 Incoloy 800H - GBE

The GBE samples were prepared in a manner similar to that reported by Tan [109]. The as-received 800H samples were cold worked 6% and annealed at 1050^{o}C for 30 minutes. After annealing, the samples were cut into 0.5" by 0.25" samples and polished. The samples were then exposed to the KCl-$MgCl_2$ salts with the same environment conditions as those for the AR 800H samples.

Scanning Electron Microscopy (SEM) of the plan view of the sample showed that Cr was depleted at the surface. Upon examination of the surface concentration, two different surface morphologies are present on the surface of the sample. The first morphology appears to be the metal surface. This metal surface occurs along the grain boundaries (pts 2, 3, and 5). These points all have about 4-5 at% of Cr, this is slightly higher than the values seen for 800H, but not really significant. The second area appears to have form a stabilized oxide surface layer. The unique characteristic of this

oxide compared to the AR sample, is the Cr has a higher atomic concentration than the Fe in this region.

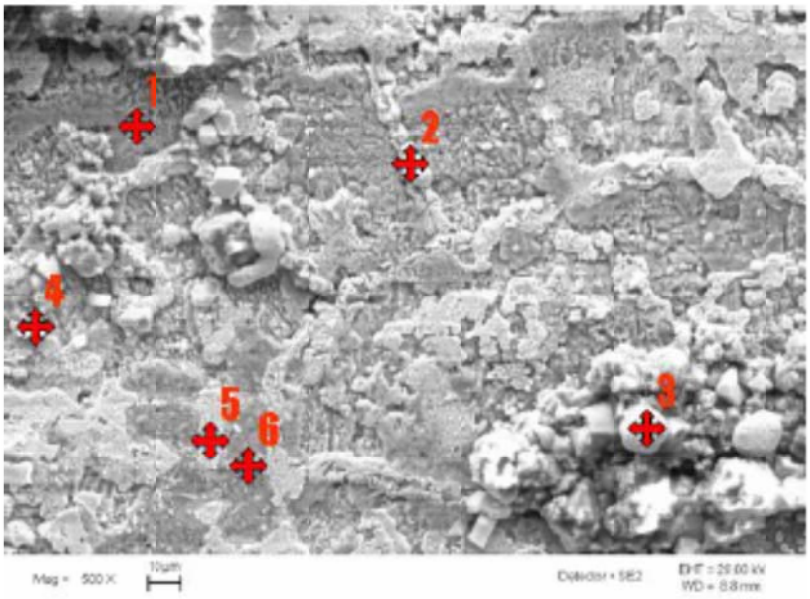

(a) Inc 800H - GBE Plan

Point	Fe	Ni	Cr	Ti	Al	Mn	V	Mg	O	Si	K	Cl	C
nominal	42.3	31.6	20.4	0.6	0.5	0.8							0.03
1	7.4	3.1	11.8	1.4	2.3	–	0.2	19.1	54.1	0.4	0.2	0.03	
2	59.3	25.9	5.6	0.5	0	–	0.1	7.4	0.00	0.5	0.09	0.1	
3	51.8	22.1	4.1	0.1	0.5	–	0.1	2.7	17.8	0.4	0.1	0.1	
4	1.5	0.7	0.9	0.3	0.4	0.6	0.1	2.6	29.3	0.0	31.1	30.1	
5	47.4	23.0	4.4	0.5	3.2	–	0.1	7.1	14.1	0.2	0.04	0.03	
6	2.8	1.2	13.5	2.8	5.9	–	0.3	18.8	54.0	0.5	0.1	0.3	

(b) EDS Data - atomic %

Figure 4.31. Plan View of Incoloy 800H - GBE with point scan data in atomic percent.

The cross section analysis of the GBE 800H sample, Figure 4.32 confirmed the gravimetric data that the thermo-mechanical treatment improved the corrosion resistance of the alloy. Not only is large amounts of Cr found near the surface, similar to a large oxide scale, the maximum depth of attack is greatly reduced in the GBE sample.

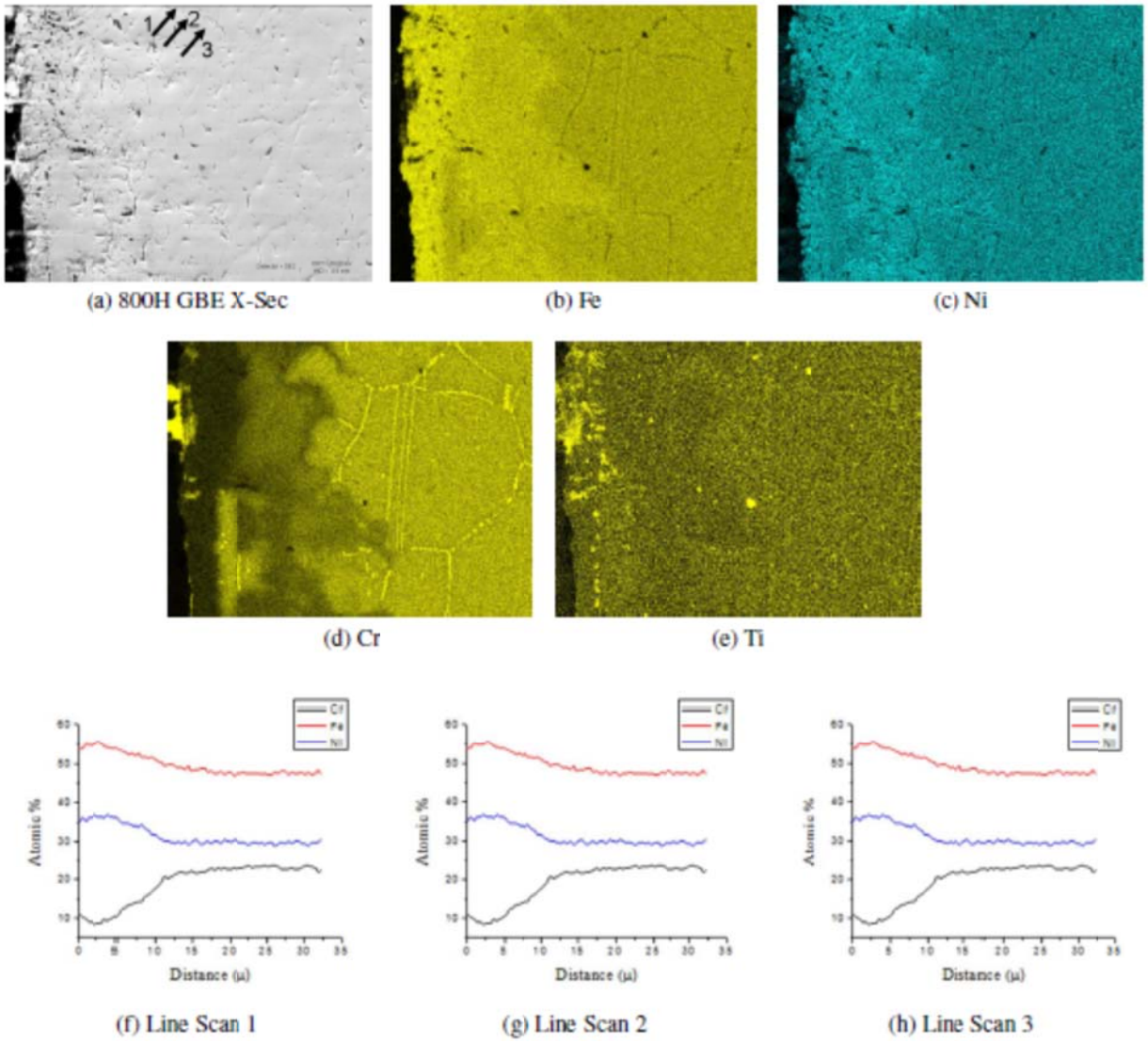

Figure 4.32. Element EDS maps from the cross-section of the GBE 800H GBE sample. The depth of attack of the GBE 800H sample is almost 1/2 the depth of the AR.

To try and better understand, the effect of GBE on the improvement on corrosion interior portions of the samples were examined. An un-corroded section in the center of each of the AR and GBE samples was examined to characterize the differences in the corrosion between the alloy conditions, Figures 4.33 and 4.34.

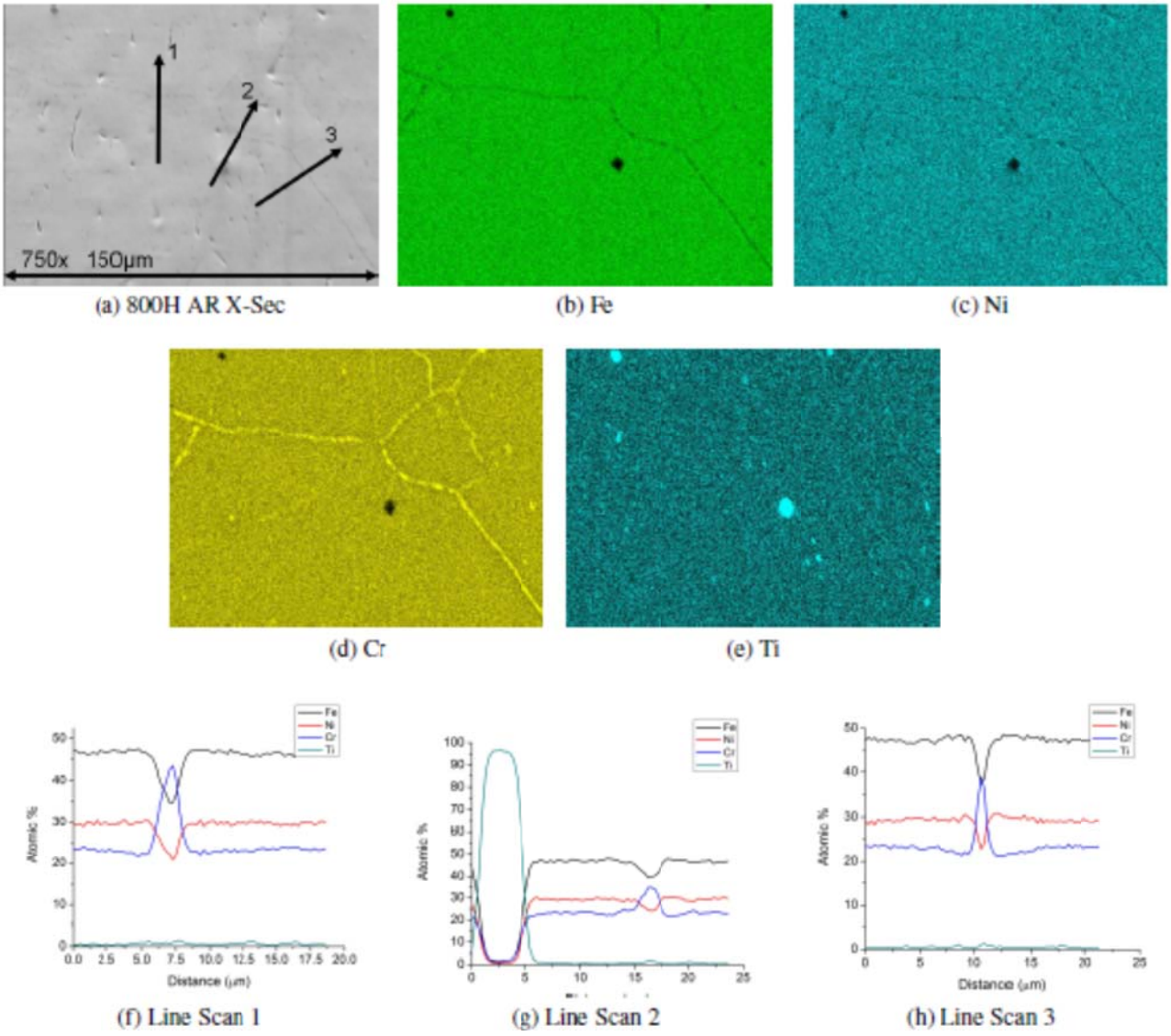

Figure 4.33. Element EDS maps from the cross-section of the AR 800H sample.

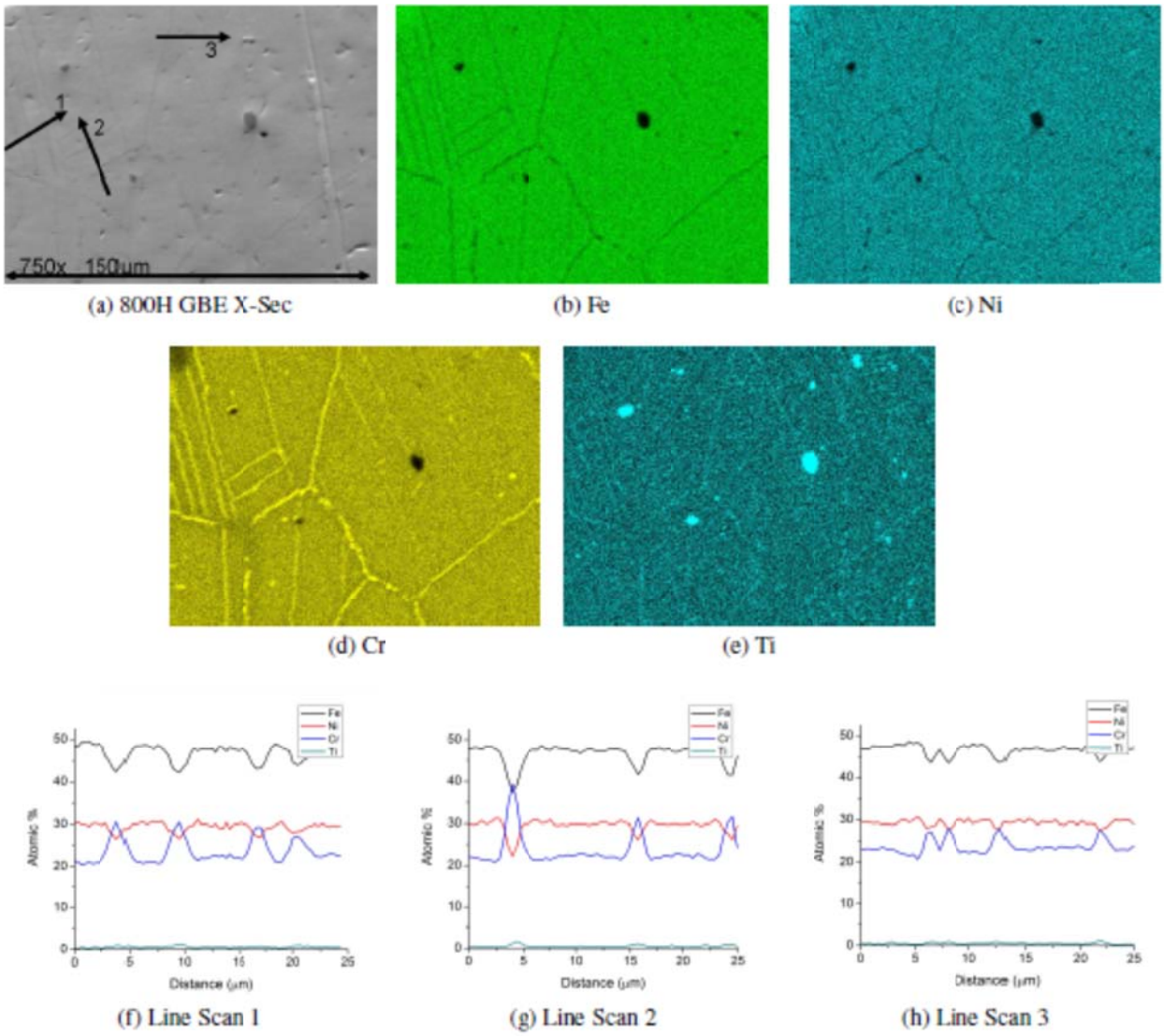

Figure 3.34. Element EDS maps from the cross-section of the GBE 800H interior to the corrosion regions.

From examination of Figures 4.34 and 4.33, some differences are seen between AR and GBE 800H samples in the Cr EDS maps. The GBE sample contains multiple twin boundaries throughout the sample as is seen by the parallel lines in the Cr EDS map. The Cr concentration on these twins is on average 30 at%, compared to the 40-45 at% of Cr measured on the AR samples grain boundaries. The increase in twin boundaries is what is expected from the GBE process. The increase in these twin grain boundaries along with the reduction of Cr at these grain boundaries are different between the alloy. It is expected that these two factors help produce a 50% improvement of the 800H GBE sample compared to the AR 800H sample.

4.11 Corrosion of SS-316 in SS-316

Corrosion tests on annealed (AR316) and grain boundary engineered samples (GBE316) were performed in SS-316 crucibles to get a better understanding the effect of the crucible on the

previous corrosion rates. Two crucibles were prepared, one for the AR samples and one for the GBE samples. 400 g of KCl-$MgCl_2$ salt was placed into each crucible and sealed by welding the crucible shut in the inert atmosphere glove box. After 500 hours, the samples were removed and washed in DI water in the ultrasonic bath for 2 - 5 minute intervals. The weight loss for the samples is seen in Figure 4.35.

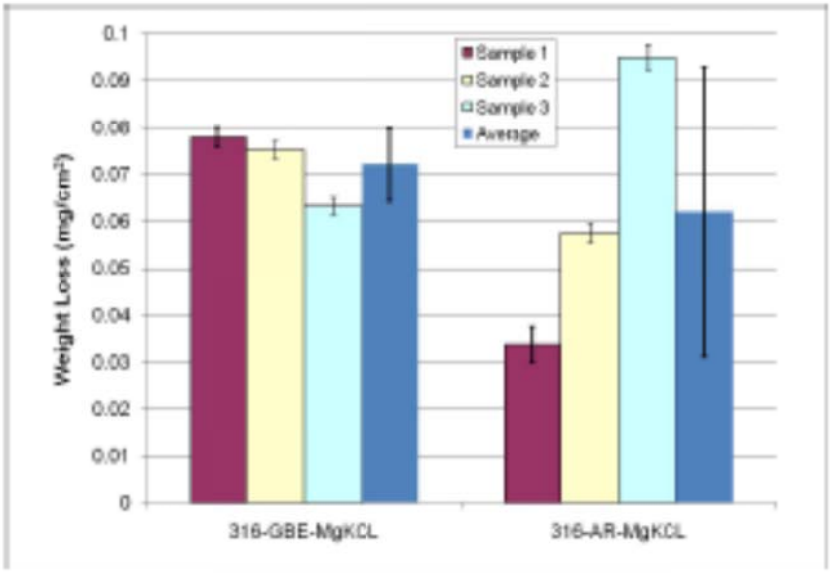

Figure 4.35. Weight loss data for the GBE and AR 316 SS samples exposed to KCl-$MgCl_2$ salt in 316 SS crucible showed no significant difference in weight loss.

4.11.1 316 AR Analysis

The AR 316 samples were analyzed in the SEM using EDS. The surface of the AR sample had light etching along the grain boundaries. No Cr depletion was seen on the surface. Mo agglomerates were also readily seen when looking at the sample. There a small amount of dark circles present on the sample. These circles turned out to be dark regions surrounding a small hole on the surface. The dark portion on these samples was rich in Mg and O while the center of the hole was rich in Cr and Mn (both active metals that are usually readily corroded). AR and GBE sample both have small crystals of MgO on the surface.

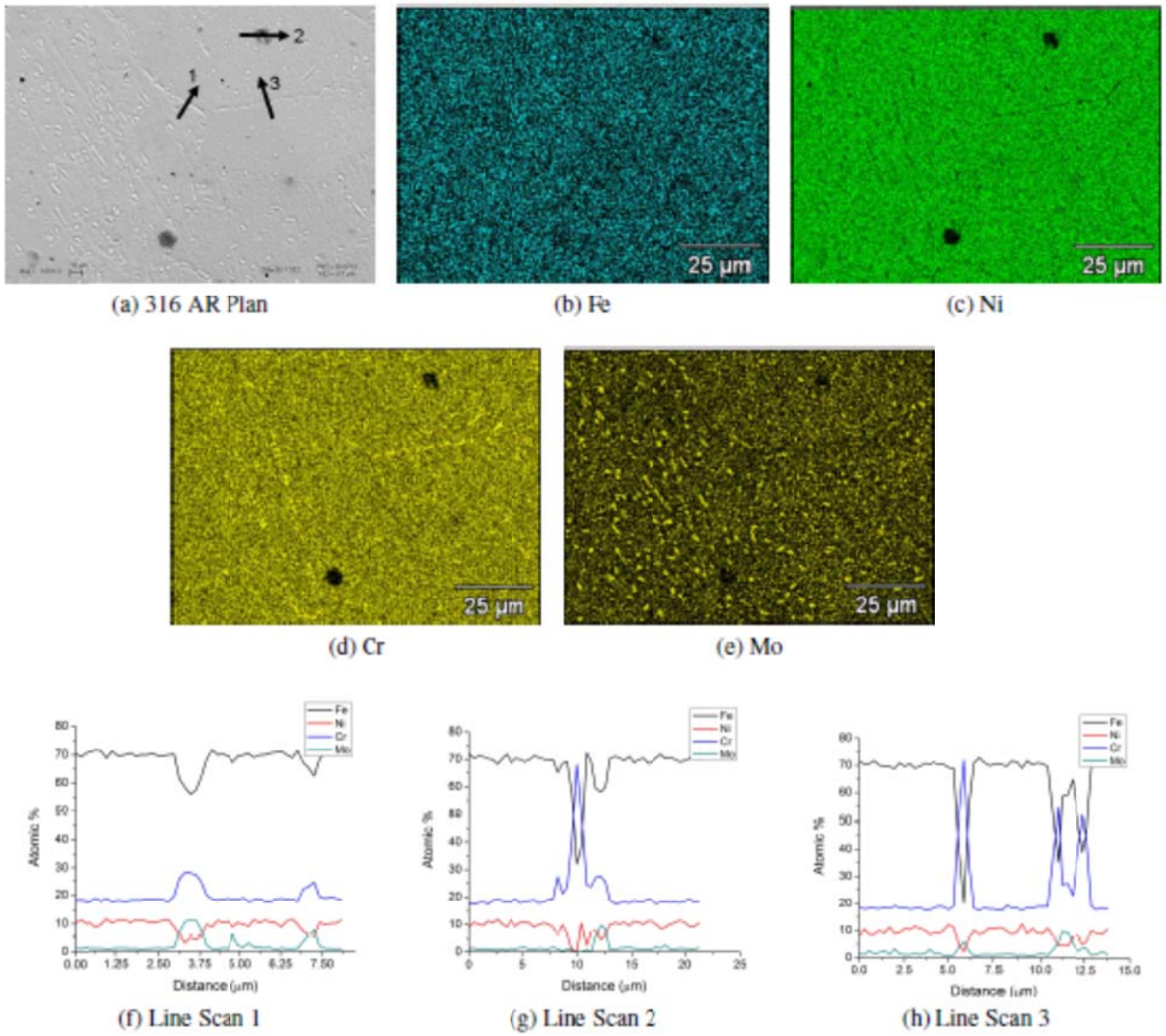

Figure 4.36. Element EDS maps from the cross-section of the AR SS-316 sample.

Cross-sectional view of the sample again showed little to no corrosion of the AR sample. Several small cracks were found in the alloy with the maximum depth of attack of 20 µm after the 500 hour exposure, Figure 4.37.

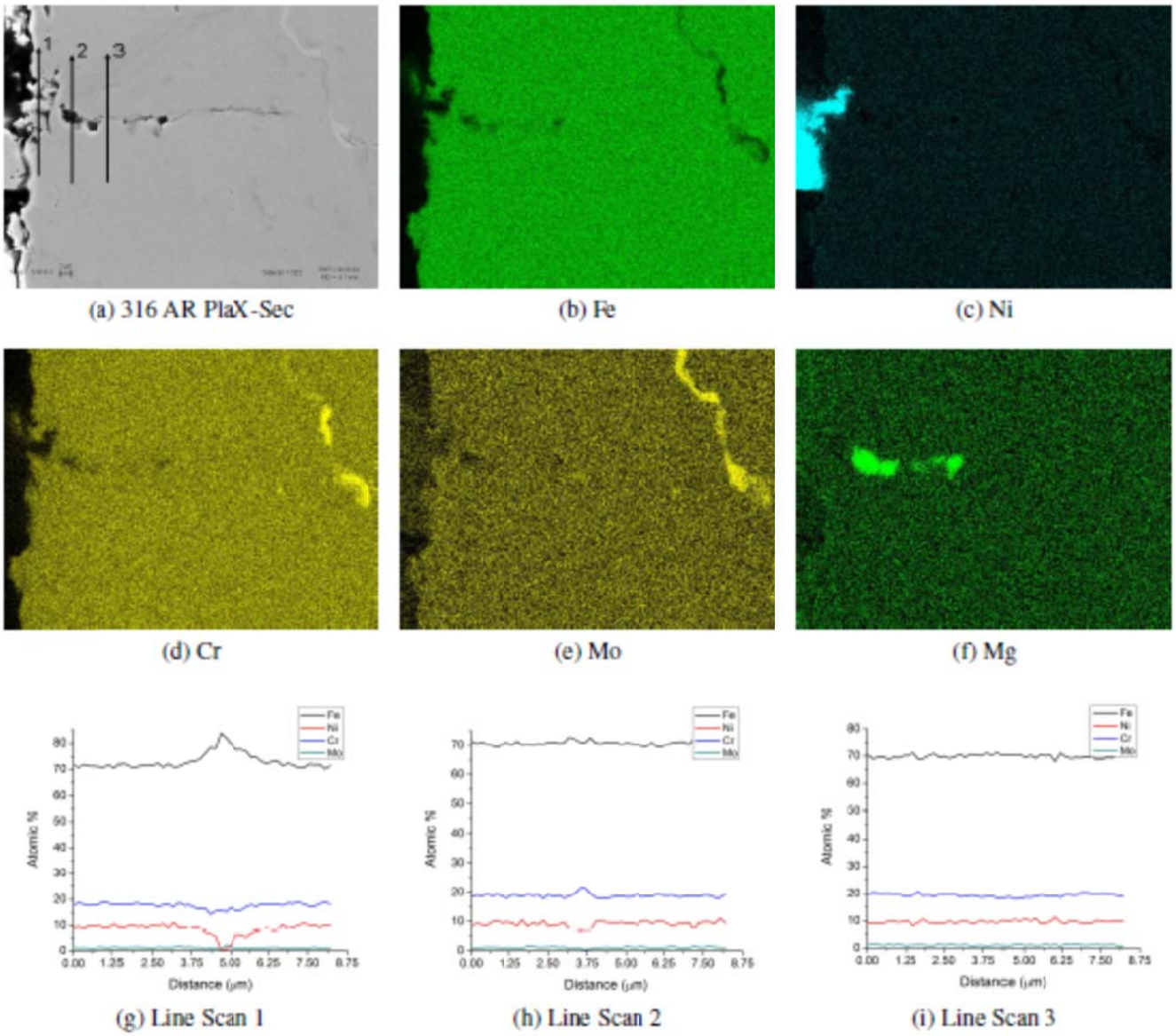

Figure 4.37. Element EDS maps from the cross-section of the AR SS-316 sample.

4.11.2 316 GBE Analysis

The corrosion of the 316 GBE samples behaved similarly to the AR samples as would be expected from nearly identical weight loss. An image from the plan view is shown in Figure 4.38, again the Cr concentration is the same as base alloy composition, or slightly enriched.

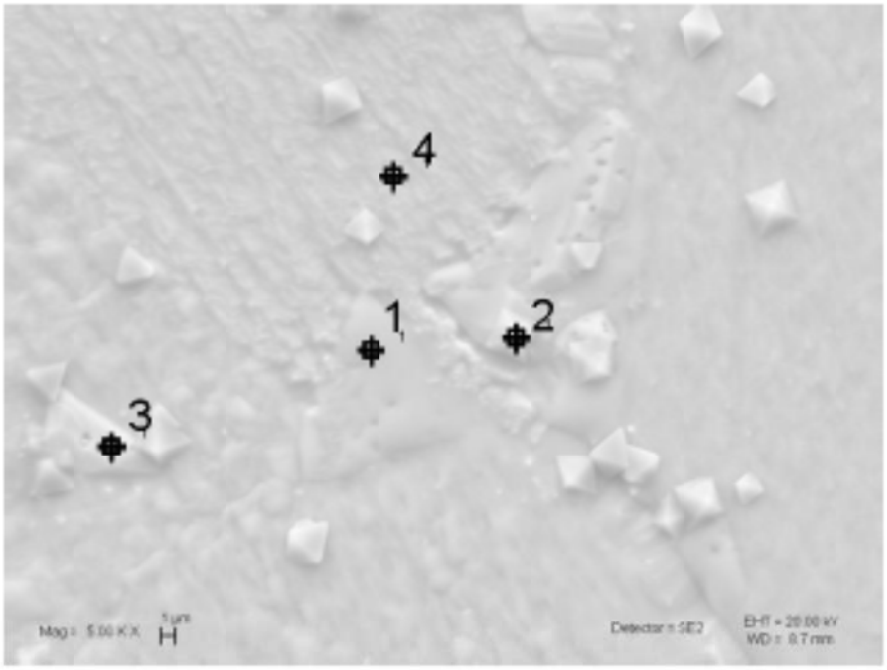

(a) SS 316 - GBE Plan

Point	Fe	Ni	Cr	Mo	Mg	O	Mn	Al	Si	Cl	C
nominal							0.8		1.0		0.03
1	69.0	9.2	18.5	1.0	0.4	47.0	0.5	0.3	1.0		
2	2.7	0.2	1.2	0.0	48.6		0.1			0.1	
3	55.5	2.9	26.9	10.4	1.7		0.9	0.3	1.8		
4	68.8	9.3	18.5	1.1	0.6	0.6	0.6	0.3	0.9		

(b) EDS Data - atomic %

Figure 4.38. Plan View of SS 316 - GBE with point scan data in atomic percent.

Very little sign of attack was seen in the cross-sectional analysis of the SS 316 GBE sample in cross section. One small region of attack was found to a depth of 6 μm, Figure 4.39.

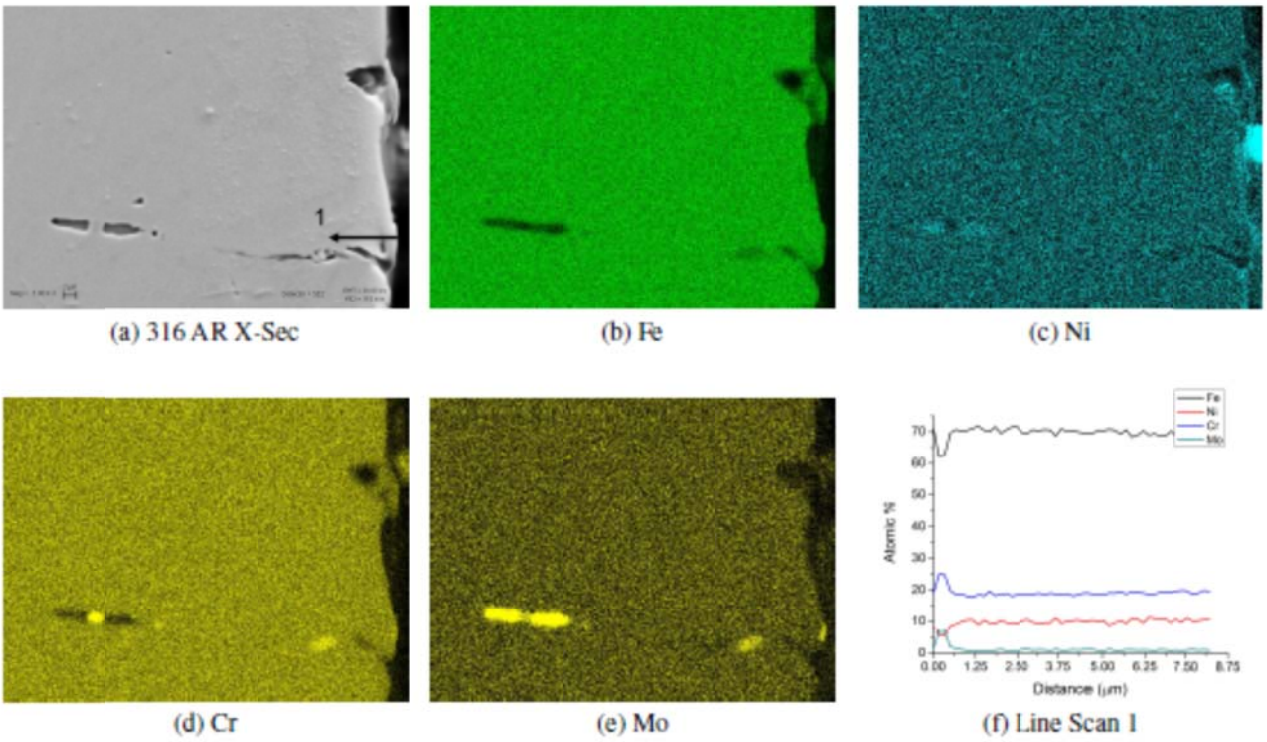

Figure 4.39. Element EDS maps from the cross-section of the GBE SS-316 sample.

The SS-316 samples (AR and GBE) showed excellent corrosion resistance in SS-316 crucibles. This is excellent when considering this alloy for construction of facilities for use with molten salts. In the corrosion study, it is difficult to determine if the AR or GBE has better corrosion resistance to attack from the molten salt.

4.12 Crucible Material

Ideally it is useful to create a crucible from the same material as is being tested. Unfortunately, this requires a significant amount of alloy and salt. This makes corrosion tests more expensive and limits the number of alloys that could be tested. This makes it necessary to find crucible material that can be used for corrosion testing. Over the course of evaluating the corrosion of SS-316 in KCl-$MgCl_2$ salts, tests were completed using three different materials for crucibles, Al_2O_3, quartz, and SS-316. The results from each of these test showed a large variation on the corrosion rate of the sample. A summary of the results for SS-316 and three other alloys is presented in Table 4.3.

Table 4.3. Corrosion rate in g/cm^2 for different alloys exposed to KCl-$MgCl_2$ salts at 850^{o}C.

	Quartz		Al2O3		SS-316	
Alloy	Rate (g/cm^2)	Depth (μm)	Rate (g/cm^2)	Depth (μm)	Rate (g/cm^2)	Depth (μm)
SS-316	7 x 10^{-3}	300	5 x 10^{-4}	10	6 x 10^{-5}	20
Inconel 617	1 x 10^{-2}	225	2 x 10^{-4}			
Hastelloy X	1 x 10^{-2}	160	4 x 10^{-4}			

The volume of salt to surface area in the Al_2O_3 and quartz tests were both 40 grams per square inch of metal surface. The SS-316 crucible was 12 grams of salt per square inch of metal surface. This is small due to the container material providing a large surface area. However, these tests were run for 500 hours, compared to 100 hours for the previous tests.

The effect of changes in crucible material on corrosion experiments has been reported previously, [81]. Quartz containment resulted in the largest weight changes for the three alloys compared in Table 4.3. From the Ellingham diagram, Figure 4.1, for chloride systems, it is seen that the Gibbs energy of formation for silicon-chloride compound is slightly more negative than for $CrCl_2$ at 850°C. This means that the silicon in the quartz is likely to participate in the corrosion processes when in contact with the melt. This is compared to the aluminum oxide which is 1.2 V more negative than the $Fe^{2+} + 2e^- \rightarrow Fe$ process in water. The aluminum oxide is more stable at these conditions and less likely to participate in the reaction.

The aluminum oxide still participates in the corrosion process in these tests. In the corrosion tests used to rank purification techniques, aluminum oxide particles were found on the surface of the 800H coupon, Figure 4.40. The corrosion rate for Al_2O_3 has been determined in literature for NaCl-KCl salt mixture at 700°C [84]. The weight change of the samples was within the value determined for Al_2O_3. For small changes in the sample weight due to corrosion processes, the Al_2O_3 islands significantly affect the weight loss measurements.

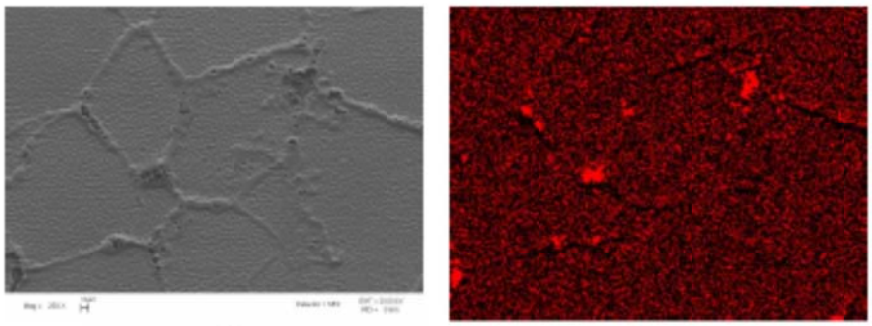

Figure 4.40. Al EDS map for after 24 hour exposure at 850°C to CCl_4 purified salt in Al_2O_3 crucible.

During corrosion tests it was found that metal would plate onto the crucible wall. Reusing of the crucibles resulted in contamination, even with cleaning the crucibles with concentrated HCl. Ni-201 sample was tested in the Al_2O_3 after a test with 800H coupon and another test with a Hastelloy X coupon. When the Ni-201 sample was analyzed in the SEM after 100 hour exposure at 850°C, 7-8 at% of Fe was found to have deposited on the surface of the alloy 4.41. These contaminants came from the previous corrosion test, even with a crucible cleaning intermediate step.

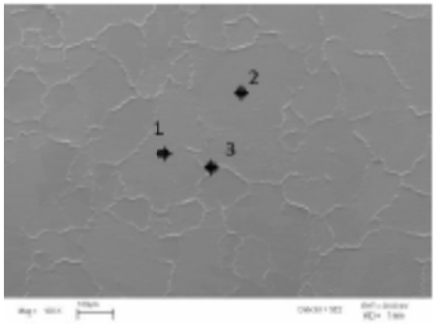

(a) Ni 201 - Al_2O_3 Crucible

Point	Ni	Fe	Cr	Al	Si
1	92.0	7.7	0.3		
2	92.2	7.5	0.3		
3	90.1	8.5	0.3	0.5	0.7

(b) EDS Data - atomic %

Figure 4.41. Plan View of Nickel 201 sample exposed to KCl-$MgCl_2$ in Al_2O_3 crucible point scan data in atomic percent.

4.13 Summary

Corrosion of metals in molten chloride salt systems is a function of the chemistry of the salt and alloy. The salt corrodes the alloys by removal of the most active metal from the alloy, Cr. Four different methods were examined to prepare a salt that would cause a minimal amount of corrosion. Contact of the salt by Mg metal or by CCl_4 bubbling were determined to be the most effective methods for preparing the KCl-$MgCl_2$ salt. Mg contact was selected as the method of choice for all other tests using the KCl-$MgCl_2$ salt.

Ten different high temperature alloys were exposed to molten KCl-$MgCl_2$ salt at 850°C for 100 hrs in quartz ampules to determine which alloy should be used to contain the salt in the forced convective loop. Haynes 230 had the smallest weight loss per unit area of the samples exposed. The results and rank for the other alloys was not clear due to large variations between the three coupons of each alloy. Cross-section analysis of the samples showed that the Cr was removed along the grain boundaries of the samples to depths up to 300 μm deep for most alloys. Nickel 201 and Hastelloy N showed little corrosion as determined by the maximum depth of attack, due to minimal amounts of Cr in these alloys. Inconel 625 and 718 were attacked by uniform depletion of Cr from the surface of the alloy. Examination of Table 4.2 show that Inconel 625 and 718 are similar to other alloys that were attacked along the grain boundaries. The main difference in 625 and 718 from the other alloys is that they contain 3-5 % of Nb in the alloy. Nb is added to the alloys to chemically bind the C in the alloy reducing the formation of chromium carbides at the grain boundaries. The addition of Nb and other C getters in alloys has been shown in the past to reduce the attack of molten salts on alloys [100, 122].

It was also seen that GBE 800H greatly reduced the rate and depth of attack of Alloy 800H. Differences in the internal structure of the 800H alloy was seen in the un-corroded zones inside the

alloy. GBE 800H samples had many regions of Cr enrichment to approximately 30 at % Cr. The AR had only a few regions of high Cr that were enriched to 40-45 at%. Initial testing with SS-316 AR and GBE both showed little to no corrosion. This made determining the effectiveness of this method for SS-316 not possible for the metal coupons exposed to KCl-$MgCl_2$. The maximum depth of attack for all samples examined is listed in Table 4.4.

Table 4.4. Maximum depth of attack of the alloys from the quartz crucible tests. The samples were exposed to KCl-$MgCl_2$ at 850^{o}C for 100 hours.

Alloy	Sample	Depth of Attack	Type of Attack
		μm	
Hastelloy N	N-3	25	
Nickel 201	1-3	35	
Inconel 625	5-1	120	Uniform
Inconel 718	8-1	125	Uniform
800H – GBE	B-1	130	Inter-granular
Hastelloy X	X-2	160	Inter-granular
Haynes 230	Y-2	180	Inter-granular
Inconel 617	7-1	225	Inter-granular
Incoloy 800H	H-1	250	Inter-granular
SS 316	6-3	300	Inter-granular
Inconel 600		no data	

Selection of crucible materials play an important role in the rate of corrosion seen in molten KCl-$MgCl_2$ salt systems. Metal crucibles from the same alloy as to be tested are expensive and require large amounts of salt to produce a large salt volume to metal surface area ratio. Tests in metal crucibles also show minimal corrosion and require a large amount of time to see differences in the corrosion between different alloys. Ceramic crucibles are stable in the chloride salts and can be used, but some interaction is expected between alloy and crucible. Quartz was beneficial in that it accelerated the corrosion of the samples allowing for differences in sample corrosion to be identified. Alumina crucibles were stable and did not accelerate the corrosion rate of the sample. Small amounts of Al were found on the surface of samples tested in Al_2O_3 crucibles. It is also necessary to develop a cleaning procedure for the crucibles between tests if they are to be re-used.

SS-316 showed excellent corrosion resistance to attack to the KCl-$MgCl_2$ salt when exposed in either SS-316 or Al_2O_3 crucibles. This alloy was selected as the material to be used in the construction of the forced convection loop for heat transfer studies at the University of Wisconsin. SS-316 has the advantage in cost and the number of available products made with this alloy.

TASK 3: Forced Convective Loop Design and Construction

One of the main design issues associated with the use of molten salts, as a secondary coolant, is the performance of the IHX that transfers the heat from the high pressure He reactor coolant to the salt system. The high operating temperature of the IHX reduces the maximum amount of stress that is allowed in the heat exchanger tubing before failure occurs. The large pressure difference between the primary and secondary coolants, He ~ 9 MPa & Salt ~ 0.2 MPa, causes large stresses in the tubing separating the two fluids in the IHX. To reduce these stresses to an acceptable level, it is necessary to have thick-walled tubes. To reduce the amount of metal, it is advantageous to use small diameter tubes with thick walls to contain the salt. To reduce the pressure drop of the fluid flowing through these small diameter channels in the IHX, the flow rate of the salt in each tube will be kept in the laminar regime. Although the friction factor in laminar flow is higher, the pressure drop is proportional to the velocity squared making the pressure drop in laminar flow region lower than in the turbulent region.

Initial design specifications for the IHX have called for the flow to have a Reynolds number of ~ 150. A limited amount of experimental data examining molten salts as a heat transfer fluid is available for design purposes in the laminar region. In order to examine the forced convection and laminar friction coefficients of the molten salt in vertical tubes, a forced convection loop was designed, constructed, and operated to measure the friction and convection coefficients of KCl-$MgCl_2$ salt. The goal of constructing this loop was to determine the heat transfer coefficient and pressure drop of the liquid salts in vertical channels under a range of experimental conditions including heat flux and $^{\Delta T}/_{L}$ similar to those proposed in the design by Peterson at University of California Berkeley [13].

In the design of heat exchangers and other components it is important to know the correlations that should be used in engineering design calculations to account for pressure drop and heat transfer of the heat transfer fluid. As part of these correlations, it is necessary to know the thermo-physical properties of the fluid that is to be used. The correlations and salt properties allow for optimization of the system to properly size heat exchangers, pipes, and pumps. Proper sizing reduces over design of the heat transfer equipment and helps in determining system response during accident type scenarios.

Heat transfer of fluids has been well studied and many different correlations exist for different geometries, fluid flow conditions, and thermal boundary conditions. As has been mentioned, laminar flow through a circular channel with a developing thermal boundary layer is of interest in the NGNP IHX design. The velocity of the boundary layer may, or may not, be developed depending on the final design. Heat transfer correlations for these conditions along with many other conditions are available in engineering textbooks and handbooks, e.g. Fundamentals of Heat and Mass Transfer & Perry's Chemical Engineering Handbook.

These correlations differ from each other depending on the thermal and hydraulic conditions of the fluid flowing through the pipe. In other words, the correlations are used by looking at the thermal and velocity boundary layers and the mode of heat transfer at the surface of the pipe: constant temperature or constant heat flux. A general review of the different correlations will be given

followed by results from previous experiments conducted with molten salts for the boundary condition of constant heat flux.

5.1 Heat Transfer and Pressure Drop

The rate of heat transfer from the wall to the bulk fluid by convection is determined by Newton's Law of Cooling

$$q = hA(T_W - T_\infty) \tag{5.1}$$

where the convection coefficient, *h*, is dependent on the fluid and the boundary conditions of the flow. It is necessary to determine the value of *h* to determine the rate of heat transfer to the fluid. Heat transfer correlations are used to estimate the convection coefficient for different boundary conditions in the fluid flow. These correlations use dimensionless numbers to make the values applicable to a wide range of flow conditions. Dimensionless numbers incorporate ratios of different aspects of physical conditions. The value of the dimensionless number gives information to help determine which condition is dominant for a given system condition. Dimensionless numbers are also useful in scaled analysis when it is simpler to work with a simulant fluid, or smaller scale. Some of the more important dimensionless numbers for heat transfer applications are listed in Table 5.1 [123].

Table 5.1. Dimensionless Numbers used in Thermal-Hydraulic Analysis of Fluids.

Dimensionless Number	Value	Ratio of
Re	$\frac{\rho V D}{\mu}$	Inertial and Viscous Forces
Pr	$\frac{C_P \mu}{k}$	Momentum and Thermal Diffusivity
Nu	$\frac{hD}{k}$	Convective and Conductive Heat Transfer
Gr	$\frac{g\alpha(T_W - T_B)D^3}{\upsilon^2}$	Buoyancy and Viscous Forces
Gz	$\mathrm{Re}\,\mathrm{Pr}\frac{D}{L}$	

In the analysis of the IHX and secondary coolant loop, it is also necessary to accurately determine the pressure drop of the fluid. It is necessary to determine pressure drop for sizing of pumps and system analysis. The pressure drop of the fluid is directly related to the pumping power required to move the fluid by Equation 5.2 [124].

$$W = Q\Delta P \tag{5.2}$$

The amount of energy necessary to move the heat transfer fluid is taken from the energy created in the system. A larger pressure drop results in a decrease in the efficiency of the balance of plant.

The pressure drop of the fluid is determined by examining the energy balance of the fluid between two points. The most common energy balance between these two points is described by Bernoulli's Equation [125],

$$\frac{\Delta P}{\rho} + \frac{\mathrm{H} V^2}{2} + g\Delta z \quad = \quad \Im \quad \left[-4f\frac{L}{D} - \left(K_{Cont} + K_{Exp}\right) \right] \frac{V^2}{2} \tag{5.3}$$

The left side of Equation 5.3 describes the energy balance as a change in the kinetic and potential energy of the fluid. The right hand side of Equation 5.3 accounts for any work done by the fluid, or on the fluid. This work term accounts for pumping power, frictional losses, and losses due to sudden contractions and expansions in the flow. To calculate the pressure drop of the system between two points, knowledge of the friction coefficient, *f*, and the losses due to expansions, contractions, or other obstacles, *K*, are needed. Equations, or graphs, are used for determining *f*, while look-up tables are usually used to determine the loss coefficient, *K*, from the obstacles in the system.

In the following sections, the methods and equations for determining heat transfer and friction coefficients of ordinary fluids is discussed, followed by a list and discussion of experimental work done with molten salts.

5.1.1 Laminar Flow

Laminar flow is defined as the region where Re < 2300. Under fully developed conditions, the Navier-Stokes Equation can be solved to determine a theoretical velocity profile in a tube. This well-defined boundary condition allows for analytical solutions to be determined for both heat transfer and pressure drop of a fluid under fully developed thermal and hydraulic flow conditions.

Heat Transfer:

Analytical solutions for heat transfer with fully developed thermal profiles have been solved by many authors for different boundary conditions. In these solutions, the Nusselt number for the fluid flowing through a tube approaches an asymptotic value as the thermal profile for the fluid is developed. The analytical solution for the asymptotic value of the Nusselt number for multiple boundary conditions is presented in Table 5.2 [126].

Table 5.2. Theoretical Nu number for different boundary conditions.

Configuration	Limiting Nusselt Number $N_{Gr} < 4.0$	
	Constant Wall Temperature	Constant Heat Flux
Circular Tube	3.66	4.33
Equilateral Triangle		3.00
Rectangles		
Aspect Ratio		
1.0 (square)	2.89	3.63
0.713		3.78
0.500	3.38	4.11
0.333		4.77
0.25		5.35
0 (parallel planes)	7.60	8.24

The theoretical situation where pure laminar heat transfer occurs in the fluid is seldom reached due to other effects in the fluid, mainly entrance effects. Thus, theoretical equations with experimentally determined coefficients, or experimentally derived correlations, are best for predicting the heat transfer coefficient of the fluid. For the IHX design by Peterson, it is desired to have correlations that take into account the entrance effects due to developing thermal and hydraulic conditions. Listed below are correlations from literature that look at developing thermal layer and developing thermal and hydraulic conditions for normal fluids under constant heat flux.

Developing Thermal

The criteria for determining the heat transfer coefficient for a developed hydrodynamic flow with a sudden change in the boundary conditions of the fluid was originally proposed by Graetz [127 - 129]. The original solution by Graetz was for the boundary condition of a constant wall temperature. Similar solutions exist for the boundary condition of a constant heat flux. From these analytical solutions, the convection coefficient along the length of the tube is theoretically solved.

There are also several correlations in the literature for the laminar heat transfer of a fluid with a fully developed hydraulic profile and developing thermal boundary layer. Most models fit the coefficients to an equation of the form determined analytically, to the experimental data. The following heat transfer correlations are for laminar flow in circular pipes with constant heat flux that accounts for thermal entrance effects.

The first equation has been reported in the VDI Heat Atlas [130] Equation 5.4 and obtained from work by Shah and London [131].

$$Nu = \left[Nu_1^3 + 0.6^3 + \left(Nu_2 - 0.6\right)^3\right]^{1/3} \tag{5.4}$$

where the Nusselt numbers are defined by

$$Nu_1 = 4.364 \tag{5.5}$$

$$Nu_2 = 1.953 Gz^{1/3} \tag{5.6}$$

The entrance effects are accounted for by the addition of the second and third terms in the correlation. Quoted error for this correlation is less than 1% over the entire entrance to fully developed range [130].

A second correlation for these boundary conditions is as follows [132]

$$Nu = 1.953 Gz^{1/3} \quad \text{Gz} >= 33.3 \tag{5.7}$$

$$= 4.364 + 0.0722 Gz \quad \text{Gz} < 33.3 \tag{5.8}$$

It should be noted that as the entrance effects become minimal for both correlations as $\mathrm{Re}\,\mathrm{Pr}\,\frac{d}{L} \to 0$. Under this limit, Equation 5.4 goes to the theoretical value of 4.364, the value in Table 5.2 under the same boundary conditions.

Developing Thermal & Hydraulic

There are also several correlations that account for simultaneously developing thermal and hydraulic layers.
Several sources exist that contain correlations to estimate the heat transfer when both thermal and boundary layers are being developed. The first correlation has been reported in the VDI Heat Atlas [130] Equation 5.9.

$$Nu = 0.924\,\mathrm{Pr}^{1/3}\left(\mathrm{Re}\,\frac{D}{L}\right)^{1/2} \tag{5.9}$$

It should be noted that Equation 5.9 should only be used when the values obtained with them are greater than the values obtained from Equation 5.4.

The second correlation that is used for comparison to the experimental data is Equation 5.10, [133]:

$$Nu = 4.364 + \frac{0.086\left(\mathrm{Re}\,\mathrm{Pr}\,D/L\right)^{1.33}}{1 + 0.1\,\mathrm{Pr}\left(\mathrm{Re}\,D/L\right)^{0.83}} \tag{5.10}$$

This correlation is valid for 0.7 < Pr < 7. If Gz < 33, then Equation 5.10 is also valid for Pr > 7.

The third correlation that is used to examine the laminar heat transfer in the tubes is a correlation proposed for the local heat transfer coefficient by [134] and Ozoe [134], Equation 5.11:

$$Nu = 4.364\left(1 + \left(\frac{Gz\frac{\pi}{4}}{29.6L}\right)^{\frac{1}{6}}\right)\left(1.0 + \left(\frac{\left(\frac{Gz\frac{\pi}{4}}{19.04L}\right)^{0.5}}{\left(1 + \frac{Gz}{0.0207}\right)^{\frac{2}{3}}}\right)^{\frac{3}{2}}\right)^{\frac{1}{2}} \tag{5.11}$$

$$Nu = 4.364\left(1 + \left(\frac{Gz\frac{\pi}{4}}{29.6L}\right)^{1/6}\right)\left(1 + \left(\frac{Gz\frac{\pi}{4}}{29.6L}\right)^{1/6}\right) \tag{5.11}$$

Pressure Drop

The well defined nature of the velocity profile of a fluid in the laminar regime also makes it possible to analytically solve for the iso-thermal pressure drop of the fluid. The friction coefficient for fully developed laminar flow is given by Equation 5.12, the Hagen-Poiseuille equation [125]:

$$f = \frac{16}{\mathrm{Re}} \tag{5.12}$$

This friction factor is independent of all conditions in the fluid except the Reynolds number, if the fluid is a Newtonian fluid.

Losses due to a sudden expansion and contraction are called form losses (K). The form losses due to expansion and contraction used in laminar flow are those outlined in Perry's Chemical Engineering Handbook [135], Equations 5.13 and 5.14, respectively

$$K_{Exp} = 2\left(1 - \frac{A_{small}}{A_{Large}}\right)^2 \qquad \mathrm{Re} < 2300 \tag{5.13}$$

$$K_{Cont} = -4f\left(0.3 + 0.04\,\mathrm{Re}\right) \qquad \frac{A_{small}}{A_{Large}} < 0.2 \;\&\; \mathrm{Re} < 2300 \tag{5.14}$$

5.1.2 Turbulent Flow

Turbulent flow is normally defined as the region when Re > 5000, and sometimes it is defined as the region when Re > 10,000. Under these conditions, the velocity boundary layer is more random with no simple analytical solution. The general velocity profile of an ordinary fluid under these conditions is a sharp increase from zero velocity at the wall to the maximum velocity profile which is flat. Unlike laminar flow, there are two components of the velocity profile in the radial and axial directions during flow through the pipe causing eddies' in the fluid. This complexity makes the number of analytical solutions under these conditions minimal, without assumptions. Much experimental work has gone into developing correlations for the heat transfer and friction coefficients in this regime for specific conditions.

Heat Transfer

The lack of an analytical solution requires the use of empirical correlations to determine the heat transfer and pressure drop. Of the many correlations, the most common correlations are the Dittus-Boelter Correlation, Equation 5.15, and the Chilton-Colborn Correlation, Equation 5.16.

$$Nu = 0.023\,\mathrm{Re}^{0.8}\,\mathrm{Pr}^{0.40} \tag{5.15}$$

$$\mathrm{Nu} = 0.023\,\mathrm{Re}^{0.8}\,\mathrm{Pr}^{0.33} \tag{5.16}$$

There are other correlations that are more specific for tube geometries and also correlations that account for other factors, such as skin temperature. The correlation that is recommended by several

authors [123, 130] and originally presented by Gnielinski is valid for Re > 3000 . Equation 5.17 also accounts for deviations due to skin temperature by addition of the last term, the ratio of bulk to wall Prandtl numbers.

$$Nu = \frac{\left(f/8\right)\left(Re-1000\right)Pr}{1+12.7\sqrt{\left(f/8\right)}\left(Pr^{2/3}-1\right)}\left[1+\frac{d}{L}\right]^{2/3}\left(\frac{Pr}{Pr_W}\right)^{0.11} \quad (5.17)$$

where f is the value defined by Equation 5.19. Equation 5.17 is recommended for use for fluids with $3000 < Re < 5 \times 10^6$ and $0.6 < Pr < 2000$.

Pressure Drop

Correlating pressure drop for a fluid flowing under conditions of Re > 5,000 is again more complicated than correlation for conditions of laminar flow. The most common method for determining friction factors for turbulent flow is with the aid of the Moody Chart [125]. The Moody Chart requires reading from a chart the value of the friction coefficient *f*. The friction coefficient, *f*, is dependent on the Reynolds number and the ratio of the roughness of the container surface divided by the diameter of the tube in transitional and turbulent flow.

For computational modeling, several different correlations exist to estimate *f* based on these conditions. The simplest assumption is for the case of a smooth pipe wall. Then the Blasius Equation 5.18 is used to correlate *f* to the Reynolds number.

$$f = \frac{0.079}{Re^{0.25}} \quad (5.18)$$

Equation 5.18 is valid for smooth pipes with 4,000 > Re > 100,000 [135].

Another form of the friction factor for smooth pipes is given by the following equation:

$$f = \frac{1}{\left[1.82\ln\left(Re\right)-1.64\right]^{-2}} \quad (5.19)$$

The friction factor, *f*, from Equation 5.19 needs to be divided by 4 to be used in Bernoulli's Equation 5.3 for the prediction of pressure drop. This factor of 4 is a constant that is sometimes applied to the friction coefficient to reduce the coefficients. Likewise *f* from Equation 5.18 needs to be multiplied by 4 to be used in Equation 5.17.

Under the conditions of turbulent flow, several analogies have been shown to relate friction and heat transfer coefficients, one of which is the Chilton and Colborn Analogy. The Chilton-Colborn Analogy relates friction, mass transfer, and heat transfer coefficients by analogy to a 'j' factor [136]:

$$j_M = \frac{f}{2} \qquad j_H = \frac{h}{C_P G}Pr^{2/3} \qquad j_D = \frac{k_C \rho}{G}N_{Sc}^{2/3} \quad (5.20)$$

The j-factors are experimental values based on geometry and flow conditions for the system. For Re > 10,000, $j_M = 0.023\ Re^{-0.2}$. Substitution into Equation 5.20, results in a solution for the Nu number identical to Equation 5.16 for heat transfer and Equation 5.18 for the friction coefficient.

$$f = \frac{0.46}{Re^{0.2}} \quad (5.21)$$

Equation 5.16 is valid for turbulent flow of fluids Re > 10,000 and 0.7 < Pr < 70.

5.1.3 Transitional Regime

In the intermediate region between turbulent and laminar flow, the flow is random and much effort has been applied to determine correlations that will fit the data for this region. Some correlations exist that predict the heat transfer and pressure drop, other methods include interpolating between the laminar and turbulent values.

Heat Transfer

A common method for determining the heat transfer coefficient is to interpolate the heat transfer coefficient from Equations 5.4 and 5.17 evaluated at Re = 2300 and Re = 5000, respectively. Mathematically the Nu number in mixed flow is defined by Equation 5.22

$$Nu = Nu_{Lam}(\mathrm{Re}=2300)*\left(1-\frac{\mathrm{Re}-2300}{5000-2300}\right)+Nu_{Turb}(\mathrm{Re}=5000)*\left(\frac{\mathrm{Re}-2300}{5000-2300}\right) \quad (5.22)$$

However, there are correlations that take into account the transitional regime, Equation 5.17 has been shown to cover the transitional regime for Re > 2300. Another equation from Gnielinski, [137], is valid for liquids over the range 1.5 < Pr < 500 and 2300 < Re < 10^6

$$Nu = 0.012\left(\mathrm{Re}^{0.87}-280\right)\mathrm{Pr}^{0.4}\left[1+\left(\frac{d}{L}\right)^{2/3}\right]\left(\frac{\mathrm{Pr}}{\mathrm{Pr}_W}\right)^{0.11} \quad (5.23)$$

Pressure Drop

Since the flow is transitional, little reliable data is available for the prediction of f in the mixed flow regime. A correlation has been proposed by Manning [126] that correlates f over the laminar, mixed, and turbulent regions. For current considerations in the transitional regime, the correlation for the friction factor in turbulent flow, Equation 5.19, is satisfactory.

5.1.4 Natural Convection

Natural convection occurs when a temperature difference in a system causes a buoyancy driven flow. The nature of this flow causes a different velocity distribution than in the forced convection cases discussed previously. As such, the convection coefficient also varies in these situations. A general rule for determining if the natural convection effects are significant is to determine the following ratio:

$$\frac{Gr}{\mathrm{Re}^2} \quad (5.24)$$

If Equation 5.24 is << 1, then forced convection is dominant. Likewise if Equation 5.24 >> 1, then natural convection is the dominant heat transfer force. Natural convection flows are also characterized by the Rayleigh number,

$$Ra = Gr\,\mathrm{Pr} \tag{5.25}$$

it is simply the Grashof number multiplied by the Prandtl number.

Many correlations exist for predicting *h* for natural convection in different geometries, again only correlations that are relevant to the geometry and conditions being examined are mentioned. The first correlation that is given for determining the heat transfer coefficient in a heated tube internal flow problem is recommended by the VDI Heat Atlas [130]:

$$Nu = 0.0625Ra \qquad \mathrm{Gr} < 1 \tag{5.26}$$

$$Nu = 0.52Ra^{1/4} \qquad \mathrm{Gr} > 1 \tag{5.27}$$

Another recommended correlation for heat transfer in a vertical channel is recommended by [132]

$$\frac{h_M}{\left[k_f^2\rho_f^2 C_P g\beta\Delta t\mu_d\right]^{1/3}} = 0.13 \tag{5.28}$$

Equation 5.28 can be simplified using the non-dimensional numbers to

$$Nu = 0.13Ra^{1/3} \qquad \mathrm{Gr} < 1 \tag{5.29}$$

5.1.5 Mixed Convection

The case when neither natural convection, or forced convection, is the dominant force is called mixed convection. Two main situations occur for the mixed convection regime, opposed and aiding. Opposed heat transfer is the case when the flow is down flow/heating, or up flow/cooling. Under these conditions, the natural convection causes a flattening of the boundary layer along the wall. This flattening decreases the rate at which heat is transferred to the fluid, which decreases the forced convective heat transfer coefficient. In the aiding situation, the buoyancy forces are in the same direction as the forced flow and generally increase the heat transfer rate to the fluid [138]. In the case of aiding flow, degradation of the boundary conditions can occur at local regions causing a decrease in the local Nusselt number and increases the local wall temperature [138, 139]. The effect of this degradation in local heat transfer is a local hot spot in the wall temperature.

In general, the heat transfer coefficient for the mixed convection regime is approximated by either adding, or subtracting, the Nusselt numbers for forced and natural convection:

$$Nu_{mixed} = \left(Nu_{FC}^n \pm Nu_{NC}^n\right)^{1/n} \tag{5.30}$$

where n = 2, 3, 7/2, or 4 [123, 130]. In the case of aided mixed flow the Nu numbers are added, in opposed flow, subtracted.

A more specific correlation for mixed convection of laminar flows with constant heat flux is the following [138]

$$Nu = 0.95\left(\frac{Gr^*}{\mathrm{Re}}\right)^{0.28} \quad (5.31)$$

This correlation is valid for the range of $100 < \mathrm{Gr}^* < 10{,}000$.

The axial distance to the increase in wall temperature was correlated also by Rouai [138]

$$\frac{z}{D} = 0.051\left[\frac{Gr^*}{\mathrm{Re}^{3.425}\,\mathrm{Pr}^{0.8}}\right]^{-0.8} \quad (5.32)$$

A more general form to calculate the heat transfer coefficient of a mixed flow problem is given by the following correlation [138]

$$\frac{Nu}{Nu_{FC}} = \left[\left|1 \pm 8x10^{-4}\,\frac{Gr^*}{\mathrm{Re}^{3.425}\,\mathrm{Pr}^{0.8}}\left(\frac{Nu}{Nu_{FC}}\right)^{-2}\right|\right]^{0.46} \quad (5.33)$$

There is a discontinuity in this equation for heated up flow at $\frac{Gr^*}{\mathrm{Re}^{3.425}\,\mathrm{Pr}^{0.8}} \sim 3 \times 10^{-6}$ [138]. However, the fractional change in the heat transfer coefficient of the fluid in aiding mixed flow can then be determined by Equation 5.33. This allows for the determination of the Nusselt number for aided mixed flow.

5.1.6 Radiation

Radiation heat transfer is a method by which the energy is transferred by means of electro-magnetic waves. The Stefan-Boltzmann Equation, Equation 5.34, is used in the determination of the rate of heat transfer by radiation between two surfaces.

$$q = \varepsilon k_B F_{H\to C} A\left(T_H^4 - T_C^4\right) \quad (5.34)$$

Through approximations as outlined by Adams, [140], the effect of radiation on the heat transfer of a participating fluid can be approximated by manipulating Equation 5.34 to a form similar to Newton's Equation of Cooling 5.1. This can be written as

$$q = h_r A\left(T_W - T_F\right) \quad (5.35)$$

combining Equation 5.34 and Equation 5.35, h_R is defined as

$$h_R = \varepsilon k_B F_{H\to C} A\left(T_H^3 + T_H^2 T_C + T_H T_C^2 + T_C^3\right) \quad (5.36)$$

For a small temperature difference, the right of Equation 5.36 can be approximated as $\overline{T^3}$, where $\overline{T}$ is the average temperature of T_H and T_C. If the geometry is known, the view factor can be computed for it. Then all that needs to be approximated to examine the radiative heat transfer is the ε term in Equation 5.34.

Combining Equations 5.35 and 5.36, the following can be used to model the amount of energy transferred by radiation from the wall to the fluid under the conditions of minimal differences in

wall and fluid temperature. The view factors are defined by the geometry of the fluid. The amount that the fluid participates in the radiation heat transfer needs to be accounted for with the ε term in Equation 5.36.

5.1.7 Salts as Coolants

Several forced convection experiments have been conducted with molten salts to determine correlations for the forced convection coefficient for nitrates[141, 142] and fluorides[29, 141, [143 - 146]. There have also been several studies of the natural convection of internally heated fluoride fuel salts [147]. The natural convection experiments were conducted in reactors with dissolved uranium salt fissions providing the heat source to drive the natural convection. A compilation of the general experimental conditions and operating parameters for these experiments is presented in Table 5.3. No detailed experiments containing chloride salts as heat transfer agents have been found in the literature.

Table 5.3. Summary of Heat Transfer Experiments with molten salts.

Salt	Metal	D (cm)	Re	Pr	T_{salt}	T_{wall}	q" (kW/m^2)	Orientation	# of Runs	Ref
FORCED CONVECTION										
FLiNaK	Ni	0.3	3,200-8,600	4.9 – 14.3	527 – 734	535 – 753	73 – 604	Hor	10	[141]
FLiNaK	SS-316	0.46	10,000-15,000	4.71-5.17	722-745	733-753	250-355	Hor	7	[141]
FLiNaK	Inc 600	0.44	3,900 – 12,000	5.62 – 7.31	646 – 702	662 – 727	29 – 540	Hor	12	[141]
FLiNaK	Inc X	0.62	2,700 – 20,800	5.03 – 13.18	540 – 729	570 – 793	28 – 606	Hor	52	[143]
FLiNaK	Inc 600	4.1	14,000 – 93,100	6.29 – 10.81	575 – 675	n/a	n/a	Vert	33	[144]
FLiNaK	Kh10N18T	0.3	5,000 – 15,000	n/a	550 – 650	n/a	30 – 60	Vert	45	[145]
LiF-BeF_2-ThF_4-UF_4	Hast N	0.46	400 – 36,000	4-14	566 – 843			Hor	70	[146]
67.5-20.0-12.0-0.5										
NATURAL CONVECTION										
LiF-BeF_2-ThF_4-UF_4	Kh10N18T	1-12	--	1.5 – 30	--	500-750	0 -25	H/V	--	[147]

A general overview of each of the FLiNaK tests showed that the analyses of the data from the experiments were done with different physical properties of the fluid. As a result, the experimental data measuring the heat transfer coefficient could not be compared across experiments. The write ups containing the experimental data allowed for re-calculation of the experimental data with consistent and accurate values for the physical properties. Upon recalculation of the experimental data, the values for each of the FLiNaK tests in Inconel alloy tubing followed the Dittus-Boelter correlation, Equation 5.15, within ±15% [71].

The data for all of the forced convective heat transfer experiments is presented in Figure 5.1. The experimental Nu number is compared to the theoretical Nusselt number computed from Equation 5.4 for Re < 2300 and Equation 5.23 for Re > 2300. From examination of Figure 5.1 and other literature sources[29], molten salts seem to behave as a Newtonian fluid and can be generally modeled by correlations for these fluids. However, little work has been done in the laminar and mixed convection regime of molten salt heat transfer.

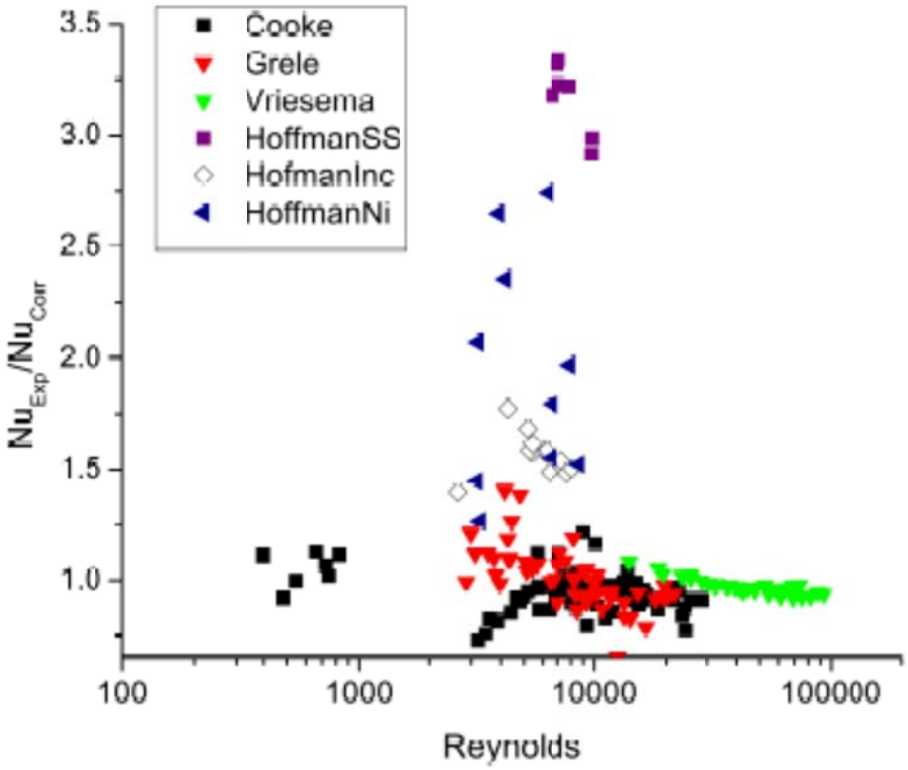

Figure 5.1. Experimental Nusselt number compared to the theoretical Nusselt number as computed from standard correlations. The data for FLiNaK was evaluated with the properties listed in [9].

Very little experimental data exists for pressure drop in molten salt flow systems. One experiment by [144] at Delft University [144] measured the isothermal pressure drop of FLiNaK in an Inconel 600 tube. The pressure drop of FLiNaK at 575, 625, and 675^{o}C was measured across an isothermal test section. The Reynolds number for the fluid ranged from 10,000 < Re < 75,000. It was found that the friction coefficient could be modeled using a form similar to the Blausius Equation 5.18 [144]

$$f = \frac{0.2657}{\mathrm{Re}^{0.2058}} \quad (5.37)$$

From the Chilton-Colborn correlation relating heat transfer of a fluid to the friction coefficient and available heat-transfer data, it is expected that the friction coefficient should also follow correlations for 'normal' fluids.

For natural convection, studies in Russia have looked at the natural convection heat transfer of salts with electrically heated walls or with a volumetric heat generation in the salt in thermosyphons. Thermosyphons are closed cylindrical tubes where the salt was heated on the bottom and cooled along the length of the test driving a natural convection flow. Tests were conducted on several different geometries and also for angles from $0 \rightarrow {}^{\pi}/_{2}$. A general review of these experiments is presented by Ignaytev [147]. From comparison of the heat transfer of water and glycerine with the molten salts, it was found that general correlations based on these fluids model the natural convection heat transfer of molten fluoride salts.

Molten salts also possess a unique characteristic in that they are transparent to most of the infrared rays emitted. This fact makes measuring the thermal conductivity of the fluids more difficult because of the ability of heat transfer by radiation during thermal conductivity experiments. Corrosion products may not be as transparent, causing the fluid to participate in radiation heat transfer [46, 148]. This interaction is believed from a decrease in the apparent thermal conductivity of the fluid over time. Re-examination of all the available heat transfer data show that the rate of heat transfer to the salts by radiation heat transfer is negligible compared to the forced convection heat transfer in the experimental data [29, 71].

5.2 Scaled Analysis

Experimental studies to better understand the thermal-hydraulic analysis of molten salts is often undertaken with a simulant fluid [149, 150]. This is done due to the complexity associated with working with high temperature molten salts. In order to assure a direct comparison between the working fluid and molten salts, it is necessary to scale the experimental geometry and fluid conditions (velocity and temperature) of the simulant fluid to match the proper dimensionless number. These experiments are usually conducted with heat transfer oils or aqueous solutions that match the dimensionless numbers under consideration. Some research on molten salts has replaced FLiBe ($2LiF\text{-}BeF_2$) with nitrate salt for ease of operation [151].

In scaled analysis it is essential that the dimensionless numbers are matched to obtain data similar to that desired for the actual fluid. In experiments studying the heat transfer and pressure drop, it is necessary to match the Reynolds and Prandtl numbers. For experiments looking at different physical phenomena in the system, other dimensionless numbers are matched to meet the desired criteria [152]. Table 5.1 lists a large number of the dimensionless numbers. For general thermal-hydraulic analysis, the first dimensionless number that is matched is the Reynolds number. To match Reynolds between the simulant fluid (sf) and the molten salt (ms), the following condition must be met:

$$\mathrm{Re}_{sf} = \mathrm{Re}_{ms} \rightarrow \frac{\rho_{sf} V_{sf} D_{sf}}{\mu_{sf}} = \frac{\rho_{ms} V_{ms} D_{ms}}{\mu_{ms}} \quad (5.38)$$

The Reynolds number is matched by changing geometry (D) of the test, flow rate of the system (v), or the temperature of the system (ρ and μ).

The other dimensionless number that must be matched for forced convection is the Prandtl number. The Prandtl number is dependent on the physical properties of the system. The only adjustable parameter is the temperature to match the Prandtl number between the simulant fluid and the molten salt.

5.3 Overview of Forced Convection Loop

To further understand the thermal-hydraulic effects of molten salts in the laminar regime, a forced-convective loop was designed, constructed, and operated. The forced convective loop was designed and built to measure the heat transfer and friction coefficients of liquid salts in different diameter tubes in vertical upflow. The tests will examine the heat transfer coefficient and friction coefficient in laminar flow conditions, including prototypical conditions similar to those expected in the IHX of the NGNP secondary loop, namely q", *Re*, and $^{\Delta T}/_{L}$ will be kept similar to the design by Peterson. The forced convection loop built for the experiment is constructed from AISI-316 Stainless Steel based on findings from corrosion studies, Chapter 4, and cost. Two single channel test sections will be used over the course of the experiment (0.083" and 0.370" ID). All test sections will be 24" in length. Commercial equipment for the loop was not available (mass flow meter and pressure sensor), or was too expensive (centrifugal pump). This equipment and instrumentation was then designed and constructed at the University of Wisconsin. A vertical-cantilever centrifugal pump was designed and constructed to move the salt through the experimental apparatus. In addition, a thermal mass flow meter was designed and calibrated using water and Paratherm NF coupled with a Coriolis mass flow meter to measure flow rate. The differential pressure across the test section is measured based on a manometer type device, using high resolution laser displacement sensors to measure the location of the liquid surface in each leg of the manometer. Figure 5.2 is a photograph of the experimental apparatus.

Figure 5.2. The forced convection loop for experiments involving high temperature molten salts.

5.4 Test Sections

To determine the heat transfer and friction coefficients for geometry similar to IHX design, two different diameter test sections were chosen. These test sections are single channel extruded seamless 316 stainless steel tubing. The diameter of the test sections are approximately 2 and 10 mm. The different parameters for each of the test sections is listed in Table 5.4.

Table 5.4. Tests sections that will be used to characterize the heat transfer and friction coefficients for molten salt.

Test Sec	Num of Channels	D (in)	D (mm)
1	1	0.083	2.1
2	1	0.370	9.4

The test sections were constructed using commercial SS tubing. A 25" long piece was cut from the 20' purchased tube. The 25" tubing was then welded into a manifold (1" D disc 1/2" deep). The manifold is then welded to the 1" SS-316 main loop tubing. The 1" tube was originally connected to the loop using 1" Swagelok fittings. These fittings failed to keep a tight seal on the loop during operation with the KCl-$MgCl_2$ salt. The Swagelok fittings were removed and the test section was welded directly into the loop on all tests with the KCl-$MgCl_2$ salt. Figure 5.3 is a photograph of test section #1.

Figure 5.3. The 0.5" test section for experimentation with the molten salt loop.

The inlet and outlet temperature of the fluid is measured 0.75" up stream and down stream from the test section using a 1/4" SS-316 clad K-type thermocouple. To ensure mixing at the exit of the test section, a simple mixer is inserted at the exit of the test section to force the fluid to change directions four times before flowing past the thermocouple. In addition, the pressure taps for the pressure drop measurement are located 2" up stream and down stream from the test section. The wall temperature is measured at 5 locations along the axial length of the test section, at 0", 6", 12", 18", and 24". The thermocouples are attached to the wall by welding K type thermocouples to the tube wall.

The test sections are heated using NiCr resistance wire wrapped around the test section. A DC power supply is used to pass the current through the NiCr wire. The wire is wrapped to make 4 turns per linear inch of tubing. Scotch 69 tape is wrapped around the tube to form an insulated barrier between the wire and the test section. 19 AWG wire is then wrapped around the test section. An 80" active length of 15 AWG - NiCr 65 wire with a 4 wire, 6" lead is used to heat the 1/2" OD test section. A 90" active length of 19 AWG - NiCr 60 wire with a 4 wire, 6" lead is used to heat the 1/4" test section.

5.5 Material Selection

In the determination of what alloy to construct the molten salt loop, several factors were examined: corrosion, raw material cost, and availability of different forms. Hastelloy N, as has been mentioned, was developed for molten fluoride salt applications at ORNL. Hastelloy N has excellent corrosion resistance to molten alkali halide salts. Hastelloy N is not currently produced in large quantities in any form (bar, rode, etc). This lack of material and the cost (Ni-based alloy and special mill) to produce more for construction make Hastelloy N too expensive an option for construction of the loop.

Two main alloys were considered for construction of the molten salt loop, AISI-316 and Inconel 600. These two alloys are widely available for purchase in many different pipe and tube sizes. In addition, it is possible to get pump components made from both of these alloys.

The corrosion characteristics of the considered alloys have been discussed in the previous section regarding corrosion. The corrosion resistance of each of these alloys was then investigated. Research at ORNL as part of the ARE tested these two alloys in similar conditions in FLiNaK salt. It was seen that the depth of attack in the SS-316 was less than that for Inconel 600 [9]. Similar results were seen for screenings of these two alloys in a chloride salt. In corrosion screening for a heat treatment salt (NaCl-KCl-$BaCl_2$, 30-20-50), the depth of attack in SS-316 was ~$^1/_2$ of that for Inconel 600 [153]. From the corrosion work with KCl-$MgCl_2$ salt, Chapter 4, and literature sources it was determined that the difference in the corrosion of these two alloys was not a determining factor in the alloy selection for construction of the loop.

The availability of the alloys was a consideration for the selection of the alloys. It was necessary to construct most of the equipment and instrumentation for the loop from parts available. For example, the molten salt pump was constructed using a suction cover, impeller, and adapter from a commercial pump. From this standpoint, more products are available off of the shelf for SS-316 than Inconel 600.

Another factor in the choice of material for construction was the cost of the alloys. SS-316 is an iron based alloy while Inconel-600 is a nickel-based alloy. The price of melt ready nickel in April 2008 was $28,777, while the cost of No. 1 heavy-melting steel was $487 dollars [154]. The nickel costs 60x more than the iron. For the alloys, similar parts of Inconel 600 is approximately 15x the cost of SS. From this aspect, using a nickel-based alloy would increase the cost of the loop from ~$10,000 to $150,000.

The resulting decision was to build the molten salt loop out of AISI-316 stainless steel. In order to limit galvanic coupling, all materials that are wetted by the salt in the loop are made out of SS-316. The decision to use SS-316 was made due to the availability and cost of the material. It was determined that SS-316 had acceptable corrosion resistance to the KCl-$MgCl_2$ salt and the corrosion products should not affect the results of the experiment.

5.6 Molten Salt Pump

To test the heat transfer coefficients and the frictional pressure drop in the molten salt loop, it is necessary to have a pump for movement of the fluid. The minimum operating temperature of the pump and pump components of the molten salt loop need to be at least 50^{o}C higher than the melting temperature of the salt of interest. This temperature cushion is to help ensure that freezing of the salt does not occur in the pump and loop components. For KCl-$MgCl_2$ this requires that the minimum operating temperature of the pump and loop be 475^{o}C. The maximum operating temperature for the pump is desired to be at least 600^{o}C. This temperature allows for the exit temperature of the salt from the test section to approach 850^{o}C, the expected outlet temperature of the salt from the IHX.

5.6.1 Commercial Pump Products

Initially, a surplus molten salt pump that could operate at temperatures up to 700^{o}C was to be obtained for the experiment. This pump was constructed from Inconel 600, but had been sold previously and was no longer available. A search of commercial vendors took place to see if a

commercial source existed for a molten salt pump, or a pump that could operate at these temperatures.

Very few commercial pumps are available that can operate at temperatures in excess of ~ 400^{o}C. This is mainly due to temperature restrictions on materials used to seal the pump and lubricate bearings. There are multiple vendors that sell molten salt pumps: Nagle, Lawrence, Wempump, and others. These pumps are vertical-cantilever centrifugal pumps that keep the bearings removed from the salt and heat. These pumps also sit in a reservoir of the process fluid to reduce concerns of leakage from the pump housing. These commercial pumps either were not designed to operate continuously (molten salt transfer pumps) at these high temperatures, or had flow rates much higher than those needed for the experiment. Several companies build custom pumps that would be able to meet the experimental requirements of high temperature and low flow rate. These custom pumps were deemed to be too expensive for this project.

After consideration of all of these facts, it was decided to build the centrifugal pump in the Engineering Physics machine shop at the University of Wisconsin. Molten salt pumps were operated as part of the ARE and MSRE projects at ONRL [155]. The MSR pumps were more complicated than the surplus pump that was never obtained. As such the molten salt pump for the current application is based off of the design of the surplus molten salt pump.

5.6.2 Molten Salt Pump Construction

As was previously mentioned, the main limitations of most commercial pumps that prevent operation at higher temperatures are degradation of the bearing lubricants and sealing materials. Vertical cantilever centrifugal pumps are advantageous because the bearings are removed from the working fluid. It is then possible to keep the temperature of the bearings at a much lower temperature than the working fluid. The pump is also placed inside a reservoir to eliminate the need for a completely leak free seal. The design for the pump and components associated with it are shown in Figure 5.4.

Figure 5.4. The molten salt pump constructed at the University of Wisconsin for use in the forced convective loop to examine mass and heat transfer.

The first requirement of the pump was the ability to have sufficient head to overcome the pressure drop across the loop at the desired flow rates. A commercial source for the pump head and impeller were then sought to meet this requirement and the pump was designed around this pump head. After examination of several pumps; the pump head: impeller, casing, and suction cover, were taken from an AMT 368 series water pump. The pump curves for this model were all listed at 3330 RPM. A WEG 3 phase motor (1.5 hp & 1760 RPM) was purchased for the power source for the molten salt pump. In order to ensure the pump could provide sufficient head, the pump curves for the commercial product were scaled using pump laws [156]. The pump curves in the commercial literature were then analyzed for the current system by using pump laws, Equation 5.41 to determine the estimated pump curves along with the system curve.

$$Q_2 = Q_1\left(\frac{N_2}{N_1}\right) \tag{5.39}$$

$$H_2 = H_1\left(\frac{N_2}{N_1}\right)^2 \tag{5.40}$$

$$P_2 = P_1\left(\frac{N_2}{N_1}\right)^3 \tag{5.41}$$

Once a satisfactory pump head was identified, the design of the pump shaft was started. The diameter of the pump shaft is sized large enough to reduce the torsional stress in the shaft to acceptable levels. In addition, as the length of the free end of the pump increases, it is necessary to increase the diameter of the shaft to reduce low frequency harmonics in the pump shaft. This increase in the shaft diameter allows for more heat to be conducted along the shaft of the pump from the fluid reservoir. This increase in conduction, increases the length of the cantilever necessary to remove the bearing from the heat. These are competing effects in the design of long

cantilever ends. The following technique was taken to determine the diameter and length of the pump shaft.

The diameter of the shaft was determined by looking at the torsional stress in the shaft to ensure material strength was maintained. With additional safety factors, the diameter of the pump shaft was calculated to be 1" D. Next it was necessary to determine the approximate height of the cantilevered end to keep the temperature of the bearings below 200°C. In order to keep the length of the pump shaft minimal, the shaft was designed to be actively cooled above the pump lid, at the packing box of the pump. The packing box seals the lid to the shaft to keep the atmosphere in the can free of oxygen. Copper tubes ($^1/_4$" D) are wrapped around the packing box and water passed through them to keep the bearing temperature below their limit. A Fluent model was used to calculate the temperature profile along the shaft using conduction analysis. The simulated average temperature of the bearings and shaft below the bearings is $T_{bearing}$= 94°C and T_{shaft} = 257°C, respectively. The bearings will be able to remain cool during pumping of 600°C molten salt with minimal amounts of cooling at the packing box.

The supports and shaft will not have the same temperature profile due to active cooling and other factors. This temperature difference will cause different thermal expansion in the pump reservoir and pump head that could cause contact of the pump impeller and casing after heating. This difference was accounted for in the design of the pump. From the previous thermal calculation, the average temperature of the shaft is 257°C compared to the average temperature of the supports, 367°C. The expected difference in thermal expansion increases the length of the support by 0.03" relative to the shaft from startup to operating conditions. That is the impeller would move further from the pump cover. The clearance in the pump casing between impeller and the suction cover is 0.11". There is sufficient clearance in the pump head so the thermal expansion of the shaft can be accounted for in the original position of the shaft relative to the bottom casing.

5.6.3 Pump Construction and Testing

The material for the pump was then purchased and machined. 1" pump quality ground shaft was purchased and machined to specifications for the pump shaft. $^3/_4$" thick plate was purchased to make the support plates and lids for the pump reservoir cans. The plate was rough cut at a commercial manufacturer using a water-jet. 12" Schedule 40 NPS pipe was purchased and cut to length for the reservoir cans. These parts can be seen in Figure 5.5

(a) Plate (b) Shaft (c) Pipe

Figure 5.5 SS-316 material for use in construction of MS Pump.

Some of the parts required machining to produce the proper dimensions and surface finishes on the pump parts. For example, holes smaller than $^{3}/_{4}$" needed to be machined in the pump lid and other plate parts. Smooth surfaces for the sealing surfaces, pump lid and flange, needed to be machined. The pipe needed to be cut and faced to ensure proper length and that the ends were parallel to each other and square to the side of the pipe wall. Figure 5.6 shows some of the process of machining the parts.

(a) Pump Lid (b) Facing Reservoir Can (c) Packing Box

Figure 5.6. The pump parts were machined to proper tolerances before assembly of the pump.

After assembly of the pump and pump reservoir, the pump curve (head vs volumetric flow rate) was determined for the pump system. It was desired to increase the pump flow capacity of the system, so a larger impeller was purchased (3680 instead of 368A SS impeller). A simple loop was constructed from $^{1}/_{2}$" NPS PVC pipe with a flow meter, pressure gage and plug valve. A Kronos electro mag flow meter was used to measure the flow rate of water while the head was measured from a bourbon pressure gage with analog dial face. Water was pumped through the system and the volumetric flow rate and pressure of the system was recorded. The valve was adjusted to change the system curve and the pressure and volumetric flow rate were recorded. This was done for many valve positions from fully open to fully closed. The motor speed was then varied and the process repeated. The experimental pump curves are compared to the expected curve, Figure 5.7.

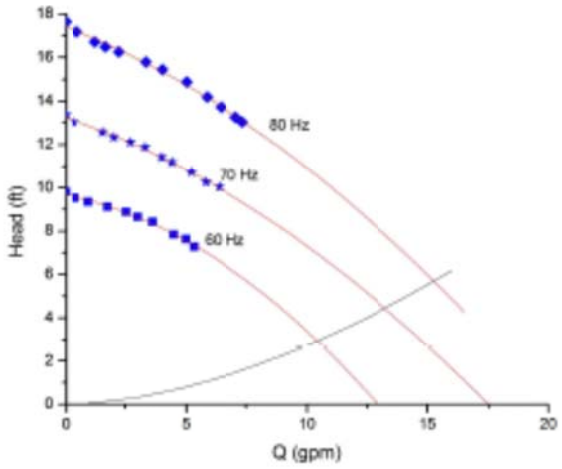

Figure 5.7. The pump curves for the molten salt pump are close to the values expected from initial design.

Before the larger impeller was put into the pump, the effect of the clearance between the impeller and the suction cover was investigated, Figure 5.8. The shaft was released from the bearings until the impeller was resting on the pump cover. The distance raised was measured using a linear displacement sensor. The clearance was investigated to see how the pump curves may change from room temperature to operating temperature. The clearance will change due to different heating profiles of the pump supports versus the pump shaft.

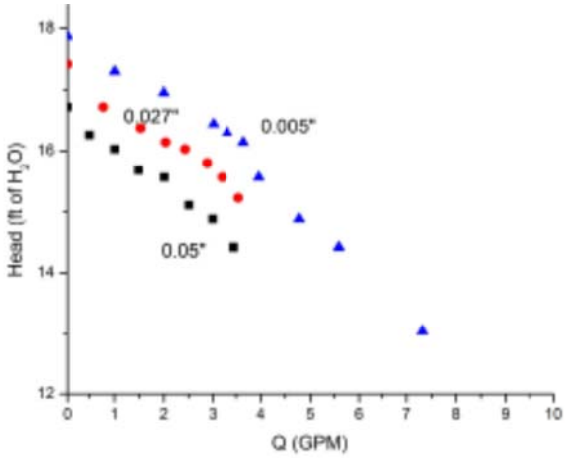

Figure 5.8. The pump curves for the molten salt pump show a reduction as the clearance between the impeller and the suction cover increases.

A change in clearance of the pump impeller and suction cover results in a change in the pump curve for the system. The change in clearance from 0.005" to 0.05" results in a decrease in the head of 7% at zero flow conditions. This change is caused by different average temperatures in the components, resulting in differences in the thermal expansion of the shaft versus the pump housing.

After assembly of the loop, it was desired to increase the flow rate of the loop to measure the heat transfer coefficient in the turbulent regime. In order to increase the flow rate of the loop, a pump head from an AMT 3690 series pump was purchased and assembled into the pump. The change in pump head increased the pump curves for the system, Figure 5.9. The pump curves for this setup were taken with the molten salt pump attached to the molten salt loop. The flow rate was measured using a Khrone ultrasonic flow meter and the pressure was measured with a Siemens differential pressure gage at the entrance to the mass flow meter.

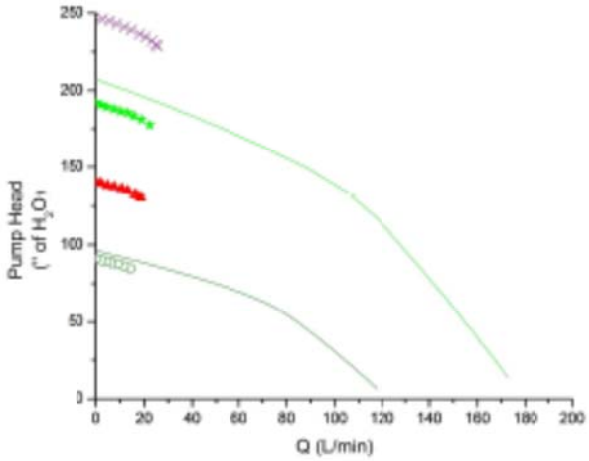

Figure 5.9. The pump curves for the molten salt pump are close to the values expected from initial design.

5.7 Mass Flow Meter

In designing the molten salt loop, it was necessary to determine a way to measure the mass flow rate of the fluid through the test sections to get an accurate determination of the friction coefficient and heat transfer coefficient at low Re numbers. As in the case of the pump, it is difficult to find a commercial product that is able to measure low flow rates of the molten salts at high temperatures ($T \sim 600^{o}C$). Of the commercial products found, only one commercial instrument was found to operate in this temperature range, which was an ultra-sonic flow meter from GE. This flow meter requires a minimum velocity of 0.03 m/s through a 2" pipe, in order to ensure accurate measurements of the velocity. It was not desirable to have a flow rate that high for the current experiment, due to power requirements that would be necessary to heat the fluid to the desired temperatures.

Previous experiments involving molten salts have used different methods for determining the mass flow rate. Early experiments at ORNL used a scale underneath the salt vessels. Salt was pushed from one vessel to the other with gas pressure. The mass flow rate was calculated from the scale underneath the vessel [141]. Work at NACA used a vessel that contained a gate that would be open or closed. A mass flow measurement would involve a closing of the gate and the salt would fill the vessel until the salt touched an electrode height detector. The gate would then open and the time necessary to fill the volume in the vessel was recorded. The volume of the salt in the vessel would then be used with the average temperature of the salt in the vessel to calculate the mass in the vessel [143]. Later work at ORNL, used an energy balance to determine the mass flow rate of

the fluid [157]. Vriesema used a venturi type flow meter for measuring the flow rate in experiments with FLiNaK [144].

It was desired to keep the mass flow meter simple with no moving parts and minimum salt volume. The mass flow meter was designed based on an energy balance across a small section of the loop. The temperature change of a fluid across the mass flow meter along with knowledge of the heat capacity and heat generated are used to determine the mass flow rate by the energy balance;

$$Q = \dot{m} C_P \Delta T \tag{5.42}$$

The engineering drawing for the mass flow meter is shown in Figure 5.10. The inner diameter of the flow meter is reduced to 0.132" from 0.76" in the structural tubing. This decrease in diameter increases the velocity of the fluid through the flow meter. This helps promote better heat transfer from the wall to the fluid. In addition, a Koflo static tube mixer is located in series with the tube and coupled with Swagelok fittings. The static tube mixer assists in mixing of the fluid to get an average temperature, while also increasing the heat transfer rate to the fluid. Heat is applied to the mass flow meter by ohmically heating 28 AWG NiCr 60 wire wrapped around the outside of the static tube mixer. The NiCr wire is soldered to 12 AWG high temperature wire to reduce ohmic heating in the leads. The NiCr wire is wrapped directly over a 4.5" section of the static tube mixer to produce the heat where the heat transfer is the highest. The centerline temperature of the fluid is measured at the inlet and outlet of the flow meter and the flow rate of the salt is determined.

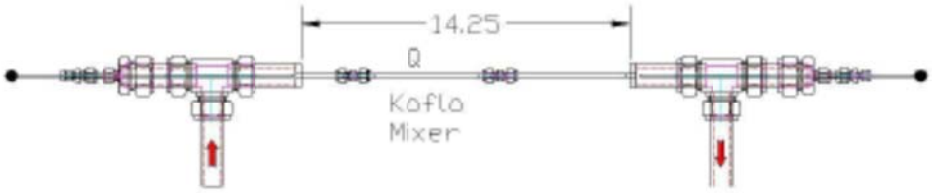

Figure 5.10. The design for the mass flow meter that will be used to measure the flow rate of KCl-$MgCl_2$ salts flowing in the forced convective loop.

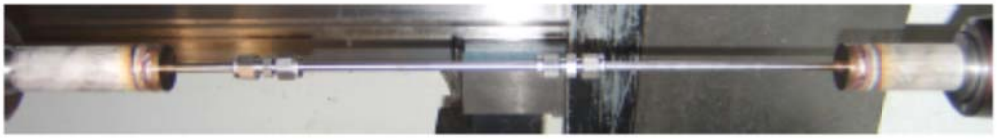

Figure 5.11. The thermal mass flow meter that will be used to measure the flow rate of KCl-$MgCl_2$ salts flowing in the forced convective loop with the Koflo static mixer located in the center.

Figure 5.12. The NiCr wire was soldered to a high temperature lead wire to reduce ohmic losses in the electrical leads to the TFM power source.

Experimentally the thermal mass-flow meter was calibrated against a commercial Coriolis flow meter using Paratherm NF as the heat transfer fluid. The coriolis flow meter was experimentally verified by diverting the mass flow through the system into a bucket over a set time period. The mass of the oil was recorded and the amount of time the fluid was diverted was known. This method reproduced the value of the coriolis flow meter within ±1%.

The thermal flow meter was calibrated using four different heat inputs (57, 85, 98, and 128 W) into the thermal mass flow meter. The result from the thermal flow meter was verified against the coriolis mass flow meter to ensure accuracy of the thermal flow meter. The data obtained during the calibration runs for the thermal flow meter is shown in Figure 5.13. All of the data falls within ±10%, with > 90% of all data points within ±5% of the coriolis flow meter. The temperature of the Paratherm NF varied from 55 to 110°C over the course of the calibration.

For each power input the slope of the line changed slightly compared to the others. This effect is due to the change in the amount of energy lost. The estimated loss from radial conduction through the insulation layers resulted in an estimated loss of 4 W due to natural convection. This value was assumed for all of the runs independent of the heat input.

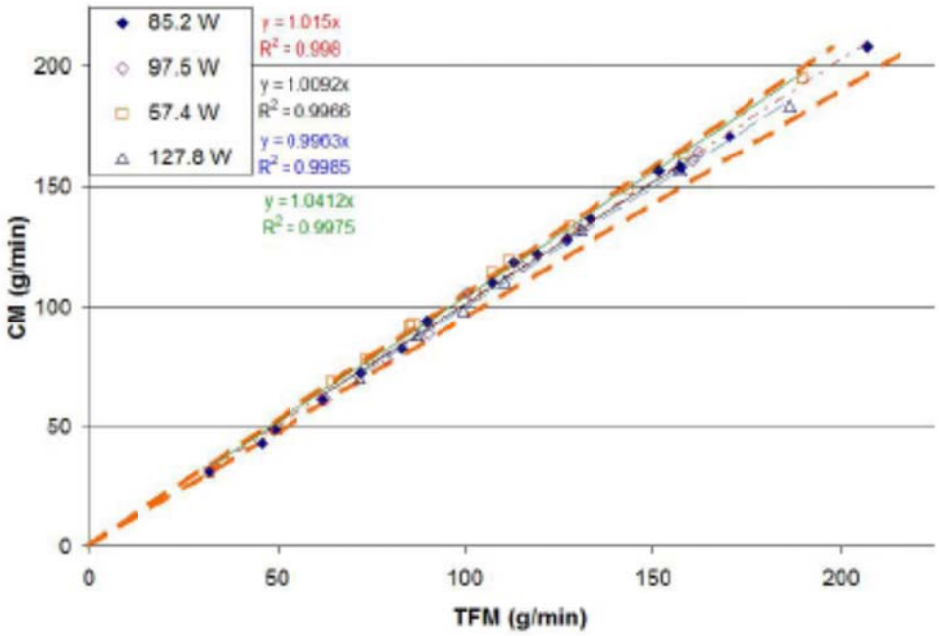

Figure 5.13. The mass flow meter closely reproduces the measured flow rate to ±5% as compared to the Coriolis flow meter.

The ability to determine mass flow rates of the fluid by applying an external heat source allows for a simple, effective way to measure the mass flow rate of the salt. Without the large salt inventory that was necessary in previous experiments.

During experiments with molten KCl-$MgCl_2$ salt as the working fluid, the heat loss and thermocouple offsets were calibrated out by measuring the temperature rise across the mass flow meter for different heat inputs at a constant flow rate. The change in the temperature rise compared

to the change in the heat input then allows for determination of the mass flow rate of the molten salt through the system. The same technique was done over the test section to verify the mass flow rate as determined by the mass flow meter.

5.8 Differential Pressure

It was also desired to measure the pressure drop of the molten salt across the test sections to verify pressure drop correlations for molten salts. It was desired to find a commercial vendor that could supply pressure devices that would be able to operate to temperatures of 475^{o}C to ensure that freezing did not occur in the pressure taps. At this temperature, it was necessary to then necessary to determine if a differential pressure gage was available to measure the differential pressure across the different test sections.

Using the friction coefficients calculated from the Pouiselle Equation, Equation 5.12, and using the expected value for Re (150) based on IHX design, the pressure drops across the different test sections were computed, Table 5.5 to size a differential pressure sensor.

Table 5.5. Expected Pressure Drop for the different test sections at Re = 150.

Test Section Inner Diameter	ΔP
(inches)	(Pa)
0.37	4
0.055	3200

In looking for pressure sensing devices, it was desired to find a differential unit that could measure the pressure of the at a minimum 24 Pa (0.96" of H_20). No commercial products were found that could meet this criterion. In fact, the lowest operating range for a commercial pressure sensor at 475^{o}C had a minimum range of ±1.25 psi (8.6 kPa).

Most commercial differential pressure transducers are backfilled behind the pressure diaphragm with an oil. The highest operating temperature that was found for an oil backfilled pressure transducer was approximately 300^{o}C. It is possible to backfill these pressure transducers with liquid sodium potassium metal eutectic, NaK. This extends the temperature range of the pressure transducer diaphragm to operate at temperatures up to 538^{o}C [158, 159]. Several vendors currently use NaK as pressure transmitting fluids, however these pressure transducers are designed for polymer processing molds and injectors. These pressure transducers are designed for high pressure processes and do not have the low range resolution desired for this current application.

In order to measure the pressure drop of the salt across the test sections, it was necessary to devise a method to measure small pressure drops at high temperatures, while keeping the system as simple as possible. The most simple pressure transducer is a manometer. A manometer simply determines pressure by measuring the difference in height of two fluids that are connected to the test section.

To measure the differential pressure of the system, two SS cans are connected at pressure taps at locations 2" before and after the test sections. The loop and SS cans are connected by 1/4" (0.035" wall) SS-316 tubing. The gas space in the two pressure cans are connected by a gas line at top to

ensure that the gas pressure over the liquid in each can is equal. The pressure drop across the test section is then determined by looking at the hydrostatic head at each test section, Figure 5.14.

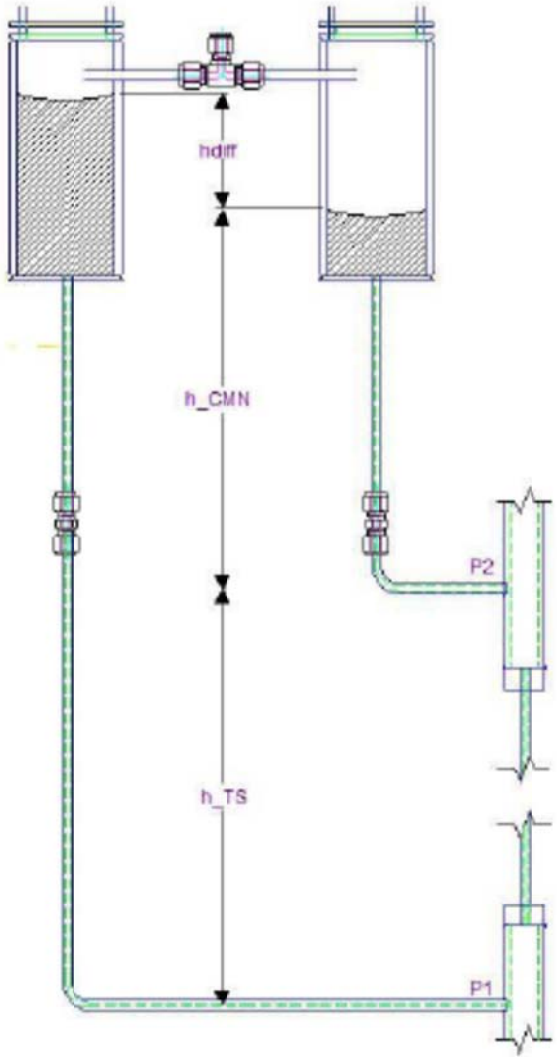

Figure 5.14. The setup and notation for determining the pressure drop of the KCl-$MgCl_2$ salt across the test sections.

The differential pressure for the system is determined by subtracting the pressure at locations 1 and 2 in Figure 5.14 and also subtracting the hydrostatic head from pressure measurement 1.

$$\Delta P = P_1 - P_2 - \rho_{TS} g h_{TS} \tag{5.43}$$

If the loop is broken down into three sections: the height between the pressure taps (h_{TS}), the height between the upper pressure tap and the SS can (h_{CMN}), and the height in the SS cans($\underline{h_{CAN}}$). The pressure in non-flow conditions for each of these sections is then determined by the sum of each hydrostatic head in each leg. Thus the differential pressure for the system can be arranged as:

$$\Delta P = g\left[\left(\rho_{1,TS} h_{TS} + \rho_{1,CMN} h_{CMN} + \rho_{1,CAN} h_{1,CAN}\right) - \left(\rho_{2,CMN} h_{CMN} + \rho_{2,CAN} h_{1,CAN}\right)\right] - \rho_{TS} g h_{TS} \tag{5.44}$$

If the common height between the two cans is added to the common term in Equation 5.44 the height difference between the two cans is noted as h_{Diff}. Combining like terms and rearranging Equation 5.44 the following is obtained:

$$\Delta P = g\left[h_{TS}\left(\rho_{1,TS}-\rho_{TS}\right)+h_{CMN}\left(\rho_{1,CMN}-\rho_{2,CMN}\right)+h_{Diff}\rho_{CAN}\right] \quad (5.45)$$

The height and temperature of the pressure legs are recorded. The only variable left to determine is h_{diff}, the height difference in the SS cans. To measure the height difference of the fluid, laser displacement sensors were chosen due to the accuracy at which the surface of the liquid can be measured, 500 μm. This is compared to the accuracy of other liquid level sensors, ultrasonic and radar, which have an accuracy of 3 mm. The high accuracy at which the liquid level of the sensors can be measured make it possible to measure pressure drops across the test section of < 2 Pa under isothermal conditions.

A 2" D quartz window is placed at the top of the pressure cans to allow for detection of the liquid surface. It was necessary to determine if the laser could see the liquid surface of the salt. To test the ability of the laser sensor to determine liquid height, a laser sensor was used to look at the surface of water. The liquid salt is similar to water in that both are transparent to visible light.

A LK-501 laser displacement sensor was obtained from Keyence Corporation. The experimental setup to detect the liquid surface of the water is presented in Figure 5.15. The laser unit is located in the center, a 24V power supply is located at the left of the figure and a voltmeter is located at the right to read the output from the control box.

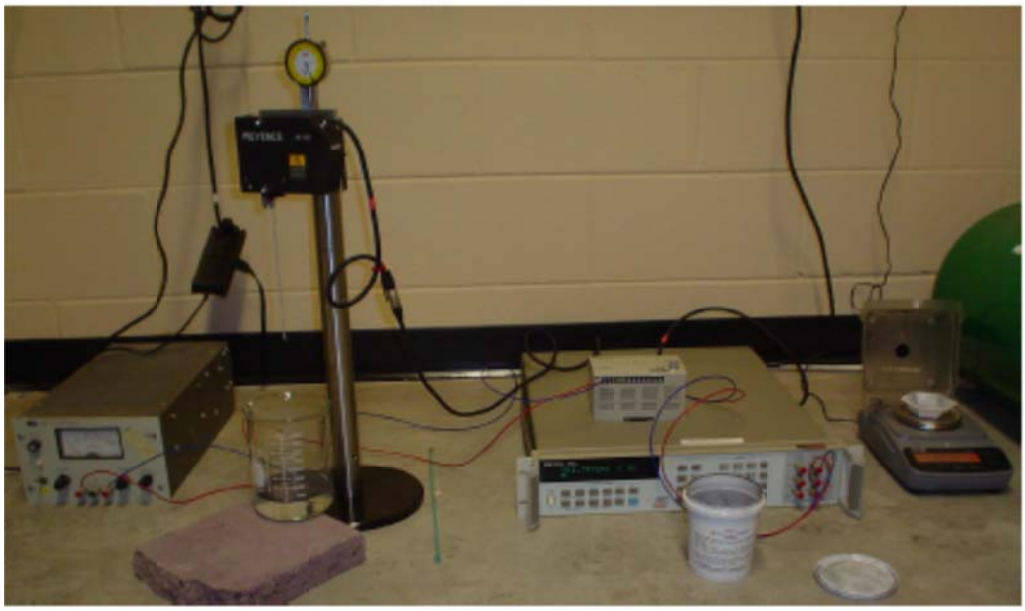

Figure 5.15. The experimental setup to verify that the laser displacement sensor would measure the liquid surface of water.

The laser sensor was not able to locate the surface of the water even though a small amount of reflection occurred from the surface interlayer. When water was added to the system, the laser output changed, but the change was not equivalent to the change in height of the surface. The change in laser output was due to the index of refraction of water bending the laser to locate it on a different point on the bottom surface.

Graphite powder was added to the surface of the water to allow for detection of the liquid surface. The graphite powder floats on the surface of the water and reflects the laser beam to allow for determination of the liquid surface. The results from this test showed a change in liquid surface height is detected by the laser. The change in height of the liquid as a function of the voltage output is presented in Figure 5.16. A slope of 50 mm / V is expected for the output according to manufacturer specifications. A slope of 50.1 mm / V was obtained in the test.

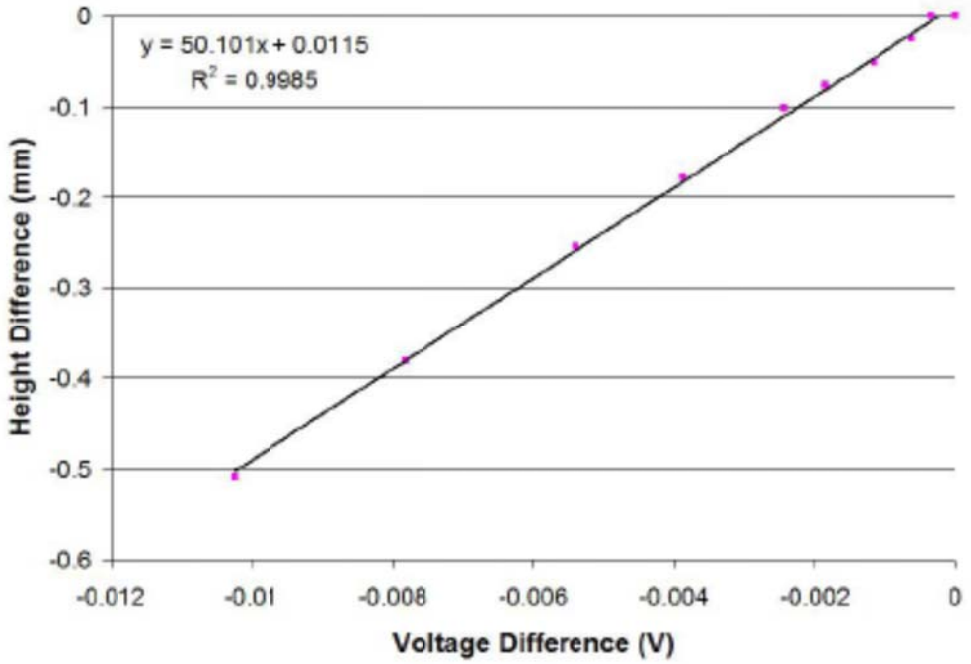

Figure 5.16. The output from the laser sensor shows a slope of 50 mm. It was necessary to add graphite to the surface of the water to detect the liquid.

The differential pressure sensors were tested in the loop by measuring the isothermal pressure drop of water and Paratherm NF through the 0.083" and 0.37" D, (L = 25") test sections. Graphite powder was added to the cans with water as the working fluid. The graphite powder did not float in the oil due to differences between the density and surface tension of the fluids. It was then necessary to find a new method to detect the liquid surface. For the oil, a polypropylene boat was used in place of the graphite powder. For the KCl-$MgCl_2$ salt, a low density graphite disc is used as a float in the molten salt. The low density graphite was checked with the KCl-$MgCl_2$ salt by placing a small disc of graphite in KCl-$MgCl_2$ at 500^{o}C for 100 hours, Figure 5.17. The graphite was still floating after the 100 hour exposure.

(a) Machined graphite discs (b) Graphite in molten KCl-$MgCl_2$

Figure 5.17. The graphite disc (1.5" D, 0.25" thick) was placed in KCl-$MgCl_2$ salt for 100 hours in the glove box to ensure that the graphite would float before testing in the molten salt loop.

The experimental pressure drop was measured and the friction coefficient was determined from Equation 5.3 for water and Paratherm NF. It is necessary to remove the pressure loss due to the contraction and expansion of the entrance and exit and the pressure drop through the structural tubing (4" length). The form losses were calculated from Equations 5.14 and 5.13 and the pressure drop due to friction was calculated with Equation 5.3 with f calculated by Equation 5.12. The experimental data was compared to the theoretical values with the properties calculated from the average temperature of the fluid across the test section. The results of the calibration tests are presented in Figures 5.18 and 5.19.

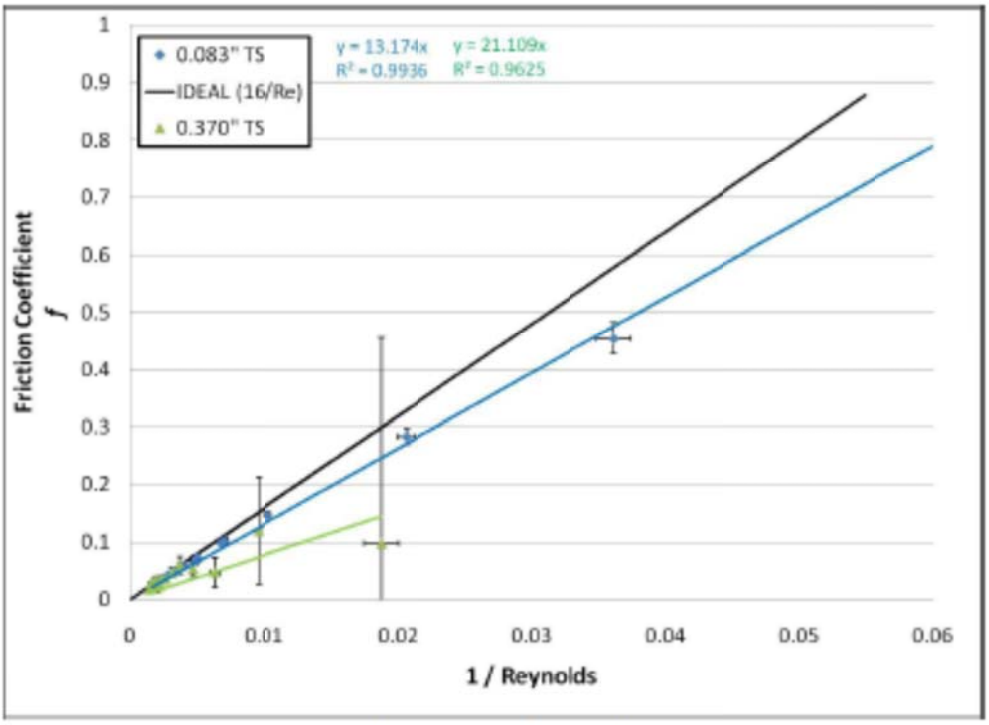

(a) All Experimental Data - Water

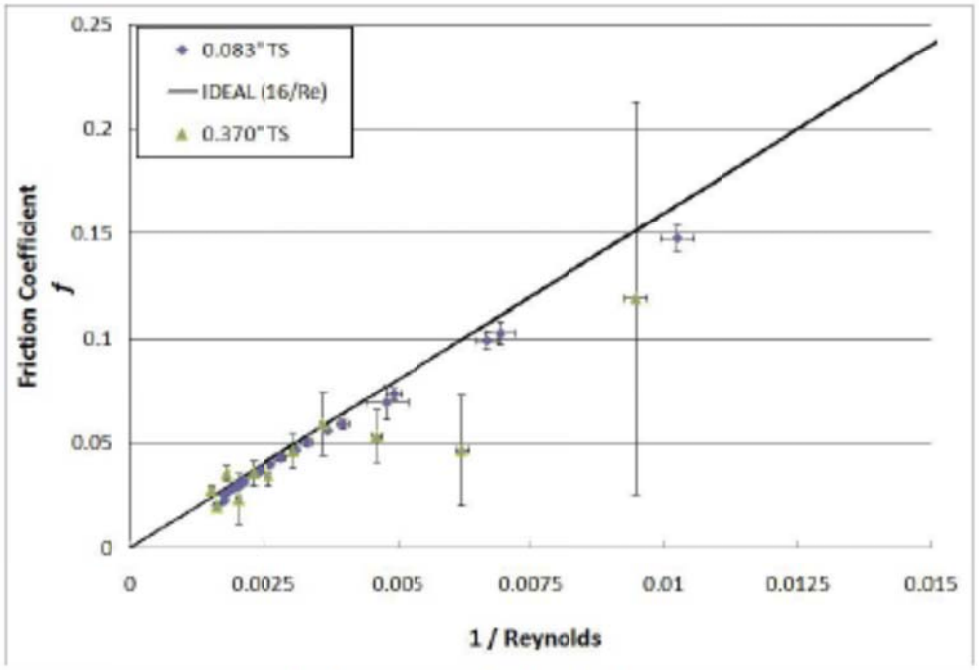

(b) More Detailed Look at Higher Re

Figure 5.18. The friction coefficient of water determined through flow a single channel test sections compared to the ideal value of 16/Re.

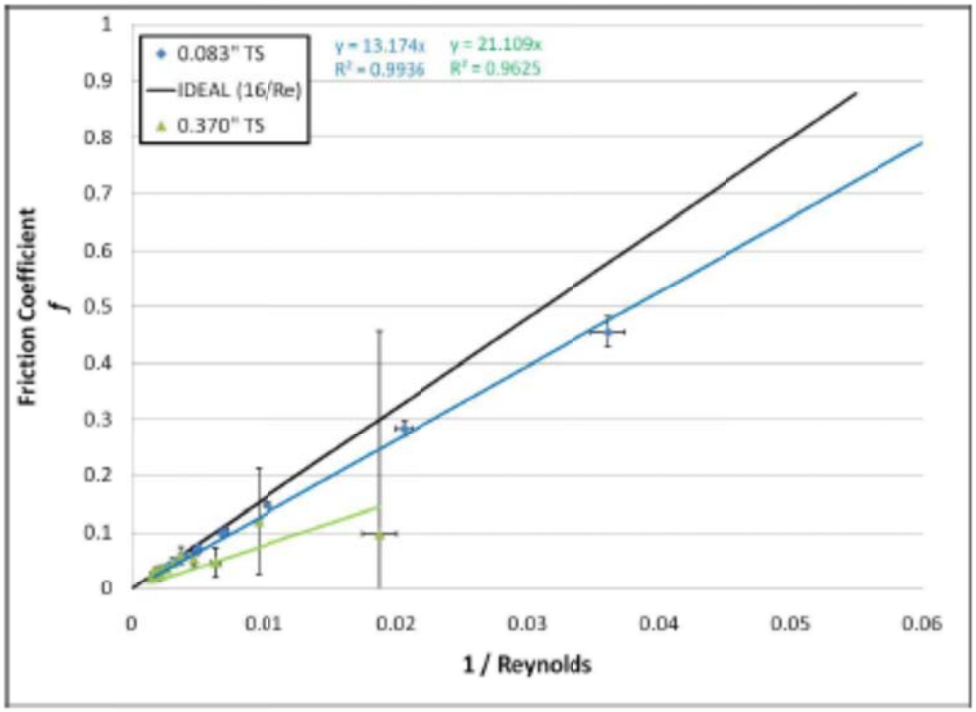

Figure 5.19. The friction coefficient determined with the Paratherm NF heat transfer oil.

It should be noted that for the isothermal pressure drop in the D = 0.37" channel with water, the pressure drop across the test section ranged from 0.001" of H_2O to 0.085" of H_2O at Re = 18 and 750, respectively, for water. The uncertainty in the differential pressure sensor is ±0.003" of H_2O (±0.9 Pa), under isothermal conditions. This uncertainty in the measurement is the cause for the large error bars.

Tests with the molten KCl-$MgCl_2$ salt to measure the pressure drop across the test section have not been run.

5.9 Convection Coefficient

The convection coefficient was measured in the laminar and transition thermal-hydraulic regimes for heated/up flow conditions in the two single channel test sections with water, Paratherm NF, and KCl-$MgCl_2$ as the working fluid. Heat is input into the test section by NiCr 60 wire wrapped around the test section every 0.25" of length. K-type thermocouples are welded to the outside wall of the tube to measure the temperature of the outside wall.

The convection coefficient is determined from the overall heat transfer coefficient, U. The overall heat transfer coefficient is determined by the following:

$$U = \frac{q}{A/LMTD} \tag{5.46}$$

where, LMTD is the log mean temperature difference. The LMTD is calculated based off of the temperature difference of the wall and fluid at both the inlet and outlet by

$$LMTD = \frac{\left(T_{s,o} - T_{f,o}\right) - \left(T_{s,i} - T_{f,i}\right)}{\ln\left(\frac{T_{s,o} - T_{f,o}}{T_{s,i} - T_{f,i}}\right)} \quad (5.47)$$

Q, in Equation *5.46*, is the energy generated in the system due to the resistive heating of the NiCr wire. A is the area for heat transfer to the fluid, the circumference of the inner tube multiplied by the length, L,

$$A = \pi D_i L \quad (5.48)$$

The heat transfer coefficient is part of the overall heat transfer coefficient, U. U is the inverse sum of the thermal resistances of the system. In the current test configurations, it is the sum of the wall resistance and the resistance due to convection to the fluid, substituting these values, for a cylindrical geometry, into Equation *5.46* results in

$$UA = \frac{1}{\frac{1}{h} + \frac{r}{k_{WALL}} \ln\left(\frac{r_O}{r_I}\right)} \quad (5.49)$$

Rearranging Equation 5.49 to solve for the convection coefficient,

$$h = \frac{1}{\frac{1}{UA} - \frac{r}{k_{WALL}} \ln\left(\frac{r_O}{r_I}\right)} \quad (5.50)$$

Combining Equations 5.50 and *5.46*,

$$h = \frac{1}{\frac{1}{q''/LMTD} - \frac{r}{k_{WALL}} \ln\left(\frac{r_O}{r_I}\right)} \quad (5.51)$$

From measurement of the temperature of the fluid and wall temperature and heat flux along with knowledge of the thermophysical properties and geometry of the system, h is determined from the experimental data. Description of the error analysis for the heat transfer calculation is presented in Appendix C.

The heat transfer coefficient for the three different fluids was measured in the two different test sections. The results for water, Paratherm NF, and KCl-$MgCl_2$ in the two different test sections is shown in Figure 5.20.

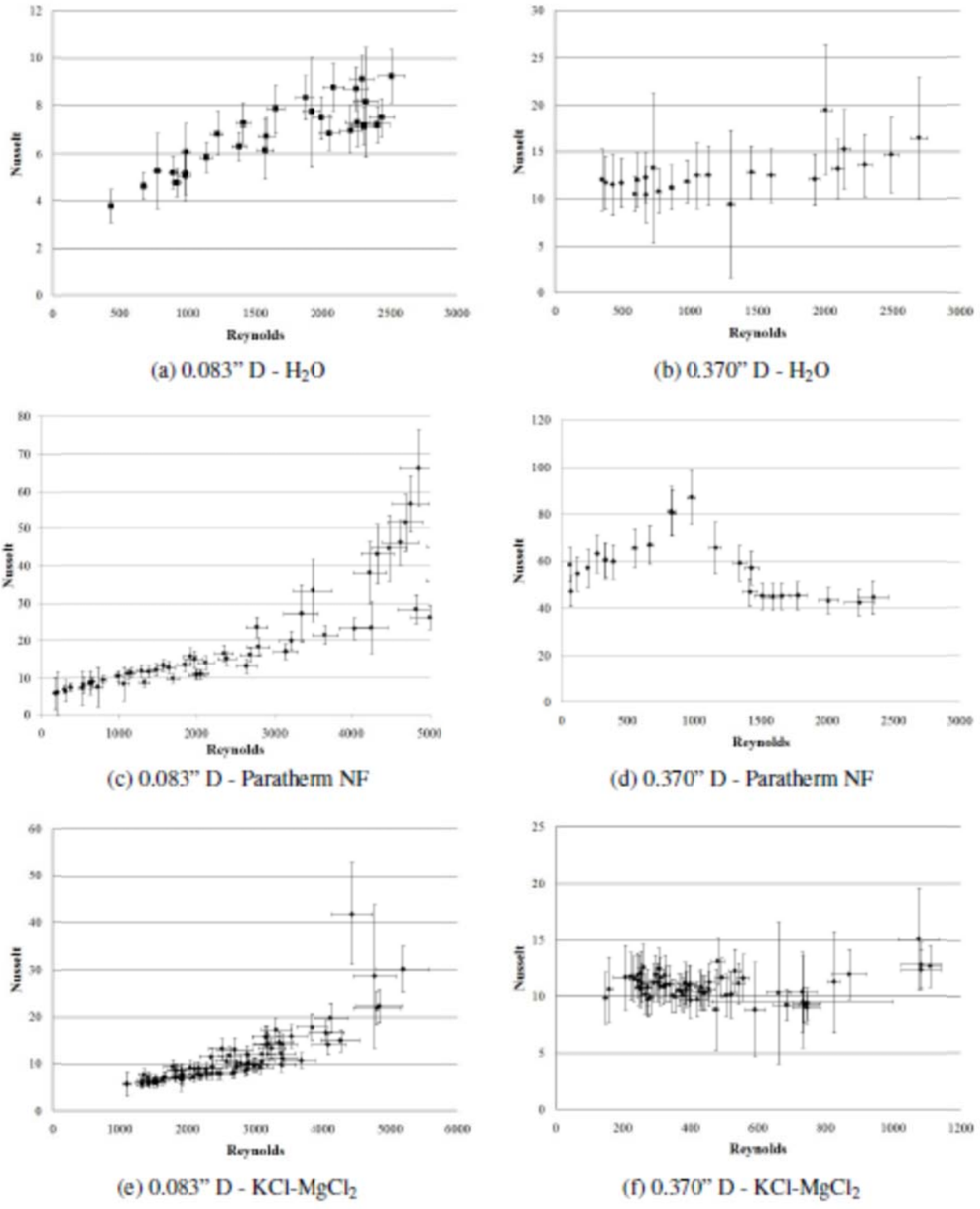

Figure 5.20. Experimental Nusselt number as a function of Reynolds number for different fluids.

The experimental heat transfer coefficients were normalized by dividing by Equation 5.4 for Re < 2300 and Equation 5.23 for Re > 2300 for the 0.083" and the 0.370" ID tubes. These correlations are for forced convective heat transfer. If the correlation predicts a value that is close to the experimental value, the value in the graphs should be close to 1, Figure 5.21.

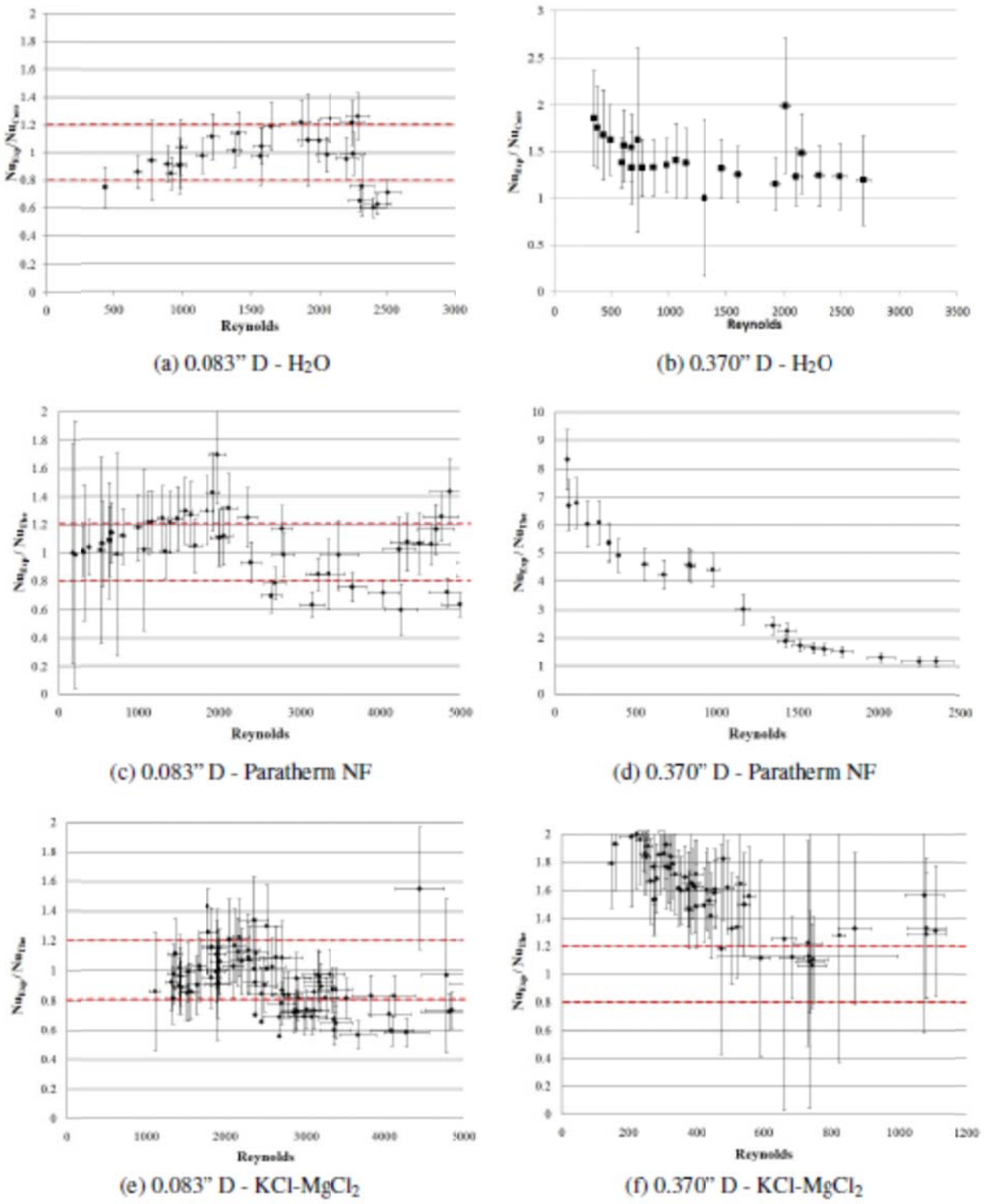

Figure 5.21. Experimental Nusselt numbers normalized by values determined from heat transfer correlations.

The heat transfer coefficient for the 0.083" D shows that all except a few data points are within ± 20% of the value expected from Equation 5.4. The heat transfer data in the 0.370" D for all fluids

show significant deviation from the expected value based on forced convection correlations. The experimental heat transfer coefficient for the 0.370" D is linear and the normalized value increases as the Reynolds number decreases. From calculation of the Grashof number based on heat flux, the current flow conditions result in the system being in the mixed heat transfer regime. From work by Martinelli, the heat transfer data for the 0.370" D tube falls in the laminar-transitional mixed regime. The experimental data for the convection coefficient was compared to the values expected from Equation 5.31. The values obtained by dividing the experimental Nusselt number by the theoretical Nusselt number from mixed convection correlation is presented in Figure 5.22 for the oil and molten salt. The heat flux for the water tests were too low to obtain mixed convection based on the parameter Gr/Re^2 as this was $<< 1$.

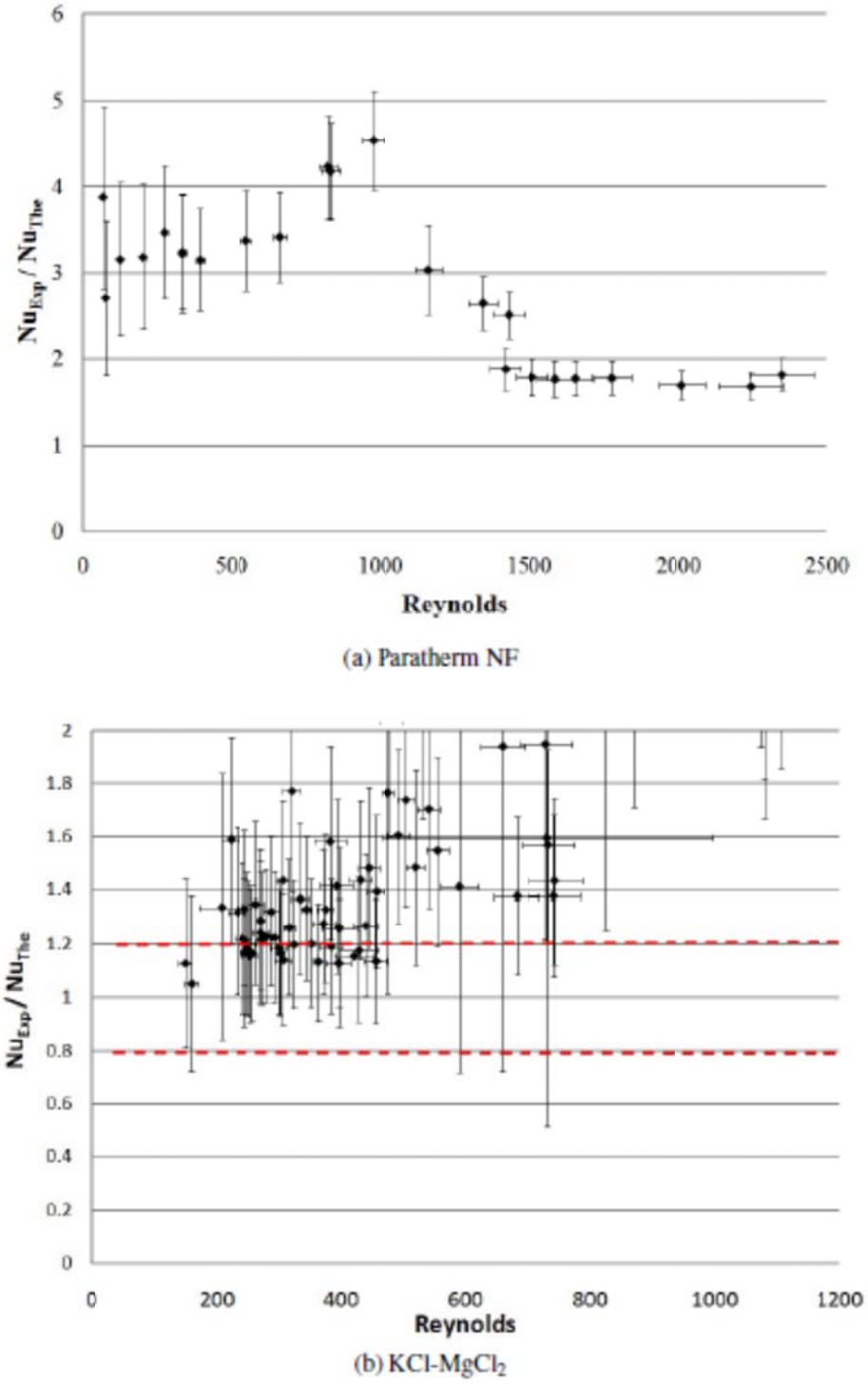

Figure 5.22. The convection coefficient for the Paratherm NF and KCl-$MgCl_2$ salt flowing through the 0.370" D test section compared to the theoretical mixed convection value determined from Equation 5.31.

The use of Equation 5.31 for the 0.37" D test section data showed an improvement when compared to the pure forced convection correlation used in Figure 5.21 for low Reynolds number flow. To

show the improvement, the normalized Nusselt number based on either forced convection or mixed convection correlations are plotted as a function of the Grashof number based on heat flux divided by the Reynolds number, Figure 5.23.

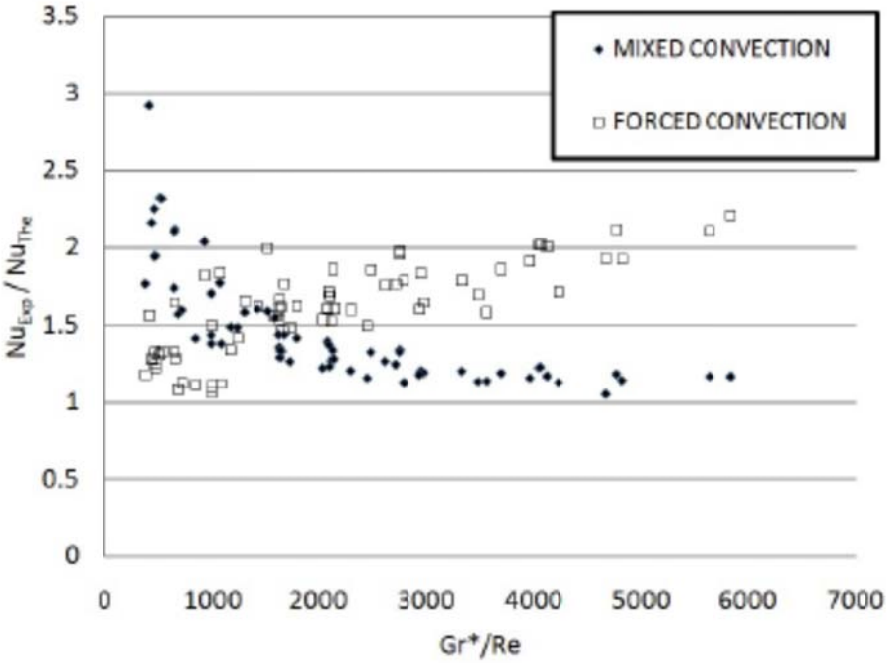

Figure 5.23. The normalized Nusselt number based on either forced or mixed convection correlations.

At a value of $Gr^*/Re > 2000$, the mixed convection correlation reproduces the experimental data for the 0.370" D test section better than the forced convection correlation.

5.10 Radiation Heat Transfer

In the earlier heat transfer experiments conducted with FLiNaK, there was a large discrepancy in the heat transfer coefficients for the FLiNaK salt in forced convection. It was desired to determine if radiation heat transfer from the container wall to the salt was affecting the heat transfer measurements in this system [71]. It was determined that in order to have 10% of the energy transfer to occur by radiation the walls fluid must be laminar in a large diameter tube. To further verify that radiation is insignificant in the heat transfer in normal operation of heat transfer equipment, the normalized Nusselt number based on forced convection correlations was plotted based on average fluid temperature. The results for the KCl-$MgCl_2$ salt is presented in Figure 5.24.

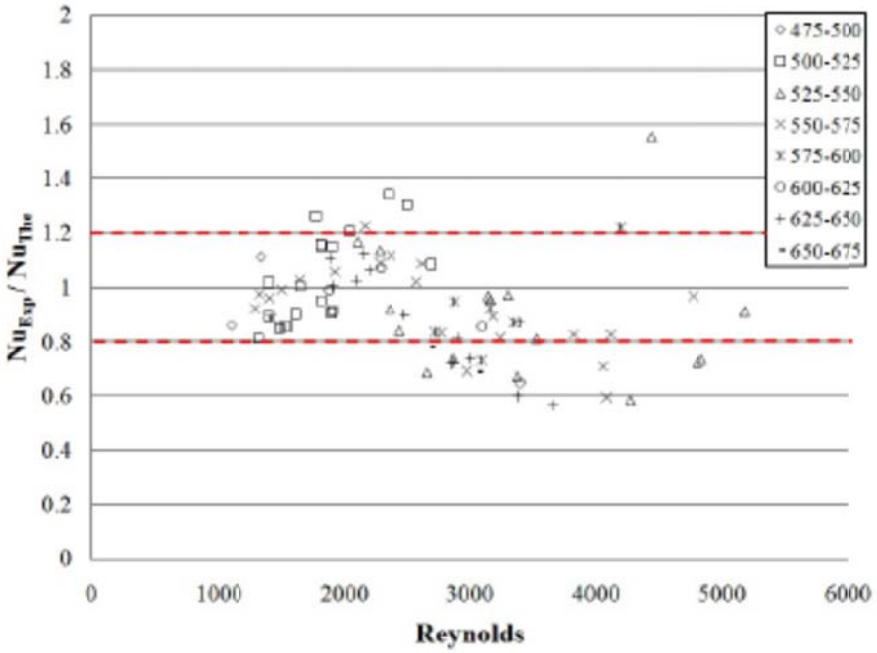

(a) 0.083" D Test Section

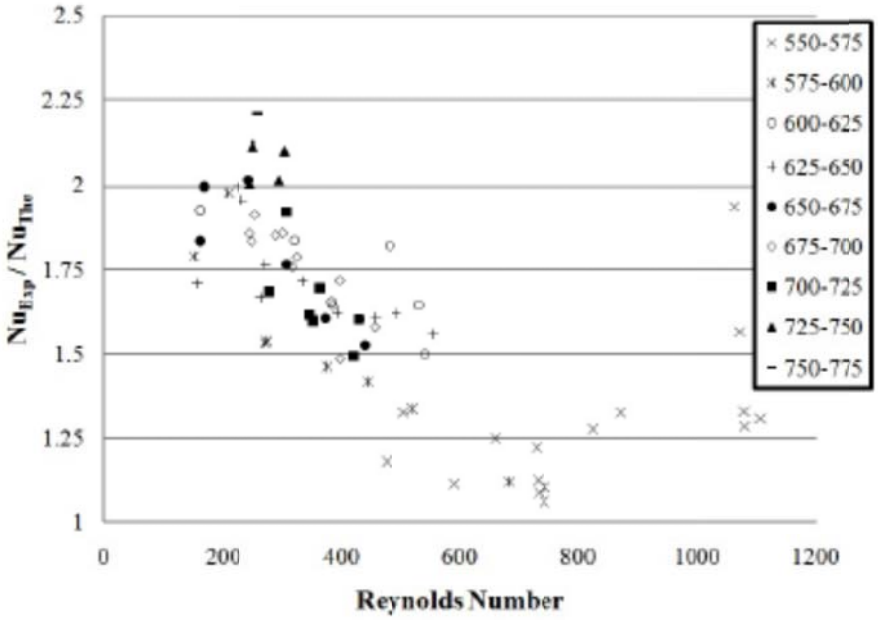

(b) 0.370" D Test Section

Figure 5.24. The normalized convection coefficient for the 0.083" and 0.370" D tests sections plotted based on average temperature of the KCl-$MgCl_2$ salt in the test section.

The Nusselt number seen in the experimental data does not increase with an increase in the average bulk temperature of the fluid. This lack of increase in the Nusselt number as the average temperature of the fluid increases shows that radiation from the wall to fluid is negligible on the salt heat transfer.

5.11 Summary

A forced convection loop has been built to study the different modes of convection heat transfer with molten salts. As part of this loop, a custom pump, mass flow meter and differential pressure system was designed, calibrated, and attached to the convection loop. A vertical-cantilever pump was designed and constructed. The molten salt pump has been in operation at temperatures above 550°C for over 500 hours. The differential pressure sensor has been shown to be highly accurate in measuring the isothermal pressure drop of water across the test sections. As the temperature of the fluid increases and the system becomes non-isothermal, the accuracy of the pressure sensor decreases as seen in the measurements with Paratherm NF. The accuracy, although still high, is not as precise for the non-isothermal flow cases. Finally, a mass flow meter was designed to measure the mass flow rate of the working fluid. Using Paratherm NF, the mass flow meter measured the mass flow rate of the oil to within ±5% when compared to a commercially purchased and calibrated Coriolis meter.

Using the forced convection loop and instrumentation, the heat transfer coefficient was measured for KCl-$MgCl_2$ salt across two different diameter test sections. The forced convection heat transfer coefficient can be predicted by the equation listed in the VDI Heat Atlas:

$$Nu = \left(4.364^3 + 0.6^3 + \left(1.953 Gz^{1/3} - 0.6\right)^3\right)^{1/3} \quad (5.52)$$

to within ± 20% for fluid conditions of $1000 < Re < 2300$.

In the larger diameter tube, the molten salt was found to be predicted by correlations for mixed convective flow, Equation 5.31, when the fluid conditions are $Gr^*/Re > 2000$. For situations when $Gr^*/Re < 2000$, the heat transfer coefficient was found to predicted by the same forced convection correlation from VDI Heat Atlas [130].

Future Research Paths

6.1 Salt Properties

All of the relevant properties for application of molten salts as heat transfer agents have reliable models that allow for prediction of these properties. This approach can be used to determine salt compositions with more desirable physical properties than current systems. It has been shown that this modeling approach works well with nitrate based salts and has been validated against the relatively large amount of data available for these nitrate based salts.

This modeling approach should be extended to other low and high temperature salts. The ability to lower the melting temperature of the fluid while maintaining properties over a wide temperature range is what allows these salts to be used in a large number of processes. Lowering of the minimum temperature of the molten salts also allows for much simpler instrumentation to be used to monitor the conditions of the system.

The models are limited by the accuracy of the experimental data in literature. As part of the improvement of the models, in addition to validation of model findings, experiments to measure the physical properties of these molten salt fluids should be extended. Namely, thermal conductivity and viscosity should be measured to improve current quasi-chemical models.

6.2 Corrosion

During testing of the different alloys, it was found that micro structural tailoring of the grain boundaries of Incoloy 800H improved the corrosion resistance of 800H. It was also seen that alloys with carbon getters, Nb and Ti, experienced uniform depth of attack and not just along the grain boundaries. The role of C and micro structure on the corrosion characteristics of metals exposed to molten salts should be investigated.

In addition, it is expected that the only way to obtain an accurate corrosion rate of an alloy contacted with a molten salt is to determine the corrosion rate in an actual system. At ORNL during the ARE and MSRE, corrosion experiments were conducted by use of a natural convection loop. This simple structure provided a means for determining the corrosion rates due to impurities and mass transfer.

6.3 Heat Transfer

Literature data on the heat transfer of molten salts shows that the heat transfer can be predicted by correlations for normal fluids. Data from this work with chloride salts show that heat transfer in chloride salts is also predicted by these same equations. follow the same general trend. However, no current data exists for pressure drop of these fluids in the laminar and transitional regimes. Of all of the current data on forced convective salt heat transfer with fluoride salts, seven points exist for laminar heat transfer.

Better methods for instrumentation of mass flow rates, pressure drop, and temperature measurement for heat transfer measurements at high temperature need to be developed. The current mass flow meter is accurate and robust, but has a significant amount of pressure drop across the tube due to the small diameter tubing. A flow meter that could operate without the large pressure drop would increase the range of experiments for the system without having to design and construct a new molten salt pump.

A second improvement is in the pressure drop sensors. Current design requires active control and soft gaskets to seat the quartz window. In the 1950's, a NaK filled pressure transducer was designed and operated for use with molten salt loops [160, 161]. Today there are commercial pressure transducers backfilled with NaK, but have a large differential pressure requirement [158, 159].

Results/Conclusions

Molten salts are excellent heat transfer media and are of interest to many different processes from moderate (nitrates) to high temperature (chloride and fluoride) applications. One application is the coupling of high temperature heat from the NGNP to a hydrogen production or other chemical plant. In one current IHX design, the flow of the salt through the IHX occurs under laminar flow conditions. A review of literature found a lack of experimental data for heat transfer and pressure drop of these fluids in this hydraulic regime. Therefore, it was necessary to build an experimental apparatus to measure the heat transfer and friction coefficients of molten salts in laminar flow conditions.

Since most of the complexity involved with use of molten salts is due to their high melting temperatures, methods for predicting a range of properties for molten salt systems was studied. Limited experimental data is available in literature for salt mixtures with more than two components. Using the experimental data available for unary and binary salt systems, models were found, or developed to interpolate the available experimental data to unstudied salt systems. Models were developed for the adiabatic compressibility and thermal conductivity using a quasi-chemical approach to allow for prediction of thermal conductivity. These property models were then used to investigate the thermo-physical properties of the $LiNO_3$-$NaNO_3$-KNO_3-$Ca(NO_3)_2$ system used in solar energy applications. Using this approach, the density, viscosity, adiabatic compressibility, thermal conductivity, heat capacity, and phase diagrams for the ternary systems were estimated. These estimated properties were then used to help in the initial selection of a molten salt for use in solar parabolic trough systems. This approach for salt property estimation can be applied to determine other molten salt systems of interest for different commercial applications, such as the NGNP heat transfer loop being studied.

It was necessary to find a suitable material for containment of the KCl-$MgCl_2$ salt for the heat transfer tests. Corrosion tests were undertaken to determine the corrosion rate of different high temperature alloys with KCl-$MgCl_2$ salt. Salt chemistry is important in minimizing the corrosion of materials exposed to molten salts and a preparation method for the salt needed to be determined. Four methods were evaluated for preparation of the KCl-$MgCl_2$ salt. The salt preparation methods were ranked by exposing Incoloy 800H for 24 hours at 850^{o}C in this salt to see which method produced the smallest amount of corrosion. Reduction of the salt by Mg contact produced the least amount of corrosion of the 800H samples. Using this purification technique, ten alloys were exposed to KCl-$MgCl_2$ in quartz ampules for 100 hrs at 850^{o}C. The salt corroded the metal coupons by removal of the most active elements. For Fe-Ni-Cr alloys, Cr is the most active and is removed from the metal by the salt. Of the alloys exposed, Haynes 230 had the least amount of weight loss per area. Nickel and Hastelloy N had the least amount of attack based on maximum depth of attack, but also contain minimal amounts of Cr. Cr depletion in the Inconel 625 and 718 alloys was a nearly uniform depletion layer from the surface of the sample. Of the other alloys with > 10% Cr, the samples were corroded by depletion of Cr along the grain boundaries to depths up to 300 μm. The difference in the corrosion mechanism in the Inconel 625 and 718 alloys is believed to be due to the Nb in the alloy composition. In addition, grain-boundary engineering (GBE) of Incoloy 800H improved the corrosion resistance (as measured by weight loss and maximum depth of attack) by nearly 50% as compared to the as-received Incoloy 800H sample.

The change in the local micro-structure of the 800H alloy by GBE resulted in a change in the diffusion rate of Cr along the grain boundaries. Thus proper chemistry control of the salt, chemistry of the alloys, and control of the grain boundaries in the alloy provide methods to reduce the corrosion rate of the metal-molten salt system. The corrosion rate of SS-316 was found to be acceptable for the current studies and was selected for use as the construction material for the loop based on corrosion, availability, and cost considerations.

Heat transfer mechanisms of these molten salts was studied over the forced and mixed convection regions for heat transfer. A forced convective loop was constructed to measure heat transfer coefficients, friction factors and corrosion rates in different diameter tubes in a vertical up flow configuration with molten salt in the laminar flow regime. As part of the design and construction of the apparatus, it was necessary to design and calibrate instrumentation for use with molten salt. Equipment and instrumentation for the forced convective loop was designed, constructed, and tested to allow for operation with the molten salt. These include a high temperature centrifugal pump, mass flow meter, and differential pressure sensing capabilities to an uncertainty of ±2 Pa. The friction coefficient was measured with water and Paratherm NF as the working fluid. Heat transfer coefficients wer measured for three different fluids: water, Paratherm NF, and KCl-$MgCl_2$ in two different diameters, single channel test sections. The heat transfer in the 0.083" D test section was accurately predicted by forced convection correlations for water. In the larger 0.370" D test section, the heat transfer coefficient was found to be accurately reproduced by forced convection correlations for values of $Gr^*/Re < 2000$ and by a mixed convection correlation for values of $Gr^* > 2000$.

Bibliography

[1] Robert W. Bradshaw. Effect of composition on the density of multi-component molten nitrate salts. Technical Report SAND2009-8221, Sandia National Laboratories, 2009.

[2] Hector R. Carveth. Study of a three-component system. Journal of Physical Chemistry, 2:216, 1898.

[3] Alexander Lehrman and David Breslow. The liquidus surface of the system sodium, lithium, and calcium nitrates. Journal of the American Chemical Society, 60:873–876, 1938.

[4] Alexander Lehrman, Edward Adler, Jacob Freidus, and Max Neimand. The liquidus curve and surface of the systems lithium and calcium nitrates and calcium, lithium and potassium nitrates. Journal of the American Chemical Society, 59:179–181, 1937.

[5] P. I. Protsenko and A. G. Bergman. An investigation of the ternary system of calcium, potassium, and sodium nitrates in melts. Journal of General Chemistry S.S.S.R., 20:1387, 1950.

[6] Christian Robelin, Partrice Chartrand, and Gunnar Eriksson. A density model for Multicomponent liquids based on the modified quasichemical model: Application to the NaCl-KCl-$MgCl_2$-$CaCl_2$ system. Metallurgical and Materials Transactions B, 38(6):869–79, December 2007.

[7] D. Inman, D. G. Lovering, and R. Narayan. Polarographic studies in molten $LiNO_3$ + $NaNO_3$ + KNO_3 Part 1. - Half-wave potentials and diffusion coefficients. Transactions of the Faraday Sociey, 63:3017–3025, 1967.

[8] Robert W. Bradshaw and Douglas A. Brosseau. Improved molten salt formulations for heat transfer fluids in parabolic trough solar power systems. In Proceedings of the 2008 14th Biennial SolarPACES Symposium, 2008.

[9] D. F. Williams, L. M. Toth, and K. T. Clarno. Assessment of candidate molten salt coolants for the Advanced High-Temperature Reactor (AHTR). Technical Report ORNL/TM-2006/12, Oak Ridge National Laboratory, March 2006.

[10] F. H. Southworth and P. E. McDonald. The Next Generation Nuclear Power Plant (NGNP) Project. Technical Report INEEL/CON-03-01150, Idaho National Engineering and Environmental Laboratory, 2003.

[11] C. B. Davis, C. H. Oh, R. B. Barner, S. R. Sherman, and D. F. Wilson. Thermal-hydraulic analyses of heat transfer fluid requirements and characteristics for coupling a hydrogen production plant to a high-temperature nuclear reactor. Technical Report INL/EXT-05-0453, Idaho National Laboratory, 2005.

[12] Cliff B. Davis. Implementation of molten salt properties into RELAP5-3D/ATHENA. Technical Report INEEL/EXT-05-02658, Idaho National Engineering and Environmental Laboratory, January 2005.

[13] Per F. Peterson. Capillary tube and shell heat exchanger design for helium to liquid salt heat transfer. Technical Report UCBTH-07-003, U. C. Berkeley, 2007.

[14] H. Susskind, F. B. Hill, L. Green, S. Lakish, L. E. Kukacka,W. E. McNulty, and Jr. E.Wirsing. Corrosion studies for a fused salt-liquid metal extraction process for the liquid metal fuel reactor. Technical report, Brookhaven National Laboratory, 1960.

[15] C. J. Raseman, H. Susskind, G. Farber, W. E. McNulty, and F. J. Salzano. Engineering experience at Brookhaven National Laboratory in handling fused chloride salts. Technical Report BNL-627, Brookhaven National Laboratory, June 1960.

[16] O. Benes and R. J. M. Konings. Thermodynamic evaluation of the NaCl-$MgCl_2$-UCl_3-$PuCl_3$ system. Journal of Nuclear Materials, 375(2-4):202–208, 2008.

[17] A. Mourogov and P. M. Bokov. Potentialities of the fast spectrum molten salt reactor concept: REBUS-3700. Energy Conversion and Management, 47(17):2761–2771, 2006.

[18] Eric. H. Ottewitte. Cursory first look at the molten chloride fast reactor as an alternative to the conventional BATR concept. Technical report, Idaho National Engineering Laboratory, April 1992.

[19] Charles W. Forsberg. Goals, requirements, and design implications for the Advanced High-Temperature Reactor. In 14th International Conference on Nuclear Energy, number ICONE14-89305, 2006.

[20] D. F. Williams. Assessment of candidate molten salt coolants for the NGNP/NHI heat transfer loop. Technical Report ORNL/TM-2006/69, Oak Ridge National Laboratory, June 2006.

[21] Charles W. Forsberg, Per F. Peterson, and Haihua Zhao. High-temperature liquid-fluoride salt closed-brayton-cycle solar power towers. Journal of Solar Energy Engineering, 129:141–146, 2007.

[22] James A Lane, H. G. MacPherson, and Frank Maslan, editors. Fluid Fuel Reactors. Addison-Wesley, 1958.

[23] A. M. Perry and H. F. Bauman. Reactor physics and fuel-cycle analyses. Nuclear Applications and Technology, 8:208–219, 1970.

[24] G. J. Janz and R. P. T. Tomkins. Physical properties data compilations relevant to energy storage. II. Molten Salts: Data on single and multi-component salt systems. Technical Report NIST-NSRDS-61-II, National Standard Reference Data Set, 1981.

[25] G. J. Janz and R. P. T. Tomkins. Physical properties data compilations relevant to energy storage. IV. Molten Salts: Data on additional single and multi-component salt systems. Technical Report NIST-NSRDS-61-IV, National Standard Reference Data Set, 1981.

[26] D. F. Williams, L. M. Toth, K. T.Clarno, and C. W. Forsberg. Assessment of properties of candidate liquid salt coolants for the Advanced High Temperature Reactor (AHTR). Technical Report ORNL/GEN4/LTR-05-001, Oak Ridge National Laboratory, June 30 2005.

[27] D. F.Williams and K. T. Clarno. Evaluation of salt coolants for reactor applications. Nuclear Technology, 163:330–343, 2008.

[28] Charles F. Bonilla. Nuclear Engineering Handbook. McGraw Hill Book Company, 1958.

[29] Marcelle Gaune-Escard, editor. Molten Salts: From Fundamentals to Applications. NATO Science Series II: Mathematics, Physics and Chemistry. Kluwer Academic Publishers, 2002.

[30] M. P. Tosi and F. G. Fumi. Ionic sizes and born repulsive parameters in the NaCl-type alkali halides II: The generalized Huggins-Mayer form. Journal of Physics and Chemistry of Solids, 25:45–52, 1964.

[31] Shima Mizani and Partrice Chartrand. A viscosity model for multi-component molten salt system. Journee des etudiants - REGAL, October 2007.

[32] Alex Kondratiev and Evgueni Jak. A quasi-chemical viscosity model for fully liquid slags in the Al_2O_3-CaO-FeO-SiO_2 system. Metallurgical and Materials Transactions B, 46(5):623–638, October 2005.

[33] R.W. Bradshaw and D. E. Meeker. High-temperature stability of ternary nitrate molten salts for solar thermal energy systems. Solar Energy Materials, 21:51–60, 1990.

[34] G. J. Janz, Ursula Krebs, H. F. Siegenthaler, and R. P. T. Tomkins. Molten salts: Volume 3, nitrates, nitrites, and mixtures. Journal of Physical Reference Data, 1:581–746, 1972.

[35] V. S. Ramachandran, Ralph M. Paroli, James J. Beaudoin, and Ana H. Delgado. Handbook of Thermal Analysis of Construction Materials. William Andrew Publishing/Noyes, 2002.

[36] Peter Atkins and Julio de Paula. Physical Chemistry, 7ed. W. H. Freeman, 2001.

[37] Vladimir Khokhlov, Victor Ignatiev, and Valery Afonichkin. Evaluating physical properties of molten salt reactor fluoride mixtures. Journal of Fluorine Chemistry, 130(1):30–37, January 2009.

[38] M. B. Smirnov, V. A. Khokhlov, and E. S. Filatov. Thermal conductivity of molten alkali halides and their mixtures. Electrochimica Acta, 32(7):1019–1026, 1987.

[39] L. P. Filippov. A method for calculating heat capacity and thermal conductivity of liquids. Journal of Engineering Physics, 32:378–381, 1977.

[40] A. M. Mamedov. Relationship between thermal conductivity, speed of sound, and isobaric heat capacity of liquids. Journal of Engineering Physics and Thermophysics, 39:897–900, 1980.

[41] K Torklep and H. A. Oye. An absolute oscillating-cylinder (or cup) viscometer for high temperatures. J. Phys. E: Sci. Instrum., 12:875–85, 1979.

[42] M. Wakao, K. Minami, and A. Nagashima. Viscosity measurements of molten LiCl in the temperature range 886 - 1275 K. International Journal of Thermophysics, 12(2):223–230, March 1991.

[43] Robert W. Bradshaw. Viscosity of multi-component molten nitrate salts – liquidus to 200 C. Technical Report SAND2010-1129, Sandia National Laboratory, 2010.

[44] J.W. Cooke. Development of the variable gap technique for measuring the thermal conductivity of fluoride salt mixtures. Technical report, Oak Ridge National Laboratory, 1973.

[45] C. T. Ewing, J. R. Spann, and R. R. Miller. Radiant transfer of heat and the thermal conductivity of FLiNaK (Salt ”A”). Technical Report NRL Report 5568, Naval Reactor Laboratory, 1960.

[46] C. T. Ewing, J. R. Spann, and R. R. Miller. Radiant transfer of heat in molten inorganic compounds at high temperatures. Journal of Chemical and Engineering Data, 7(2):246–250, April 1962.

[47] N. Araki. E_ect of radiation heat transfer on thermal diffusivity measurements. International Journal of Thermophysics, 11(2):329–337, 1990.

[48] A. Nagashima. Measurement of transport properties of high-temperature fluids. International Journal of Thermophysics, 12(1):1–15, January 1991.

[49] I. Barin and O. Knacke. Themochemical Properties of Inorganic Substances. Springer-Verlag Berlin Heidelberg New York, 1973.

[50] J. M. Smith, H. C. van Ness, and M. M. Abbott. Introduction to Chemical Engineering Thermodynamics. McGraw Hill, 2001.

[51] J. P. Stark. On the quasi-chemical theory of solutions. Journal of Statistical Physics, 3:395–399, 1971.

[52] A. D. Pelton, S. A. Degterov, G. Eriksson, C. Robelin, and Y. Dessureault. The modified quasichemical model I - Binary solutions. Metallurgical and Materials Transactions B, 31:651–659, 2000.

[53] Arthur D. Pelton and Partrice Chartrand. The modified quasi-chemical model: Part II. multi-component solutions. Metallurgical and Materials Transactions: Part A Physical Metallurgy and Materials Science, 32A:1355–1360, 2001.

[54] James Sangster and Arthur D. Pelton. Phase diagrams and thermodynamic properties of the 70 binary alkali halide systems having common ions. Journal of Physical and Chemical Reference Data, 16:509–561, 1987.

[55] Y Dessureault, J Sangster, and A. D. Pelton. Evaluation critique des donnees thermodynamiques et des diagammes de phases des systemes AOH-AX, ANO3-AX, ANO3-BNO3, AOH-BOH ou A, B = Li, Na, K et X = Cl, F, NO3, OH. J. Chim. Phys., 87:407–453, 1990.

[56] J. P. M. van der Meer, R. J. M. Konings, K. Hack, and H. A. J Oonk. Modeling and calculation of the LiF-NaF-MF3 (M = La, Ce, Pu) phase diagrams. Chemistry of Materials, 18:510–517, 2006.

[57] Amy Sun. Phase equilibria calculations of ternary $LiNO_3$-KNO_3-$NaNO_3$ mixture. email January 2010.

[58] Arthur Pelton and Patrice Chartrand. Thermodynamic evaluation and optimization of the LiCl-NaCl-KCl-RbCl-CsCl-$MgCl_2$-$CaCl_2$ system using the modified quasi-chemical model. Metallurgical and Materials Transactions A, 32:1361–1383, 2001. 10.1007/s11661-001-0227-2.

[59] M Revere and M P Tosi. Structure and dynamics of molten salts. Reports on Progress in Physics, 49:1001–1081, 1896.

[60] J. Sangster and A. D. Pelton. Thermodynamic calculation of phase diagrams of the 60 common-ion ternary systems containing cations Li, Na, K, Rb, Cs and anions F, Cl, Br, I. Journal of Phase Equilibria, 12:511–537, 1991.

[61] Robert W. Cahn and Peter Haasen, editors. Physical Metallurgy. North Holand, 1996.

[62] Robert T DeHoff. Thermodynamics In Materials Science. McGraw-Hill, 1993.

[63] O. J. Kleppa. Calorimetric investigations of liquid solutions of the alkaline earth nitrates in the alkali nitrates. J. Phys. Chem., 66(9):1668–1671, 1962.

[64] Clodagh Ettarh and Andrew K. Galwey. A kinetic and mechanistic study of the thermal decomposition of calcium nitrate. Thermochimica Acta, 288:203–219, 1996.

[65] O. Kubaschewski. Thermochemical Properties of Inorganic Substances. Springer Verlag, 1973.

[66] R. D. Shannon. Revised effective ionic radii and systematic studies of interatomic distances in halides and chalcogenides. Acta Cryst., A32:751–767, 1976.

[67] O. J. Kleppa and L. S. Hersh. Heats of mixing in liquid alkali nitrate systems. The Journal of Chemical Physics, 34:351–358, 1961.

[68] Solar Millenium. The parabolic trough power plants Andasol 1 to 3. Press Release, 2008. http://www.solarmillennium .de/upload/Download/Technologie/eng/Andasol1-3engl.pdf accessed on 03/20/2011.

[69] Kate Guerin. Acciona dedicates Nevada Solar One Plant. Press Release, February 2008. http://www.acciona-na.com/getattachment/1320040c-3b3c-4c96-a20ab30fa875fba1 / accessed on 03/20/2011.

[70] F. Burkholder and C. Kutscher. Heat-loss testing of solel's uvac3 parabolic trough receiver. Technical Report NREL/TP-550-42394, National Renewable Energy Laboratory, 2008.

[71] J. Ambrosek, M. Anderson, K. Sridharan, and T. Allen. Current status of knowledge of the fluoride salt (FLiNaK) heat transfer. Nuclear Technology, 165:1–8, 2009.

[72] Jackson Harvey DeVan. E_ect of alloying additions on corrosion behavior of nickel molybdenum alloys in fused fluoride mixtures. Master's thesis, University of Tennessee, 1960.

[73] G. M. Adamson, R. S. Crouse, and W. D. Manly. Interim report on corrosion by alkali-metal fluorides: Work to may 1, 1953. Technical report, ORNL, 1959.

[74] J. W. Koger. Corrosion product deposition in molten fluoride salt systems. Corrosion - NACE, 30(4):125–130, April 1974.

[75] Victor Ignatiev, Raul Zakirov, and Konstantin Grebenkine. Molten salts as possible fuel fluids for TRU fueled systems. Technical Report ISTC 1606, ISTC, 2006.

[76] R. Littlewood. Diagrammatic representation of the thermodynamics of metal-fused chloride systems. Journal of the Electrochemical Society, 109(6):525–534, June 1962.

[77] R. Littlewood and E. J. Argent. Electrochemical studies of the behavior of metals in fused chlorides. Electrochimica Acta, 4(2-4):155–169, 1961.

[78] R. Littlewood. Electrochemical equilibrium of alloys with chloride melts. Electrochimica Acta, 7(3):399–401, May-June 1962.

[79] S. N. Flengas and T. R. Ingraham. Electromotive force series of metals in fused salts and activities of metal chlorides in 1:1 molar KCl-NaCl solutions. Journal of the Electrochemical Society, 106(8):714–721, 1959.

[80] H. C. Gaur and H. L. Jindal. Standard electrode potentials in molten chlorides — II. Electrochimica Acta, 15:1113–1126, 1970.

[81] I. N. Ozernaya. Corrosion of metals by molten salts in heat-treatment processes. Metal Science and Heat Treatment, 27(3):184–188, March 1985.

[82] J. E. Indacochea, J. L. Smith, K. R. Litko, and E. J. Karell. Corrosion performance of ferrous and refractory metals in molten salts under reducing conditions. Journal of Materials Research, 14(5):1990–1995, May 1999.

[83] J. E. Indacochea, J. L. Smith, K. R. Litko, E. J. Karell, and A. G. Raraz. High-temperature oxidation and corrosion of structural materials in molten chlorides. Oxidation of Metals, 55(1-2):1–16, 2001.

[84] M. Takeuchi, T. Kato, K. Hanada, T. Koizumi, and S. Aose. Corrosion resistance of ceramic materials in pyrochemical reprocessing condition by using molten salt for spent nuclear oxide fuel. Journal of Physics and Chemistry of Solids, 66(2-4):521–525, 2005. Proceedings of the 11th International Conference on High Temperature Materials Chemistry (HTMCXI).

[85] G. A. Gogotsi, Uy. C. Gogotsi, V. P. Zavada, and S. I. Sopenko. Action of salts on the strength and crack resistance of silicon nitride ceramics. Problemy Prochnosti, 11(11):1515–1519, November 1984.

[86] Yuji Hosoya, Takayuki Terai, Toshiaki Yoneoka, and Satoru Tanaka. Compatibility of structural materials with molten chloride mixture at high temperature. Journal of Nuclear Materials, 248:348–353, 1997.

[87] George J. Janz and Reginald P. T. Tomkins. Corrosion in molten salts: An annotated bibliography. Corrosion - NACE, 35:485–504, 1979.

[88] Tz. Tzvetko_, A. Girginov, and M. Bojinov. Corrosion of nickel, iron, cobalt and their alloys in molten salt electrolytes. Journal of Materials Science, 30:5561–5575, 1995.

[89] Luke C. Olson, James W. Ambrosek, Kumar Sridharan, Mark. H. Anderson, Todd R. Allen, and Michael L. Corradini. Evaluation of material corrosion in molten fluoride salt. In AICHE-2006, 2006.

[90] Denny A. Jones. Principles and Prevention of Corrosion. Prentice Hall, 1996.

[91] H. C. Gaur and H. L. Jindal. Standard electrode potentials in molten chlorides. Electrochimica Acta, 13(4):835–842, 1968.

[92] H. C. Gaur and H. L. Jindal. Standard electrode potentials in molten chlorides — III. Electrochimica Acta, 15:1127–1134, 1970.

[93] S. N. Flengas and T. R. Ingraham. Voltaic cells in fused salts: Part V. the systems Sn/SnCl2 (KCl-NaCl), Fe/$FeCl_2$ (KCl-NaCl), and Mn/$MnCl_2$ (KCl-NaCl). Canadian Journal of Chemistry, 36:1662–1667, 1958.

[94] Donald L. Maricle and David N. Hume. A new method for preparing hydroxide-free alkali chloride melts. Journal of the Electrochemical Society, 107(4):354–356, April 1960.

[95] V. P. Kochergin and L. E. Maletina. Corrosion of iron in fused alkali metal and barium chlorides in the presence of sodium tetraborate. Zhurnal Prikladnoi Khimii, 37(8):1823–1825, August 1964.

[96] C. Edeleanu and R. Littlewood. Thermodynamics of corrosion in fused chlorides. Electrochimica Acta, 3(3):195–207, October 1960.

[97] R. Littlewood and E. J. Argent. The e_ect of aqueous contaminants on the redox potential of chloride melts. Electrochimica Acta, 4(2-4):114–128, August 1961.

[98] V. P. Kochergin, L. G. Khaibullina, and O. G. Potapova. Solubility of iron in fused zinc, alkali metal, and alkaline-earth metal chlorides. Journal of Inorganic Chemistry, USSR, 1:191–196, 1956.

[99] David F.Williams, Dane F.Wilson, Louis M. Toth, Joe Caja, and James R. Keiser. Research on molten fluorides as high temperature heat transfer agents. In Global 2003, 2003.

[100] J. H. Jackson and M. H. LaChance. Resistance of cast Fe-Ni-Cr alloys to corrosion in molten neutral heat treating salts. Transactions of the ASM, 46:157–183, 1954.

[101] R. T. Coyle, T. M. Thomas, and G. Y. Lai. Exploratory corrosion tests on alloys in molten salts at 900 C. Journal of Materials for Energy Systems, 7(4):345–352, March 1986.

[102] J.W. Koger. Corrosion product deposition in molten fluoride salt systems. Technical Report CONF-730308, Oak Ridge National Laboratory, March 1973.

[103] R. B. Evans, J. W. Koger, and J. H. DeVan. Corrosion in polythermal loop systems II. A solid-state diffusion mechanism with and without liquid film effects. Technical Report ORNL-4575, V 2, Oak Ridge National Laboratory, 1971.

[104] D. C. Vreeland, E. E. Ho_man, and W. D. Manly. Corrosion tests for liquid metals, fused salts at high temperatures. Nucleonics, 11:36–39, 1953.

[105] David A. Petti, G. R. Smolik, Michael F. Simpson, John P. Sharpe, R. A. Anderl, S. Fukada, Y Hatano, M. Hara, Y. Oya, T. Terai, D. K. Sze, and S. Tanaka. JUPITER-II molten salt Flibe research: An update on tritium, mobilization and redox chemistry experiments. Fusion Engineering and Design, 81:8–14, 2006.

[106] W. R. Grimes. Chemical research and development for molten-salt breeder reactors. Technical report, ORNL, 1967.

[107] T. R. Johnson, F. G. Teats, and R. D. Pierce. A method for the purification of molten chloride salts. Technical Report ANL-7603, Argonne National Laboratory, 9700 South Cass Avenue Argonne, Illinois 60439, August 1969.

[108] A. I. Agulyanskii and P. T. Stangrit. Purification of certain alkali metal halides. Zhurnal Prikladnoi Khimii, 50(6):1201–1204, June 1977.

[109] L. Tan and T. R. Allen. An electron backscattered diffraction study of grain boundary engineered INCOLOY 800H. Metallurgical and Materials Transactions A, 36A:1921–1925, 2005.

[110] L. Tan, K. Sridharan, and T. R. Allen. The effect of grain boundary engineering on the oxidation behavior of INCOLOY Alloy 800H in supercritical water. Journal of Nuclear Materials, 348(3):263–271, 2006.

[111] L. Tan, K. Sridharan, T. R. Allen, R. K. Nanstad, and D. A. McClintock. Microstructure tailoring for property improvements by grain boundary engineering. Journal of Nuclear Materials, 374(1-2):270–280, 2008.

[112] M. Michiuchi, H. Kokawa, Z. J.Wang, Y. S. Sato, and K. Sakai. Twin-induced grain boundary engineering for 316 austenitic stainless steel. Acta Materialia, 54:5179–5184, 2006.

[113] Kuan-Chia Chen,Wen-WeiWy, Chien-Neng Liao, Lih-Juann Chen, and K. N. Tu. Observation of atomic diffusion at twin-modified grain boundaries of copper. SCIENCE, 321:1066–1069, 2008.

[114] M. Lebl and Trnka H. Entfernung von sauersto_haltigen anionen aus alkalihalogeniden (distance of oxygen-containing anions from alkali-halides). Zeitschrift Fur Physik A: Hadrons and Nuclei, 186(2):128–136, 1965.

[115] G. O. Hayner, R. L. Bratton, R. E. Mizina, W. E. Windes, W. R. Corwin, T. D. Burchell, C. E. Duty, Y. Katoh, J.W. Klett, T. E. McGreevy, R.K. Nanstad,W. Ren, P. L. Rittenhouse, L. L. Snead, R. W. Swinderman, and D.F. Wilson. Next Generation Nuclear Plant materials research and development program plan. Technical Report INL/EXT-06-11701, Idaho National Laboratory, 2006.

[116] R. E. Mizia. Next generation nuclear plant intermediate heat exchanger. Technical Report

INL/EXT-08-14054, Idaho National Laboratory, 2008.

[117] Nickel. Technical Report SMC-061, Special Metals, 2006.

[118] J. W. Koger. Evaluation of Hastelloy N alloys after nine years exposure to both a molten fluoride salt and air at temperatures from 700 to 560 C. Technical report, Oak Ridge National Laboratory, 1972.

[119] J. W. Koger and A. P. Litman. Compatibility of Hastelloy N and Croloy 9M with NaBF4-NaF-KBF4 (90-4-6 mole %) fluoroborate salt. Technical Report ORNL-TM-2490, Oak Ridge National Laboratory, 1969.

[120] I. V. Oryshich and O. S. Kostyrko. Influence of molybdenum, tungsten, and cobalt on the corrosion of high-temperature strength nickel alloys in molten salts. Metal Science and Heat Treatment, 27(10):740–746, October 1985. Translated form Metallovedenie i Termicheskaya Obrabotka Metallov.

[121] Inconel alloy 718. Technical Report SMC-045, Special Metals, 2007.

[122] Robert P. Lee and Oliver E. Olsen. Analysis of the failure of a high nickel alloy in molten salt. Practical Metallography, 12:648–653, 1975.

[123] F. P. Incorpera and D. P. DeWitt. Fundamentals of Heat and Mass Transfer. JohnWiley and Sons, Co, 2002.

[124] Samuel Glasstone and Alexander Sesonske. Nuclear Reactor Engineering. D. Van Nostrand Company, Inc., 1963.

[125] Noel de Nevers. Fluid Mechanics for Chemical Engineers'. McGraw Hill, 1991.

[126] J. G. Knudsen, H. C. Hottel, A. F. Sarofim, P. C. Wankat, and K. S. Knaebel. Perry's Chemical Engineers' Handbook. McGraw Hill, 1997.

[127] R. Siegel, E. Sparrow, and T. Hallman. Steady laminar heat transfer in a circular tube with prescribed wall heat flux. Applied Scientific Research, 7:386–392, 1958. 10.1007/BF03184999.

[128] Chia-Jung Hsu. An exact mathematical solution for entrance-region laminar heat transfer with axial conduction. Applied Scientific Research, 17:359–376, 1967. 10.1007/BF02116438.

[129] Eleftherios Papoutsakis, Doraiswami Ramkrishna, and Henry C. Lim. The extended Graetz problem with prescribed wall flux. AIChE Journal, 26(5):779–787, 1980.

[130] Verein Deutscher Ingenieure, editor. VDI Heat Atlas. VDI-Verlag, 1993.

[131] R. K. Shah and A. I. London. Laminar Flow Forced Convection in Ducts. New York,

London, San Francisco: Academic Press, 1978.

[132] Adrian Bejan and Allan D. Kraus. Heat Transfer Handbook. John Wiley and Sons, 2003.

[133] Dr. Bernhard Spang. Correlations for convective heat transfer. world wide web. http://www.cheresources.com/convection.pdf accessed on 1/7/2010.

[134] S. W. Churchill and H. Ozoe. Correlations for laminar forced convection with uniform heating in flow over a plate and in developing and fully developed flow in a tube:. ASME Journal of Heat Transfer, 95:78–84, 1973.

[135] James N Tilton. Perry's Chemical Engineers' Handbook. McGraw Hill, 1997. 208

[136] J. D. Seader and E. J. Henley. Separation Process Principles. John Wiley and Sons, Co, 1998.

[137] Von Volker Gnielinski. Neue gleichungen fur den warme- und den sto_ubergang in turbulent durchstromten rohren und kanalen. Forsch. In.-Wes, 41:8–16, 1975.

[138] J. D. Jackson, M. A. Cotton, and B. P. Axcell. Studies of mixed convection in vertical tubes. International Journal of Heat and Fluid Flow, 10:2–15, 1989.

[139] D. D. Joye and M. J. Wohnovich. Aiding and opposing mixed-convection heat transfer in a vertical tube: loss of boundary condition at di_erent Grashof numbers. International Journal of Heat and Fluid Flow, 17:468–473, 1996.

[140] J. Alan Adams and David F. Rogers. Computer-Aided Heat Transfer Analysis. McGraw Hill, 1973.

[141] H. W. Hoffman and J. Lones. Fused salt heat transfer - Part II: Forced convection heat transfer in circular tubes containing NaF-KF-LiF eutectic. Technical Report ORNL-1777, Oak Ridge National Laboratory, 1955.

[142] Liu Bin, Wu Yu-ting, Ma Chong-fang, Ye Meng, and Guo Hang. Turbulent convective heat transfer with molten salt in a circular pipe. International Communications in Heat and Mass Transfer, 36(9):912–916, November 2009.

[143] Milton D. Grele and Louis Gedeon. Forced-convection heat-transfer characteristics of molten FLiNaK flowing in an Inconel X system. Technical Report NACA RM E53L18 C2, National Advisory Committee for Aeronautics, Lewis Flight Propulsion Laboratory Cleveland, Ohio, May 1954.

[144] Ir. B. Vriesema. Aspects of Molten Fluorides as Heat Transfer Agents for Power Generation. PhD thesis, Delft University of Technology the Netherlands, January 1979. 209

[145] V. V. Ignat'ev, S. V. Keronovskii, A. I. Surenkov, O. P. Shcherbanyuk, S. P. Manchkha, and Yu. B. Smirnov. Heat exchange during the flow of a melt of LiF-NaF-KF fluoride salts in a circular tube. Atomnaya Energiya, 57(2):123–124, August 1984.

[146] J. W. Cooke and B. Cox. Forced-convection heat-transfer measurements with a molten fluoride salt mixture flowing in a smooth tube. Technical Report ORNL-TM-4079, ORNL, 1973.

[147] V. V. Ignatyev, V. M. Novikov, and A. I. Surenkov. Heat transfer in closed thermosyphons as applied to molten salt reactor designs. Kerntechnik, 54:44–50, 1989.

[148] Y. Nagasaka and A. Nagashima. Measurement of the thermal diffusivity of molten KCl up to 1000 C by the forced rayleigh scattering method. International Journal of Thermophysics, 9:923–, 1988.

[149] Philippe M. Bardet and Per F. Peterson. Options for scaled experiments for high temperature liquid salt and helium fluid mechanics and convective heat transfer. Nuclear Technology, 163:344–357, 2008.

[150] J. Takeuchi, S. Satake, R. Miraghaie, K. Yuki, T. Yokomine, T. Kunugi, N.B. Morley, and M.A. Abdou. Study of heat transfer enhancement/suppression for molten salt flows in a large diameter circular pipe: Part I: Benchmarking. Fusion Engineering and Design, 81(1-7):601 – 606, 2006. Proceedings of the Seventh International Symposium on Fusion Nuclear Technology - ISFNT-7 Part A.

[151] K. Abe, A. Kohyama, S. Tanaka, C. Namba, T. Terai, T. Kunugi, T. Muroga, A. Hasegawa, A. Sagara, S. Berk, S.J. Zinkle, D.K. Sze, D.A. Petti, M.A. Abdou, N.B. Morley, R.J. Kurtz, L.L. Snead, and N.M. Ghoniem. Development of advanced blanket performance under irradiation and system integration through JUPITER-II project. Fusion Engineering and Design, 83(7-9):842 – 849, 2008. Proceedings of the Eight International Symposium of Fusion Nuclear Technology - ISFNT-8 SI.

[152] Daniel T. Ingersoll, Charles W. Forsberg, and Phil E. MacDonald. Trade-studies for the Liquid-Salt-Cooled Very High-Temperature Reactor: Fiscal year 2006 progress report. Technical Report ORNL/TM-2006/140, Oak Ridge National Laboratory, 2007.

[153] David E. Fluck, Robert B. Herchenroeder, George Y. Lai, and Michael F. Rothman. Selecting alloys for heat treating equipment. Metal Progress, 128:35–40, 1985.

[154] Miguel Barrientos. index mundi. website. http://www.indexmundi.com/commodities/?commodity=metals-price-index accessed on 02/10/2011.

[155] W. B. Cottrell, H. E. Hungerford, J. K. Leslie, and J. L. Meew. Operation of the aircraft reactor experiment. Technical Report ORNL-1845, Oak Ridge National Laboratory, 1955.

[156] R. K. Turton. Rotodynamic Pump Design. Cambridge University Press, 1994.

[157] W. R. Huntley and P. A. Gnadt. Design and operation of a forced-circulation corrosion test facility (MSR-FCL-1) employing Hastelloy N alloy and sodium fluoroborate salt. Technical report, Oak Ridge National Laboratory, 1973.

[158] Gefran. NaK FILLED MELT PRESSURE TRANSMITTERS: KN SERIES, Feb 2011.

[159] OneHalf20. Model RTNAK: NaK Filled Melt Pressure Transducer, 2011.

[160] Stephen A. Hluchan. A differential pressure instrument for high temperature service. In Nuclear Engineering and Science Conference, volume 60. American Institute of Electrical Engineers, Engineers Joint Council, April 6-9 1959.

[161] S. A. Hluchan. Pressure and temperature transducers for high temperature and nuclear radiation environments. In National Telemetering Conference. Bourns Inc., 1964.

[162] Yves Dessureault, James Sangster, and Arthur D. Pelton. Coupled phase diagram thermodynamic analysis of the nine common-ion binary systems involving the carbonates and sulfates of lithium, sodium, and potassium. Journal of The Electrochemical Society, 137(9):2941–2950, 1990.

[163] Patrice Chartrand and Arthur Pelton. Thermodynamic evaluation and optimization of the LiF-NaF-KF-MgF_2-CaF_2; system using the modified quasi-chemical model. Metallurgical and Materials Transactions A, 32:1385–1396, 2001. 10.1007/s11661-001-0228-1.

[164] James Sangster. Thermodynamics and phase diagrams of 32 binary common-ion systems of the group Li,Na,K,Rb,Cs//F,Cl,Br,I,OH,NO3. Journal of Phase Equilibria, 21:241–268, 2000.

[165] O. Benes and R.J.M. Konings. Thermodynamic evaluation of the MF-LaF_3 (M=Li, Na, K, Rb, Cs) systems. Calphad, 32(1):121 – 128, 2008.

[166] O. Benes and R.J.M. Konings. Thermodynamic evaluation of the (LiF+NaF+BeF_2+PuF_3) system: An actinide burner fuel. The Journal of Chemical Thermodynamics, 41(10):1086 – 1095, 2009.

Appendix A

Salt Properties

A.1 Gibbs Excess Energies Binary Mixtures

The Gibbs excess energy of binary salt mixtures is what is used in the assessment of the thermo-physical properties of the salt systems. The Gibbs excess energy for many binary systems has been analyzed previously in literature [54, 55, 58, 162, 163]. The original thermodynamic data was optimized using either the linear expansion or Modified Quasi-Chemical Models. The optimized parameters as reported in the literature is listed in Table A.1 and A.2 for the polynomial expansion and MQCM, respectively.

Table A.1. Gibbs excess energies of the liquid phases for the binary salt systems as found in literature based on polynomial expansion.

Salt	Excess Enthalpy	Excess Entropy	Reference
LiF – RbF	$X_{LiF}\,X_{RbF}\,(-17155 - 6275\,X_{LiF})$	$X_{LiF}\,X_{RbF}\,(-22.166 - 49.02\,X_{RbF} - 33.890\,X_{RbF}^2)$	[54]
NaF – RbF	$X_{NaF}\,X_{RbF}\,(375)$	$X_{NaF}\,X_{RbF}\,(-2.658 + 4.140\,X_{RbF} - 4.702\,X_{RbF}^2)$	[54]
KF – RbF	$X_{KF}\,X_{RbF}\,(360)$	0	[54]
RbF – CsF	0	0	[54]
$LiNO_3$-$NaNO_3$	$X_{LiNO3}\,X_{NaNO3}\,(-1906 + 32\,(X_{NaNO3}-X_{LiNO3}))$	$X_{LiNO3}\,X_{NaNO3}\,(0.874)$	[55]
$LiNO_3$-KNO_3	$X_{LiNO3}\,X_{KNO3}\,(-8026 - 182\,(X_{LiNO3}-X_{KNO3}) + 484\,(X_{LiNO3}-X_{KNO3})^2)$	$X_{LiNO3}\,X_{KNO3}\,(5.334)$	[55]
$LiNO_3$-$RbNO_3$	$X_{LiNO3}\,X_{RbNO3}\,(-10010 - 854\,X_{LiNO3} - 4160\,X_{LiNO3}\,X_{RbNO3})$	$X_{LiNO3}\,X_{RbNO3}\,(10.215 - 6.954\,X_{RbNO3})$	[164]
$LiNO_3$-$CsNO_3$	$X_{LiNO3}\,X_{RbNO3}\,(-14350 - 1000\,X_{LiNO3} - 6444\,X_{LiNO3}\,X_{RbNO3})$	$X_{LiNO3}\,X_{RbNO3}\,(-4.672)$	[164]
$NaNO_3$-KNO_3	$X_{NaNO3}\,X_{KNO3}\,(-1780 - 140\,(X_{NaNO3}-X_{KNO3})$	0	[55]
$NaNO_3$-$RbNO_3$	$X_{NaNO3}\,X_{RbNO3}\,(-2960 - 954\,X_{NaNO3} - 987\,X_{NaNO3}\,X_{RbNO3})$	$X_{NaNO3}\,X_{RbNO3}\,(2.629 - 3.198\,X_{RbNO3})$	[164]
$NaNO_3$-$CsNO_3$	$X_{NaNO3}\,X_{RbNO3}\,(-4356 - 1820\,X_{NaNO3} - 389\,X_{NaNO3}\,X_{RbNO3})$	$X_{NaNO3}\,X_{RbNO3}\,(1.284)$	[164]
KNO_3-$RbNO_3$	$X_{KNO3}\,X_{RbNO3}\,(-187 - 138\,X_{KNO3})$	0	[164]
KNO_3-$CsNO_3$	$X_{KNO3}\,X_{RbNO3}\,(-374 - 366\,X_{KNO3})$	0	[164]
$RbNO_3$-$CsNO_3$	$X_{RbNO3}\,X_{RbNO3}\,(-59)$	$X_{RbNO3}\,X_{RbNO3}\,(2723 + 1373\,X_{RbNO3})$	[164]
Li_2CO_3 - Na_2CO_3	$X_{Na2CO3}\,X_{Li2CO3}\,(-11195 - 1295\,(X_{Na2CO3} - X_{Li2CO3}))$	$X_{Na2CO3}\,X_{Li2CO3}\,(-5.600)$	[162]
Li_2CO_3 - K_2CO_3	$X_{Li2CO3}\,X_{K2CO3}\,(-33060 - 5500\,(X_{Li2CO3} - X_{K2CO3}))$	$X_{Na2CO3}\,X_{Li2CO3}\,(-14.065 + 2.329\,(X_{Li2CO3} - X_{K2CO3}))$	[162]
Na_2CO_3 - K_2CO_3	$X_{Na2CO3}\,X_{K2CO3}\,(-5665 - 635\,(X_{Na2CO3} - X_{K2CO3}))$	0	[162]

Table A.2. Gibbs excess energies of the liquid phases for the binary salt systems as found in literature for the MQCM.

Salt (A - B)	ΔG_{AB}	Reference
LiF - NaF	-2161.0 + 0.6698 T - 574.1 X_{AA} -332.8 X_{BB}	[163]
LiF - KF	-5404.6 + 0.6249 T + (-1100.9 + 1.0431 T) X_{AA}	[163]
LiF - CsF	-5038.7 + 1375 X_{BB}	[165]
LiF - BeF_2	-8200.6 - 6.276 T + (12552-17.154*T) X_{BB} + (18158.6-7.513*T) X^2_{BB} + 1.674*T*X_{AA}	[166]
LiF - MgF_2	-7175.0 - 888.8 X_{AA} - 8607.8 X_{BB}	[163]
LiF - CaF_2	-2183.5 + 1.3951 T + 595.7 X_{AA} - 790.8 X_{BB}	[163]
NaF – CsF	-2893.0 + 3.252 T + 283.4 X_{BB}	[165]
NaF - BeF_2	-29288 + (-10460+9.456 T) X_{AA} + (33472-29.832 T) X^2_{BB}	[166]
NaF - MgF_2	-14564 + 0.7765 T + (-19886+5.4 T) X_{BB}	[163]
NaF - CaF_2	-4266.1 + 2.6145 T + -2863.4 X_{AA} + (-11746.5 + 6.4326 T) X_{BB}	[163]
KF – RbF	120.32	[165]
KF – CsF	964.2	[165]
KF - MgF_2	-23974.4 + 6.8813 T + (1730.7 - 3.2421 T) X_{AA} + (-35478. + 2.0 T) X_{BB} + 18875 X^2_{AA}	[163]
KF - CaF_2	-10223.2 + 5.0779 T - 907.3 X_{AA} + (-9438.7 + 5.516 T) X_{BB}	[163]
MgF_2 - CaF_2	-2859.0 - 2872.8 X_{AA} - 1417.2 X_{BB}	[163]
LiCl – NaCl	-1562	[58]
LiCl – KCl	-4884.6 + 1.1 T + (-1147.3 + 1.5146 T) X_{BB} + (-864.7 - 0.3805 T) X_{AA}	[58]
LiCl - RbCl	-5955.3 + 2.4507 T - 1602.0 X_{AA} + 2.2417 T X_{BB} - 1325.0 X_{AA} X_{BB}	[58]
LiCl - CsCl	-6485.3 + 6.8470 T + (2482.7 - 1.0950 T) X_{AA} - 3026.7 X_{AA} X_{BB}	[58]
LiCl - $MgCl_2$	-4147.1 + 0.2356 T + (8274.0 - 1.3821 T) X_{AA} + (2079.9 - 2.6524 T) X_{BB}	[58]
LiCl – $CaCl_2$	-682.4 - 24.2 X_{AA} - 299.6 X_{BB}	[58]
NaCl – KCl	-695.5 – 67 X_{AA}	[58]
NaCl – RbCl	-1074.0 + 0.2257 T - 111.7 X_{AA} + 1.7483 T X_{BB}	[58]
NaCl – CsCl	-1436.7 + 1.9213 T + (139.3 - 1.9670 T) X_{AA}	[58]
NaCl – $MgCl_2$	-10395.8 + 660.5 X_{AA} - 4641.5 X_{BB}	[58]
NaCl – $CaCl_2$	-4710.2 + 0.7805 T + (-1347.8 + 0.5726 T) X_{AA} + (-1580.0 + 0.1473 T) X_{BB}	[58]
KCl – RbCl	28	[58]

KCl – CsCl	265	[58]
KCl - $MgCl_2$	-19223. - 5.9468 T + 0.8491 T ln(T) + (3324.3 - 1.0130 T) X_{AA} -3158. X_{BB} - 9481.7 X^2_{BB}	[58]
KCl - $CaCl_2$	-12281 + 3.9760 T - 852.6 X_{AA} - 5930.6 X_{BB}	[58]
RbCl – CsCl	112	[58]
RbCl - $MgCl_2$	-22369.8 + 0.4469 T + 4863.0 X_{AA} - 3120. X^2_{AA} - 6667.0 X_{BB} - 11781 X^2_{BB}	[58]
RbCl - $CaCl_2$	-1668.0 + 0.9375 T + (-4179 + 4.5342 T) X_{AA} + (-12662.0 + 7.2799 T) X_{BB}	[58]
CsCl - $MgCl_2$	-24130 + 0.5996 T + (1404.2 + 0.1129 T) X_{AA} - 26822 X_{BB} + 43985.0 * X^2_{BB} - 42805.0 X^3_{BB}	[58]
CsCl - $CaCl_2$	-15595.0 - 3.6829 T + 1610.0 X_{AA} - 8744 X_{BB}	[58]
$MgCl_2$ - $CaCl_2$	437.6 - 0.5171 T + (1467.6 - 0.1921 T) X_{AA} + (-730.2 + 1.6255 T) X_{BB}	[58]

As part of the application of the system, the excess Gibbs energy from Table A.1 has been converted to a format suitable for use in the MQCM using site fractions. This was accomplished using a Matlab script to equate the excess energies. The script computes the Gibbs energy of the system from reported values and computes the Gibbs excess energy needed using the MQCM approach to reproduce the same Gibbs energy for the system. A list of the optimized values from this approach is presented in Table A.3.

Table A.3. Parameters to compute Gibbs excess energies of the liquid phase using the MQCM model for the binary salt systems.

Salt	Gibbs excess energy
LiF - RbF	$-6564.866 + 7148.743\ X_{AA} + 3507.528\ X_{BB}$
NaF - RbF	$389.934 + 869.647\ X_{AA} + 1111.417\ X_{BB}$
KF - RbF	120.32
RbF - CsF	0
$LiNO_3$-$NaNO_3$	$-806.9 + 12.755\ X_{BB}$
$LiNO_3$-KNO_3	$-3412.4 - 208.29\ X_{AA}$
$LiNO_3$-$RbNO_3$	$-4022.8 - 1837.4\ X_{AA} - 222.6\ X_{BB}$
$LiNO_3$-$CsNO_3$	$-3798.8 - 494.5\ X_{AA} - 181.0\ X_{BB}$
$NaNO_3$-KNO_3	$-556.88 - 90.142\ X_{AA}$
$NaNO_3$-$RbNO_3$	$-1375.2 - 481.9\ X_{AA} + 478.2\ X_{BB}$
$NaNO_3$-$CsNO_3$	$-1779.6 - 580.8\ X_{AA}$
KNO_3-$RbNO_3$	$-84.788 - 23.57\ X_{AA} + 22.36\ X_{BB}$
KNO_3-$CsNO_3$	$-183.45 - 63.30\ X_{AA} + 58.37\ X_{BB}$
$RbNO_3$-$CsNO_3$	-19.660
Li_2CO_3 - Na_2CO_3	$-2406.4 + 740.1\ X_{AA}$
Li_2CO_3 - K_2CO_3	$-5186.5 - 4570.1\ X_{AA}$
Na_2CO_3 - K_2CO_3	$-1702.0 - 413.9\ X_{AA}$

The Gibbs excess energies are then computed for the different systems to compute site fractions for optimization of other thermodynamic properties.

A.2 Heat Capacity

The heat capacity of FLiNaK and KCl-$MgCl_2$ was measured at the University of Wisconsin using modulated differential scanning calorimetry (MDSC). A sample of the salt (10 - 20 mg) was placed in a hermetic stainless steel pan and sealed in an inert glove box. The sample was then moved from the glove box to the DSC unit. Samples of each salt (9 FLiNaK samples and 5 KCl-MgCl2) samples were run and the average heat capacity for the two salts is shown in Figures A.1 and A.2 compared to the values from thermodynamic optimization. The Gibbs energies for the LiF, NaF, and KF were the values reported in literature [163]. The excess Gibbs energy from FLiNaK were obtained using the Kohler method with the excess energies for the binary systems from literature [54]. The KCl and $MgCl_2$ values and excess Gibbs energies used in the model were from work by Chartrand and Pelton [58].

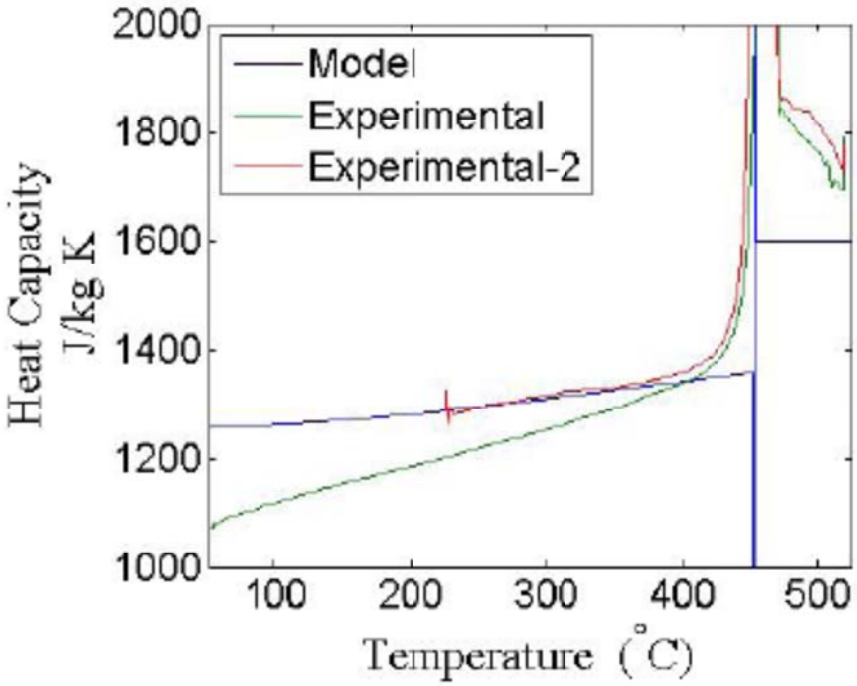

Figure A.1. The heat capacity of FLiNaK was measured by MDSC and compared to the heat capacity from modeling. Experimental - 5 samples averaged and Experimental 2 - 4 samples averaged.

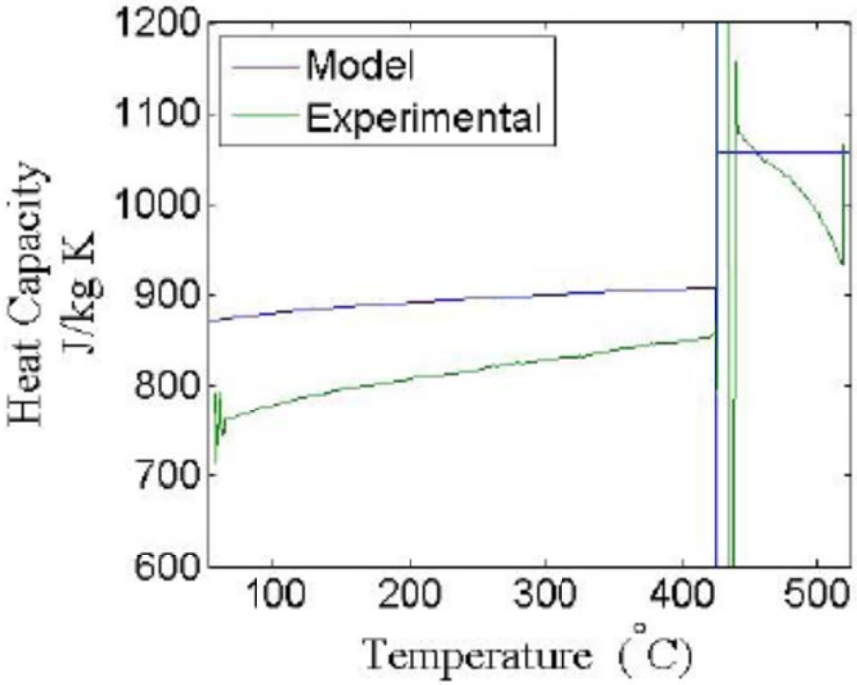

Figure A.2. The heat capacity of KCl-$MgCl_2$ was measured by MDSC at University of Wisconsin compared to the model heat capacity: 4 samples averaged.

A.3 Molar Volumes

The molar volumes of many different components have been determined by linear regression of experimental data that was presented by Janz in his compilations [24, 25]. The molar volumes of the unary salt compounds have been fitted to the linear equation as found in Equation A.2.

The experimental values for the molecular volumes of the unary salts are determined from the density data. The volume for the unary salt is then fit to the following equation:

$$V(T) = V(T_{Ref})\exp\left(\int_{T_{Ref}}^{T}\alpha(T)dT\right) \quad \text{(A.1)}$$

where $\alpha(T)$ is a polynomial representation of the thermal expansion of the salt

$$\alpha(T) = a_0 + a_1T + a_2T^{-1} + a_3T^{-2} \quad \text{(A.2)}$$

Taking the natural log of each side of Equation 3.59 to reduce it to a linear equation that is solved for the parameters $V(T_{Ref})$, a_0, a_1, a_2, and a_3. These parameters for many different molten salts are presented in the following table.

Table A.4. The constants used in Equation A.2 for the determination of the thermal expansion used in calculating the molar volume of unary components.

Salt	$V(T_{Ref})$	$\alpha_O \times 10^{-4}$	$\alpha_1 \times 10^{-8}$	$\alpha_2 \times 10^{-2}$	$\alpha_3 \times 10^{2}$
LiF	2.4636	1.2285	4.7127	3.4654	
NaF	2.5715	1.2586	2.4895	1.512	
KF	3.1781	0.6399	8.8502	8.2984	
RbF	3.3211	0.5682	9.9048	8.8915	
BeF_2	3.1735	0.07352	0.00277	5.39E-05	
CaF_2	3.2225	0.77703	1.7361	3.1958	
LiCl	3.1865	1.6184	5.4296	2.2637	
NaCl	3.3689	0.74636	9.3191	7.7993	
KCl	3.6303	0.7653	12.035	7.8969	
RbCl	3.7346	0.58641	11.597	9.0497	
CsCl	3.8688	1.0435	11.384	6.7702	
$MgCl_2$	3.9297	1.2527	1.5582	0.51119	
$CaCl_2$	3.8455	1.2962	2.2621	1.131	
$LiNO_3$	3.5595	1.5602	12.814	7.5075	0.12207
$NaNO_3$	3.7061	2.2844	7.3148	1.2776	
KNO_3	3.8681	0.84741	14.958	12.301	0.22559
$RbNO_3$	3.9635	1.0304	15.511	11.254	0.19548
$CsNO_3$	4.0923	2.0957	10.961	2.8048	
$Ca(NO_3)_2$*	4.1194	292.19	-85.774	-16.031	-29.576
Li_2CO_3	3.5505	1.4461	3.1094	1.3739	
Na_2CO_3	3.8151	1.3223	3.0329	1.7753	
K_2CO_3	4.092	1.2768	3.8155	2.6213	

The binary interactions for multiple binary solutions was also determined according to the method described by Robelin [6] and in Chapter 3. The density for the binary systems was determined using the equations for the density tabulated in the NIST database by Janz [24, 25]. The values in Table A.5 are those for use in the following equation:

$$\Delta G_{AB}^{P} = \beta_0 + \beta_1 T + \beta_2 X_{AA} + \beta_3 X_{BB} \quad \text{(A.3)}$$

Table A.5. The binary interaction parameters for binary systems as determined using the site fraction data obtained from the MQCM. Salts are listed as A,B//X, where A and B are the cations and X is the anion.

Binary Salt	$\beta_0 \times 10^{-2}$	β_1	$\beta_2 \times 10^{-2}$	$\beta_3 \times 10^{-2}$
Li,Na//F	2.1854			
Li,K//F	-0.90376		6.1983	
Li,Rb//F	11.611			
Li,Be//F	-18.97		70.359	40.262
Li,Ca//F	-0.5291			28.603
Na,K//F	-42.33		67.656	96.458
Na,Be//F	-2.6779		1.1057	
Na,Ca//F	1.1246			
Li,Na//Cl	0.85024			
Li,K//Cl	0.42372			
Li,Rb//Cl	3.6758			
Li,Mg//Cl	-0.65846			-38.770
Li,Ca//Cl	4.781			
Na,K//Cl	2.2749			
Na,Rb//Cl	164.27		-253.46	-255.14
Na,Cs//Cl	6.9289			
Na,Mg//Cl	9.9897		-3.5657	-43.942
Na,Ca//Cl	7.211			
K,Rb//Cl	1.45			
K,Cs//Cl	3.7243			
K,Mg//Cl	26.798			
K,Ca//Cl	0.26021			20.296
Rb,Cs//Cl	3.2689			
Rb,Mg//Cl	33.672		-25.896	-62.887
Rb,Ca//Cl	9.1611			
Cs,Mg//Cl	31.098			
Cs,Ca//Cl	-82.816		115.49	101.33
Mg,Ca//Cl	-16.481			
Li,Na// NO_3	3.5005			
Li,K// NO_3	-7.8478		-40.617	76.719
Li,Rb// NO_3	2.216			
Li,Cs// NO_3	12.883			-14.759
Li,Ca//NO_3	Assumed Ideal due to lack of data			
Na,K// NO_3	-0.54067			
Na,Rb//NO_3	1.0607			
Na,Cs//NO_3	1.8839			

$Na,Ca//NO_3$	-0.47278			
$K,Rb//NO_3$	4.4915			
$K,Cs//NO_3$	-1.1079			
$K,Ca//NO_3$	0.001685			
$Rb,Cs//NO_3$	-0.32139			
$Li,Na//CO_3$	2.9065			
$Li,K//CO_3$	3.5814			
$Na,K//CO_3$	-0.71301			

A.4 Viscosity

The viscosity for many different binary salt mixtures has been optimized for both of the viscosity models described in Section 3.10. The optimized parameters for the different systems are listed in Table A.6 and A.7.

Table A.6. The binary interaction parameters for the viscosity of binary systems using Equation 3.64.

	Component A		Component B		AB Mixture	
Salt	E_A	ε	E_A	ε	E_A	ε
Li,Na//F	37237	2.5348	43635	2.5809	39946	2.5439
Li,K//F	40869	2.5656	42275	2.5834	44593 - 2185.8 X_{AA}	2.6070 + 0.015681 X_{AA}
Li,Rb//F	37237	2.5348	38909	2.5836	57257	2.7259
Na,K//F	58300	2.6612	39082	2.5672	26925	2.5154
Li,Na//Cl	31490	2.5372	36211	2.5648	33850	2.5500
Li,K//Cl	36017	2.5746	40234	2.5886	37344 - 18326 X_{AA}	2.5899 - 0.16163 X_{AA}
Li,Rb//Cl	38196	2.5956	37840	2.5771	39013 - 22124 X_{AA}	2.6099 - 0.1819 X_{AA}
Li,Cs//Cl	39071	2.6056	35216	2.5662	5933.3 + 37213 X_{AA} + 69703 X_{BB}	2.2708 + 0.46110 X_{AA} + 0.72733 X_{BB}
Li,Mg//Cl	34440	2.5567	34932	2.5447	54751 - 57760 X_{AA} + 39394 X_{BB}	2.7535 - 0.5270 X_{AA} + 0.36547 X_{BB}
Na,K//Cl	53229	2.6807	42360	2.6055	46566 - 437.25 X_{AA}	2.6450 - 0.042365 X_{AA}
Na,Mg//Cl	36211	2.5663	36801	2.5627	51170 - 165310 X_{AA}	2.7598 - 1.7929 X_{AA}
Na,Ca//Cl	56254	2.6975	42120	2.5388	-69735 + 219540 X_{AA} 193850 X_{BB}	1.6795 + 1.6904 X_{AA} + 1.5093 X_{BB}
K,Rb//Cl	40908	2.5937	37840	2.5771	35003	2.5552
K,Cs//Cl	40975	2.5942	35283	2.5668	41097 - 8453.1 X_{AA}	2.6168 - 0.062011 X_{AA}
K,Mg//Cl	41297	2.5946	36828	2.562	56907 - 87073 X_{AA} - 77682 X_{BB}	2.6168 - 0.71117 X_{AA} - 0.61453 X_{BB}
Rb,Cs//Cl	37840	2.5771	35283	2.5668	22145	2.3506
Li,Na//NO_3	26362	2.4024	24975	2.4011	22145	2.3506
Li,K//NO_3	26362	2.4024	26784	2.4193	23780	2.3889
Li,Rb//NO_3	26362	2.4024	24613	2.3768	22351 + 11771 X_{BB}	2.2836 + 0.2747 X_{BB}
Li,Cs//NO_3	26362	2.4024	31173	2.4826	15222 + 11068 X_{AA} + 8286.7 X_{BB}	2.2466 + 0.22631 X_{AA} + 0.19865 X_{BB}
Li,Ca//NO_3	26362	2.4024	82830	3.1707	93426 - 402880 X_{BB}	3.3836 - 7.6053 X_{BB}
Na,K//NO_3	24614	2.3949	27452	2.4285	24322	2.4001
Na,Rb//NO_3	24945	2.4006	24924	2.3822	30849	2.5098
Na,Cs//NO_3	24614	2.3949	31173	2.4826	24851	2.4200
Na,Ca//NO_3	24080	2.3879	82830	3.1707	54212 - 239550 X_{BB}	2.8011 - 4.8239 X_{BB}
K,Ca//NO_3	27440	2.3578	82830	3.1707	35933 + 29510 X_{BB}	2.5304 + 0.16802 X_{BB}

Table A.7. The binary interaction parameters for the viscosity of binary systems for use in Equation 3.65.

Salt	G_{AA}	G_{BB}	G_{AB}
Li,Na//F	18431 + 18.718 T	21066 + 19.837 T	29395 + 12.090 T
Li,K//F	22459 + 15.090 T	22728 + 19.667 T	26747 + 13.729 T
Li,Rb//F	18274 + 18.538 T	21067 + 21.903 T	48853 - 5.6320 T
Li,Be//F	18274 + 18.538 T	244050 - 94.692 T	-2708700 + 1925.0 T
Na,K//F	35843 + 10.689 T	19401 + 21.553 T	9008.9 + 25.164 T
Na,Be//F	21674 + 19.484 T	244050 - 94.692 T	-84474 + 86.237 T
Li,Na//Cl	16707 + 19.663 T	18058 + 21.328 T	-22469 + 58.259 T
Li,K//Cl	18058 + 21.328 T	22176 + 20.091 T	22328 + 16.541 T
Li,Rb//Cl	23593 + 13.163 T	20944 + 22.591 T	24878 + 14.794 T
Li,Mg//Cl	20258 + 16.899 T	19990 + 27.764 T	-15546 + 54.506 T
Na,K//Cl	35286 + 8.0055 T	24430 + 18.096 T	29001 + 12.815 T
Na,Mg//Cl	18185 + 21.164 T	22251 + 25.458 T	13239 + 24.000 T
Na,Ca//Cl	38701 + 5.5627 T	26733 + 27.828 T	70910 - 13.795 T
K,Rb//Cl	22476 + 20.051 T	20944 + 22.591 T	12814 + 29.043 T
K,Mg//Cl	23511 + 19.186 T	21886 + 25.917 T	4506.1 + 35.188 T
Rb,Cs//Cl	20944 + 22.591 T	19054 + 24.865 T	23541 + 20.062 T
Li,Na//NO_3	17415 + 19.683 T	15525 + 21.699 T	14902 + 22.357 T
Li,K//NO_3	17415 + 19.683 T	17244 + 21.320 T	15177 + 22.495 T
Li,Rb//NO_3	17415 + 19.683 T	15112 + 27.127 T	20233 + 14.824 T
Li,Cs//NO_3	17415 + 19.683 T	19652 + 21.763 T	7793.3 + 33.827 T
Li,Ca//NO_3	18580 + 17.164 T	60459 - 62.723 T	-116620 + 315.43 T
Na,K//NO_3	15038 + 22.452 T	17016 + 21.808 T	15693 + 21.425 T
Na,Rb//NO_3	15206 + 22.211 T	14973 + 27.350 T	21185 + 14.279 T
Na,Cs//NO_3	14848 + 22.765 T	20188 + 21.019 T	9754.5 + 31.542 T
Na,Ca//NO_3	14828 + 22.548 T	60459 - 62.723 T	-111230 + 233.80 T
K,Rb//NO_3	17159 + 21.560 T	14987 + 27.324 T	15277 + 25.356 T
K,Cs//NO_3	16969 + 21.866 T	20189 + 21.016 T	12162 + 29.555 T

K,Ca//NO_3	17971 + 20.355 T	60459 - 62.723 T	32469 + 17.968 T
Rb,Cs//NO_3	14987 + 27.324 T	20189 + 21.017 T	13845 + 28.868 T
Li,Na//CO_3	26467 + 27.944 T	26305 + 29.168 T	19969 + 30.874 T
Li,K//CO_3	26539 + 28.094 T	24377 + 29.187 T	35419 + 16.092 T
Na,K//CO_3	26305 + 29.167 T	24119 + 31.864 T	24479 + 31.173 T

A.5 Adiabatic Compressibility

The following tables show the determined values for the equations used to modelt the adiabatic compressibility of the unary and binary salt systems, Table A.8 and A.9.

Table A.8. The coefficients to reproduce the adiabatic compressiblity for unary systems using Equation 3.69.

Salt	$\kappa(T_{Ref})$	$\chi_1 \times 10^4$	$\chi_2 \times 10^7$	$\chi_3 \times 10$	$\chi_4 \times 10^{-2}$
LiF	-23.181	-0.79501	3.9880	4.0116	
NaF	-22.603	-3.3187	4.4474	5.8096	
KF	-21.806	-1.6107	4.4716	4.6265	
LiCl	-22.458	-0.40511	4.0597	3.8491	
NaCl	-22.005	-2.9720	4.5579	5.5880	
KCl	-21.365	-1.6200	4.7107	4.6745	
$LiNO_3$	-20.834	5.3066	4.2363	1.9002	0.24296
$NaNO_3$	-20.995	82.758	-28.118	-25.901	-4.0573
KNO_3	-20.804	48.903	-9.3760	-15.822	-2.9210
$RbNO_3$	-20.417	78.134	-20.491	-27.815	-4.8767
$CsNO_3$	-19.888	24.457	-1.4703	-2.1050	

Table A.9. The coefficients to account for the binary interactions on the adiabatic compressiblity.

Salt	Binary Interaction
Li,Na//F	9.5462×10^{-12}
Li,K//F	5.3410×10^{-12}
Na,K//F	$-1.4534 \times 10^{-10} + 2.7198 \times 10^{-10} X_{AA} + 4.5620 \times 10^{-10} X_{BB}$
Li,Na//Cl	2.0303×10^{-11}
Li,K//Cl	4.3326×10^{-11}
Na,K//Cl	$1.4088 \times 10^{-12} + 1.2301 \times 10^{-10} X_{AA} + 2.4547 \times 10^{-10} X_{BB}$
Li,K//NO_3	$-3.2878 \times 10^{-11} - 6.3109 \times 10^{-11} X_{AA} + 2.5241 \times 10^{-10} X_{BB}$
Li,Cs//NO_3	2.1495×10^{-12}
Na,K//NO_3	-4.8410×10^{-12}
Na,Cs//NO_3	-1.3841×10^{-10}
K,Rb//NO_3	-1.6008×10^{-10}
K,Cs//NO_3	$-3.2566 \times 10^{-10} - 1.4073 \times 10^{-10} X_{AA} + 2.4466 \times 10^{-10} X_{BB}$
Rb,Cs//NO_3	-9.5952×10^{-11}

A.6 Thermal Conductivity

The following are the parameters determined for the thermal conductivity model for the unary and binary salts, Tables A.10 and A.11.

Table A,10. Coefficients for calculation of γ using Equation 3.73 for the thermal conductivity model.

Salt	γ_0	$\gamma_1 \times 10^3$	$\gamma_2 \times 10^7$	γ_3	γ_4
LiF	3.48915	5.52749	-2.82048	-4.84575	
NaF	3.90418	4.62886	-0.697842	-4.78811	
KF	3.86958	5.34641	-1.64919	-5.21794	
LiCl	1.80114	4.09969	-6.42607	-3.11393	
NaCl	1.91902	3.09840	1.46486	-2.76227	
KCl	3.24306	4.83211	-6.17276	-4.59668	
$LiNO_3$	6.1064	0.53381	4.7514	1.7576	3.2111
$NaNO_3$	5.08766	8.31932	-27.6984	-1.06053	2.60342
KNO_3	5.5256	5.6627	-10.600	0.0063381	2.9372

Table A.11. Binary interaction coefficients to account for deviation in the thermal conductivity of salt mixtures.

Salt	Binary Interaction
Li,Na//F	$-0.103152 + 0.0157324\ X_{AA} - 0.0377589\ X_{BB}$
Li,K//F	$-0.0875173 - 0.102498\ X_{AA}$
Na,K//F	$-0.153565 + 0.227229\ X_{AA} + 0.301574\ X_{BB}$
Li,Na//Cl	$-0.103065 + 0.015220\ X_{AA} - 0.037856\ X_{BB}$
Li,K//Cl	$-0.203018 + 0.091135\ X_{AA} + 0.208979\ X_{BB}$
Na,K//Cl	$-0.135734 + 0.204097\ X_{AA} + 0.276336\ X_{BB}$
$Li,Na//NO_3$	-0.00191580
$Li,K//NO_3$	assumed to be ideal due to lack of exp data
$Na,K//NO_3$	-0.0150753

Appendix B

Pump Design

B.1 Pump Head Gaskets

The original AMT pump comes with three gaskets in the pump head that will not operate at higher temperatures and need to be replaced and/or removed. The first gasket is spring loaded to form a leak tight seal between the casing and impeller. The other two are o-ring gaskets for sealing of suction cover to casing and impeller to shaft. These gaskets have been completely removed from molten salt pump. The pump is located in a reservoir of molten salt to allow for small amountthe will be replaced with graphite, or Grafoil, or completely removed. The two gaskets for the suction cover have been completely removed. The spring loaded gasket along the shaft was replaced with a Macor bushing that is oversized. This reduces the efficiency of the pump as the fluid is able to flow up the shaft instead of being forced out of the volute.

B.2 Stress Calculations

The stress in a rotating solid cylinder is determined by the following:

$$\Lambda_{max} = \frac{P}{\omega} \quad \text{(B.1)}$$

P is the power of the motor and ω is the angular frequency determined by

$$\omega = 2\pi f \quad \text{(B.2)}$$

The radius for the shaft is determined by

$$r = \sqrt[3]{\frac{2\Lambda_{max}}{\pi G}} \quad \text{(B.3)}$$

For the molten salt pump the following conditions were used in the design of the shaft radius: RPM = 1760, P = 1.5 hp, T_{MAX} = 6.072, and G - modulus of rigidity = 61.2 MPa for SS-316 at 600ºC. Solving Equations B.1-B.3 with a factor of safety of 5 for G, results in a diameter of 0.536". The diameter of the shaft was chosen to be an inch in part due to ease in machining and ability to buy pump quality ground shaft.

B.3 Bearing Temperatures

The flanged bearings purchased for use in the pump were specified for normal operation up to 200°C. To ensure that the bearings would remain below this temperature, a conduction analysis of the pump can and shaft was analyzed using FLUENT. A 2-D model of the pump can and the shaft to the first bearing was modeled and meshed. The temperature of the reservoir can wall and along the base was set to 600°C. The heat removal rate at the bearings was set to *-5 kW/m²*. This cooling rate is equal to $^1/_5{}^{th}$ the expected cooling rate for the copper tubes based on previous experiments

using copper tubes for cooling on a super-critical water loop. The thermal profile of the pump reservoir and shaft as determined from the Fluent simulation is shown in Figure B.1.

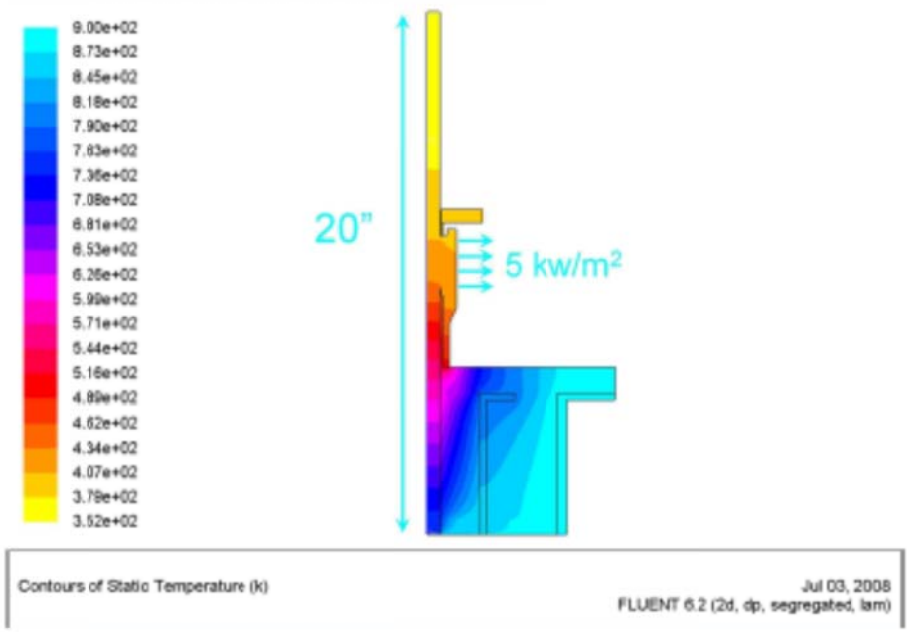

Figure B.1. The model and results from Fluent calculation examining the temperature profile of the shaft and bearings. The model height is 19.9" with the bearings located at 15" from the bottom of the model.

The temperature of the lower bearings was estimated to be 94°C. This temperature is easily within the limits of the bearing specifications. If necessary a small amount of heat removal (5 kw/m^2) along the packing box was determined sufficient for the pump design to keep the bearings below their maximum operating temperature.

B.4 Thermal Expansion

It was seen from the analysis examining bearing temperatures (Section B.3) that the shaft and reservoir can had different average temperatures. This difference in temperatures between the support system and the shaft results in movement of the impeller relative to the pump suction cover. It was necessary to ensure that during heating the impeller would have enough room to account for the thermal expansion differences. The average temperature of the shaft and support system was determined from the Fluent model used in Section B.3. The differences in the average temperature of the two parts was 160°C. Using a linear expansion coefficient of 316 SS of 18 x 10^{-6} $^1/_K$ and length of the shaft of 0.38 m, the total expansion difference was determined to be ~0.04". The amount of clearance in the pump head for the impeller is ~ 0.19".

B.5 Purchased Pump Parts

A WEG 1.5 hp, 3 phase inverter duty motor is used to power the pump. A Danfoss VLT-3004 three phase inverter is used to control the motor speed. FYH flanged ball bearings rated for

temperatures up to 200^{o}C were purchased for use along with a coupler to connect the motor to the shaft. These bearings are rated to 204^{o}C and allow for 3^{o} misalignment. A Martin Quadra-flex coupling unit is used to mechanically join the shaft to the motor. The shaft coupling is rated for maximum rotation speeds of 6000 rpm and 450 in-lbs of torque. The maximum misalignment is 0.015" parallel, 1^{o}g angular, and 0.125" axial. The pump head (suction cover, impeller, and casing) were obtained from an AMT 3690

Appendix C

Uncertainty Analysis

The molten salt loop at the University of Wisconsin is constructed from SS-316 and is designed to measure the heat transfer and pressure drop of molten salts in the laminar and transitional regime through small diameter channels. These small diameter channels are of interest in the intermediate heat exchanger between high pressure He coolant and liquid salts.

C.1 Mass Flow Meter

The mass flow meter determines the mass flow rate utilizing an energy balance over the fluid. The energy balance over the system is determined by the following

$$\frac{\partial E}{\partial t} = E_{IN} - E_{OUT} + E_{GENERATED} - E_{CONSUMED} \quad \text{(C.1)}$$

The mass flow meter is operated under steady state conditions, this eliminates the left hand side of Equation 5.42. There is also no process in the system that consumes energy. This allows Equation 5.42 to be simplifed to the following form:

$$E_{OUT} - E_{IN} = E_{GENERATED} \quad \text{(C.2)}$$

The energy in and out of the system are described by the change in enthalpy of the fluid over the region of interest multiplied by the mass flow rate,

$$E_{IN} = \dot{m} H_{IN} \quad \text{(C.3)}$$

$$E_{OUT} = \dot{m} H_{OUT} \quad \text{(C.4)}$$

For small temperature rise across the flowmeter and no phase change, the change in energy across the flowmeter is approximated by Equation C.5

$$H_{OUT} - H_{IN} = C_P \left(T_{OUT} - T_{IN} \right) \quad \text{(C.5)}$$

Combining Equation C.5 and Equation C.6 results in Equation C.6:

$$\dot{m} C_P \Delta T = E_{GENERATED} = \text{Q} \quad \text{(C.6)}$$

It is now necessary to define the amount of energy that is added to the system.

Energy is created for the mass flow meter by resistive heating of a NiCr wire to produce the energy for heating of the fluid. For resistive heating, the rate of energy generated is related to the product of the current and voltage passed through the resistive heating elements. The rate of energy loss is related to the natural convection losses and the losses in the leads of the wire leads.

$$Q = VI - E_{NAT,CONV} - \Omega_{LEADS} I^2 \quad \text{(C.7)}$$

For the current situation, the energy input will just be called Q and Equation C.7 will be utilized in determining the uncertainty in Q.

Simply put, the mass flow rate of the fluid is determined by knowledge of energy input (Q), heat capacity (C_P), and the temperature rise in the fluid (ΔT) across the region of interest, Equation C.8.

$$\dot{m} = \frac{Q}{C_P \Delta T} \tag{C.8}$$

The uncertainty in $\dot{m}$ is calculated using the uncertainties in each of the individual values;

$$\sigma_{\dot{m}} = \dot{m}\sqrt{\left(\frac{\sigma_Q}{Q}\right)^2 + \left(\frac{\sigma_{C_P}}{C_P}\right)^2 + \left(\frac{\sigma_{\Delta T}}{\Delta T}\right)^2} \tag{C.9}$$

It is then necessary to determine the uncertainties in each of the individual constituents. The uncertainty in the temperature difference across the test section is the easiest to determine. The uncertainty in the change in temperature is expressed as

$$\sigma_{\Delta T} = \sqrt{\sigma_{T^2} + \sigma_{T^2}} = \sqrt{2\sigma_{T^2}} \tag{C.10}$$

For the sheathed thermocouples from Omega (K-type), the uncertainty in each of the thermocouples is estimated to be 0.15°C. This results in an uncertainty in the temperature difference across the flowmeter to be 0.21°C. This value is the minimum uncertainty in the thermocouple measurements. Due to noise in the measurement system, often times the uncertainty in the system is calculated from the standard deviation in the thermocouple measurements of the fluid temperature. The larger of these two values, the standard deviation or 0.15°C, is used to determine the uncertainty in the mass flow rate of the fluid, Equation C.9.

The uncertainty in the heat capacity of the fluid is often given in literature as a set value of the correlation, e.g. ±5% or 10%. This is equivalent to stating: $\left(\frac{\sigma_{C_P}}{C_P}\right)$ is equal to 0.05 or 0.10. It is also necessary to account for the uncertainty in the average temperature of the fluid in the flow meter. An uncertainty analysis using the equation for the heat capacity is estimated. In general, the heat capacity of the fluid is usually given by a linear equation with respect to temperature.

$$C_P = a + bT \tag{C.11}$$

If a and b are constants, the uncertainty in the heat capacity is determined by

$$\sigma_{C_P} = b\frac{\sigma_{\Delta T}}{2} \tag{C.12}$$

Finally, the uncertainty in Q must be determined to determine the uncertainty in the mass flow rate. From Equation C.7, the total uncertainty in Q is determined by the following equations:

$$\sigma_{GEN} = VI\sqrt{\left(\frac{\sigma_V}{V}\right)^2 + \left(\frac{\sigma_I}{I}\right)^2} \tag{C.13}$$

$$\sigma_{LEADS} = R_{LEAD} I^2 \sqrt{\left(\frac{\sigma_{R_{LEAD}}}{R_{LEAD}}\right)^2 + 2\left(\frac{\sigma_I}{I}\right)^2} \tag{C.14}$$

$$\sigma_Q = \sqrt{\sigma_{GEN}^2 + \sigma_{LEADS}^2 + \sigma_{NC}^2} \quad \text{(C.15)}$$

with the uncertainty in the natural convection loss based off of free convection correlations.

With the uncertainties for each of the variables in the energy balance determined it is now possible to determine the uncertainty in the mass flow rate of the system. Using the previous determined values for the uncertainty in the properties;

C.2 Heat Transfer Coefficient

Now it is necessary to determine the uncertainties in the heat transfer coefficient, *h*. The convection coefficient is determined from the overall heat transfer coefficient, *U*. The overall heat transfer coefficient is determined by the following:

$$U = \frac{Q}{A / LMTD} \quad \text{(C.16)}$$

where, LMTD is the log mean temperature difference and is calculated based off of Equation C.17:

$$LMTD = \frac{\left(T_{s,o} - T_{f,o}\right) - \left(T_{s,i} - T_{f,i}\right)}{\ln\left(\frac{T_{s,o} - T_{f,o}}{T_{s,i} - T_{f,i}}\right)} \quad \text{(C.17)}$$

Q is the energy generated in the system due to the resistive heating of the NiCr wire. In this situation, the resulting equation for Q is the same as that determined previously for the mass flow meter, Equation C.7. *A* is the area for heat transfer to the fluid, the circumference of the inner tube multiplied by the length, *L*.

$$A = \pi D_i L \quad \text{(C.18)}$$

The heat transfer coefficient is part of the overall heat transfer coefficient, *U*. *U* is the inverse sum of the thermal resistances of the system. In the current test configurations, it is the sum of the wall resistance and the resistance due to convection to the fluid, in cylindrical coordinates:

$$UA = \frac{1}{\frac{1}{h} + \frac{r}{k_{WALL}} \ln\left(\frac{r_O}{r_I}\right)} \quad \text{(C.19)}$$

The overall heat transfer coefficient in terms of the resistances, cylindrical coordinates and using the area based off the inside of the wall

Rearranging Equation C.19 to solve for the convection coefficient,

$$h = \frac{1}{UA - \frac{r}{k_{WALL}} \ln\left(\frac{r_O}{r_I}\right)} \quad \text{(C.20)}$$

Combining Equations C.20 and C.16,

$$h = \frac{1}{\frac{Q}{LMTD} - \frac{r}{k_{WALL}} \ln\left(\frac{r_O}{r_I}\right)} \quad \text{(C.21)}$$

From measurement of the temperature of the fluid and wall temperature and heat flux along with knowledge of the thermophysical properties and geometry of the wall, *h* is then determined.

Now that there is an expression for the heat transfer coefficient, *h*, the uncertainty in the reported values can be determined from the experimental data. First, the uncertainty in the LMTD will be determined.

The LMTD is defined in Equation C.17. The uncertainty in the LMTD is based on the uncertainties in the wall and fluid temperatures. The uncertainty in the numerator of Equation C.17 is determined by

$$\sigma_{LMTD,num} = \sqrt{\sigma_{T_{S,O}}^2 + \sigma_{T_{F,O}}^2 + \sigma_{T_{S,I}}^2 + \sigma_{T_{F,I}}^2} \quad \text{(C.22)}$$

The uncertainty in the term inside the logarithim in the denominator is determined by the following

$$\Delta T_O = \sqrt{\sigma_{T_{S,O}}^2 + \sigma_{T_{F,O}}^2} \quad \text{(C.23)}$$

$$\sigma_{\Delta Y_I} = \sqrt{\sigma_{T_{S,I}}^2 + \sigma_{T_{F,I}}^2} \quad \text{(C.24)}$$

$$\sigma_{LMTD,den,\log} = \frac{\Delta T_O}{\Delta T_I} \sqrt{\left(\frac{\sigma_{\Delta T_O}}{\Delta T_O}\right)^2 + \left(\frac{\sigma_{\Delta T_I}}{\Delta T_I}\right)^2} \quad \text{(C.25)}$$

For the whole denominator the resulting term is then determined by

$$\sigma_{LMTD,den} = \frac{\sigma_{LMTD,den,\log}}{\ln\left(\frac{\Delta T_O}{\Delta T_I}\right)} \quad \text{(C.26)}$$

Finally, the total uncertainty in the LMTD is determined by using the total error for the numerator and denominator to determine the total uncertainty:

$$\sigma_{LMTD} = LMTD \sqrt{\left(\frac{\sigma_{LMTD,num}}{LMTD_{num}}\right)^2 + \left(\frac{\sigma_{LMTD,den}}{LMTD_{den}}\right)^2} \quad \text{(C.27)}$$

The uncertainty in *Q* is determined by Equation C.15, as developed in the section on the mass flow meter. While the uncertainty in *A* is determined by:

$$\sigma_A = A \sqrt{\left(\frac{\sigma_D}{D}\right)^2 + \left(\frac{\sigma_L}{L}\right)^2} \quad \text{(C.28)}$$

Finally, the uncertainty in U is then determined by combining the two equations, Equation C.29 and Equation C.28

$$\sigma_U = U\sqrt{\left(\frac{\sigma_Q}{Q}\right)^2+\left(\frac{\sigma_A}{A}\right)^2+\left(\frac{\sigma_{LMTD}}{LMTD}\right)^2} \quad (C.29)$$

Now to determine the uncertainty in the convection coefficient it is necessary to determine the uncertainty in the wall resistance, Equation 5.49

$$R_{WALL} = \frac{r_i}{k_{SS}}\ln\left(\frac{r_o}{r_i}\right) \quad (C.30)$$

The uncertainty in the radius fraction is determined by the following

$$\sigma_{r,rat} = \frac{r_o}{r_i}\sqrt{\left(\frac{\sigma_{r,o}}{r_o}\right)^2+\left(\frac{\sigma_{r,i}}{r_i}\right)^2} \quad (C.31)$$

The uncertainty in the logarithm term is then

$$\sigma_{\ln} = \frac{\sigma_{r,rat}}{r_0/r_i} \quad (C.32)$$

The uncertainty in the thermal resistance in the wall is then determined by

$$\sigma_{R_{Wall}} = R_{WALL}\sqrt{\left(\frac{\sigma_{r,i}}{r_i}\right)^2+\left(\frac{\sigma_{k_{SS}}}{k_{SS}}\right)^2+\sigma_{\ln}^2} \quad (C.33)$$

Combining the uncertainties for U and A, the following is determined

$$\sigma_{UA} = UA\sqrt{\left(\frac{\sigma_U}{U}\right)^2+\left(\frac{\sigma_A}{A}\right)^2} \quad (C.34)$$

The error in the convection coefficient is then determined by

$$\sigma_h = \sqrt{\sigma_h^2+\sigma_{UA}^2} \quad (C.35)$$

C.3 Friction Coefficient

The uncertainty in the friction coefficient is the last of the experimental values that needs to be determined for the thermal-hydraulic analysis of the molten salt loop. The friction coefficient is determined by calculating the pressure drop across the test section and then solving for the friction coefficient.

The pressure drop across the test section is experimentally measured by measuring the difference in the height between two resorvoirs and determining the pressure in each leg.

$$P_2 - P_1 = \rho_{B,2} g h_B - \left(\rho_{A,1} g h_A + \rho_{B,1} g h_B\right) + \rho_{C,1} g h_C \quad \text{(C.36)}$$

$$P_2 - P_1 = -\rho_{A,TS} g h_A - P_{Loxx} \quad \text{(C.37)}$$

were the P_{Loss} term accounts for the pressure drop due to friction, expansions, and contractions between pressure sensing devices.

Simplifying Equation C.37, the following is obtained.

$$\Delta P_{Loss} = g\left[\left(\rho_{B,1} - \rho_{B,2}\right)h_B + \left(\rho_{A,1} - \rho_{A,TS}\right)h_A + \rho_{C,1} h_{\text{(illegible)}} \quad \text{(C.38)}$$

The uncertainty in the system is now dependent on the uncertainty in the densities and height of each section. First lets analyze the uncertainty in the density differences:

$$\sigma_{\Delta\rho} = \sqrt{\sigma_{B,1}^2 + \sigma_{B,2}^2} \quad \text{(C.39)}$$

Next the uncertainty in the height and density differences are then determined:

$$\sigma_{\rho,h} = \rho h \sqrt{\left(\frac{\sigma_\rho}{\rho}\right)^2 + \left(\frac{\sigma_h}{h}\right)^2} \quad \text{(C.40)}$$

The uncertainty in the differential pressure is then

$$\sigma_{\Delta P} = \Delta P \sqrt{\sigma_{\rho,h_A}^2 + \sigma_{\rho,h_B}^2 + \sigma_{\rho,h_C}^2} \quad \text{(C.41)}$$